Probing Physics Beyond the Standard Model in Neutrino Oscillation Experiments

A thesis submitted to the
Indian Institute of Technology Gandhinagar
for the award of the degree

of

Doctor of Philosophy

by

Supriya Pan
(Roll No. 18330023)

Under the guidance of

Prof. Srubabati Goswami
Senior Professor
Physical Research Laboratory, India

Department of Physics
Indian Institute of Technology Gandhinagar
Gujarat, 382055, India

February 2024

Dedicated to,

My beloved Ma, Baba, Bon, Priya, Bestie, and friends without whose endless love and support, I could not achieve this.

Department of Physics
Indian Institute of Technology Gandhinagar
Palaj, Gandhinagar, 382055, Gujarat, India

CERTIFICATE

This is to certify that the thesis entitled "**Probing Physics Beyond the Standard Model in Neutrino Oscillation Experiments**", submitted by **Supriya Pan** (Roll No. 18330023) to **Indian Institute of Technology Gandhinagar**, is a record of bona fide research work under my supervision and guidance. I consider it worthy of consideration for the award of the degree of *Doctor of Philosophy* of the Institute.

Date: 24/02/2024
Place: Ahmedabad, India

Prof. Srubabati Goswami
Senior Professor
Theoretical Physics Division
Physical Research Laboratory Ahmedabad
Gujarat, India

DECLARATION

I certify that

a. the work contained in the thesis is original and has been done by myself under the general supervision of my supervisor.

b. the work has not been submitted to any other institute for any degree or diploma.

c. I have followed the guidelines provided by the institute in writing the thesis.

d. I have conformed to the norms and guidelines given in the ethical code of conduct of the institute.

e. whenever I have used materials (data, theoretical analysis, and text) from other sources, I have given due credit to them by citing them in the text of the thesis and giving their details in the references.

f. whenever I have quoted written materials from other sources, I have put them under quotation marks and given due credit to the sources by citing them and giving required details in the references.

Date: 24/02/2024
Place: Ahmedabad, India

Supriya Pan
Roll No.: 18330023

Acknowledgments

The journey of my Ph.D. has not been without a few turbulence, yet it's been a learning, enjoyable, and successful one. There have been a lot of people and factors that made this journey possible. The most important person is my supervisor Prof. Srubabati Goswami. Her invaluable guidance, persistent effort, and continuous support have been the key factors. Her immense knowledge in the field and plentiful experience have been very helpful to me. She has greatly improved my ways of looking at a problem as well as simply conveying the results with impactful writing. Apart from her academic guidance, she has also been sensitive, kind, understanding, and approachable, making this journey a bit easier. Hopefully, I can keep learning many good traits from her.

I would also like to express my heartfelt gratitude to my senior collaborator Dr. Animesh Chatterjee, for numerous insightful discussions and for being very supportive. His help with the numerical work has been especially important and invaluable to this thesis.

I am immensely thankful to my collaborators Dr. Monojit Ghosh, Dr. Kaustav Chakraborty and Bartol Pavlovic. Working with them, I have learned a lot.

I am grateful to the members of my DSC committee Dr. Ketan Patel, Dr. Satyajit Seth, and Prof. S. Ramachandran for their useful inputs and suggestions. Their feedback has helped me grow as a researcher and elevate my presentation skills.

Over the last five years, I have benefited from many courses by Prof. Dilip Angom, Dr. Ketan Patel, Dr. Navinder Singh, Prof. Srubabati Goswami, Prof. Namit Mahajan, Prof. Jitesh Bhat, and Prof. Som Kumar Sharma. I would also like to thank my project supervisors, Ketan Sir, Dr. Sachindra Nayek, and Dr. Arvind Singh Rajpurohit for their guidance and support. The learnings from the English literature course by Prof. Sharmita Lahiri, Dr. Bhaskar Datta, and Dr. Arka Chattopadhyay have assisted me well during my Ph.D. I am thankful to all of them.

I have also learned a lot from my seniors Dr. Tanmay Poddar, Dr. Dipyaman Pramanik, and Dr. Soumita Pramanick. My batchmates from the division Dayanand Mishra, Deepak Gaur, and Anupam Ghosh, have also contributed to my knowledge. Every other research scholar from our theoretical physics division has enriched me in many ways.

I have asked several questions to my juniors, Saurabh Kumar Shukla and Debashis Pachhar and these discussions were always very stimulating. Besides academic engagements Me, Debashis, Bharathi, and Gurucharan have had great fun playing football, volleyball, cricket, and other friends. From going to lunch together to having late-night tea, over the past few years, I have spent a lot of great times with them that have helped me keep going. I extend my gratefulness to Divya and Hintal for helping in various official activities during my PhD.

I was introduced to the field of neutrino physics during my master's project under the supervision of Dr. Sovan Chakraborty. I am thankful to him for this learning experience, which turned out to be quite helpful in later times.

I am very lucky to have had a supportive, motivating, and loving upbringing through my parents. Elderly figures of the extended maternal family have inspired me to be a better version of myself with their constant guidance and invaluable life lessons. Since childhood, my elder uncles, *boro mamu, mejo mamu, choto mamu*, have played a significant role in my education, generously imparting their knowledge on various subjects. *Na mamu* has been a steadfast source of support and motivation throughout my journey, contributing significantly to whatever modest successes I've achieved. Bubai da (Dr Dibyojyoti Ghosh) has been a mentor to me in my pursuit of following my passion for learning physics, which led to this PhD. His support, along with that of Tinku di (Dr. Susmita Ghosh), has been instrumental in navigating the challenges I've encountered along the way, making my academic journey more manageable and comfortable. I am deeply grateful for the presence of these brilliant minds within my family, whose influence has been instrumental in shaping my academic and personal development.

During this long five-year journey, being around friends has been peaceful and relieving. I found friends very early in Sandeep, Meghna, Akanksha, Yogesh, Binal, Arijit, Naba, and Vijay who have helped me settle down here and been reasons for good and fun times. Then there came certain Siddhartha Sarkar as my neighbor who became an integral part of my life and introduced me to a few more friends. Siddhartha, Deva, Kimi, Swagatika, Atif bhai, Amit bhai and Jiban became close friends during the COVID times. I also became good friends with Chaaya, Chand, Aishwarya, Pooja, and Shivali, with whom I had a great time traveling. I am also indebted to Shreya for the CR7 jersey from Portugal and for filling my tummy with well-cooked foods in the past three months. Playing with Hanchi and Zorro has always relieved all my day's stress.

Engaging in co-curricular activities has given me immense joy. I would like to thank all those with whom I have regularly played various sports. I also had a great time cooking food with my friends and juniors. Being fond of dancing, I enjoyed a lot over the years performing at cultural events with Sandeep, Meghna, Naba, Sarika, Shivani, Soumya, Naman bhai, Tanya, Mansi, Birendra, Ranjan, etc. Thanks to my friends, juniors, and seniors for making this journey enjoyable.

In my life, there has been no substitute for friends, especially at my difficult times. I am grateful to have friends like Spandan, Tanmoy, Tuhin, Rudrangsu from school and Piklu, Priyanka, Laboni, Arpita from college, who have been important to me in many ways. During my M.Sc. days, I learned much from my friends Arnab, Sourav, Kushal, Moonsun, Atanu, Susmita, Sudeshna, Bihan, Sounak, and Joydipto. It was a great couple of years of life.

Some friends do become family. Rudrangsu, Piklu, and Priyanka have been my pillars of strength for over a decade. Whenever I had a bad day, they were there with their unconditional support. I can't say how many times over the years my bestie Priyanka has motivated me or solved my problems. During the past five years, Siddhartha, Deva, Sandeep, Yogesh and Akanksha have also been with me through ups and downs, making me stay sane and calm. I can't thank them enough for what they mean to me and this entire journey.

Now, I would like to express my gratitude to Priya. She has been a great source of my energy and a sink to negatives in my life. I am fortunate to have her love, care, and support.

All of this journey would not have been possible without my parents. All the knowledge and basic human values they have instilled in me have been profoundly important in every step of my life. Their support and belief in me always kept me going, even on my worst day.

My journey also became a lot easier due to my youngest friend, my sister. Many times, she has been strict like mother, and at other times, she was just my sweet sister standing with me at my happiest and saddest moments.

Last but not least, I would like to thank that teenager who dreamed of making cool inventions and being a scientist and never gave up on his dream. Now all grown up and on the eve of submitting his Ph.D. thesis, there is a sense of a small achievement. However, there is a lot of journey left and many aspirations and achievements to be accomplished.

Date: 24/02/2024
Place: Ahmedabad, India

Supriya Pan
Roll No.: 18330023

Abstract

The paradigm of the standard three neutrino oscillation is experimentally well established. The parameters governing the three neutrino oscillations are the mixing angles $\theta_{12}, \theta_{13}, \theta_{23}$, CP phase δ_{13}, and the mass squared differences $\Delta_{21} = m_2^2 - m_1^2, \Delta_{31} = m_3^2 - m_1^2$ where m_1, m_2, m_3 are mass eigenvalues of neutrino mass states. Among these parameters, the octant of θ_{23}, the sign of Δ_{31}, i.e., mass ordering (MO) and the CP phase δ_{13} are yet to be determined with considerable precision. The major aim of the current and future neutrino oscillation experiments is to extract accurate values of these parameters. These experiments can also probe into the effects of beyond standard model (BSM) physics in neutrino oscillation signals, like sterile neutrinos, long rang force, non-standard interaction (NSI), Lorentz invariance violations(LIV), CPT violations, neutrino decay, non-unitary mixing, etc. In this thesis, we explore three such BSM scenarios of sterile neutrino, LIV, and NSI. In these contexts, we use experimental configurations similar to the proposed DUNE experiment with a liquid argon detector at 1300 km baseline from the source beam to study both accelerator and atmospheric neutrino, the proposed setup of T2HK/T2HKK with accelerator neutrino, and the detected events of astrophysical origin at IceCube.

Results from the experiments like LSND, and MiniBooNE hint towards the possible presence of an extra eV scale sterile neutrino. The addition of such a neutrino will significantly impact the standard three flavor neutrino oscillations; in particular, it can give rise to additional degeneracies due to new sterile parameters. In the third chapter, we investigate how the sensitivity to determine the octant of the neutrino mixing angle θ_{23} and the sign of Δ_{31} is affected by introducing an eV scale sterile neutrino to the standard three generation framework. We compute the oscillation probabilities analytically in the presence of a sterile neutrino, using the approximation that Δ_{21}, the smallest mass squared difference, is zero. We use these probabilities to understand the degeneracies analytically at different baselines. We present our results on the sensitivity to the octant of θ_{23} and the sign of Δ_{31} for beam neutrinos using a liquid argon time projection chamber (LArTPC) detector. We also obtain the octant and MO sensitivity using atmospheric neutrinos using the same LArTPC detector. For the latter, we present our results assuming (i) no charge identification capability and (ii) partial charge identification capability using the charge tagging ability of muon capture in Argon which allows one to differentiate between muon neutrino and antineutrino events. The combined sensitivity of beam and atmospheric neutrinos in a similar experimental setup is also delineated.

For an eV scale sterile neutrino, the cosmological constraints dictate that the sterile state is heavier than the three active states. However, for lower masses of sterile neutrinos, it can be lighter than one and/or more of the three states. In such cases, the mass ordering of the sterile neutrinos also becomes unknown, along with the mass ordering of the active states. In the fourth chapter, we explore the mass ordering sensitivity in the presence of a sterile neutrino assuming the mass squared difference $|\Delta_{41}|$ to be in the range $10^{-4} - 0.1$ eV^2. We study how the possible determination of (i) the sign of Δ_{31}, (ii)the sign of Δ_{41}, and (iii)the octant of θ_{23} gets affected by the presence of a sterile neutrino in the above mass range. This analysis is done in the context of a liquid argon detector using beam neutrinos travelling a distance of 1300 km and atmospheric neutrinos, which propagate through a distance ranging from 10 - 10000 km, allowing resonant matter effects. Apart from presenting separate results from these sources, we also do a combined study and probe the synergy between these two in giving an enhanced sensitivity.

In the fifth chapter, we study the implications of the Dark Large Mixing Angle (DLMA) solutions of θ_{12} using the IceCube data. DLMA solution of θ_{12} refers to $\theta_{12} > 45^\circ$ as opposed to the standard Large Mixing Angle (LMA) solution of $\theta_{12} < 45^\circ$. DLMA solutions can arise if non-standard interactions are included. We study the consequences in the determination of the neutrino oscillation parameters, namely octant of θ_{23} and δ_{CP} in the light of both LMA and DLMA solutions of θ_{12}. We find the degeneracies at the probability level related to LMA and DLMA solutions involving parameters θ_{23}, δ_{CP}. We perform a chi-square fit of flavour ratios using three different astrophysical sources, i.e., μ source, π source, and n source and find the sensitivity to the two solutions of θ_{12}.

In the sixth chapter, the considered BSM scenario is CPT violating LIV. Lorentz invariance and CPT are fundamental symmetries of nature. The violation of Lorentz invariance can also lead to CPT violations. Neutrino oscillation provides an avenue to probe small LIV. In our work, we focus on the effect of LIV parameters on the sensitivity to CP violation. We evaluate the sensitivity in two proposed configurations; (i)T2HK experiment: one detector each placed at 295 km and 1100 km, and (ii)T2HKK experiment: two identical detectors at 295 km. This study probes the effect of CPT violating parameters $a_{e\mu}, a_{e\tau}, a_{\mu\tau}$. We compare the CP sensitivities at T2HK and T2HKK configurations and explore the synergistic effects between the two baselines in the T2HKK configuration.

Keywords— sterile neutrino, octant of θ_{23}, mass ordering, CP sensitivity, DLMA, atmospheric, astrophysical, accelerator, DUNE, T2HK, T2HKK, IceCube

Table of Contents

List of Figures

List of Tables

List of Symbols

α	Alpha Particle
β	Beta Particles
Δ_{ij}	Mass-squared difference
$\delta_{ij}, \phi_{\alpha\beta}$	Phases
$\epsilon_{\alpha\beta}$	NSI parameters
γ	gamma ray
γ_5	Chirality operator
$\mu^{\pm}$	Positively, negatively charged muon
$\nu(\bar{\nu})$	Neutrino (Anti-neutrino)
ν_μ	Muon Neutrino
ν_τ	Tau Neutrino
ν_e	electron neutrino
ϕ	Wave function
ρ	Density of electrons in matter
τ	Tau
θ_{ij}	Mixing angles
$a_{\alpha\beta}$	LIV parameters
E	Energy
$e^{\pm}$	Electron, Positron
G_F	Fermi Constant

h	helicity operator
L	Baseline Length
$p, \vec{p}$	momentum
$P_{L,R}$	Left handed, right handed chirality
Q	Electric Charge
T_3	Third component of Isospin
Y	Hyper charge

"I have done a terrible thing; I have postulated a particle that cannot be detected".

Wolfgang Pauli

1
Introduction

This chapter contains the history of the neutrino, the various sources of these particles, neutrinos in the standard model, as well as a brief introduction to neutrino oscillation. A short review of the topics studied in this thesis is also outlined.

Neutrinos are tiny charge-neutral elementary particles. They interact via the short-range weak interaction. Their inherent charge neutralness forbids them to interact electromagnetically. Being one of the lightest particles, neutrinos also experience feeble gravitational interaction. As neutrinos interact very weakly, this allows them to travel through matter unhindered for very large distances of the scale of a galaxy. This same property makes the detection of a neutrino very difficult, making it the most elusive particle. The neutrinos were born out of the great mind of Wolfgang Pauli to explain the continuous energy spectrum observed in beta decay. He first proposed the hypothesis of `a particle, later named as neutrino,` being emitted from beta decay along with electron in an open letter[1] to the *radioactive ladies and gentlemen* in 1930 at Tübingen conference of radioactivity.

1.1 The ghosts in β decay

The discovery of radioactivity[2] in 1896 by Henri Becquerel ushered in a new era of physics. In 1899, Ernest Rutherford distinguished two different radiations, namely α and β in Uranium [3]. Later in 1900, Paul Villard observed neutral radiation called γ in radium[4]. The α particle was found to be positively charged. Several experimental observations by various scientists, Becquerel, Egon von Schweidler, and Freidrich Giesel confirmed the mass-to-electric charge ratio of β particles to be the same as that of the electrons.

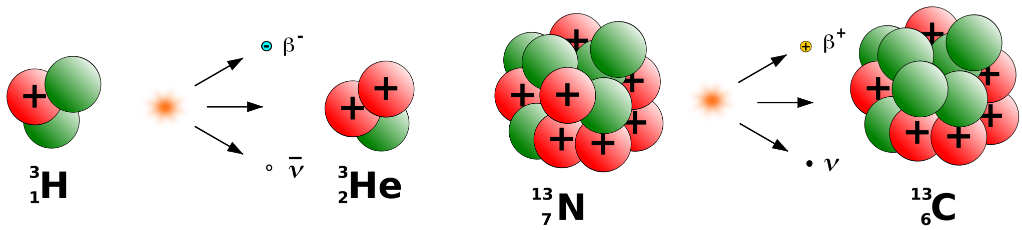

Figure 1.1: Illustration of β^- (left) decay and β^+ (right) decay [https://openclipart.org]

The velocity and the energy of the emitted α particles in a particular decay were observed by William Bragg to have a fixed value [5]. Walter Kaufmann found that the velocity spectrum of β particles coming out of radium has a wide range

[6], unlike α, γ rays. Scientists suggested that the sources were impure and contained various radioactive elements, leading to different energies in β decay. Another hypothesis was that the energies of mono-energetic electrons are absorbed exponentially while traveling through matter. This hypothesis was proven wrong when William Wilson observed that the absorption of mono-energetic electrons by various mediums is a linear function of the thickness of the material[7]. He further demonstrated that exponential absorption would require a continuous energy spectrum by making fixed energy electrons pass through a second absorber to have a continuous spectrum before finally detecting them. In 1914, using Hans Geiger's newly built counters, the beta decay spectrum of radium was observed to be continuous by James Chadwick[8]. This result was puzzling and couldn't be explained by the existing theories. The law of conservation of energy and momentum seemed to be violated in this observation. The violation of conservation of angular momentum was also observed in beta decay as the spin of the parent nucleus was changed by $\hbar$, and an electron has a spin of $\hbar/2$, leading to a mismatch. All these concerns were addressed in the letter presented in 1930 by Pauli. He postulated a new particle that he named `neutron` emitting in a beta decay alongside an electron. Later, in 1933, Pauli himself presented his idea of a neutral, spin-half, very light particle (now renamed as `neutrino`) being produced in beta decay at an international conference in Brussels. After the Brussels conference, Fermi formulated a complete quantum field theoretical description of beta decay. In his theory, a charge-neutral particle, anti-neutrino, is produced along with the electron in a pair in decays of proton-rich nuclei. However, the challenge of detecting such a particle was an alien idea even to Pauli.

1.2 The ghost hunters

In Pauli's own words,*"I admit that my remedy may seem almost improbable because one probably would have seen those neutrinos, if they exist, for a long time"*. Pauli's hypothesis was well received as it explained all the recurring questions of the continuous beta decay spectrum. However, neutrinos must be detected to establish their existence. This was accomplished almost 25 years after Pauli's hypothesis by Clyde Cowan and Frederick Reines of Los Alamos National Laboratory. They detected anti-neutrinos from a nearby nuclear reactor at the Savannah River Plant in South Carolina. Two water tanks of 200 liters injected with cadmium chloride of 40 kg were used as a target for neutrinos. These two tanks were placed in between the tanks filled with liquid scintillators. When an anti-neutrino interacted with a proton, it produced a neutron and positron pair. The positron getting annihilated by an electron in the medium creates a pair of gamma rays producing photons while passing through the liquid scintillators. These photons were detected by the photomultiplier tubes (PMTs). The produced neutron is absorbed by cadmium, preceded by another gamma-ray. Therefore, two simultaneous signals were followed by another signal a few microseconds later. They measured a cross-section of 6.3×10^{-44} cm^2 against a prediction of 6×10^{-44} cm^2. The results were published in the July 20, 1956 issue of Science[9]. Reines was awarded the Nobel Prize in 1995 for this discovery.

Discovery of the muon from cosmic ray showers[10] and the eventual detection of a muon decaying to an electron made physicists conjecture the presence of a second type of neutrino. In 1962, physicists Leon Lederman, Melvin Schwartz, and Jack Steinberger discovered a second type of neutrino. This neutrino, created in the decay of pions produced through the collision of high energetic protons with beryllium target, produced muon when interacting in the detector[11] at Brookhaven National Laboratory. As this type of neutrino created a muon instead of an electron, it was confirmed as a second type of neutrino called the muon neutrino. This established that the leptons μ^+, ν_μ, and e^-, ν_e exist in a pair, laying the foundation of a doublet structure of lepton. Nobel Prize in 1988 was given to the scientists involved in the detection of ν_μ *"for the neutrino beam method and the demonstration of the doublet structure of the leptons through the discovery of the muon neutrino"*[1]. The existence of a third type of neutrino was postulated when the third charged lepton tauon (τ) was detected[12] in 1975 at the SLAC National Accelerator laboratory by a group of scientists led by Martin Lewis Perl. Finally, in 2000, tau neutrino was discovered in the DONUT experiment[13].

[1] https://www.nobelprize.org/prizes/physics/1988/summary/

1.3 Neutrinos: the chameleons of SM

The standard model of particle physics is a mathematical model that describes three fundamental interactions: electromagnetic, strong, and weak. It incorporates all the elementary particles primarily classified as fermions and bosons. The theoretical framework of the SM[14–16] was formulated throughout the latter half of the twentieth century, with the current form being finalized in the mid-1970s. The SM is represented by non-abelian gauge theory based on a symmetry group $SU(3)_C \times SU(2)_L \times U(1)_Y$, where C denotes the color quantum number and Y is the hypercharge. In contrast, L in the $SU(2)$ group signifies the left-handed chirality of the fermions.

The chirality of a fermion is an abstract concept. The eigenstates of the chirality operator γ_5 are not the same as the eigenstates of the Dirac Hamiltonian. One gets the left chiral or right chiral part of state ψ by projection operators $P_L = \frac{1-\gamma_5}{2}$, $P_R = \frac{1+\gamma_5}{2}$. Any particle state thus can be represented by a superposition of both left-chiral (ψ_L) and right-chiral (ψ_R) states as;

$$\psi = \psi_L + \psi_R = P_L\psi + P_R\psi \tag{1.1}$$

For massless (relativistic) particles, like neutrinos, the chirality is the same as the helicity. The helicity of a particle is the projection of spin $\vec{\Sigma}$ in the direction of momentum $\vec{p}$, defined as $h = \vec{\Sigma}.\hat{p}$. The helicity of a particle can be either positive (right-handed),i.e., spin and momentum are parallel, or negative (left-handed),i.e., spin and momentum are anti-parallel. The helicity states of a particle are also the eigenstates of the Dirac Hamiltonian.

The fermions, the fundamental constituents of all the visible matter, occur in two groups: leptons and quarks. Each of these groups consists of three generations of particle pairs. In table 1.1, the fermionic representations of leptons and quarks are displayed along with their quantum number under the SM gauge groups.

Fermions	Lepton Doublet	Quark Doublet	Lepton Singlet	Up Singlet	Down Singlet
Quantum No	$l_L(1,2,-\frac{1}{2})$	$Q_L(3,2,\frac{1}{6})$	$l_R(1,1,-1)$	$u_R(3,1,-\frac{1}{3})$	$d_R(3,1,\frac{2}{3})$
1st Gen	$\begin{pmatrix}\nu_{eL}\\ e_L\end{pmatrix}$	$\begin{pmatrix}u_L\\ d_L\end{pmatrix}$	e_R	u_R	d_R
2nd Gen	$\begin{pmatrix}\nu_{\mu L}\\ \mu_L\end{pmatrix}$	$\begin{pmatrix}c_L\\ s_L\end{pmatrix}$	μ_R	c_R	s_R
3rd Gen	$\begin{pmatrix}\nu_{\tau L}\\ \tau_L\end{pmatrix}$	$\begin{pmatrix}t_L\\ b_L\end{pmatrix}$	τ_R	t_R	b_R

Table 1.1: Fermionic representations under the $SU(3)_C \times SU(2)_L \times U(1)_Y$ group.

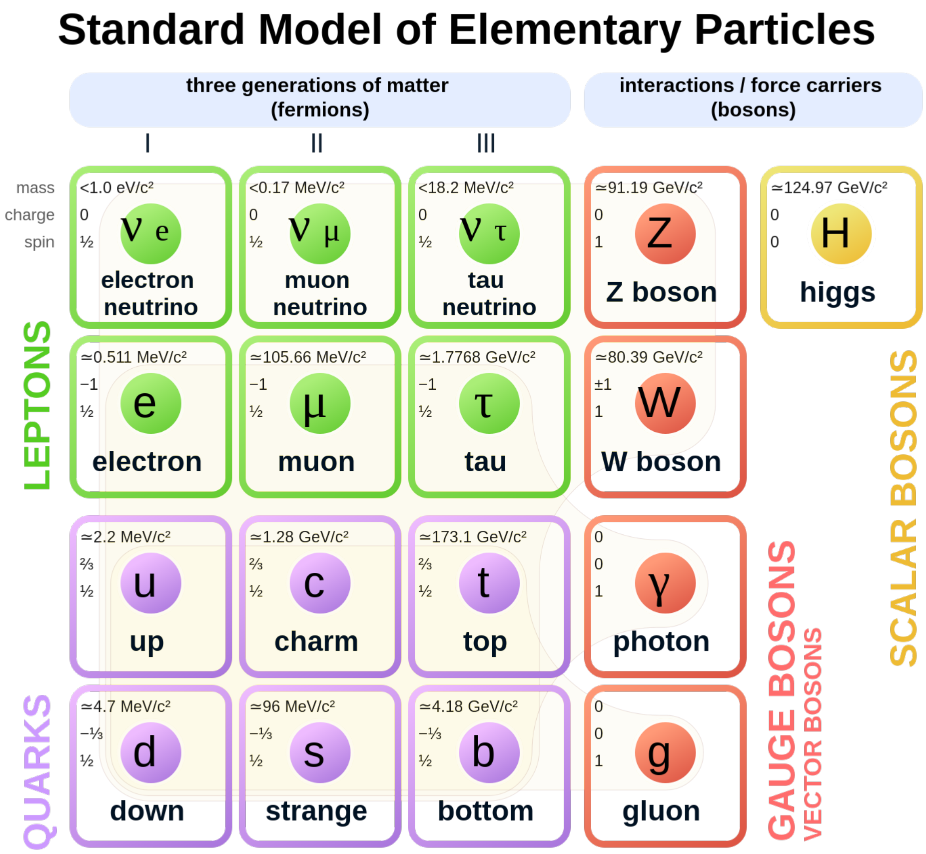

Figure 1.2: The Standard Model of Particle Physics.[https://physics.aps.org/articles/v13/123]

The first generation of particles is the lightest and most stable, whereas the third generation is the heaviest. The leptons are singlets under $SU(3)$ while quarks are triplets under $SU(3)$. Charged fermions in the SM have both or one of the left-handed or right-handed chirality. The left-handed fermions form the $SU(2)$ doublets, whereas the right-handed fermions form a singlet. The neutrinos ν_e, ν_μ, ν_μ along with their charged partners e^-, μ^-, τ^- respectively form doublets. However, right-handed neutrinos aren't included in the SM. The left-handed quarks up, charm, and top also form SU(2) doublets with down, strange, and bottom, respectively, while the right-handed quarks form a singlet. The up type and down type quarks have two-thirds and a negative one-third of a unit electric charge, respectively. The numbers in the second row of table 1.1 refer to quantum no corresponding to $SU(3)$, $SU(2)$, and $U(1)$ gauge groups, respectively. The entry $l_L(1, 2, -\frac{1}{2})$ signifies that lepton doublets are singlet under $SU(3)$, doublet under $SU(2)$ and contains hypercharge $Y = -\frac{1}{2}$. The electric charge Q can be obtained by $Q = T_3 + Y$.

Besides the Fermions, SM also contains Bososns, the mediator particles of the fundamental interactions. The electromagnetic interaction is mediated by massless photons. The massless gluons are the carriers of the strong interaction. The $W^{\pm}$, Z^0 bosons are exchanged in the weak interactions, known as charge-current (CC) and neutral-current (NC) interactions, respectively. Every fermion in the SM interacts weakly, whereas only quarks show strong interaction, and all except neutrinos participate in EM. The mass term of a fermion, $\bar{\psi}_L\psi_R$, is not gauge invariant as $\bar{\psi}_L$ is a doublet and ψ_R is a singlet under $SU(2)$. This is solved through the interaction with the scaler boson called the Higgs boson. The spontaneous symmetry breaking(SSB) of $SU(2)_L \times U(1)_Y \to U(1)_{EM}$ leads to masses to the gauge bosons and fermions through the Higgs mechanism. The mass term in SM can be written as,

$$m = \phi\bar{\psi}_L\psi_R; \tag{1.2}$$

where ϕ is the Higgs doublet. Higgs boson was discovered in 2012 by CMS and ATLAS experiments[17, 18], thus establishing the SM on a firm footing.

Neutrinos are massless in SM, as right-handed neutrinos don't exist. This was motivated by the observation of parity violation. In 1956, scientists led by Chien Shiung Wu showed the parity violation and measured[19] the angular distribution of the electrons to find that electrons produced in the decay of ^{60}Co were emitted more in the opposite direction to the spin than along the spin, suggesting the right-handed nature of anti-neutrinos;

$$^{60}\mathrm{Co} \rightarrow^{60} \mathrm{Ni} + \mathrm{e}^{-} + \bar{\nu}_{\mathrm{e}} \tag{1.3}$$

The non-existence of right-handed electrons implied parity violation in this process, as suggested by Lee and Yang [19]. Later, in 1958, scientists at Brookhaven National Laboratory determined that neutrinos are always left-handed in the famous Goldhaber experiment[20]. In the SM, the neutrinos are always left chiral, and anti-neutrinos are right chiral.

Neutrinos, like chameleons, have been observed to change their flavors while traveling. This is a quantum mechanical phenomenon known as neutrino oscillation that requires neutrinos to be massive.

1.4 Phantom neutrinos and where to find them

The neutrinos are the second most abundant particle in the universe after the photons. There are several natural and artificial sources of neutrinos. The natural sources of neutrinos are the sun and other stars, supernovae, active galactic nuclei (AGN), the interaction of cosmic rays in the Earth's atmosphere, radioactive materials inside the Earth, etc. There are also neutrinos created at the time of the big bang that are yet to be detected. The nuclear reactors and the accelerators that produce the neutrino beam serve as artificial sources. The energy of these neutrinos from various sources ranges from micro electron volt (μeV) to 10^{15} eV (PeV) as can be seen in fig. 1.3.

1.4.1 Cosmological Neutrinos (Cosmic neutrino background)

The Big Bang is the initializing event of the vast universe from a singular point of enormous temperature and heat. Therefore, information on these early times is of great interest. One way to look at these earlier times of the universe is to capture the lights, known as cosmic microwave background(CMB). Observation of neutrinos is another way to look into the signatures of the early universe. The neutrinos,

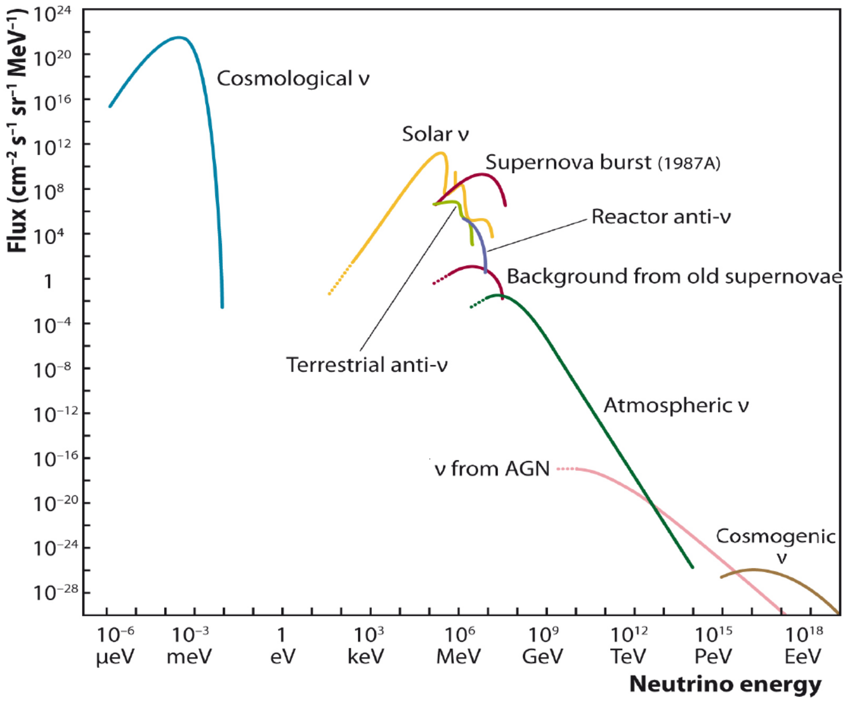

Figure 1.3: Energy spectrum of neutrinos.[https://masterclass.icecube.wisc.edu]

referred to as cosmological or relic neutrinos, created at the time of the Big Bang, have the highest flux, and lowest energy as shown in fig. 1.3. However, these neutrinos are yet to be detected. The photon decoupled from other matters(quarks and leptons) around 380000 years after the Big Bang. However, according to the model of standard Big Bang theory, light neutrinos would have thermally decoupled approximately 1 second after the Big Bang, when the temperature decreased to about 10^{10} K (MeV). Thus, these neutrinos remain the first witnesses of the Big Bang and constitute the cosmic neutrino background (CNB). Estimation by the scientists shows that the temperature of CNB neutrinos has now decreased to 1.95 K, and the density of the CNB neutrinos, including all the species, will be around 330 neutrinos per cm^3 at present. The energy of these neutrinos will be in the range of $10^{-4} - 10^{-6}$ eV making their detection more challenging. The presence of CNB is predicted to evoke irregularities in the phases of the CMB fluctuations. In 2015, such a phase difference was observed in CMB[21], and this result can be attributed to the neutrinos of almost exactly the temperature (1.96 $\pm$ 0.02 K) predicted by the Big Bang Theory.

Upcoming experiment PTOLEMY[22], which will be made up of 100 g of tritium target, aims to detect of Big Bang neutrinos. This can be accomplished by detecting[23] the electrons produced in the process of capturing the relic neutrinos through tritium as;

$$\nu + {}^3H \rightarrow {}^3He + e^- \tag{1.4}$$

1.4.2 Solar neutrinos

Nuclear fission inside the sun's core is the most prominent source of neutrinos that travels through Earth. The neutrinos produced in the sun have energy ranging from a few eV to 18 MeV. The primary source, the proton-proton (pp) chain, accounts for 98.4% of the solar neutrino flux.

$$p^+ + p^+ \rightarrow {}^2H + e^+ + \nu_e \tag{1.5}$$

The rest comes from the Carbon-Nitrogen-Oxygen (CNO) chain. The pp chain produces five different types of neutrinos as illustrated in fig. 1.5: pp, pep, ^{7}Be, ^{8}B, and hep neutrinos. Almost 91% of the solar neutrino flux comes from pp neutrinos having energy less than 0.4 MeV. ^{7}Be neutrinos have a significant 7% contribution in solar neutrino flux. Neutrinos created from the decay of ^{8}B in the ppIII chain have energy up to 15 MeV, but they are only 0.02% of the total solar neutrinos. The pep neutrinos with energy 1.5 MeV are produced in the reaction of two protons and an electron. The hep neutrinos emerge from the fusion of helium-3 and proton with energy up to 18 MeV. In the CNO cycle, most of the neutrinos emerge from the decay of ^{13}N ($E_\nu \leq$ 1.2MeV) and ^{15}O ($E_\nu \leq$ 1.7 MeV).

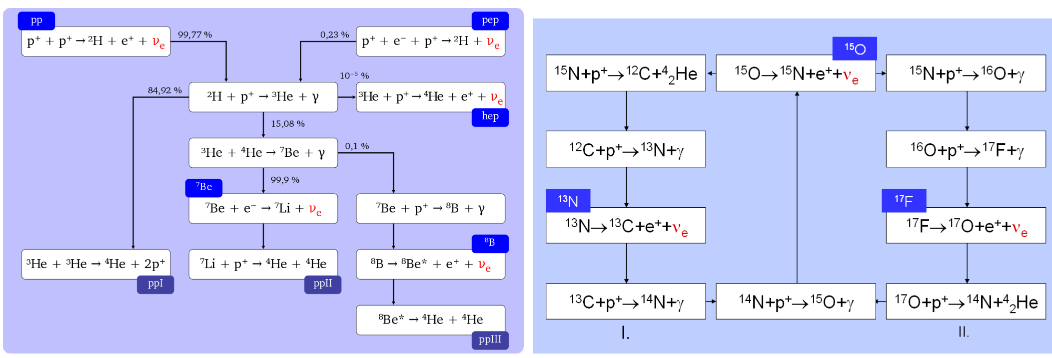

Figure 1.4: Schematics of the pp chain [https://en.wikipedia.org/wiki/Proton-proton-chain] (left) and CNO cycle [https://commons.wikimedia.org/wiki] (right).

The first detection of solar neutrinos was performed by Ray Davis in the Homestake gold mine experiment in 1968[24]. The other notable experiments to observe solar neutrinos are Kamiokande[25], Super-Kamiokande, GALLEX[26], GNO[27], SAGE[28], and SNO[29].

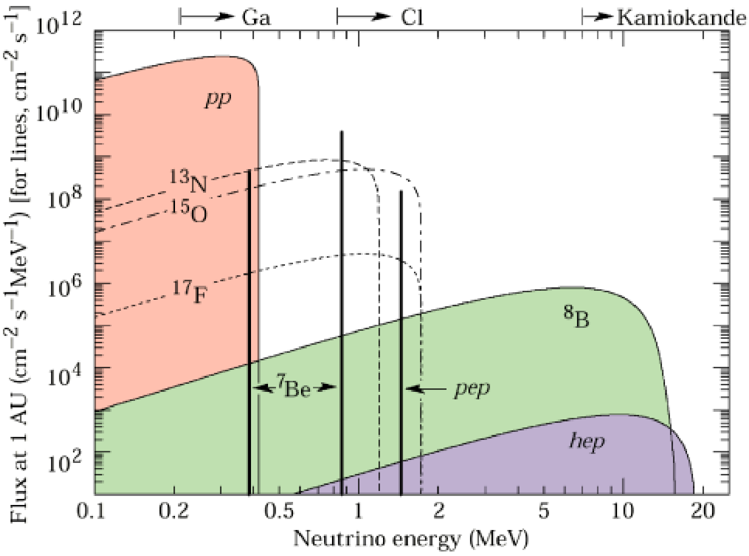

Figure 1.5: Solar neutrino energy spectrum [https://neutrino-history.in2p3.fr/]. The thresholds of different solar experiments are shown at the top.

1.4.3 Supernova neutrinos

Supernovae are the last evolutionary stage of a massive star. A supernova is formed with a luminous explosion expelling a huge amount of matter at high velocity, along with neutrinos carrying almost 99% of the gravitational potential energy of the dying star. These neutrinos are of all kinds of lepton flavors, having a typical energy of 10-20 MeV.

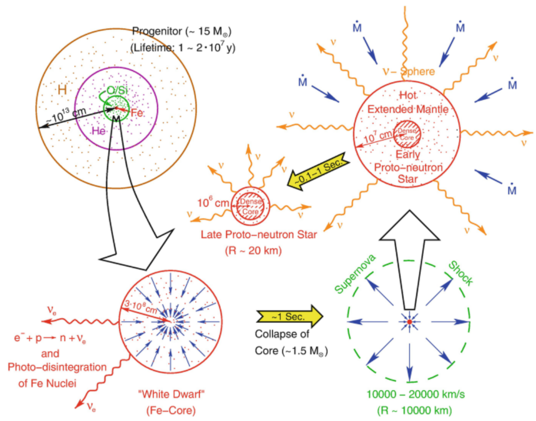

Figure 1.6: Supernova evolution[30]

The water Cherenkov detector of Kamiokande detected[31] 11 high-energy neutrinos in 1987. Along with it, two other detectors, BASKAN[32] and IMB[33], detected a total of 24 events within a time frame of 12 seconds. The direction of the neutrinos pointed towards a very bright explosion observed by telescopes in the Larger Magellanic Cloud, later known as supernova SN1987A. The models of supernova suggest neutrinos play an important role in their evolution[34, 35]. Thus, the detection of these neutrinos will provide valuable information about supernovae and stellar evolution.

1.4.4 Geo neutrinos

The anti-neutrinos produced naturally in the β decay process from radioactive metals like uranium, potassium, and thorium within the earth are known as geo-neutrinos. These neutrinos have energies of the order of a few MeV. Although the amount and distribution of radioactive material in the Earth's crust are well known, there is a scarcity of data from the Earth's interior beyond about 10 km. The measurements of geo-neutrinos can help determine the profile of the radioactive metals inside the earth and consequently understand the heat generation in the earth's interior.

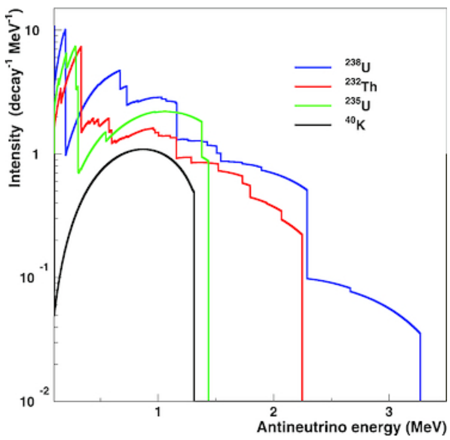

Figure 1.7: The antineutrino intensity energy spectra per decay of U, Th, & K[36]

Krauss, Glashow, and Schramm calculated[37] the flux of geo neutrinos in 1984, along with providing possible detection techniques. Geo-neutrinos are captured through the inverse beta decay process on free the proton.

$$\bar{\nu}_e + p \rightarrow e^+ + n \tag{1.6}$$

This requires anti-neutrinos with at least 1.8 MeV energy, and only $\bar{\nu}_e$ coming from Th^{232} and U^{238} can be detected. In 2005, the KamLAND experiment presented[38] the first ever measurement of around 54 geo-neutrino events. In 2011, updated results of KamLAND identified 106 geo-neutrino events and found that Th^{232} and

U^{238} together account for 20.0 TW of radiogenic power [39]. In 2010, Borexino in Italy observed[40] 10 geo-neutrinos rejecting the null geo-neutrino hypothesis by 4.2σ. The detection of 24 geo-neutrino events[41] at Borexino in 2015 showed that 20-23 TW of radiogenic power is accounted for U and Th, and the amount of U and Th in the Earth's crust is similar to that of the mantle.

1.4.5 Atmospheric neutrinos

Neutrinos are also generated due to the interaction of high energy cosmic rays ($E < 10^{12}$ eV), mostly made of high energy protons, alpha particles along with a few heavy nuclei, with the particles of the Earth's atmosphere. After the cosmic rays strike the particles in the atmosphere, pions $\pi^\pm$ and kaons $K^\pm$ are produced, which decay to produce neutrinos and anti-neutrinos in the following way,

$$\pi^\pm/K^\pm \to \mu^\pm + \nu_\mu(\bar{\nu}_\mu) \tag{1.7}$$

$$\mu^\pm \to e^\pm + \nu_e(\bar{\nu}_e) + \bar{\nu}_\mu(\nu_\mu) \tag{1.8}$$

The atmospheric neutrino flux contains four different types of neutrinos. For the above decay chain, the ratio of muon to electron neutrinos is predicted to be around 2. The atmospheric neutrinos come from everywhere in the atmosphere and can have baselines from 15-12000 km. These neutrinos have high energies ranging from few MeV to 10^6 GeV, although the flux falls off drastically for higher energies above 1 GeV. The cosmic rays are isotropic around the Earth, and neutrino flux is up-down symmetric for $E >$ GeV as seen from the right panel of fig. 1.8, i.e., $\phi(E, \cos\theta) = \phi(E, -\cos\theta)$ with θ being the zenith angle. The fluxes of atmospheric neutrinos on the Earth are well calculated[42–45] by several simulation studies using the inputs of the measured cosmic ray flux and the hadronic interactions. The first detection of atmospheric neutrinos came from two experiments in India[46] and South Africa[47] in 1965. Subsequently, Kamiokande[48] and its successor Super-Kamiokande(SK)[49] detected atmospheric neutrinos.

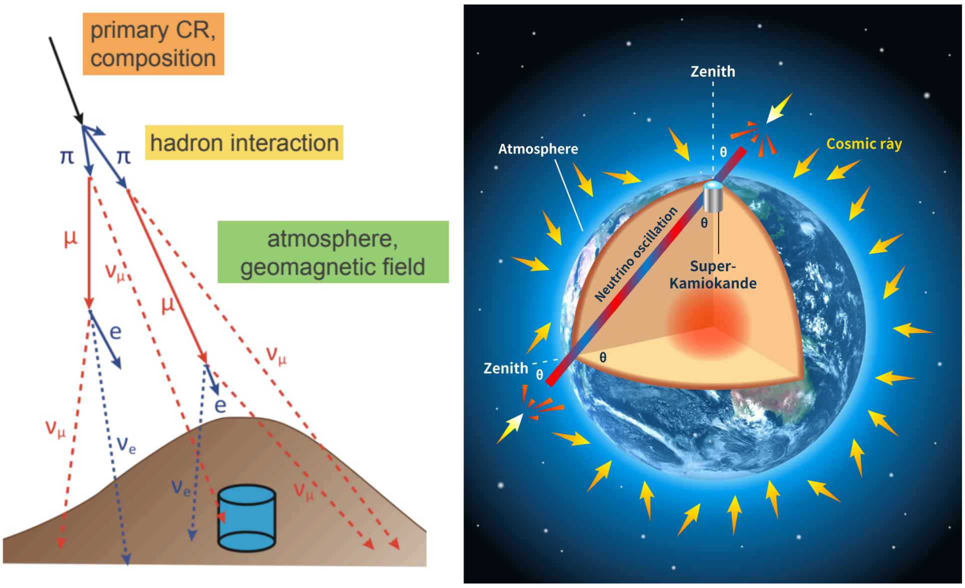

Figure 1.8: Production of atmospheric neutrinos (left)[https://indico.cern.ch/]. Atmospheric neutrino flux around Earth (right)[https://www-sk.icrr.u-tokyo.ac.jp/]

1.4.6 Ultra high energy neutrinos

Very high energy neutrinos are hypothesized to be generated in astrophysical sources like active galactic nuclei (AGN), gamma-ray bursts (GRB), pulsars, blazars, high-energetic cosmic rays, etc. As these neutrinos travel without being affected by interstellar magnetic fields, detection of these will lead us to identify the source of events in the cosmos and important information about the source.

Currently, the experiments aiming to detect these ultra-high energy neutrinos are IceCube, ANtarctic Impulsive Transient Antenna (ANITA), Astronomy with a Neutrino Telescope, and Abyss environmental RESearch (ANTARES). In 2013, IceCube detected[50] 28 neutrinos with origins outside the Solar System, and among those a pair of high energy neutrinos in the peta-electron volt range, making them the highest energy neutrinos discovered to date. Later in 2014, the number of detected events[51] increased to 37 candidates, including a new high energy neutrino at 2000-TeV given the name of "Big Bird". In 2018, for the first time, IceCube traced[52] a high-energy cosmic neutrino back to its source, later identified as a blazar TXS 0506+056, an energetic galaxy powered by a supermassive black hole. This ushered neutrinos into the age of multi-messenger astronomy to study cosmic phenomena.

1.4.7 Reactor Neutrinos

Reactors are the most prominent terrestrial source for neutrinos. Nuclear fission creates abundant electron anti-neutrinos through beta decay. In the reactors, heavy elements such as uranium (^{235}U, ^{238}U) or plutonium (^{239}P, ^{241}P), when bombarded with high energy particles, break up into lighter elements and becomes more stable through beta decay. Reactor neutrinos are purely electron anti-neutrinos with energies of 0.1-10 MeV. Every fission reaction creates six $\bar{\nu}_e$, which carry about 4.5% of the process's total energy (200 MeV). Large no of $\bar{\nu}_e$'s are created; for example, 2×10^{20} per second in 4π solid angle in a reactor with 1 GW power. The first neutrino detection was also from a reactor source in 1956 by Reines and Cowan, as mentioned earlier. Subsequently, many experiments have been able to detect neutrinos coming from reactors.

1.4.8 Accelerator neutrinos

Intense neutrino beams can be generated using particle accelerators. In this way, one can have a neutrino beam with well-known properties. Most of the neutrinos produced in these accelerators are either muon neutrinos or antineutrinos, although there are few electron neutrinos (anti-neutrino). A schematic diagram of a typical accelerator neutrino beam setup is given in fig. 1.9.

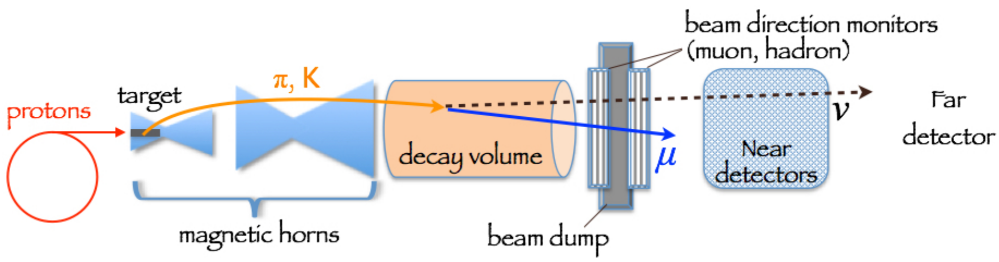

Figure 1.9: Schematic diagram of a typical accelerator neutrino setup [53]

Firstly, accelerated protons collide into a fixed target, often made of beryllium or graphite, creating secondary charged particles, like pions and kaons. These charged mesons decay to produce neutrinos through two mechanisms: (i) decay in flight (DIF) and (ii) decay at rest (DAR).

In the DIF mechanism, positively or negatively charged particles are selected through magnetic horns and focused on the decay volume. These mesons decay while traveling through decay volume, creating high energy neutrino or antineutrino beams of $0.5 - 50$ GeV. The main sources of DIF (anti)neutrinos are;

$$\pi^+/K^+ \to \mu^+ + \nu_\mu, \qquad \pi^-/K^- \to \mu^- + \bar{\nu}_\mu \tag{1.9}$$

Most of the charged pions decay in flight inside the long decay pipe to respective muon and muon (anti)neutrino. The length of the decay pipe is optimized for producing the highest no of muon neutrinos; however, few electron neutrinos are also created through muon decay;

$$\mu^+ \to e^+ + \nu_e + \bar{\nu}_\mu, \qquad \mu^- \to e^- + \bar{\nu}_e + \nu_\mu \tag{1.10}$$

There are also neutrinos with lower energies of 10-50 MeV created through the decay at rest (DAR) of the mesons. These DAR neutrinos are created very near the target or at the end of the decay volume at beam dumps. Main channels of DAR neutrinos are

$$\pi^+ \to \mu^+ + \nu_\mu, \qquad \mu^+ \to e^+ + \nu_e + \bar{\nu}_\mu \tag{1.11}$$

A neutrino beam spreads out as it travels, and the intensity decreases. Near detectors placed close to the source characterize the neutrino beam. The far detectors at significantly large distances (from a few hundred to a few thousand km) from the source aim to study the neutrino oscillation. Two types of beams: (i) on-axis and (ii) off-axis, are used for far detectors.

On-axis beams where the beam position is linear to the detector position give a higher flux. However, the on-axis beam is a wide-band beam with a certain energy distribution. When the beam and the detector are placed at an angle for the off-axis beams, the energy spectrum becomes narrower, and its maximum shifts towards lower energies. Off-axis beam also provides better background suppression. The T2K[54] experiment is the first to use the off-axis neutrino beam. This beam will also be used in future T2HK/T2HKK. The NUMI off-axis beam at Fermilab is being used by the NOνA experiment.

1.5 Neutrino Oscillation

The phenomenon of a neutrino changing its flavor to a different flavor is known as neutrino oscillation. Bruno Pontecorvo proposed the idea of electron neutrinos and anti-neutrinos oscillating between themselves in 1957[55, 56], similar to that of the observed $K^0 \rightleftharpoons \bar{K}^0$ oscillations. After muon neutrino ν_μ was discovered, Maki, Nakagawa and Sakata proposed[57] the mixing between ν_e and ν_μ. The first framework of oscillations between two flavors through mixing between the neutrinos was suggested by Pontecorvo in 1967 [58]. After the τ discovery, the existing two flavor oscillation framework was modified to incorporate three flavor oscillations. Neutrinos are created in flavor states but propagate in mass states. Neutrino oscillations require them to have small masses. In such a situation, the neutrinos flavour states ($|\nu_\alpha\rangle$) are linear combinations of mass eigenstates ($|\nu_i\rangle$) connected through a unitary mixing matrix known as Pontecorvo-Maki-Nakagawa-Sakata(PMNS) matrix U as follows,

$$|\nu_\alpha\rangle = U^*_{\alpha i}|\nu_i\rangle \tag{1.12}$$

where $\alpha = e, \mu, \tau$ refer to lepton flavors electron, muon, and tauon, respectively, whereas $i = 1, 2, 3$ denote the index of mass eigenstates. The PMNS matrix is defined in terms of the rotation matrices R_{ij} as,

$$U = R_{23}(\theta_{23})U^\delta(\delta_{13})R_{13}(\theta_{13})U^{\dagger\delta}(\delta_{13})R_{12}(\theta_{12}) \tag{1.13}$$

$$= \begin{bmatrix} c_{12}c_{13} & s_{12}c_{13} & s_{13}e^{-\iota\delta_{13}} \\ -s_{12}c_{23} - c_{12}s_{23}s_{13}e^{\iota\delta_{13}} & c_{12}c_{23} - s_{12}s_{23}s_{13}e^{\iota\delta_{13}} & s_{23}c_{13} \\ s_{12}s_{23} - c_{12}c_{23}s_{13}e^{\iota\delta_{13}} & c_{12}s_{23} - s_{12}c_{23}s_{13}e^{\iota\delta_{13}} & c_{23}c_{13} \end{bmatrix} \tag{1.14}$$

The parameters of PMNS matrix are three mixing angles θ_{12}(solar angle), θ_{13}(reactor angle), θ_{23}(atmospheric angle) and Dirac CP phase δ_{13}. The probability of ν_α transitioning to ν_β over a distance L in vacuum can be expressed as,

$$\begin{aligned} P_{\alpha\beta} = \delta_{\alpha\beta} - 4\sum_{i>j}^{3} \mathrm{Re}(U_{\alpha i}U^*_{\beta i}U^*_{\alpha j}U_{\beta j}) \sin^2[1.27\Delta_{ij}L/E] \\ + 2\sum_{i>j}^{3} \mathrm{Im}(U_{\alpha i}U^*_{\beta i}U^*_{\alpha j}U_{\beta j}) \sin[2(1.27\Delta_{ij}L/E)] \end{aligned} \tag{1.15}$$

where the mass square difference corresponding to two mass eigenvalues m_i, m_j is defined as $\Delta_{ij} = m_i^2 - m_j^2$. There are only two independent mass-squared differences in the three flavor framework: the atmospheric mass squared difference Δ_{31} and the solar mass squared difference Δ_{21}.

The current unknowns of the three flavor framework are: (i) octant of θ_{23}, i.e. if the value of $\theta_{23} < 45°$ (lower octant, LO) or $\theta_{23} > 45°$ (higher octant, HO), (ii) the sign of Δ_{31} (mass ordering), i.e. if $\Delta_{31} > 0$ (normal ordering, NO) or $\Delta_{31} < 0$ (inverted ordering, IO), and (iii) the value of δ_{13}. Precision measurement of these parameters is hindered due to the presence of degenerate solutions corresponding to the generalized hierarchy-octant-δ_{13} degeneracy. A detailed discussion of the oscillation framework and degeneracy can be found in the next chapter. Future planned experiments like DayaBay(reactor), DUNE, T2HK/T2HKK, ESSnuSB, as well as atmospheric neutrino detectors at Hyper-Kamiokande, INO, ORCA, PINGU, IceCube Gen 2, etc are gearing towards addressing these issues.

1.6 Signatures of BSM physics in neutrino oscillations

New physics beyond the standard model can influence the standard neutrino oscillations. These BSM scenarios manifest as sub-leading effects and need more precise and high statistics experiments to detect any possible signatures. Some of the BSM scenarios explored in neutrino oscillation experiments are; sterile neutrinos, non-standard interactions (NSIs), non-unitarity violation, Lorentz invariance violation (LIV), CPT violations, decoherence of neutrinos, neutrino decay, etc. Future experiments providing higher statistics and greater precision are well suited for probing the effect of new physics. There are two types of studies related to BSM physics: (i) constraining the values of the parameters of new physics and (ii) studying the effects of these new physics parameters in neutrino oscillation. Three BSM scenarios relevant to this thesis are discussed below.

1.6.1 Sterile neutrinos

In 1993, *Liquid Scintillator Neutrino Detector(LSND)* experiment observed[59] an excess $\bar{\nu}_e$ in their study of muon neutrino beam from positive pion decay

$$\pi^+ \to \mu^+ + \nu_\mu \qquad\qquad \mu^+ \to e^+ + \nu_e + \bar{\nu}_\mu$$

This excess corresponding to neutrino mean energy $E = 30$ MeV and baseline $L = 30$m can be explained by $\bar{\nu}_\mu \to \bar{\nu}_e$ oscillation in appearance channel with 3.8σ significance. Later *MiniBooNE* experiment at Fermi lab also reported[60] $\bar{\nu}_\mu \to \bar{\nu}_e$ signal at 4.8σ significance level for energy $E = 400$MeV and baseline $L = 450$m confirming the *LSND* results.

The observation of electron neutrino ν_e deficit in gallium-based radio-chemical experiments SAGE and GALLEX (*Gallium anomaly*) [61, 62] also corroborated the sterile neutrino hypothesis. Recent results from BEST experiment[63] also gave similar implications at 5σ.

There was also the *reactor antineutrino anomaly* in which several reactor neutrino experiments showed a deficit in the measured flux with an improved calculation of the inverse beta decay cross-section [64, 65]. These could also be explained in terms of a sterile neutrino with a mass of the order of eV. However, the results from reactor experiments such as DANSS[66, 67], NEOS[68], STEREO[69], and PROSPECT[70] excluded most of the *reactor antineutrino anomaly* region[71] at more than 90% C.L.

If we want to interpret these results through effective two flavor oscillations then corresponding to $L/E \sim 1$GeV/Km in these experiments, there should be a new mass squared difference $\Delta_s \sim 1$ eV^2 which certainly doesn't fit in the current standard three flavor oscillation scheme. So we need to modify the standard 3 flavor oscillation framework by including an extra neutrino with a mass around 1 eV[72]. The result of the invisible decay width of the Z boson at CERN suggests that there can only be three neutrinos with SM interactions below the mass range of half of the Z boson[73]. Thus, this additional neutrino should be a singlet under the Standard Model and not interact by weak interactions. This points towards this neutrino being inert to SM interaction, i.e., a *sterile neutrino* leading to a proposed beyond SM structure with the inclusion of at least one sterile neutrino with three active neutrinos. The new sterile neutrino field ν_s must be the superposition of four massive neutrino fields (mass eigenstates), leading to a 4×4 mixing matrix. The new mixing matrix with three additional mixing angles related to mixing between active and sterile states and two additional CP phases can be parameterized as,

$$U = \tilde{R}_{34}(\theta_{34}, \delta_{34}) R_{24}(\theta_{24}) \tilde{R}_{14}(\theta_{14}, \delta_{14}) R_{23}(\theta_{23}) \tilde{R}_{13}(\theta_{13}, \delta_{13}) R_{12}(\theta_{12}) \tag{1.16}$$

These additional parameters will cause more parameter degeneracies, leading to difficulties in determining oscillation parameters.

One of the sternest challenges for the existence of sterile neutrino comes from cosmology[74]. Including an extra sterile neutrino increases the effective no of neutrinos relevant for the Big Bang Nucleosynthesis. From the recent measurement of Planck data[75] and combining together with the Hubble parameter measurement [76] and Supernova Ia data from the Pantheon sample [77], the extended fit to the parameters are

$$\begin{gathered} N_{eff} = 3.11^{+0.37}_{-0.36} (95\% \text{ CL}) \\ \sum m_\nu < 0.16 \text{ eV} \end{gathered} \tag{1.17}$$

To get around cosmological constraints, we shall introduce new physics directly affecting the cosmological phenomenology of the light sterile states. Since the main problem of the canonical light sterile neutrino is that its thermalization in the early universe raises N_{eff} to an unacceptably large level for BBN and CMB/LSS constraints. So far, all known new physics solutions involve tampering with the thermalization process to maintain N_{eff} close to the SM value as possible. A number of ideas have been proposed and explored throughout the years, e.g., large chemical potentials or, equivalently, number density asymmetries for the active neutrinos[78]; secret interactions of the sterile neutrinos[79, 80] and low reheating temperature of the universe[81] etc. The proposed remedy of secret interaction between sterile neutrinos in [80] was later disfavoured by cosmic microwave background analysis [82]. A joint analysis of short baseline and cosmological data recently showed that a sterile neutrino with a mass around 1 eV can interact with a new light pseudo scalar. To summarize, the existence of sterile neutrinos is still an open question, and more experimental efforts are underway to resolve this.

1.6.2 Non standard interactions

Neutrinos interact with matter through W, Z bosons in the standard model, leading to effective standard matter potential, first contemplated by *Wolfenstein*[83]. Neutrino can also interact with matter through new heavy mediators in BSM scenarios. These BSM physics in neutrino interactions can be suitably parameterized in terms of the low-energy effective field theory (EFT) of non-standard interactions (NSI) [83–86]. This formalism contemplates modifications to neutrino interactions with SM particles while respecting the SM vector current structure[2]. The model-independent effective Lagrangian for NSI in neutrino oscillations is given by

$$\mathcal{L}_{NSI}^{NC} = -2\sqrt{2}G_F \sum_{f,P,\alpha,\beta} (\bar{\nu}_\alpha \gamma^\mu P_L \nu_\beta)\epsilon_{\alpha\beta}^{fP}(\bar{f}\gamma_\mu P f) \tag{1.18}$$

$$\mathcal{L}_{NSI}^{CC} = -2\sqrt{2}G_F \sum_{f,f',P,\alpha,\beta} (\bar{\nu}_\alpha \gamma^\mu P_L l_\beta)\epsilon_{\alpha\beta}^{ff'P}(\bar{f}\gamma_\mu P f')) \tag{1.19}$$

where $G_F \simeq 1.167 \times 10^{-5} GeV^{-2}$ is Fermi constant, $P \in [P_L, P_R]$ and $\epsilon_{\alpha\beta}^{fP}, \epsilon_{\alpha\beta}^{ff'P}$ are dimensionless strength of NSI. For neutrinos interacting with ordinary matter (made up of electrons, protons, and neutrons), only interactions with the first generation of SM fermions need to be considered,i.e., the indices $f = e, u, d$ and

[2]There can also be scalar and tensor NSIs.

$\alpha, \beta = e, \mu, \tau$ (the neutrino flavors). At the Hamiltonian level, the NSI parameters are connected to Lagrangian level parameters as

$$\epsilon_{\alpha\beta} = \sum_{fP} \frac{N_f}{N_e} \epsilon_{\alpha\beta}^{fP} \tag{1.20}$$

where N_f, N_e are the number density of the fermions and electrons in matter, respectively. For charged current(CC) interaction, the neutrinos couple with two types of charged fermions f, f'. CC NSI are heavily constrained. Whereas for neutral current interaction, the coupling of neutrinos is with the same type of fermions f. The Hamiltonian due to NC NSI is,

$$H_{NSI} = \sqrt{2} G_F N_e \begin{bmatrix} \epsilon_{ee} & \epsilon_{e\mu} & \epsilon_{e\tau} \\ \epsilon_{e\mu}^{\star} & \epsilon_{\mu\mu} & \epsilon_{\mu\tau} \\ \epsilon_{e\tau}^{\star} & \epsilon_{\mu\tau}^{\star} & \epsilon_{\tau\tau} \end{bmatrix} \sim \sqrt{2} G_F N_e \begin{bmatrix} \epsilon_{ee} - \epsilon_{\mu\mu} & \epsilon_{e\mu} & \epsilon_{e\tau} \\ \epsilon_{e\mu}^{\star} & 0 & \epsilon_{\mu\tau} \\ \epsilon_{e\tau}^{\star} & \epsilon_{\mu\tau}^{\star} & \epsilon_{\tau\tau} - \epsilon_{\mu\mu} \end{bmatrix}; \tag{1.21}$$

where $\sqrt{2} G_F N_e$ is the Wolfenstein matter potential. The diagonal NSI terms are real and provide a mechanism for breaking lepton flavor universality, while the off-diagonal terms are generally complex and responsible for flavor-changing. The non-diagonal terms are parameterized as $\epsilon_{\alpha\beta} = |\epsilon_{\alpha\beta}| e^{\iota \phi_{\alpha\beta}}$ with accompanying phase $\phi_{\alpha\beta}$. The oscillation experiments are not sensitive to one free parameter along the diagonal, like they cannot measure the absolute neutrino mass scale. So, we can subtract out $\epsilon_{\mu\mu}\mathbf{I}$ without any loss of generality, and we get the NSI Hamiltonian at the right of eq. (1.21).

NSIs parameterize the new interactions in terms of the effective dimension-6 operator(1.18)(1.19). If the effective coupling comes through integrating out a new state, say X of mass m_X and coupling g_X, the strength of the NSI parameters can be given as $\epsilon \propto \frac{g_X^2 m_W^2}{m_X^2}$. Thus, to experimentally detect signatures of the NSI ($\geq 10^{-2}$), the new particle X cannot be much heavier than the electroweak scale.

The presence of NSI parameters affects the determination of standard model parameters due to the presence of degeneracies. One such interesting degeneracy is the possibility of $\theta_{12} > 45°$ solutions. This degenerate solution of θ_{12} in the second octant is called Dark-Large Mixing Angle (DLMA) solution ($\theta_{12}^{DLMA} = 90° - \theta_{12}$).

1.6.3 Lorentz invariance violations

Lorentz invariance is one of the basic symmetries in fundamental physics. Lorentz invariance protects isotropy and homogeneity of the local relativistic QFT in space-time. In the minimal $SU(3)\times SU(2)\times U(1)$ SM, this symmetry is conserved. However, there are higher dimensional theories (related to the Plank scale $\sim 10^{19}$ GeV)where Lorentz invariance violation is generated spontaneously[87–91]. String theories obeying Lorentz covariant dynamics are shown to facilitate the spontaneous breaking of Lorentz symmetry in [87–90]. The violation of Lorentz invariance and CPT have been tested using Kaons [92, 93], neutral $\mathrm{B_d}$ or $\mathrm{B_s}$ mesons [93, 94], and neutral D mesons [93, 95]. Lorentz invariance violation(LIV) can be comprehended through a standard model extension (SME) framework in the context of a low energy effective theory[96]. The neutrino behavior is contained in the terms,

$$\mathcal{L} = \frac{1}{2}\iota \bar{L}_a \gamma^\mu \overleftrightarrow{D_\mu} L_a - (a_L)_{\mu ab}\bar{L}_a\gamma^\mu L_b + \frac{1}{2}(c_L)_{\mu\nu ab}\bar{L}_a\gamma^\mu \overleftrightarrow{D^\nu} L_b \tag{1.22}$$

where the first term is the usual Standard-Model kinetic term for the left-handed doublets L_a with index a ranging over the three generations e, μ, τ. The coefficients for Lorentz violation are $(a_L)_{\mu ab}$, which has mass dimension one and controls the CPT violation, and $(c_L)_{\mu\nu ab}$ which is dimensionless and is CPT conserving. The Lorentz-violating terms in (1.22) modify both interactions and propagation of neutrinos. Any interaction effects are expected to be tiny and well beyond existing sensitivities. In contrast, propagation effects can be significant if the neutrinos travel large distances. The time evolution of neutrino states is controlled as usual by the effective Hamiltonian extracted from (1.22) as,

$$(\mathcal{H}_{eff})_{ab} = E\delta_{ab} + \frac{m^2_{ab}}{2E} + \frac{1}{E}(a^\mu_L p_\mu - c^{\mu\nu}_L p_\mu p_\nu)_{ab} \tag{1.23}$$

The LIV-induced parameter a^μ_L (CPT-violating) will change the sign in case of anti-neutrinos while $c^{\mu\nu}_L$ will remain unchanged. In this thesis, we will focus on only the isotropic component of these parameters in the Sun-centered celestial-equatorial frame and fix μ, ν to zero(0) and redefine $(a_L)^0_{ab} \equiv a_{ab}, (c_L)^{00}_{ab} \equiv c_{ab}$.

The Hamiltonian due to LIV is given by

$$H_{LIV} = \begin{bmatrix} a_{ee} & a_{e\mu} & a_{e\tau} \\ a^{\star}_{e\mu} & a_{\mu\mu} & a_{\mu\tau} \\ a^{\star}_{e\tau} & a^{\star}_{\mu\tau} & a_{\tau\tau} \end{bmatrix} - \frac{4}{3}E \begin{bmatrix} c_{ee} & c_{e\mu} & c_{e\tau} \\ c^{\star}_{e\mu} & c_{\mu\mu} & c_{\mu\tau} \\ c^{\star}_{e\tau} & c^{\star}_{\mu\tau} & c_{\tau\tau} \end{bmatrix} \tag{1.24}$$

The diagonal elements of H_{LIV} are real, whereas the off-diagonal terms are generally complex in nature and can be defined as $a_{\alpha\beta} = |a_{\alpha\beta}|e^{\iota\phi_{\alpha\beta}}$ where $\phi_{\alpha\beta}$ is additional phase.

1.7 An overview of the thesis

In this thesis, we have studied the capability of future long baseline experiments like DUNE, T2HK/T2HKK, and IceCube to probe the effects of several beyond standard model signals on the oscillation framework. The octant of θ_{23}, mass hierarchy, and $\delta_{\rm CP}$ are yet to be determined in the standard three flavor oscillation framework. Any new physics will impact the determination of these parameters in the upcoming detectors. We study three BSM physics signatures: sterile neutrino, non-standard interaction, and Lorentz invariance violations in the context of current and future experiments.

The first chapter introduces the history of neutrinos, their sources, and neutrinos in the SM. In addition, we present a brief introduction to the phenomenon of neutrino oscillation, we also discuss the scope of this thesis.

In the second chapter, the derivation of the neutrino oscillation probabilities in vacuum as well as in the presence of matter for two and three generations are presented. We address the existing degeneracies affecting the precise determination of the parameters and discuss the salient features of the present and future neutrino experiments studied in this thesis.

In the third chapter, we focus on the effect on determining θ_{23} and mass ordering when an eV scale sterile neutrino is present. We discuss the potential of a liquid argon time projection chamber (LArTPC) detector at a baseline length of

1300 km (as proposed in the DUNE experiment) to determine these parameters using both beam neutrinos as well as atmospheric neutrinos.

Next, in the fourth chapter, neutrino oscillation is studied in the presence of a very light sterile neutrino corresponding to a mass difference of 10^{-4} : 0.1 eV^2. Four possible mass ordering scenarios arise in the presence of a very light sterile neutrino due to the unknown sign of Δ_{31} (atmospheric mass ordering) and Δ_{41} (sterile mass ordering). The sensitivity of determining the sign of Δ_{41}, Δ_{31} and the octant of θ_{23} have been investigated using beam neutrinos traveling 1300 km from the source and atmospheric neutrinos in a LArTPC detector (similar to the proposed DUNE experiment).

In the fifth chapter, we explore the possibility of distinguishing between LMA and DLMA solutions of θ_{12}, in the context of the IceCube data. Firstly we discuss the probabilities and address various degeneracies related to θ_{12} with θ_{23}, δ_{CP}. To study the sensitivity of LMA and DLMA solution, we compare the experimental flux ratio from IceCube data with the theoretical flux ratio corresponding to various astrophysical sources, namely μ, π, and n source and check the quality of the fit.

In the sixth chapter, we study the impact of CPT violating LIV parameters in the detection of CP sensitivity. CPT violating LIV parameters introduces additional phases that also contribute to CP violation. A comprehensive analysis of the effect of these phases on CP discovery is performed in the context of T2HK and T2HKK experiments. We explore the synergy between 295 km and 1100 km baselines in the T2HKK. As T2HK and T2HKK are two different proposals of the same experiment, comparative studies have been presented to show which one is more suitable.

Finally, in the seventh chapter, we summarize the results of our work.

"Neutrinos ... win the minimalist contest: zero charge, zero radius, and very possibly zero mass."

Leon M. Lederman

2

Neutrino Oscillation Framework

This chapter discusses the theoretical framework of neutrino oscillations. The calculation of two flavor and three flavor oscillation probabilities in vacuum and in the presence of matter effects are presented. The parameter degeneracies in the three flavor framework are also described. The procedure followed for the numerical analysis is also explained in this chapter. We present the experimental evidence in favor of oscillations and a brief discussion of different neutrino experiments used in the thesis.

2.1 Analytical calculation of neutrino oscillation probability in vacuum

In this section, we will present the derivations of neutrino oscillation probability in vacuum. To start with, the general case of N flavor oscillations in the vacuum is discussed.

In general, for N flavor states, there will be N mass states, and the mixing between the states can be generalized from eq. (1.12) as follows,

$$\begin{pmatrix} |\nu_{\alpha 1}\rangle \\ |\nu_{\alpha 2}\rangle \\ . \\ |\nu_{\alpha N}\rangle \end{pmatrix} = U^*_{N\times N} \begin{pmatrix} |\nu_1\rangle \\ |\nu_2\rangle \\ . \\ |\nu_N\rangle \end{pmatrix} \tag{2.1}$$

where $\nu_{\alpha N}$ are flavor states, and ν_N denote mass states. The parametrization for the mixing matrix for N neutrino flavors requires N^2 independent parameters with $N(N-1)/2$ angles and $N(N+1)/2$ phases. Among these, $(2N-1)$ phases can be absorbed by $2N$ fields of the Lagrangian when neutrinos are Dirac particles. So the remaining no of physical phases is $(N-1)(N-2)/2$.

For all the calculations, we use the natural unit, i.e., $\hbar = c = 1$ Energies of neutrinos E_i can be expressed in the natural unit as,

$$E_i^2 = p_i^2 + m_i^2 \tag{2.2}$$

In the relativistic limit, $m_i << p$, and it leads to the energy of a neutrino with mass m_i as;

$$\begin{aligned} E_i &= p\left[1 + \frac{m_i^2}{p^2}\right]^{1/2} \\ &\simeq p + \frac{m_i^2}{2p} \simeq E + \frac{m_i^2}{2E}; \end{aligned} \tag{2.3}$$

where we have assumed that all the neutrino mass eigenstates have equal momenta[1]. The Hamiltonian in mass basis is given by,

$$H_m^{vac} = E\mathbf{I} + \frac{1}{2E}\begin{pmatrix} m_1^2 & 0 & 0 \\ 0 & m_2^2 & 0 \\ .. & .. & .. \\ 0 & 0 & m_N^2 \end{pmatrix} \tag{2.4}$$

As the mass states are eigenstates of H_m^{vac},

$$H_m^{vac}|\nu_i\rangle = E_i|\nu_i\rangle \tag{2.5}$$

The time evolution of mass eigenstates is given by,

$$\iota\frac{d}{dt}\nu_i = H_m^{vac}\nu_i \tag{2.6}$$

Therefore, the mass eigenstates will evolve in time as,

$$|\nu_i(t)\rangle = e^{-\iota E_i t}|\nu_i\rangle \tag{2.7}$$

Therefore, using eq. (2.7), (1.12) the flavor eigenstates at time $t = 0$ and $t = t$ can be expressed as,

$$|\nu_\alpha(0)\rangle = \sum_1^N U_{\alpha i}^*|\nu_i\rangle \tag{2.8}$$

$$|\nu_\alpha(t)\rangle = \sum_1^N U_{\alpha i}^* e^{-\iota E_i t}|\nu_i\rangle \tag{2.9}$$

The oscillation probability for $\nu_\alpha \longrightarrow \nu_\beta$ is given by

$$\begin{aligned} P_{\alpha\beta} &= |\langle\nu_\alpha(0)|\nu_\beta(t)\rangle|^2 \\ &= \sum_i\sum_j (U_{\alpha i}U_{\beta i}^* e^{-\iota E_i t})(U_{\alpha j}^* U_{\beta j} e^{\iota E_j t}) \\ &= \sum_{i=j}|U_{\alpha i}|^2|U_{\beta i}|^2 + \sum_{i\neq j} U_{\alpha i}U_{\beta i}^* U_{\alpha j}^* U_{\beta j} e^{-\iota(E_i - E_j)t} \end{aligned} \tag{2.10}$$

[1]There is also wave-packet formalism that considers neutrino state to be a wave-packet comprising states of various momenta

Now we can expand the terms in eq.(2.10) as follows,

$$\begin{aligned}
|\sum_i U_{\alpha i} U^*_{\beta i}|^2 &= \sum_i |U_{\alpha i}|^2 |U_{\beta i}|^2 + \sum_{i>j} (U_{\alpha i} U^*_{\beta i} U^*_{\alpha j} U_{\beta j} + U^*_{\alpha i} U_{\beta i} U_{\alpha j} U^*_{\beta j}) \\
&= \sum_i |U_{\alpha i}|^2 |U_{\beta i}|^2 + 2 \sum_{i>j} Re(U_{\alpha i} U^*_{\beta i} U^*_{\alpha j} U_{\beta j})
\end{aligned} \tag{2.11}$$

$$\begin{aligned}
\sum_{i \neq j} U_{\alpha i} U^*_{\beta i} U^*_{\alpha j} U_{\beta j} e^{-\iota(E_i - E_j)t} &= \sum_{i>j} U_{\alpha i} U^*_{\beta i} U^*_{\alpha j} U_{\beta j} e^{-\iota(E_i - E_j)t} \\
&+ \sum_{i>j} U^*_{\alpha i} U_{\beta i} U_{\alpha j} U^*_{\beta j} e^{\iota(E_i - E_j)t}
\end{aligned} \tag{2.12}$$

As $(a + \iota b)e^{-\iota\theta} + (a - \iota b)e^{\iota\theta} = 2(a\cos\theta + b\sin\theta)$, we can rewrite equation (2.12) as

$$\begin{aligned}
\sum_{i \neq j} U_{\alpha i} U^*_{\beta i} U^*_{\alpha j} U_{\beta j} e^{-\iota(E_i - E_j)t} &= 2 \sum_{i>j} \mathrm{Re}(U_{\alpha i} U^*_{\beta i} U^*_{\alpha j} U_{\beta j}) \cos[(E_i - E_j)t] \\
&+ 2 \sum_{i>j} \mathrm{Im}(U_{\alpha i} U^*_{\beta i} U^*_{\alpha j} U_{\beta j}) \sin[(E_i - E_j)t]
\end{aligned} \tag{2.13}$$

Using $\sum_i U_{\alpha i} U^*_{\beta i} = \delta_{\alpha\beta}$ and using equations (2.11), (2.13) in expression of $P_{\alpha\beta}$, we get,

$$\begin{aligned}
P_{\alpha\beta} = \delta_{\alpha\beta} &+ 2 \sum_{i>j} \mathrm{Re}(U_{\alpha i} U^*_{\beta i} U^*_{\alpha j} U_{\beta j})(\cos[(E_i - E_j)t] - 1) \\
&+ 2 \sum_{i>j} \mathrm{Im}(U_{\alpha i} U^*_{\beta i} U^*_{\alpha j} U_{\beta j}) \sin[(E_i - E_j)t]
\end{aligned} \tag{2.14}$$

The time t traveled by relativistic neutrinos is the same as the distance traveled L in the natural unit. Also, the difference in energies can be expressed in terms of the mass-squared difference as,

$$E_i - E_j \simeq \frac{1}{2E}(m_i^2 - m_j^2) = \frac{\Delta_{ij}}{2E} \tag{2.15}$$

If we want to have L in km and energy E in GeV while keeping Δ_{ij} in eV^2;

$$\frac{(E_i - E_j)t}{2} = \frac{\Delta_{ij} L}{4E} = \frac{\Delta_{ij} L(/\mathrm{km}) \times 10^{10}}{4 \times 1.9 \times E(/\mathrm{GeV}) \times 10^9} = \frac{1.27 \Delta_{ij} L(/\mathrm{km})}{E(/\mathrm{GeV})} \tag{2.16}$$

Using the eq. (2.16) in the probability expression in (2.14), we have,

$$\begin{aligned} P_{\alpha\beta} = \delta_{\alpha\beta} - 4\sum_{i<j} \mathrm{Re}(U_{\alpha i}U^*_{\beta i}U^*_{\alpha j}U_{\beta j})\sin^2[1.27\Delta_{ij}L/E] \\ + 2\sum_{i<j} \mathrm{Im}(U_{\alpha i}U^*_{\beta i}U^*_{\alpha j}U_{\beta j})\sin[2(1.27\Delta_{ij}L/E)] \end{aligned} \tag{2.17}$$

For the oscillation probability in matter, we shall replace the elements of the mixing matrix U and mixing angles and mass-squared differences in the above eq. (2.17) with the respective modified versions in matter.

2.1.1 Oscillation probability in vacuum (Two flavor)

In two flavor case, considering ν_e, ν_μ as the flavor eigenstates, and ν_1, ν_2 as the mass eigenstates, one can write,

$$\begin{pmatrix} |\nu_e\rangle \\ |\nu_\mu\rangle \end{pmatrix} = \begin{pmatrix} \cos\theta & \sin\theta \\ -\sin\theta & \cos\theta \end{pmatrix} \begin{pmatrix} |\nu_1\rangle \\ |\nu_2\rangle \end{pmatrix} \tag{2.18}$$

The mixing matrix in the two flavor case is a simple 2×2 rotation matrix parameterized by a single angle θ. The flavor states will evolve in time t as,

$$|\nu_e(t)\rangle = e^{-\iota E_1 t}\cos\theta|\nu_1\rangle + e^{-\iota E_2 t}\sin\theta|\nu_2\rangle \tag{2.19}$$

$$|\nu_\mu(t)\rangle = -e^{-\iota E_1 t}\sin\theta|\nu_1\rangle + e^{-\iota E_2 t}\cos\theta|\nu_2\rangle \tag{2.20}$$

The survival probability of electron neutrino is evaluated as follows,

$$\begin{aligned} P_{ee} &= |\langle\nu_e(t=0)|\nu_e(t)\rangle|^2 \\ &= |(\langle\nu_1|\cos\theta + \langle\nu_2|\sin\theta)(e^{-\iota E_1 t}\cos\theta|\nu_1\rangle + e^{-\iota E_2 t}\sin\theta|\nu_2\rangle)|^2 \\ &= |\cos^2\theta e^{-\iota E_1 t} + \sin^2\theta e^{-\iota E_2 t}|^2 \\ &= 1 - \sin^2 2\theta \sin^2[(E_1 - E_2)t/2] \end{aligned} \tag{2.21}$$

Using the equations (2.16),(2.21), the electron survival probability is given as,

$$P_{ee} = 1 - \sin^2 2\theta \sin^2\left[\frac{1.27\Delta_{21}L}{E}\right] \tag{2.22}$$

The ν_μ appearance probability is given as,

$$P_{e\mu} = 1 - P_{ee} = \sin^2 2\theta \sin^2 \left[\frac{1.27\Delta_{21}L}{E}\right] \tag{2.23}$$

From eq. (2.23), (2.22), it can be noted that the oscillatory part is given by $\sin^2[1.27\Delta_{21}L/E]$ with corresponding phase $\phi = 1.27\Delta_{21}L/E$, whereas the amplitude of probability is given by $\sin^2 2\theta$. The above expression shows that if $m_2^2 - m_1^2 = 0$, the probability will go to zero, i.e., non-zero probability indicates that at least one of neutrino mass eigenstates is massive. We can also see the probability is invariant under the transformation of $\theta \to \frac{\pi}{2} - \theta$, i.e., $\theta > 45^\circ$ (lower octant) or $\theta < 45^\circ$ (higher octant) gives the same probability. The probability will also remain unchanged over changing the sign of Δ_{21}. The oscillatory nature depends on the $\Delta_{21}L/E$ value. Normally, the experiments (with L being constant) are designed such that neutrino flux is highest around the energies near oscillation maxima. As there is no phase involved in the two flavor case, these probabilities are CP (Charge parity) and T (time reversal) transformation invariant, i.e., the direct and time-reversed oscillation probability of neutrino and antineutrino are all equal,

$$P_{\nu_\alpha \to \nu_\beta} = P_{\nu_\beta \to \nu_\alpha} = P_{\bar{\nu}_\alpha \to \bar{\nu}_\beta} = P_{\bar{\nu}_\beta \to \bar{\nu}_\alpha} \tag{2.24}$$

The above expression in eq. (2.23) can be also expressed as

$$P_{\mu e} = \sin^2 2\theta \sin^2[\pi \frac{L}{L_{osc}}], \tag{2.25}$$

where the *oscillation length* L_{osc} is the distance at which the phase of oscillation ϕ becomes π,

$$L_{osc} = \frac{2.48 \times E(/\text{GeV})}{\Delta_{21}(/\text{eV}^2)}\text{km} \tag{2.26}$$

To obtain the maximum probability, i.e., flavor conversion, $\theta = 45^\circ$ and $\frac{1.27\Delta_{21}L}{E} = \frac{\pi}{2}$. For $L_{osc} >> L$ oscillation is not observed, and for $L_{osc} << L$ the oscillation probability averages out to $P \sim \frac{1}{2}\sin^2 2\theta$. For obtaining maximum oscillation, $L_{osc} = 2L$. This condition can also be interpreted as $\frac{\Delta L}{E} \sim 1$; i.e., $\Delta \sim E(GeV)/L(km)$.

2.2 Analytical calculation of oscillation probability in the presence of matter

2.2.1 Interaction potential of neutrinos in matter

Neutrinos interact with the matter particles (n^0, p^+, e^{-1}) through various standard model processes. The coherent forward scatterings of neutrinos with matter particles give rise to effective potentials as first pointed out by *Wolfenstein* in 1978[83]. The coherent forward elastic scatterings are of two types; charge-current(CC) and neutral current(NC). The Feynman diagrams of these interactions are shown in fig. 2.1.

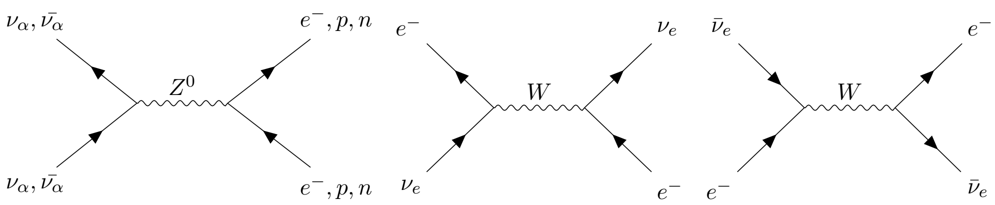

Figure 2.1: Feynman diagrams of (anti)neutrinos undergoing neutral current (left) and charge current (middle and right) interaction

2.2.2 Charge Current Interaction

The effective CC Hamiltonian density for an electron neutrino ν_e propagating through a homogeneous isotropic gas of electrons at rest is given by,

$$H^{cc}_{eff}(x) = \frac{G_F}{\sqrt{2}} J_{W\rho} J^{\dagger\rho}_{W} = \frac{G_F}{\sqrt{2}} [\bar{\nu}_e(x)\gamma^\rho(1-\gamma^5)e(x)][\bar{e}(x)\gamma_\rho(1-\gamma^5)\nu_e(x)] \tag{2.27}$$

where $J^\rho_W = \bar{\nu}_e(x)\gamma^\rho(1-\gamma^5)e(x)$ is the current density. Applying Fierz transformation in the above eqn,

$$H^{cc}_{eff}(x) = \frac{G_F}{\sqrt{2}} [\bar{\nu}_e(x)\gamma^\rho(1-\gamma^5)\nu_e(x)][\bar{e}(x)\gamma_\rho(1-\gamma^5)e(x)] \tag{2.28}$$

The presence of electrons in the medium leads us to consider two conditions. First of all, the statistical energy distribution of the electrons in the medium is accounted for by integration over the Fermi function $f(E_e, T)$ with normalization

$\int f(E_e, T)N_e(p_e)d^3p_e = N_eV$ where N_e is the electron no density and N_eV the total no of electrons. Secondly, we need to consider averaging over spins $1/2\sum_{h_e=\pm 1}$ as the polarisation of electrons h_e is unknown. The following derivations in this subsection are based on [97].

$$\begin{aligned}\bar{H}^{cc}_{eff}(x) =& \langle \nu_e(p_1, h_1)e^-(p_e, h_e)|\frac{G_F}{\sqrt{2}}\bar{\nu}_e(x)\gamma^\rho(1-\gamma^5)\nu_e(x)\int f(E_e, T)d^3p_e \\ &\times \frac{1}{2}\sum_{h_e=\pm 1}\bar{e}(x)\gamma_\rho(1-\gamma^5)e(x)|\nu_e(p_1, h_1)e^-(p_e, h_e)\rangle\end{aligned} \tag{2.29}$$

The electron states before and after the scattering process have the same four momenta and helicity to leave the medium unchanged in order to contribute coherently to the neutrino potential. We consider finite normalization volume V for electron background and define one-electron states as

$$|e^-(p_e, h_e)\rangle = \frac{1}{2EV}a_e^{(h_e)\dagger}(p_e)|0\rangle \tag{2.30}$$

Now we calculate the average over helicities for the electron matrix element.

$$\begin{aligned}&\frac{1}{2}\sum_{h_e=\pm 1}\bar{e}(x)\gamma_\rho(1-\gamma^5)e(x)|\nu_e(p_1, h_1)e^-(p_e, h_e)\rangle \\ =&\frac{1}{4E_eV}\sum_{h_e=\pm 1}a(p_e, h_e)^\dagger a(p_e, h_e)\bar{u}(p_e, h_e)\gamma_\rho(1-\gamma^5)u(p_e, h_e)|\nu_e(p_1, h_1)e^-(p_e, h_e)\rangle \\ =&\frac{1}{4E_eV}\sum_{h_e=\pm 1}\mathrm{Num}(p_e, h_e)\bar{u}(p_e, h_e)\gamma_\rho(1-\gamma^5)u(p_e, h_e)|\nu_e(p_1, h_1)e^-(p_e, h_e)\rangle \\ =&\frac{1}{4E_eV}N_e(p_e)Tr[(\not{p}_e + m_e)\gamma_\rho(1-\gamma^5)]|\nu_e(p_1, h_1)e^-(p_e, h_e)\rangle \\ =&\frac{1}{E_eV}N_e(p_e)p_{e\rho}|\nu_e(p_1, h_1)e^-(p_e, h_e)\rangle\end{aligned} \tag{2.31}$$

Using the above relation and $\not{p}_e = p_{e\rho}\gamma^\rho$ we get

$$\begin{aligned}\bar{H}^{cc}_{eff}(x) =& \langle \nu_e(p_1, h_1)e^-(p_e, h_e)|\frac{G_F}{\sqrt{2}V}\bar{\nu}_e(x)\int d^3p_e f(E_e, T)N_e(p_e)\frac{\not{p}_e}{E_e}(1-\gamma^5) \\ &\times \nu_e(x)|\nu_e(p_1, h_1)e^-(p_e, h_e)\rangle\end{aligned} \tag{2.32}$$

Since the integral of $\vec{p}_e/E_e$ is zero, being an odd integral, we can calculate the integration in the above equation as follows

$$\begin{aligned}\int d^3p_e f(E_e,T)N_e(p_e)\frac{\not{p}_e}{E_e} &= \int d^3p_e f(E_e,T)N_e(p_e)(\gamma^0 - \frac{\vec{p}_e.\vec{\gamma}}{E_e}) \\ &= N_e V\gamma^0\end{aligned} \tag{2.33}$$

This leads to

$$\bar{H}^{cc}_{eff} = \langle\nu_e(p_1,h_1)e^-(p_e,h_e)|\frac{G_F N_e}{\sqrt{2}}\bar{\nu}_e(x)\gamma^0(1-\gamma^5)\nu_e(x)|\nu_e(p_1,h_1)e^-(p_e,h_e)\rangle \tag{2.34}$$

Now we integrate over x to get CC potential V_{cc}

$$\begin{aligned}V_{cc} &= \langle\nu_e(p_1,h_1)e^-(p_e,h_e)|\frac{G_F N_e}{\sqrt{2}}\int\bar{\nu}_e(x)\gamma^0(1-\gamma^5)\nu_e(x)dx|\nu_e(p_1,h_1)e^-(p_e,h_e)\rangle \\ &= \langle\nu_e(p_1,h_1)e^-(p_e,h_e)|\frac{G_F N_e}{\sqrt{2}}\times\frac{1}{2VE_\nu}\int Tr[(\not{p}_\nu + m_\nu)\gamma^0(1-\gamma^5)] \\ &\times a^\dagger(p_1,h_1)a(p_1,h_1)dx|\nu_e(p_1,h_1)e^-(p_e,h_e)\rangle \\ &= \langle\nu_e(p_1,h_1)e^-(p_e,h_e)|\frac{G_F N_e}{\sqrt{2}}\times\frac{1}{2VE_\nu}\int 4E_\nu dx|\nu_e(p_1,h_1)e^-(p_e,h_e)\rangle \\ &= \langle\nu_e(p_1,h_1)e^-(p_e,h_e)|\frac{G_F N_e}{\sqrt{2}}\times\frac{2}{V}\int dx|\nu_e(p_1,h_1)e^-(p_e,h_e)\rangle \\ V_{cc} &= \sqrt{2}G_F N_e\end{aligned} \tag{2.35}$$

For anti-neutrinos $V_{cc} = -\sqrt{2}G_F N_e$. It can understood in a simple manner as follows, As the last two components go to zero at the rest frame of unpolarised electrons, the final effective potential is given by

$$\begin{aligned}\bar{H}_{eff} &= \frac{G_F}{\sqrt{2}}N_e\bar{\nu}_e\gamma^0(1-\gamma_5)\nu_e \\ &= \sqrt{2}G_F N_e[\nu_e^\dagger\frac{1-\gamma_5}{2}\gamma^0]\gamma^0[(\frac{1-\gamma_5}{2})\nu_e] \\ &= \sqrt{2}G_F N_e\bar{\nu}_{eL}\gamma^0\nu_{eL} = v_{cc}j_\nu\end{aligned} \tag{2.36}$$

where $V_{cc} = \sqrt{2}G_F N_e$ and $j_\nu = \bar{\nu}_{eL}\gamma^0\nu_{eL}$ is current density. For anti-neutrino, we have to consider conjugate of $j_\nu \longrightarrow j_\nu^C$

$$\begin{aligned} j_\nu^C &= \bar{\nu}_{eL}^C\gamma^0\nu_{eL}^C = -\nu_{eL}^T C^{-1}\gamma^0 C\bar{\nu}_{eL}^T \\ &= \nu_{eL}^T(\gamma^0)^T\bar{\nu}_{eL}^T \\ &= -\bar{\nu}_{eL}\gamma^0\nu_{eL} = -j_\nu \end{aligned} \tag{2.37}$$

Thus, the effective potential for anti-neutrino is given by

$$\bar{H}_{eff} = \bar{v}_{cc} j_\nu \tag{2.38}$$

where $\bar{v}_{cc} = -\sqrt{2}G_F N_e$.

2.2.3 Neutral Current Interaction

NC interaction occurs between ν_e, ν_μ, ν_τ and leptons e^-, p, n but effectively interaction with neutrons only contributes as interaction with e^-, p cancel each other.The effective NC Hamiltonian density for an electron neutrino ν_e propagating through a homogeneous isotropic gas of electrons at rest is given by

$$H_{eff}^{nc}(x) = \frac{4G_F}{\sqrt{2}} J_{Z\rho} J_Z^{\dagger\rho} \tag{2.39}$$

where $J_Z^\rho = \frac{1}{2}\sum_i \bar{\psi}_i\gamma^\rho[I_i^3(1-\gamma_5) - 2Q_i\sin^2\theta_w]\psi_i,\ i = (l, u, d, \nu_l),\ I_i^3, Q_i$ are corresponding isospin and particle charge respectively(θ_w: Weinberg Angle). The calculations in this subsection are inspired from [97].

Calculation of V_{nc}^n

The scattering between n and $\nu_\alpha(\alpha = e, \mu, \tau)$ is mediated through Z^0 boson. Neutron consists of one u and two d quarks. The relevant Hamiltonian densities for both of them are

$$\begin{aligned} H_u^{nc}(x) &= \frac{G_F}{2\sqrt{2}}[\bar{u}(x)\gamma^\rho(1-\gamma^5-\frac{8}{3}\sin^2\theta_w)u(x)][\bar{\nu}_\alpha(x)\gamma_\rho(1-\gamma^5)\nu_\alpha(x)] \\ H_d^{nc}(x) &= -\frac{G_F}{2\sqrt{2}}[\bar{d}(x)\gamma^\rho(1-\gamma^5-\frac{4}{3}\sin^2\theta_w)d(x)][\bar{\nu}_\alpha(x)\gamma_\rho(1-\gamma^5)\nu_\alpha(x)] \end{aligned} \tag{2.40}$$

The Hamiltonian for $\nu_\alpha n$ scattering is obtained by addition of $H_u^{nc}(x), H_d^{nc}(x)$ in $1:2$ ratio as

$$H_n^{nc}(x) = -\frac{G_F}{2\sqrt{2}}[\bar{n}(x)\gamma^\rho(1-\gamma^5)n(x)][\bar{\nu}_\alpha(x)\gamma_\rho(1-\gamma^5)\nu_\alpha(x)] \tag{2.41}$$

If we take $f(E_n,T)$ as the Fermi distribution for neutrons, then the average of effective Hamiltonian over unpolarised neutron medium is given as

$$\begin{aligned} \bar{H}_{n,eff}^{nc}(x) =& \langle \nu_\alpha(p_1,h_1)n(p_n,h_n)|\frac{-G_F}{2\sqrt{2}}\bar{\nu}_\alpha(x)\gamma^\rho(1-\gamma^5)\nu_\alpha(x)\int f(E_n,T)d^3p_n \\ &\times \frac{1}{2}\sum_{h_n=\pm 1}\bar{n}(x)\gamma_\rho(1-\gamma^5)n(x)|\nu_\alpha(p_1,h_1)n(p_n,h_n)\rangle \end{aligned} \tag{2.42}$$

Apart from a $-\frac{1}{2}$ being present as a multiple $\bar{H}_{n,eff}^{nc}(x)$ is similar to $\bar{H}_{eff}^{cc}(x)$. Carrying out similar steps, we get potential due to $\nu_\alpha n$ scattering as

$$V_{nc}^n = -\frac{G_F N_n}{\sqrt{2}} \tag{2.43}$$

As in normal matter $N_n \sim N_e$ we can say

$$V_{nc}^n = -\frac{G_F N_e}{\sqrt{2}} = -\frac{V_{cc}}{2} \tag{2.44}$$

For anti-neutrinos $V_{nc}^n = G_F N_e/\sqrt{2}$

Calculation of V_{nc}^p, V_{nc}^e

The scatterings between p and ν_α are also mediated by Z^0 boson. A proton consists of two u quarks and one d quark. The effective Hamiltonian density for

$\nu_\alpha p$ scattering is obtained by adding $H_u^{nc}(x), H_d^{nc}(x)$ in $2:1$ ratio as

$$H_p^{nc}(x) = \frac{G_F}{2\sqrt{2}}[\bar{p}(x)\gamma^\rho(1-\gamma^5 - 4\sin^2\theta_w)p(x)][\bar{\nu}_\alpha(x)\gamma_\rho(1-\gamma^5)\nu_\alpha(x)] \tag{2.45}$$

The effective Hamiltonian density for $\nu_\alpha e^-$ scattering is

$$H_p^{nc}(x) = -\frac{G_F}{2\sqrt{2}}[\bar{e}(x)\gamma^\rho(1-\gamma^5 - 4\sin^2\theta_w)e(x)][\bar{\nu}_\alpha(x)\gamma_\rho(1-\gamma^5)\nu_\alpha(x)] \tag{2.46}$$

Thus, the NC interaction potential of p, e^- cancels each other in an electrically neutral medium.

2.2.4 Oscillation probability in matter: Two flavor

In matter, the evolution equation for neutrinos gets modified by the inclusion of matter potential term V_{cc} in the Hamiltonian as follows,

$$\iota\frac{d}{dt}\begin{pmatrix}\nu_e\\ \nu_\mu\end{pmatrix} = H_F^{mat}\begin{pmatrix}\nu_e\\ \nu_\mu\end{pmatrix} \tag{2.47}$$

where matter Hamiltonian H_F^{mat} in flavor basis is defined as,

$$H_F^{mat} = E\mathbf{I} + \frac{1}{2E}U\begin{pmatrix}m_1^2 & 0\\ 0 & m_2^2\end{pmatrix}U^\dagger + \frac{1}{2E}\begin{pmatrix}A & 0\\ 0 & 0\end{pmatrix} \tag{2.48}$$

where $A = 2EV_{cc} = 2\sqrt{2}G_F N_e E$. As addition or subtraction of matrix proportional to unit matrix doesn't change probabilities, $(E + \frac{A}{4E} + \frac{m_1^2}{2E})\mathbf{I}$ is subtracted from H_F^{mat} to obtain the Hamiltonian as,

$$H_F^{mat} = \frac{1}{4E}\begin{pmatrix}A - \Delta_{21}\cos 2\theta & \Delta_{21}\sin 2\theta\\ \Delta_{21}\sin 2\theta & -A + \Delta_{21}\cos 2\theta\end{pmatrix} \tag{2.49}$$

The eigenvalues of H_F^{mat} are evaluated as follows,

$$E_{1,2}^M = \frac{1}{4E}[A \pm \sqrt{(-A + \Delta_{21}\cos 2\theta)^2 + (\Delta_{21}\sin 2\theta)^2}] \tag{2.50}$$

If we compare the above energy eigenvalues with that of vacuum energy eigenvalues where $\Delta E = E_2 - E_1 = \Delta_{21}/2E$, the mass difference Δ_{21} is modified to Δ_{21}^M as follows,

$$\Delta_{21}^M = (E_2^M - E_1^M)2E = \sqrt{(-A + \Delta_{21}\cos 2\theta)^2 + (\Delta_{21}\sin 2\theta)^2} \tag{2.51}$$

The matter modified Δ_{21}^M will revert back to Δ_{21} if we put $A = 0$ in eq. (2.51). Similar to the mass eigenvalues, the mixing angles will also be modified to $\theta \longrightarrow \theta_M$ leading to $U(\theta) \longrightarrow U_M(\theta_M)$. The Hamiltonian in matter basis $H_M^{mat} = U_M^\dagger H_F^{mat} U_M$ will be diagonal;

$$H_M^{mat} = \frac{1}{4E}\begin{pmatrix} \cos\theta_M & -\sin\theta_M \\ \sin\theta_M & \cos\theta_M \end{pmatrix}\begin{pmatrix} 2A - \Delta_{21}\cos 2\theta & \Delta_{21}\sin 2\theta \\ \Delta_{21}\sin 2\theta & \Delta_{21}\cos 2\theta \end{pmatrix}\begin{pmatrix} \cos\theta_M & \sin\theta_M \\ -\sin\theta_M & \cos\theta_M \end{pmatrix} \tag{2.52}$$

Imposing non-diagonal terms of H_M^{mat} is equal to zero leads to the relation between θ_M and θ,

$$\tan 2\theta_M = \frac{\Delta_{21}\sin 2\theta}{-A + \Delta_{21}\cos 2\theta} \tag{2.53}$$

The $\nu_e \longrightarrow \nu_\mu$ conversion probability in matter is expressed as,

$$P_{e\mu} = \sin^2 2\theta_M \sin^2[1.27\Delta_{21}^M L/E] \tag{2.54}$$

But unlike in vacuum, in this case, the probability is sensitive to the sign of Δ_{21} and the octant of θ as seen from the dependence of Δ_{21}^M and θ_M respectively on them from the equations (2.51),(2.53). The Mikheyev–Smirnov–Wolfenstein (MSW) resonance[83, 98] happens at $A = \Delta_{21}\cos 2\theta$ where the mixing is maximal with $\theta_M = \pi/4$. A is positive for neutrinos and negative for anti-neutrinos. Hence MSW resonance is only seen in the neutrino(anti-neutrino) channel for Δ_{21} =+ve(-ve).

2.2.5 Oscillation probability in matter: Three flavor

The exact analytical expression for probability can't be evaluated for three flavors without proper approximation. The total Hamiltonian in flavor basis for constant matter density can be written as,

$$H_F^{mat} = \frac{1}{2E} U \begin{pmatrix} 0 & 0 & 0 \\ 0 & \Delta_{21} & 0 \\ 0 & 0 & \Delta_{31} \end{pmatrix} U^\dagger + \begin{pmatrix} \sqrt{2} G_F N_e & 0 & 0 \\ 0 & 0 & 0 \\ 0 & 0 & 0 \end{pmatrix} \tag{2.55}$$

The exact diagonalization of the above Hamiltonian analytically is a non-trivial calculation. Therefore, we need to resort to approximation methods. We also consider constant matter density. The two often used approximate methods are; (i) one mass scale dominance method and (ii) $\alpha - s_{13}$ method. A summary of the various analytical approaches in the context of 3 flavors has been discussed in ref. [99].

One Mass Scale Dominance (OMSD) Approximation

First, we use OMSD approximation[100] method. The value of Δ_{21} has been found[2] to be significantly less than Δ_{31}. So we can neglect Δ_{21} in the Hamiltonian. It leads to the mixing matrix being U independent of θ_{12} and δ_{cp}. The new mixing matrix will be

$$U = R_{23} R_{13} = \begin{pmatrix} c_{13} & 0 & s_{13} \\ -s_{23}s_{13} & c_{23} & s_{23}c_{13} \\ -c_{23}s_{13} & -s_{23} & c_{23}c_{13} \end{pmatrix} \tag{2.56}$$

Now we go to a new basis by rotating U by $R_{23}^\dagger$ leading to an effective two flavor scenario between $1-3$ sector,

$$\tilde{U} = R_{23}^\dagger U = R_{13} = \begin{pmatrix} c_{13} & 0 & s_{13} \\ 0 & 1 & 0 \\ -s_{13} & 0 & c_{13} \end{pmatrix} \tag{2.57}$$

[2] $\Delta_{21} = 7.4 \times 10^{-5} \mathrm{eV}^2$, $\Delta_{31} = 2.5 \times 10^{-3} \mathrm{eV}^2$[101]

We use this new basis to calculate energy eigenvalues of the following H_F^{mat}

$$H_F^{mat} = \frac{\Delta_{31}}{4E}\begin{pmatrix} 2s_{13}^2 + \frac{2A}{\Delta_{31}} & 0 & 2c_{13}s_{13} \\ 0 & 0 & 0 \\ 2c_{13}s_{13} & 0 & 2c_{13}^2 \end{pmatrix} \tag{2.58}$$

It can be seen that the matter effect impacts the 1-3 sector. The energy eigenvalues are as follows,

$$E_1 = \frac{1}{4E}[(\Delta_{31} + A) - \sqrt{(\Delta_{31}\cos 2\theta_{13} - A)^2 + (\Delta_{31}\sin 2\theta_{13})^2}] \tag{2.59}$$

$$E_2 = 0 \tag{2.60}$$

$$E_3 = \frac{1}{4E}[(\Delta_{31} + A) + \sqrt{(\Delta_{31}\cos 2\theta_{13} - A)^2 + (\Delta_{31}\sin 2\theta_{13})^2}] \tag{2.61}$$

It gives us the modified mass difference as

$$\Delta_{31}^M = \sqrt{(\Delta_{31}\cos 2\theta_{13} - A)^2 + (\Delta_{31}\sin 2\theta_{13})^2} \tag{2.62}$$

As this an effective two flavor case, we will get the new modified mixing matrix $U^M = R_{23}R_{13}^M$, but here only θ_{13} will be modified as θ_{13}^M. The mixing angle θ_{23} will not be modified as the matter effect only modifies the evolution equation of ν_e whose mixing doesn't depend on θ_{23}. The relation between the modified θ_{13}^M and vacuum mixing angle θ_{13} can be found by making the non-diagonal term of modified Hamiltonian in matter basis to go zero,

$$\tan 2\theta_{13}^M = \frac{\Delta_{31}\sin 2\theta_{13}}{\Delta_{31}\cos 2\theta_{13} - A} \tag{2.63}$$

Now using the vacuum formula for probability from equation 1.15, and replacing $\theta_{13} \to \theta_{13}^M$, and $\Delta_{ij} \to \Delta_{ij}^M$, the transition probability is obtained as,

$$P_{e\mu} = \sin^2\theta_{23}\sin^2 2\theta_{13}^M \sin^2\left[\frac{\Delta_{31}^M L}{4E}\right] \tag{2.64}$$

The validity of this approximation depends on two conditions: (I) $\frac{\Delta_{21}L}{E} << 1$ and (II) θ_{13} to be large enough to make the terms with Δ_{21} smaller w.r.t leading order terms with θ_{13}.

$\alpha - s_{13}$ Approximation

Parameters $\alpha = \Delta_{21}/\Delta_{31}, \sin\theta_{13}$ are by far smaller[3] than the other oscillation parameters and can be used as parameters for the series expansion[102] method to calculate probabilities in constant matter density. The effective Hamiltonian in flavor basis is

$$\begin{aligned} H_F^{mat} &= \frac{\Delta_{31}}{2E}[U diag(0,\alpha,1)U^\dagger + diag(\hat{A},0,0)] \\ &= \frac{\Delta_{31}}{2E} R_{23}U^\delta[R_{13}R_{12}diag(0,\alpha,1)R_{12}^T R_{13}^T + diag(\hat{A},0,0)]U^{\dagger\delta}R_{23}^T \\ &= \frac{\Delta_{31}}{2E} R_{23}U^\delta M U^{\delta\dagger}R_{23}^T = R_{23}U^\delta H_F^{\prime mat}U^{\delta\dagger}R_{23}^T \end{aligned} \tag{2.65}$$

Where we define[4]

$$H_F^{\prime mat} = \frac{\Delta_{31}}{2E}\begin{pmatrix} s_{12}^2c_{13}^2\alpha + s_{13}^2 + \hat{A} & \alpha c_{12}c_{13}s_{12} & s_{13}c_{13}(1-\alpha s_{12}^2) \\ \alpha s_{12}c_{12}c_{13} & \alpha c_{12}^2 & -\alpha c_{12}s_{12}s_{13} \\ s_{13}c_{13}(1-\alpha s_{12}^2) & -\alpha s_{12}c_{12}s_{13} & \alpha s_{12}^2 s_{13}^2 + c_{13}^2 \end{pmatrix} \tag{2.66}$$

We will diagonalize using perturbation theory up to second order in the small parameters $\alpha, \sin\theta_{13}$. After putting $\cos\theta_{13} = 1$, Hamiltonian $H_F^{\prime mat}$ can be expressed as,

$$M = M^0 + M^1 + M^2 \tag{2.67}$$

where M^0, M^1, M^2, respectively zeroth, first, and second order Hamiltonian, are expressed as

$$M^0 = diag(\hat{A},0,1) = diag(\lambda_1^0, \lambda_2^0, \lambda_3^0) \tag{2.68}$$

$$M^1 = \begin{pmatrix} \alpha s_{12}^2 & \alpha s_{12}c_{12} & s_{13} \\ \alpha s_{12}c_{12} & \alpha c_{12}^2 & 0 \\ s_{13} & 0 & 0 \end{pmatrix} \tag{2.69}$$

$$M^2 = \begin{pmatrix} s_{13}^2 & 0 & -\alpha s_{13}s_{12}^2 \\ 0 & 0 & -\alpha s_{13}s_{12}c_{12} \\ -\alpha s_{13}s_{12}^2 & -\alpha s_{13}s_{12}c_{12} & -s_{13}^2 \end{pmatrix} \tag{2.70}$$

[3] $\alpha = 0.03$, $\sin\theta_{13} = 0.15$ whereas $\sin\theta_{12} = 0.56$, $\sin\theta_{23} = 0.75$

[4] Here I've used notations as following $s_{ij} = \sin\theta_{ij}$, $c_{ij} = \cos\theta_{ij}$

The eigenvalues λ_i's of M are written as

$$\lambda_i = \lambda_i^0 + \lambda_i^1 + \lambda_i^2 \tag{2.71}$$

Similarly eigenvectors of M are

$$v_i = v_i^0 + v_i^1 + v_i^2 \tag{2.72}$$

Where $v_i^0 = e_i$ as M^0 are diagonal. The first and second order corrections to eigenvalues are as follows,

$$\lambda_i^1 = M_{ii}^1 = \langle v_i^0 | M^1 | v_i^0 \rangle \tag{2.73}$$

$$\lambda_i^2 = M_{ii}^2 + \sum_{j \neq i} \frac{(M_{ii}^1)^2}{\lambda_i^0 - \lambda_j^0} \tag{2.74}$$

where $M_{ii}^2 = \langle v_i^1 | M^2 | v_i^1 \rangle$. The corrections to the eigenvectors are given as

$$v_i^1 = \sum_{j \neq i} \frac{M_{ij}^1}{\lambda_i^0 - \lambda_j^0} e_j \tag{2.75}$$

$$v_i^2 = \sum_{j \neq i} \frac{1}{\lambda_i^0 - \lambda_j^0} [M_{ij}^2 + (M^1 v_i^1)_j - \lambda_i^1 (v_i^1)_j] e_j \tag{2.76}$$

Using the above equations (2.73),(2.74),(2.75) we get the energy eigenvalues $E_i = \frac{\Delta_{31}}{2E} \lambda_i$ as

$$E_1 = \frac{\Delta_{31}}{2E} \left(\hat{A} + \alpha \sin^2\theta_{12} + \sin^2\theta_{13} \frac{\hat{A}}{\hat{A}-1} + \alpha^2 \frac{\sin^2 2\theta_{12}}{4\hat{A}} \right) \tag{2.77}$$

$$E_2 = \frac{\Delta_{31}}{2E} \left(\alpha \cos^2\theta_{12} - \alpha^2 \frac{\sin^2 2\theta_{12}}{a\hat{A}} \right) \tag{2.78}$$

$$E_3 = \frac{\Delta_{31}}{2E} \left(1 - \sin^2\theta_{13} \frac{\hat{A}}{\hat{A}-1} \right) \tag{2.79}$$

We also calculate the corresponding eigenvectors v_1, v_2, v_3.
Using modified mixing matrix $U_M = R_{23} U^\delta W$ where $W = (v_1, v_2, v_3)$, here we diagonalize the Hamiltonian to mass basis and also get the probability by using

eq. (2.17) for neutrinos (Normal Hierarchy) for $N = 3$ as follows,

$$
\begin{aligned}
P_{e\mu} &= \sin^2\theta_{13}\sin^2\theta_{23}\frac{\sin^2[(\hat{A}-1)\Delta]}{(\hat{A}-1)^2} + \alpha^2\sin^2 2\theta_{12}\cos^2\theta_{23}\frac{sin^2[\hat{A}\Delta]}{\hat{A}^2} \\
&+ 2\alpha\sin\theta_{13}\sin 2\theta_{12}\sin 2\theta_{23}\cos[\Delta-\delta_{cp}]\frac{\sin[\hat{A}\Delta]}{\hat{A}}\frac{\sin[(\hat{A}-1)\Delta]}{(\hat{A}-1)}
\end{aligned} \tag{2.80}
$$

$$P_{\mu\mu} = 1 - \sin^2 2\theta_{23}\sin^2\Delta + \text{higher order terms} \tag{2.81}$$

where $\Delta = \Delta_{31}L/4E$. For Inverted Hierarchy solutions $\Delta \to -\Delta$ and $\hat{A} \to -\hat{A}$. We will get anti-neutrino probability by replacing $\hat{A} \to -\hat{A}$ and $\delta_{cp} \to -\delta_{cp}$.

The $\alpha - s_{13}$ approximation is not valid if $\alpha\Delta = \frac{\Delta_{21}L}{4E}$ is close to the order of unity letting oscillation properties controlled by Δ_{21}. So, this approximation must not be applied for very long baselines or very low energies.

Validity of OMSD & $\alpha - s_{13}$ Approximation

These above-cited approximations are valid at different limits, as discussed. We will now check the validity of these approximations by comparing the probabilities calculated analytically with the numerical solution obtained using GLoBES [103, 104] at different baselines of 1300 km and 7000 km. In figure. 2.2, appearance probability $P_{\mu e}$ has been plotted using OMSD (blue), $\alpha - s_{13}$ (brown) approximations and using GLoBES(orange). From the left panel of fig. 2.2, it's clear that

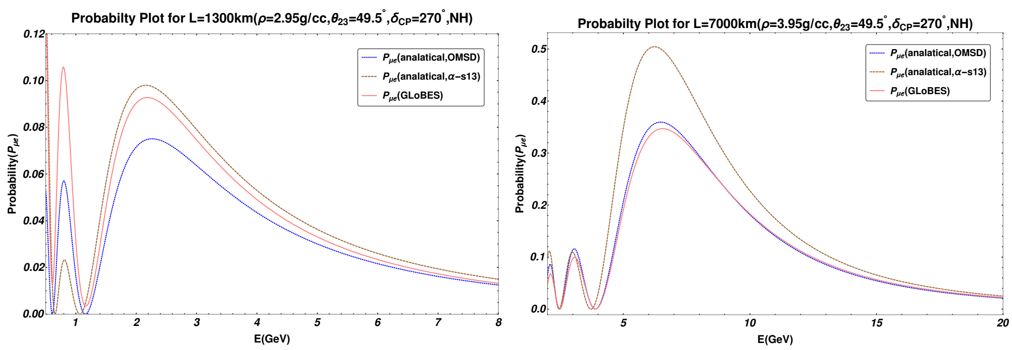

Figure 2.2: Comparing the analytical & GLoBES probability as function of energy at baseline of 1300 km(left), and 7000 km(right)

OMSD is not a good approximation for the baselines 1300 km. In these baselines, $\alpha - s_{13}$ approximation provides more accurate results w.r.t GLoBES plot and, therefore, best suited for probing sub-leading δ_{CP} effects in current long-baseline experiments. The right panel of fig. 2.2 shows that at the higher baseline of 7000 Km near the MSW resonance region, OMSD approximation being exact in θ_{13} holds up better than $\alpha - s_{13}$ and therefore is best suited for atmospheric experiments. We also present Cayley Hamilton's formalism to calculate the probabilities in the appendix.

2.3 Evidences of Neutrinos Oscillations

Neutrino oscillations have been experimentally verified in various solar, atmospheric, reactor, and accelerator neutrino experiments over the years.

2.3.1 Solar Neutrino Anomaly

John Bahcall first predicted that neutrinos created in the sun can be detected through the chlorine-argon reaction [105]. Ray Davis set up an experiment at Homestake Gold mine in South Dakota with a tank filled with 390 liters of perchloroethylene (C_2Cl_4) to detect the solar neutrinos with a threshold energy of 0.814 MeV through the following reaction;

$$\nu_e +^{37} \mathrm{Cl} \rightarrow^{37} \mathrm{Ar} + \mathrm{e}^- \tag{2.82}$$

The produced ^{37}Ar would then be extracted chemically to count the no of neutrino interactions. The results of the experimental analysis showed 2.1 ± 0.3 solar neutrino unit (SNU) against a prediction of 7.8 SNU, i.e., almost a two-third difference from the expected value. This discrepancy of missing neutrinos came to be known as the *solar neutrino anomaly.*

This created lots of debate in the scientific community, with three possible reasons: (i) the solar model or the calculation of neutrino flux or both are inaccurate, (ii) the experiment is wrong, (iii) ν_e conversion to some other flavor. Questions were raised about the radiochemical detection technique used by Davis and its inability to point out the direction of the source. New experiments were proposed to detect the solar neutrinos to better understand the solar neutrino anomaly.

The Kamiokande experiment in Japan at 2700 meters underground had a huge detector filled with 3 ktons of pure water and surrounded by 1000 PMTs. This detector provided advantages of real-time detection and direction reconstruction of neutrinos with a threshold energy of 7 MeV. Neutrinos were detected through the formation of Cherenkov radiation. At the end of a few years of the experimental run, Kamiokande found only half of the predicted neutrino flux. They could also confirm the direction of neutrinos pointing toward the sun.

At the same time, in the early 1990s, radio chemical neutrino experiments GALLEX and SAGE with detectors filled with Gallium were planned to detect solar electron neutrinos with a threshold energy of 0.2 MeV undergoing the following reaction,

$$\nu_e +^{71}\mathrm{Ga} \rightarrow^{71}\mathrm{Ge} + \mathrm{e}^- \tag{2.83}$$

The produced germanium (^{71}Ge) would then be extracted and counted from its radioactive decay, giving the count of an ν_e interaction. Unlike previous water Cherenkov and chlorine experiments, gallium experiments could detect pp neutrinos, allowing them to cover the whole spectrum of solar neutrinos. Both of them detected[106, 107] only around 60% of theoretically predicted solar neutrino flux.

In 1985, Herbert Chen suggested[108] the use of heavy water containing deuterium (^{2}H) to detect neutrinos of other flavors than ν_e, confirming the theory of solar neutrinos changing their identity. The Sudbury neutrino observatory detector consisted of 1000 tons of heavy water surrounded by 9600 PMTs in a spherical mount. Detectors in SNO could observe the charge current, neutral current, and elastic scattering(ES) interactions of neutrinos.

$$\mathrm{CC}: \quad \nu_e + {}^2d^+ \rightarrow {}^1p^+ + {}^1p^+ + e^- \tag{2.84}$$

$$\mathrm{NC}: \quad \nu_{e,\mu,\tau} + {}^2d^+ \rightarrow {}^1n + {}^1p^+ + \nu_{e,\mu,\tau} \tag{2.85}$$

$$\mathrm{ES}: \quad \nu_{e,\mu,\tau} + e^- \rightarrow \nu_{e,\mu,\tau} + e^- \tag{2.86}$$

Only ν_e shows the CC interactions, whereas all the flavors participate in NC interactions. Mostly, ν_e takes part in ES as the reaction cross section for ν_μ and

ν_τ are lower. The CC/NC ratio in the detectors would be 1 if only ν_e were detected. But in the presence of another neutrino flavor, the ratio would be less than 1. The results of CC and ES in 2001 showed the flux of ν_e to be similar to Kamiokande results [109]. However, from the results of neutral current interaction in 2002, the total flux was around the prediction by the solar model[110], and the CC/NC ratio was around 1/3. These two results confirmed the validation of the solar model along with the confirmation that solar neutrinos oscillate to other flavors.

2.3.2 Atmospheric Neutrino Anomaly

The atmospheric neutrino flux is mostly isotropic around the Earth. The atmospheric neutrino flux is mostly up-down symmetric, i.e., the zenith angle θ_{in} of neutrino entering and θ_{out} of exiting the Earth are related by $\theta_{in} = 180^\circ - \theta_{out}$. The detection of atmospheric neutrinos is possible from both up and downside, with the baseline varying from 15 km to 13000 km. As discussed in the previous chapter, there are both muon and electron neutrinos and anti-neutrinos in the atmospheric neutrino flux. The initial experiments detected the double ratio of these neutrino fluxes as,

$$R = \frac{[N_\mu/N_e]_{data}}{[N_\mu/N_e]_{MC}}, \tag{2.87}$$

where "*data*" suggests the experimental observed and "*MC*" refers to events calculated from Monte Carlo simulations. When the prediction of the model is exactly the same as the experimental results, then $R = 1$. The initial atmospheric neutrino experiments Kamiokande[48, 111], Sudan2[112], and IMB[113, 114] observed the value of R as significantly less than 1. This discrepancy came to be known as the `atmospheric neutrino anomaly`.

Contrary to the results of Kamiokande, the observations from experiments like Frejus[115, 116] and Nusex[117] show no discrepancy. Finally, the anomaly was resolved when Super-Kamiokande at an upgraded version of Kamiokande, observed[118] the zenith angle dependence of the neutrino flux. In the absence of neutrino oscillations, the atmospheric flux is symmetric for neutrino with multi-GeV energy. However, if the neutrino oscillates to other flavors, then upward-going neutrinos have more chances to oscillate due to more exposure to earth matter and change their flavors, leading to an asymmetry in the detected neutrino flux. Therefore, the detection of zenith angle dependence[119] established that atmospheric neutrinos undergo oscillation while traveling through the Earth.

2.3.3 Reactor Neutrino Experiments

In nuclear reactors, we have an apt and convenient source for studying neutrino oscillations as reactors produce a large flux of pure electron antineutrinos with well-known characteristics. The reactor neutrino experiments probe the disappearance of $\bar{\nu_e}$ through inverse beta decay. Although the first detected neutrinos were from a reactor, the signature of neutrinos changing flavors was not observed for a long time. At first, the neutrino oscillation experiments like ILL-Grenoble [120], Gosgen[121], Rovno [122], Krasnoyarsk [123], BUGEY [124], and Savannah River [125], couldn't detect neutrino oscillations at a distance <100 m from the reactor. Afterwards, various experiments like CHOOZ [126, 127] and Palo Verde [128, 129] increased the detector distance to 1 Km and yet failed to observe evidence of neutrino oscillations.

In 2002, the first observation of neutrino oscillations using reactor νs was achieved at a baseline length of $\sim$ 180 km from the source by KamLAND [130] experiment. The observation was very important as it could probe oscillation due to the solar neutrino mass squared difference of the order of $\sim 10^{-5}\text{eV}^2$ using a terrestrial source.

CHOOZ and Palo Varde experiments provided a bound on the mixing angle θ_{13} from the non-observance of oscillation. Later, the angle θ_{13} became known as the reactor mixing angle. Later, oscillation signatures were detected in experiments like Double-CHOOZ [131], RENO [132] and Daya Bay [133] with baselines of the order of a few kilometers that correspond to the atmospheric mass-squared difference $\sim 10^{-3}\text{eV}^2$. These experiments pioneered in establishing the non-zero value of θ_{13}.

2.3.4 Accelerator Neutrino Experiments

Accelerator neutrino experiments are powerful for studying neutrino oscillations because neutrinos are artificially produced with prominently known energies and fluxes. Accelerator neutrinos are two types: neutrinos with low energy produced through decay at rest, whereas decay in flight creates neutrinos with higher energy.

Several accelerator neutrino experiments have successfully witnessed neutrino oscillations. Accelerator experiments with long baselines allow neutrinos to travel through the earth and are hence ideal for studying matter effects. Long baseline experiments like MINOS [134], and K2K [135] had observed neutrino oscillations using DIF neutrinos beam of energy $\sim$ GeV and baselines of several hundred km. MINOS probed both $\nu_\mu \to \nu_\mu$ disappearance and $\nu_\mu \to \nu_e$ appearance channels while K2K studied the $\nu_\mu \to \nu_\mu$ disappearance channel. Both experiments confirmed oscillations driven by the atmospheric mass-squared difference of 10^{-3}eV^2.

The experiments Tokai to Kamioka (T2K) [136–138] in Japan with 295 km baseline and NuMI Off-axis ν_e Appearance (NOνA) experiment [139–141] at Fermilab with 810 km baseline are taking oscillation data in both the appearance and disappearance channels in both neutrino and anti-neutrino modes.

Accelerator neutrino experiments with short baselines lead the search for sterile neutrinos and neutrino interactions with other particles. The LSND experiment probed the $\nu_\mu \to \nu_e$ and $\bar{\nu_\mu} \to \bar{\nu_e}$ channel with DAR neutrinos and DIF neutrinos respectively. The signature of excess electron neutrinos, first observed in LSND[142], was anomalous as it corresponds to neutrino oscillation related to mass-squared difference eV^2. The MiniBooNE experiment was designed to test the LSND anomaly with the same L/E as LSND but with different energy and baseline lengths. MiniBooNE has confirmed[143] the LSND anomaly in both neutrinos and anti-neutrino channels. The current MicroBooNE experiment is probing neutrino oscillations related to the sterile neutrino.

2.4 Current status of three flavor neutrino oscillation paradigm

All the above experimental results confirmed the phenomena of neutrino oscillations and brought this field of study to the limelight. Neutrino oscillation requires these particles to be massive. This was the first experimental evidence of physics beyond the standard model. The consequences of this can be far-reaching and this was also acknowledged by the Nobel committee in 2015 by awarding the Nobel prize to Takaki Kajita of SK and Arthur B. McDonald of SNO jointly "for the discovery of neutrino oscillations, which shows that neutrinos have mass"[5].

The parameters governing three flavor oscillation probabilities are the three mixing angles $\theta_{12}, \theta_{13}, \theta_{23}$ corresponding to mixing between the mass eigenstates with mass eigenvalues m_1, m_2, m_3, the Dirac CP phase $\delta_{13}(\delta_{CP})$, the two mass squared differences $\Delta_{21} = m_2^2 - m_1^2$ driving the solar neutrino transitions and $\Delta_{31} = m_3^2 - m_1^2$ governing the atmospheric neutrino oscillations. Most of the parameters have been measured with considerable precision[144–146]. Currently, the unknowns in the standard oscillation sector are the mass ordering among the three neutrino states, the octant of the atmospheric mixing angle θ_{23}, and the value of the CP phase δ_{CP}. The mass ordering refers to whether the sign of the atmospheric mass squared difference Δ_{31} is positive (Normal Ordering/NH) or negative (Inverted Ordering/IH). The octant of θ_{23} signifies if the value of the angle lies above (Higher Octant/HO) or below (Lower Octant/LO) 45°. The current best fit values of the oscillation parameters are provided in table 2.1,

Parameters	3σ range	Best Fit	3σ range	Best Fit
$\sin^2\theta_{12}$	0.270 - 0.341	0.303	0.270 - 0.341	0.303
θ_{12}	$31.31° - 35.74°$	$33.41°$	$31.31° - 35.74°$	$33.41°$
$\sin^2\theta_{13}$	$0.0202 - 0.0239$	0.0220	$0.0202 - 0.0239$	0.0220
θ_{13}	$8.19° - 8.89°$	$8.54°$	$8.23° - 8.90°$	$8.57°$
$\sin^2\theta_{23}$	$0.406 - 0.620$	0.572	$0.412 - 0.623$	0.578
θ_{23}	$39.6° - 51.9°$	$49.1°$	$39.9° - 52.1°$	$49.5°$
δ_{13}	$197°$	$108° - 404°$	$286°$	$192° - 360°$
$\Delta_{21}/10^{-5}\mathrm{eV}^2$	$6.82 - 8.03$	7.41	$6.82 - 8.03$	7.41
$\Delta_{31}/10^{-3}\mathrm{eV}^2$	$2.428 - 2.597$	2.511	$-(2.581 - 2.408)$	-2.498

Table 2.1: 3σ levels and Best fit values extracted of oscillation parameters [101]

[5] https://www.nobelprize.org/prizes/physics/2015/summary/

2.5 Degeneracies

One of the most impeding factors in the precise determination of these three parameters is the presence of parameter degeneracies. Degeneracies occur when multiple sets of values of the parameter(s) give the same oscillation probabilities, making an unambiguous determination of these parameters difficult;

$$P_{\alpha\beta}(x_1, x_2, ...) = P_{\alpha\beta}(y_1, y_2, ...). \tag{2.88}$$

These degeneracies make an exact evaluation of the current unknowns of oscillation difficult. The degeneracies observed in the $P_{\mu\mu}$ channel(2.81) are as follows,

- Intrinsic degeneracy corresponding to sign of Δ_{31} is defined as,

$$P_{\mu\mu}(\Delta_{31}) = P_{\mu\mu}(-\Delta_{31}) \tag{2.89}$$

- Intrinsic degeneracy of the octant of θ_{23}[147] is defined as,

$$P_{\mu\mu}(\theta_{23}) = P_{\mu\mu}(90^\circ - \theta_{23}) \tag{2.90}$$

The presence of these degeneracies means the precise determination of mass ordering and the octant of θ_{23} is hindered. Before with the unknown θ_{13}, there was $\theta_{23} - \theta_{13} - \delta_{CP}$ degeneracy in the $P_{\mu e}$ channel. However, this has been ruled out following precise measurement of θ_{13}. The following degeneracies are seen in $P_{\mu e}$ channel(2.80),

- For a specific mass hierarchy, the same value of $P_{\mu e}$ for both $\theta_{23} < 45^\circ$(LO) and $\theta_{23} < 45^\circ$(HO) with different δ_{CP} leads to *octant-δ_{CP}* degeneracy, defined as

$$P_{\mu e}(\theta_{23}[\mathrm{HO}], \delta_{\mathrm{CP}}) = \mathrm{P}_{\mu e}(\theta'_{23}[\mathrm{LO}], \delta'_{\mathrm{CP}}) \tag{2.91}$$

- For a specific θ_{23}, the same value of $P_{\mu e}$ for both mass hierarchy NH($\Delta_{31} > 0$), IH($\Delta_{31} < 0$) with different value of δ_{CP} leads to *hierarchy-δ_{CP}* degeneracy, defined as

$$P_{\mu e}(\Delta_{31}[\text{NH}], \delta_{\text{CP}}) = \text{P}_{\mu e}(-\Delta'_{31}[\text{IH}], \delta'_{\text{CP}}) \tag{2.92}$$

- When all three parameters θ_{23}, δ_{CP} and mass hierarchy are unknown, the above two degeneracies combine to a generalized 8-fold *hierarchy-θ_{23}-δ_{CP}* degeneracy[148], defined as

$$P_{\mu e}(\text{NH}, \theta_{23}, \delta_{\text{CP}}) = \text{P}_{\mu e}(\text{IH}, \theta'_{23}, \delta'_{\text{CP}}) \tag{2.93}$$

2.5.1 The Hierarchy-δ_{CP} Degeneracy

To understand the degeneracy, we have plotted probability for a baseline of 810 km for a constant matter density of 3.2 g/cc considering $\theta_{23} = 45°$, $\Delta_{21} = 7.50 \times 10^{-5}\text{eV}^2$, $\theta_{12} = 33.48°$, $\theta_{13} = 8.50°$, $\theta_{23} = 45.00°$. and δ_{CP} being varied in the range $-180° : 180°$ creating the bands. For NH we consider $\Delta_{31} = 2.45 \times 10^{-3}\text{eV}^2$ and for IH $\Delta_{31} = -2.45 \times 10^{-3}\text{eV}^2$ is taken.

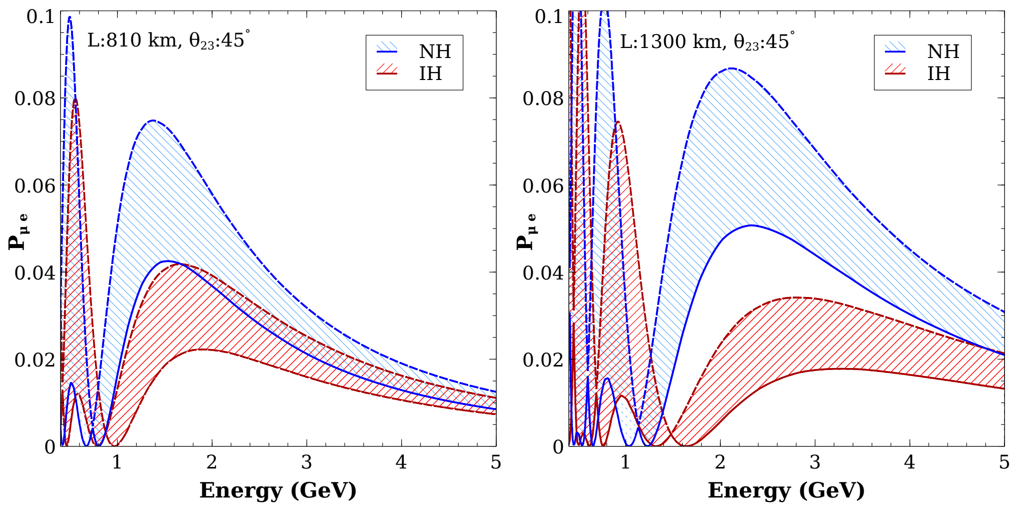

Figure 2.3: Probability $P_{\mu e}$ as a function of energy at a baseline of 810 Km(left), 1300 km (right). The blue(red) band corresponding to NH(IH) is formed due to variation of δ_{CP}.

In figure 2.3, probability bands of $P_{\mu e}$ are depicted as a function of energy at 810 km (left) and 1300 km (right). The blue(red) band corresponds to NH (IH) due to variation of δ_{CP} is the full range. The dashed and solid curves refer to $\delta_{CP} = -90°, 90°$, respectively. Overlap between regions of NH and IH leads to *wrong hierarchy solutions* whereas a gap between the bands suggests *true hierarchy* can be distinguished. The following observations can be made from fig. 2.3,

- The matter effect enhances the neutrino channel probability for NH to be higher w.r.t. IH.
- In the left panel, the overlap between both bands is around NH-$\delta_{CP} = 90°$ and IH-$\delta_{CP} = -90°$ reflects the degeneracy.
- $\delta_{CP} = -90°(90°)$ corresponds to maximum (minimum) probability as dictated by the last term in eq. (2.80).
- Around oscillation maxima ($\Delta = 90°$), there is a small gap between the bands in the left panel, whereas in the right panel, the gap is significant.
- This suggests true hierarchy can be determined at higher baselines as at large matter in higher baselines will elevate the probability for NH to a greater extent, creating a clear difference between the probabilities at maxima.

The hierarchy-δ_{CP} degeneracy will vanish if the last term containing δ_{CP} in the equation 2.80 becomes zero. There are two criteria for it,

$$\sin(\hat{A}\Delta) = 0 \tag{2.94}$$

$$\sin((\hat{A} - 1)\Delta) = 0 \tag{2.95}$$

Magic Baseline

The condition in (2.94) defines the magic baseline[149]. The baseline length is given in (2.96).

$$\begin{aligned} \hat{A}\Delta &= n\pi \\ L &= \frac{2n\pi}{\sqrt{2}G_F N_e} \end{aligned} \tag{2.96}$$

where n is any positive integer. The physical interpretation of the magic baseline was highlighted in [150]. For both NH and IH, the magic baseline length is

$L = 7640$ km with (n=1). So, there will be no hierarchy-δ_{CP} degeneracy if an experiment is designed around this baseline. However, this experiment will also not be sensitive to the value of δ_{CP}. The decreasing neutrino flux as $1/L^2$ means we will need larger detectors and more collimated neutrino beams to study oscillations at these baselines. However, for bimagic conditions, we do get smaller baselines.

Bimagic Baseline

In the bimagic baseline, the hierarchy-δ_{CP} degeneracy is removed along with the presence of CP sensitivity[151]. This can be achieved if the following two conditions must be satisfied simultaneously,

1. $\sin((\hat{A}-1)\Delta) = 0$ for one hierarchy
2. $\sin((\hat{A}-1)\Delta) = 1$ for the opposite hierarchy

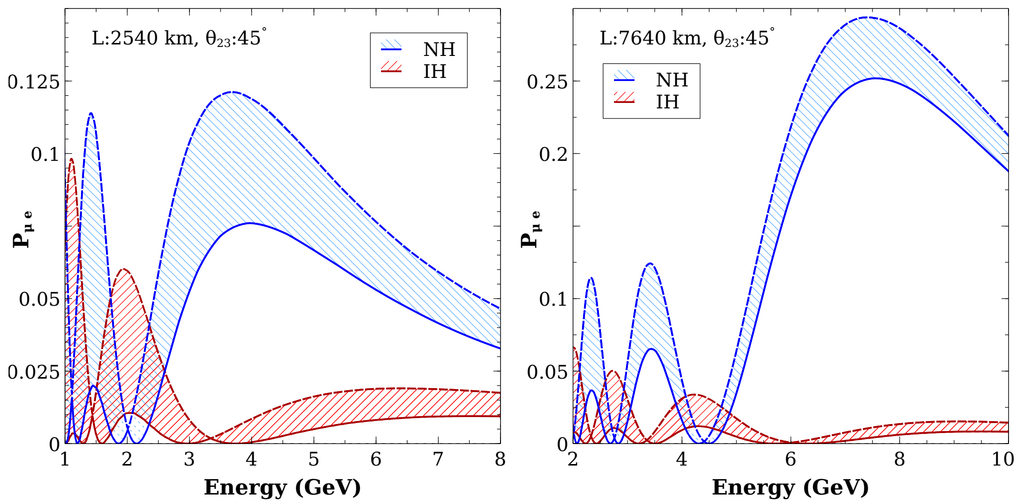

Figure 2.4: $P_{\mu e}$ as a function of energy at a bimagic baseline of 2540 Km (left) and magic baseline of 7640 km (right). The blue(red) band refers to the variation of δ_{CP} in NH(IH).

These criteria being fulfilled will lead to the minima of probability for one hierarchy occurring along with the maxima of the probability and the maximal δ_{CP} sensitivity for the opposite hierarchy at the same energy. At first, we consider the absence of δ_{CP} dependence (no degeneracy) in IH and maximum probability at

NH, i.e.,

$$(\hat{A}+1)|\Delta| = n\pi \tag{2.97}$$

$$(\hat{A}-1)|\Delta| = (m-1/2)\pi \tag{2.98}$$

Solving the above equations with suitable unit changes of baseline L (Km) and matter density ρ (g/cc) we have,

$$E_\nu^{IH}(GeV) = \frac{2\times 1.27\times \Delta_{31} L(km)}{\pi(n+m-1/2)} \tag{2.99}$$

$$L^{IH}(km) = \frac{16300\times(n-m+1/2)}{\rho} \tag{2.100}$$

If we consider $n=1, m=1$, $\Delta_{31} = 2.52\times 10^{-3} eV$ and $\rho = 3.2 g/cc$, then the corresponding baseline is $L^{IH} = 2540$ km and energy $E_\nu^{IH} = 3.45 GeV$. Figure 2.4 illustrates the variation of $P_{\mu e}$ with energy at 2540 Km bi-magic baseline with the blue (red) band corresponding to NH(IH). It can be observed that the hierarchy-δ_{CP} degeneracy vanishes at minima for IH and maxima for NH at energy 3.45 GeV.

Similarly, we can get baseline length for no δ_{CP} sensitivity in NH along with maximum probability in IH as following

$$L^{NH}(km) = \frac{16300\times(m-n-1/2)}{\rho} \tag{2.101}$$

In this case, energy E_ν^{NH} has the same expression as E_ν^{IH} in equation (2.99).

If we consider $n=1, m=2$ and the same matter density, we get the same baseline length at $L^{NH} = 2540$ Km with energy $E_\nu^{NH} = 2.07$ GeV also seen in the figure 2.4. However, it is to be noted that at energy 2.07 GeV, degeneracy is just lifted with separation between the regions being narrow, unlike at 3.45 GeV. The specialty of the 2540 km baseline is we can have hierarchy sensitivity for both NH and IH at different energies, with CP dependence in one of them together with CP independence in the other hierarchy. That's why this 2540 Km baseline is called bimagic.

2.5.2 The Octant-δ_{CP} Degeneracy

In this part, the focus is on the octant-δ_{CP} degeneracy. To explain this degeneracy in a better way, we have generated probability plots at a baseline of 810 Km with a constant matter density of 3.2 g/cc, taking normal mass hierarchy with $\theta_{23} = 41°$(LO), $\theta_{23} = 49°$(HO). The bands are created due to variation of δ_{CP} in the range of $-180°$ to $180°$. Values of other parameters taken for numerical calculations for plots are,
$\Delta_{21} = 7.50 \times 10^{-5}$ eV^2, $\Delta_{31} = 2.45 \times 10^{-3}$ eV^2(NH), $\theta_{12} = 33.48°$, $\theta_{13} = 8.50°$

In figure 2.5 $P_{\mu e}$ (left), $P_{\bar{\mu}\bar{e}}$ (right) is presented as a function of energy at a baseline of 810 km. The green(orange) band refers to the variation of δ_{CP} at $\theta_{23} = 49°(41°)$. In the top panels, δ_{CP} is carried over the full range, whereas in the bottom panels, the variation is on LHP(UHP) for θ_{23} in HO(LO). The dashed, dotted, and solid curves refer to $\delta_{CP} = -90°, 0°, 90°$ respectively. There are overlaps between regions of LO and HO, giving us the *wrong octant solution* for a specific experimentally observed probability. The notable observations from fig. 2.5 are as follows,

- The HO region is higher than LO. It is due to the fact that probability in (2.80) is directly proportional to $\sin^2\theta_{23}$.
- The region of overlap is around LO-$\delta_{CP} = -90°$ and HO-$\delta_{CP} = 90°$) for neutrino as seen in the top-left panel.
- For anti-neutrino the overlap is around LO-$\delta_{CP} = 90°$ and HO-$\delta_{CP} = -90°$ as seen in the top-right.

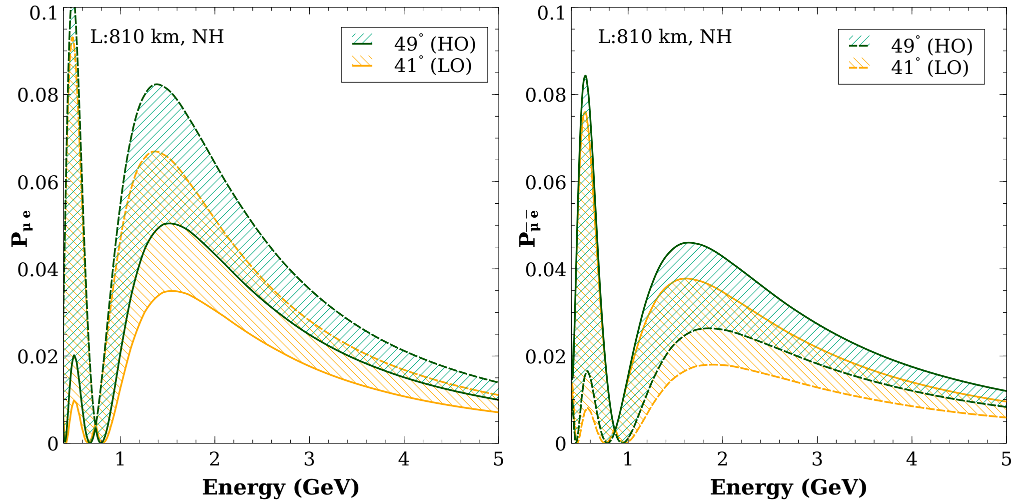

Figure 2.5: $P_{\mu e}$(left), $P_{\bar{\mu}\bar{e}}$(right)as a function of energy at 810 Km baseline. The green (orange) bands referring to HO(LO) are formed due to variation of δ_{CP}.

In figure 2.6, probability bands of $P_{\mu e}$ in HO and LO are plotted as a function of energy ta 1300 km (left) and 7000 km(right). As we go to higher baselines, the matter effect will be higher as $\sin\Delta$ increases with L. This will shift the region corresponding to HO to higher values and the region corresponding to LO to lower values and lift the degeneracy.

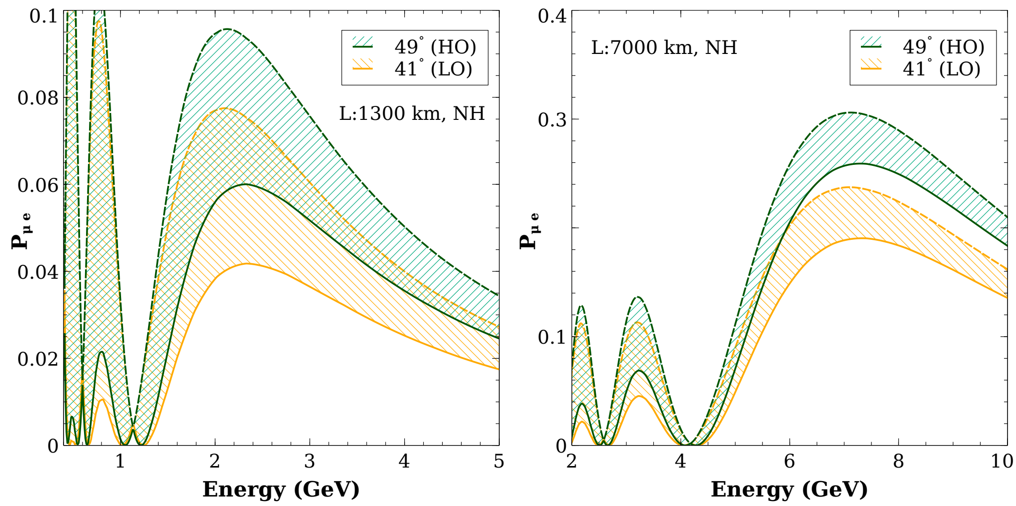

Figure 2.6: $P_{\mu e}$ as function of energy at 1300 km(left), 7000 Km (right) baseline. The green (orange) bands referring to HO(LO) are formed due to variation of δ_{CP}.

The maximum probabilities for neutrino and anti-neutrino are obtained at $\delta_{CP} = -90°, 90°$, respectively. So, the combination of the two through a bi-probability plot at the energy corresponding to oscillation maxima allows us to separate the degenerate solutions of HO and LO (figure:2.7). As atmospheric neutrinos include both neutrino and anti-neutrino, bi-probability plots, first used in [152], are useful to resolve the octant-δ_{CP} degeneracy in atmospheric neutrino experiments.

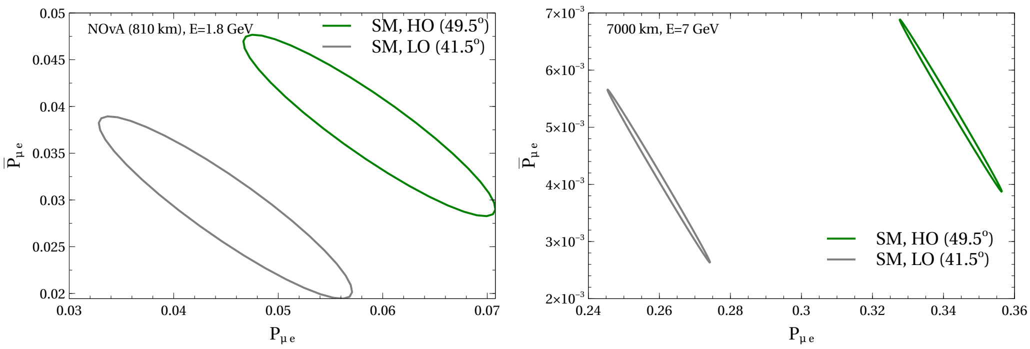

Figure 2.7: Bi-probability plot of neutrino and anti-neutrino channels at 810 km (left) and 7000 km (right) baseline.

2.6 Oscillation Experiments

Experiments to observe neutrinos played an important role not only in establishing the three neutrino oscillation framework and measuring the neutrino oscillation parameters but also in probing signatures of new physics.

Due to high energy and long baselines providing large matter effects, atmospheric neutrinos are useful for studying new physics scenarios in neutrino experiments.

The ongoing neutrino experiments like T2K[153], NOνA[154], IceCube, RENO, and SuperKamiokande will further help towards determining the unknown oscillation parameters. To measure these parameters with increased precision, experiments are planned such as DUNE[155], T2HK/T2HKK, ESSνSB[156], etc. Planned atmospheric neutrino experiments like HyperKamiokande[157], KM3NeT[158], PINGU[159], INO[160], etc can also throw light on these parameters. The works in the thesis focus on experimental setups with LArTPC detector similar to DUNE, water Cherenkov detectors such as T2HK/T2HKK, and observed data of IceCube.

2.6.1 Deep Underground Neutrino Observatory (DUNE)

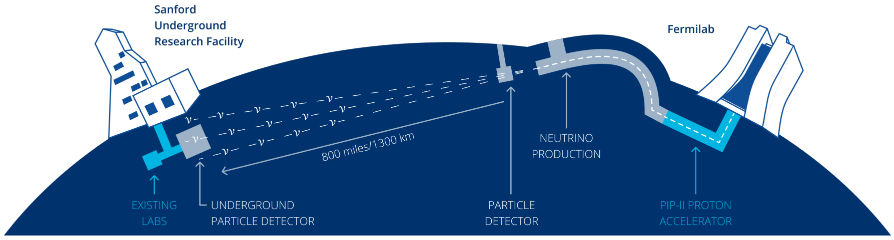

Figure 2.8: Schematic diagram of the setup of DUNE experiment. [https://lbnf-dune.fnal.gov/how-it-works/introduction/]

Deep Underground Neutrino Experiment (DUNE)[161, 162] is a promising up-coming long-baseline neutrino oscillation experiment supported by Long-Baseline Neutrino Facility (LBNF). LBNF and DUNE facilities together will constitute a high intensity neutrino beam of 0.5-8 GeV energy, a near detector at the Fermilab site, a 40 kt liquid argon time-projection chamber (LArTPC) as far detector 1300 km away at Sanford Underground Research Facility (SURF), South Dakota. Simulation of the DUNE experiment is done by considering a beam power of 1.2 MW, resulting in a total exposure of 10×10^{21} Protons on Target(POT) for a 10 years experimental run. The ν: $\bar{\nu}$ run time ratio for DUNE is considered 1:1. The experimental specifications for our simulation of DUNE are taken from the ref. [161]. DUNE is also capable of detecting atmospheric neutrinos.

2.6.2 IceCube Neutrino Observatory (IceCube)

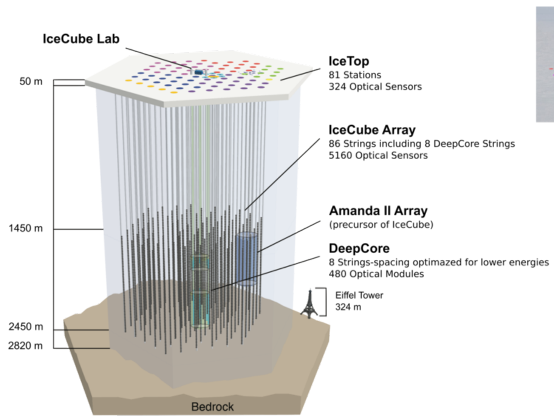

Figure 2.9: Schematic diagram of the setup of IceCube experiment and the Digital optical module[https://iihe.ac.be/icecube]

The IceCube Neutrino Observatory[163] (simply known as IceCube) is situated at the Amundsen–Scott South Pole Station in Antarctica. It contains thousands of sensors located under the Antarctic ice, distributed over a cubic kilometer. The in-ice component of IceCube has 5,160 digital optical modules (DOMs), each with a 10-inch PMT tube. Sixty DOMS attached to each of the 86 vertical strings are oriented in a hexagonal pattern at a depth of 1450 meters to 2500 meters. When neutrinos do interact with the molecules of water in the ice, they create charged leptons (electrons, muons, or taus). These charged leptons can, if they are energetic enough, emit Cherenkov radiation. This radiation is detected by photomultiplier tubes within the digital optical modules making up IceCube. IceCube is sensitive mostly to high-energy neutrinos, in the range of 10^7 eV to about 10^{21} eV.

The signals from the PMTs are digitized and then sent to the laboratory on the surface of the glacier on a cable. Data from PMTs can reconstruct the kinematical parameters of the incoming neutrino. High-energy neutrinos may cause a large signal in the detector, pointing back to their origin. Clusters of such neutrino directions indicate point sources of neutrinos.

IceCube is more sensitive to muons than other charged leptons because they are the most penetrating and thus have the longest tracks in the detector. An electron resulting from an electron neutrino event typically scatters several times before losing enough energy to fall below the Cherenkov threshold. This results in electron neutrino events typically being unable to point back to sources. However, they are more likely to be fully contained in the detector, and thus they can be useful for energy studies. These events are more spherical, or "cascade"-like, than "track"-like muon neutrino events. A tau could be distinguished from an electron with a "double bang" event, where a cascade is seen both at the tau creation and decay. This is only possible with the very high energy of PeV scale taus as their lifetime is very short. Such searches are underway but have not so far isolated a double bang event from background events[164].

IceCube has accomplished major landmarks in the detection of ultra-high energy neutrinos from astrophysical sources. It detected neutrino with energy peta electron volt, in ref. [50]. In 2020, IceCube observed[165] evidence of the Glashow resonance, i.e., the formation of the W boson in antineutrino-electron collisions of antineutrino (energy peV) and electron at 2.3σ. In June 2023, IceCube, for the first time, mapped [166] our galaxy through the detection of the neutrino diffuse emission from the Galactic plane at the 4.5σ level of significance.

2.6.3 Tokai to Hyper Kamiokande (T2HK) via Korea (T2HKK)

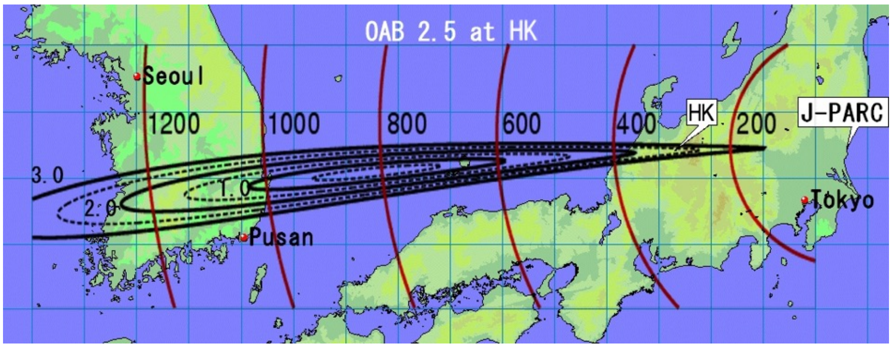

Figure 2.10: Schematic diagram of the location of detectors for T2HK/T2HKK experiment.[https://neutrino.skku.edu/hyper-kt2hkk/]

T2HK (Tokai to Hyper-Kamiokande)[167], is a natural extension to the existing T2K experiment. The default plan was to have two Hyper-Kamiokande detectors (cylindrical water tanks) of 187 kt at 295 km baseline in Kamioka. T2HKK is a newly proposed experiment that is planned to have one of the detectors at 295 Km in the Kamioka mine and another at 1100 km in Korea. The water-Cherenkov detector in Korea could be placed at one of the three suggested off-axis (OA) angles $1.5°$, $2°$ or $2.5°$. The optimization of these OA angles to give maximum sensitivity to various neutrino oscillation parameters has been explored in ref. [167]. This study indicates that the optimal configuration is to place the detector at $1.5°$ OA angle. Therefore, we have considered the 187 kt Korean detector at an OA angle of $1.5°$ in our simulations. The proposed runtime for both configurations is 1:3 in neutrino and antineutrino modes, and the total exposure of 27×10^{21} Protons on Target(POT) which is obtained by a beam energy of 1.3 MW and 10 years of the runtime of the experiment.

2.7 Numerical Analysis

For performing the numerical simulation, we have used the package General Long Baseline Experiment Simulator (GLoBES) [103, 104].

2.7.1 Events Calculation

The number of events observed at the detector depends on the neutrino flux (Φ_α), probability of oscillation ($P_{\alpha\beta}$), the interaction cross-section (σ_β), and the efficiency (ϵ), which is given by,

$$N = \Phi_\alpha P_{\alpha\beta} \sigma_\beta \epsilon \tag{2.102}$$

The atmospheric neutrino and anti-neutrino events are obtained by folding the relevant incident fluxes with the appropriate disappearance and appearance probabilities, charge current (CC) cross sections, detector efficiency, resolution, detector mass, and exposure time. The μ^-, and e^- event rates in an energy bin of width dE_ν and in a solid angle bin of width $\mathrm{d}\Omega_\nu$ are as follows,

$$\frac{\mathrm{d^2N_\mu}}{\mathrm{d\Omega\ dE}} = \frac{\mathrm{D_{eff}}\sigma_{\mathrm{CC}}}{2\pi}\left[\left(\frac{\mathrm{d^2\Phi_\mu}}{\mathrm{d}\cos\theta\ \mathrm{dE}}\right)\mathrm{P}_{\mu\mu} + \left(\frac{\mathrm{d^2\Phi_e}}{\mathrm{d}\cos\theta\ \mathrm{dE}}\right)\mathrm{P}_{\mathrm{e}\mu}\right]. \tag{2.103}$$

$$\frac{\mathrm{d^2N_e}}{\mathrm{d\Omega\ dE}} = \frac{\mathrm{D_{eff}}\sigma_{\mathrm{CC}}}{2\pi}\left[\left(\frac{\mathrm{d^2\Phi_\mu}}{\mathrm{d}\cos\theta\ \mathrm{dE}}\right)\mathrm{P}_{\mu\mathrm{e}} + \left(\frac{\mathrm{d^2\Phi_e}}{\mathrm{d}\cos\theta\ \mathrm{dE}}\right)\mathrm{P}_{\mathrm{ee}}\right] \tag{2.104}$$

Here Φ_μ and Φ_e are the ν_μ and ν_e atmospheric fluxes respectively obtained from Honda et.al.[168] at the Homestake site; $P_{\mu\mu}(P_{ee})$ and $P_{\mu e}$ are disappearance and appearance probabilities; σ_{CC} is the total charge current (CC) cross-section and $\mathrm{D_{eff}}$ is the detector efficiency. The μ^+, and e^+ event rates are similar to the above expression with the fluxes, probabilities, and cross sections replaced by those for $\bar{\nu}_\mu$ and $\bar{\nu}_\mathrm{e}$ respectively. For the LArTPC detector, the energy and angular resolution are implemented using the Gaussian resolution function as follows,

$$\mathrm{R}_{\mathrm{E}_\nu}(\mathrm{E_t}, \mathrm{E_m}) = \frac{1}{\sqrt{2\pi}\sigma}\exp\left[-\frac{(\mathrm{E_m}-\mathrm{E_t})^2}{2\sigma^2}\right]. \tag{2.105}$$

$$\mathrm{R}_{\theta_\nu}(\Omega_\mathrm{t}, \Omega_\mathrm{m}) = \mathrm{N}\exp\left[-\frac{(\theta_\mathrm{t}-\theta_\mathrm{m})^2 + \sin^2\theta_\mathrm{t}\,(\phi_\mathrm{t}-\phi_\mathrm{m})^2}{2(\Delta\theta)^2}\right], \tag{2.106}$$

where N is a normalization constant. Here, $\mathrm{E_m}$ (Ω_m), and $\mathrm{E_t}$ (Ω_t) denote the measured and true values of energy (zenith angle) respectively. The smearing width σ is a function of the energy $\mathrm{E_t}$. The smearing function for the zenith angle is a bit more complicated because the direction of the incident neutrino is specified by two variables: the polar angle θ_t and the azimuthal angle ϕ_t. We denote both these angles together by Ω_t. The measured direction of the neutrino, with polar angle θ_m and azimuthal angle ϕ_m, which together we denote by Ω_m, is expected to be within a cone of half-angle $\Delta\theta$ of the true direction. Assumptions of the far detector (LArTPC) parameters are mentioned in table 2.2[169].

Parameter uncertainty	Value
$\mu^{+/-}$ Angular	2.5°
$e^{+/-}$ Angular	3.0°
($\mu^{+/-}$, $e^{+/-}$) Energy	GLB files for each E bin [170]
Detection efficiency	GLB files for each E bin [170]
Flux normalization	20%
Zenith angle dependence	5%
Cross section	10%
Overall systematic	5%
Tilt	5%

Table 2.2: Assumptions of the LArTPC far detector parameters and uncertainties.

2.7.2 Charge identification using muon capture in liquid argon

Magnetizing the large 40 kt LArTPC detector is difficult and expensive, but the charge id of the muon can be identified using the capture vs decay process of the muon inside the argon as studied previously for the DUNE detector[171]. We have implemented the charge id of the muon as follows: some fraction of the μ^- like events that undergo the capture process are identified using capture fraction efficiency, and the rest of the muons as well as all the μ^+ undergo muon decay. The lifetime of the muon resulting from the capture and decay processes can be written as,

$$\tau = \left(\frac{1}{\tau_{cap}} + \frac{Q}{\tau_{free}}\right)^{-1} \tag{2.107}$$

where τ_{cap} is the lifetime in the capture process, τ_{free} is the decay lifetime, and Q is the Huff correction factor[172]. We can define μ^- capture fraction as,

$$\epsilon^{cap} = \frac{\tau}{\tau_{cap}} = 1 - \frac{\tau}{\tau_{free}} \tag{2.108}$$

We use the most precise value of μ^- lifetime in argon[173], μ^- capture fraction becomes ϵ^{cap}= 71.9%. Electron charge identification is impossible at GeV energies, and electron events are summed for each energy and angular bin. For the sensitivity calculation, the μ^- and μ^+ are separated as follows: the μ^- events selected that undergo muon capture are given by,

$$N_{i,j,\mu^-}{}^{cap} = \epsilon^{cap} \times N_{\mu^-} \tag{2.109}$$

and the remaining μ^- events are included within the μ^+ event bin as follows,

$$N^{rest}_{i,j,\mu^+} = \left(1 - \epsilon^{cap}\right) N_{i,j,\mu^-} + N_{i,j,\mu^+} \tag{2.110}$$

2.7.3 χ^2 Analysis

The computation of χ^2 is performed using the method of pulls. This method allows us to take into account the various statistical and systematic uncertainties straightforwardly. The flux, cross sections, and other systematic uncertainties are included by allowing these inputs to deviate from their standard values in the computation of the expected rate in the i-j$^{\rm th}$ bin, $\rm N^{th}_{ij}$. Let the k$^{\rm th}$ input deviate from its standard value by $\sigma_{\rm k}\,\xi_{\rm k}$, where $\sigma_{\rm k}$ is its uncertainty. Then the value of $\rm N^{th}_{ij}$ with the modified inputs is given by,

$$\rm N^{th}_{ij} = N^{th}_{ij}(std) + \sum_{k=1}^{npull} c^k_{ij}\xi_k\,, \tag{2.111}$$

where $\rm N^{th}_{ij}(std)$ is the expected rate in the i-j$^{\rm th}$ bin calculated with the standard values of the inputs and *npull*=5 is the number of sources of uncertainty. The $\xi_{\rm k}$'s are called the *pull* variables and they determine the number of σ's by which the k$^{\rm th}$ input deviates from its standard value. In Eq. (2.111), $\rm c^k_{ij}$ is the change in N_{ij}^{th} when the k^{th} input is changed by σ_k (i.e. by 1 standard deviation). Since the uncertainties in the inputs are not very large, we only consider changes in N_{ij}^{th} that is linear in ξ_k. Thus we have the modified χ^2 as,

$$\chi^2(\xi_k) = \sum_{i,j} \frac{\left[N_{ij}^{th}(std) \; + \; \sum_{k=1}^{npull} \; c_{ij}^{k} \; \xi_k - N_{ij}^{ex} \; \right]^2}{N_{ij}^{ex}} + \sum_{k=1}^{npull} \; \xi_k^2 \, , \tag{2.112}$$

where the additional ξ_k^2-dependent term is the penalty imposed for moving the value of the k^{th} input away from its standard value by $\sigma_k \, \xi_k$. The χ^2 with pulls, which includes the effects of all theoretical and systematic uncertainties (as mentioned in table 2.2), is obtained by minimizing $\chi^2(\xi_k)$ with respect to all the pulls ξ_k as follows,

$$\chi^2_{pull} = \mathrm{Min}_{\xi_k} \left[\chi^2(\xi_k) \right] \tag{2.113}$$

In the case of a LArTPC detector without charge-id and with change-id, χ^2 is defined as,

$$\chi^2_{w/o \; charge-id} = \chi^2_{\mu^- + \mu^+} + \chi^2_{e^- + e^+} \tag{2.114}$$

$$\chi^2_{charge-id} = \chi^2_{\mu^-} + \chi^2_{\mu^+} + \chi^2_{e^- + e^+} \tag{2.115}$$

The final $\Delta\chi^2$ is obtained by marginalizing over the oscillation parameters.

"Imagination is more important than knowledge. Knowledge is limited. Imagination encircles the world".

Albert Einstein

3

Resonant Matter effect in the presence of an eV scale sterile neutrino

The appearance of electron (anti)neutrinos from muon (anti)neutrino sources in the short baseline experiments like LSND and MiniBooNE can be explained by the inclusion of a fourth neutrino with no SM interactions and a mass of the order of 1 eV. In this 3+1 framework with an extra eV scale neutrino, the neutrino oscillation will depend on additional parameters, leading to more parameter degeneracies. In this chapter, we study the neutrino propagation in matter in the presence of an eV scale sterile neutrino and determine the octant of θ_{23} and the sign of Δ_{31} using a LArTPC detector with beam and atmospheric neutrinos. This chapter is based on [174].

The *3+1 framework*, including a light sterile neutrino with a mass of 1 eV, was first introduced in [175] to explain the results of LSND. Since then, several studies have analyzed the global oscillation data in the presence of sterile neutrino. The *3+1 framework* suffers from a tension between the ν_μ disappearance and $\nu_\mathbf{e}$ appearance data. This tension[176] originates from the non-observation of any similar supportive signal in the accelerator-based disappearance experiments in $P_{\mu\mu}$ channel like CDHSW, MINOS[177, 178], Super-Kamiokande[179], IceCube DeepCore[180], MicroBooNE[181], NOνA[182]. Reactor-based electron disappearance searches in the experiments Bugey3[183] and DayaBay[184] also didn't provide any evidence in support of sterile neutrino. The global fit performed in [185], allowed three narrow regions around $\Delta_{41} \approx 1 - 2$ eV^2 with $0.00048 < \sin^2 2\theta_{\mu e} < 0.002$. However, after adding Bugey3, DayaBay, and MINOS+ data, the goodness of fit decreases drastically[184]. The most recent results from the MicroBooNE experiment did not report any evidence of electron neutrino disappearance in their three years of data[186, 187]. However, it was shown in [188] that MicroBooNE data can not exclude the electron neutrino excess observed in MiniBooNE in a model independent way. The joint analysis of results from MiniBooNE and MicroBooNE experiments preferred the 3+1 scenario over no oscillation[189].

The upcoming TRISTAN detector at the KATRIN[190], SBN[191] at Fermilab, JSNS^2 detector[192] at J-PARC are following up the results of LSND, MiniBooNE. The results from these experiments are expected to help in reaching a definitive conclusion about the existence of an eV scale sterile neutrino. If these experiments confirm the presence of an eV scale neutrino, then some new physics will be required to explain the tension between the disappearance and the appearance data. Some ideas in this direction can be found [193, 194].

If we consider the sterile neutrino hypothesis to be true, then the standard framework of neutrino oscillations is going to see some important modifications. The addition of a light sterile neutrino comes with three extra active-sterile sector mixing angles and two additional CP phases. These will compound the effect of the parameter degeneracies already existing in the standard three flavor framework. In particular, it was shown in [195] that for the 3+1 oscillation framework, the octant degeneracy is more pronounced due to the effect of an additional interference term in the $\nu_\mu \to \nu_e$ vacuum oscillation probability relevant at long baseline setups in the context of the DUNE detector. It is well known that the addition of neutrino and anti-neutrino can evade the octant-δ_{13} degeneracy for three flavor case[148, 196]. However, in presence of a sterile neutrino, the octant-δ_{14} degeneracy can't be resolved even after the addition of neutrino plus anti-neutrino[197]. Implications of additional octant degeneracies associated with the new phases in the 3+1 framework have also been studied in the context of the NOνA[197, 198] experiment. Other studies in the context of long baseline experiments in presence of a sterile neutrino can be found for instance in [199–206].

We comprehensively study the octant and mass ordering sensitivity using a LArTPC detector in the 3+1 framework. LArTPC, first proposed in [207] constitutes one of the most important classes of scintillator detectors at present because of its superior capabilities which provide several advantages in the precise reconstruction of neutrino events. Some current and future detectors using this technology are MicroBooNE, SBND, DUNE, etc. Earlier studies performed for three neutrino generations and atmospheric neutrinos in a liquid argon (LAr) detector can be found for instance, in [208–210]. In this chapter, we extend our scope to investigate if the effect of additional degeneracies arising from an extra light sterile neutrino can be reduced in the presence of a large matter effect encountered at higher baselines. This has been studied for the combined analysis of beam neutrinos at a baseline of 1300 km and atmospheric neutrinos, which provide larger baselines as well as higher energies in this experimental setup, along with a separate study for each. Additionally, we present the results, including the charge tagging capability of muon capture in liquid argon, allowing one to differentiate between μ^+ and μ^- events in the context of atmospheric neutrinos.

To properly understand the octant and mass ordering degeneracy seen from numerical analysis, the study of the analytic expressions of neutrino oscillation probabilities is important. We obtain analytic expressions of the neutrino oscillation/survival probabilities assuming the solar mass squared difference Δ_{21} to be negligible as compared to the mass squared differences Δ_{31}, and $\Delta_{41} = m_4^2 - m_1^2$ driving the atmospheric and sterile neutrino oscillations respectively. We use the analytic expressions to understand the octant degeneracy at the representative baselines, e.g., 1300 km and 7000 km. There are other analytical calculations of oscillation probabilities in the presence of sterile neutrino in matter using the rotation methods[211], an exact analytical method[212]. We discuss the region of validity and the error of the analytic expressions compared to the exact numerical probabilities.

Studies related to sterile neutrinos in the context of atmospheric neutrino observations at India-based Neutrino Observatory (INO) experiment have been performed in [213, 214]. More recently, an analysis in [215] considered sterile neutrinos in atmospheric baselines for a wide Δ_{41} mass squared range 10^{-5} : 100 eV^2 in the context of the INO experiment. This paper obtained bound on the active-sterile mixing angles as well as the sensitivity to the neutrino mass ordering in the 3+1 oscillation framework. Our study in this paper focuses on the impact of resonant matter effect on the probabilities at very long baselines and its influence on the sensitivity to determine the octant and mass ordering. We also explore this aspect in the context of atmospheric and beam neutrinos in a long baseline experimental setup of 1300 km separately and together using a LArTPC detector and examine the complementarities between these two.

The plan of this chapter is as follows. To start with, we discuss the analytic framework for neutrino oscillations in the presence of sterile neutrino in section 3.1. The subsequent section 3.2 details the calculation of the probabilities. Next, section 3.3 contains the discussion on octant degeneracy for different baselines and energies as well as the dependence on the CP phases δ_{13}, and δ_{14}. In section 3.5, we describe the experimental details for the LArTPC detector and outline the procedure of χ^2 analysis adopted. We discuss the results in section 3.6. Finally, we conclude in section 3.7.

3.1 The 3+1 Framework

The minimal scheme postulated to explain the results of LSND and MiniBooNE is the 3+1 framework in which one light sterile neutrino is added to the three active neutrinos in the SM. In the *3+1 oscillation framework*, the mixing matrix U depends on three additional mixing angles $\theta_{14}, \theta_{24}, \theta_{34}$ corresponding to mixing between the light sterile neutrino ν_s and the active sector neutrinos, two new CP phases δ_{14}, δ_{34} along with the standard oscillation parameters $\theta_{12}, \theta_{13}, \theta_{23}, \delta_{13}$ and can be expressed as,

$$U = \tilde{R}_{34}(\theta_{34}, \delta_{34}) R_{24}(\theta_{24}) \tilde{R}_{14}(\theta_{14}, \delta_{14}) R_{23}(\theta_{23}) \tilde{R}_{13}(\theta_{13}, \delta_{13}) R_{12}(\theta_{12}) \tag{3.1}$$

where $\tilde{R}_{ij} = U^{\delta}_{ij}(\delta_{ij}) R_{ij}(\theta_{ij}) U^{\dagger\delta}_{ij}(\delta_{ij})$, $R_{ij}(\theta_{ij})$'s are the rotation matrices in i-j plane and $U^{\delta}_{ij} = diag(1, 1, 1, e^{\iota\delta_{ij}})$ with δ_{ij}'s being the CP phases (For δ_{13}: we have $U^{\delta}_{13} = diag(1, 1, e^{i\delta_{13}}, 1)$. In the presence of an additional light sterile neutrino, there is a new mass squared difference Δ_{41}. The 3+1 picture considered here is $m_4 >> m_3 >> m_2 >> m_1$ which corresponds to m_4 being the heaviest mass state. The case with m_4 as the lowest state is disfavoured from cosmology. The mass ordering for three generation is considered to be NH.

Recent studies about the best-fit values and allowed ranges of the parameters associated with eV scale sterile neutrino can be found in [176, 185, 216]. In particular, the global analysis of data performed in [185] illustrates the following 3σ bounds and best-fits in sterile mixing angles for $\Delta_{41} = 1.3$ eV^2,

Parameters	3σ range	Best Fit	Mixing angles	3σ range	Best Fit
$\sin^2 2\theta_{14}$	0.04 - 0.09	0.079	θ_{14}	$5.76^\circ - 8.73^\circ$	8.15°
$\sin^2 \theta_{24}$	$6.7 \times 10^{-3} - 0.022$	0.015	θ_{24}	$4.68^\circ - 8.6^\circ$	7.08°

Table 3.1: 3σ Levels and Best fit values extracted from [184]

However, the analysis performed in [184] including the MINOS+ data disfavoured the allowed regions in θ_{24} from above with a new bound at 90% C.L. $\sin^2 \theta_{24} \leq 0.006$, i.e., $\theta_{24} \leq 4.5^\circ$. Also, the analysis of DayaBay and Bugey3 gives at 90% C.L. $\sin^2 2\theta_{14} \leq 0.046$. i.e., $\theta_{14} \leq 6.2^\circ$.

3.2 Oscillation Probability

The effective matter interaction Hamiltonian in flavor basis is given as follows,

$$H_{int} = diag(V_{CC}, 0, 0, -V_{NC}) = diag(\sqrt{2}G_F N_e, 0, 0, \sqrt{2}G_F N_n/2) \tag{3.2}$$

where $V_{CC} = \sqrt{2}G_F N_e$ is the charge current interaction potential, $V_{NC} = -\sqrt{2}G_F N_n/2$ is the neutral current interaction potential, G_F is the Fermi coupling constant, N_e, and N_n correspond to electron density and neutron density, respectively, of the medium in which neutrinos travel. In order to obtain the probabilities in the matter, one has to solve the neutrino propagation equation with the total Hamiltonian given as follows.

$$H = \frac{1}{2E_\nu} U \begin{bmatrix} 0 & 0 & 0 & 0 \\ 0 & \Delta_{21} & 0 & 0 \\ 0 & 0 & \Delta_{31} & 0 \\ 0 & 0 & 0 & \Delta_{41} \end{bmatrix} U^\dagger + \frac{1}{2E_\nu} \begin{bmatrix} A & 0 & 0 & 0 \\ 0 & 0 & 0 & 0 \\ 0 & 0 & 0 & 0 \\ 0 & 0 & 0 & \frac{A}{2} \end{bmatrix} \tag{3.3}$$

where the propagation medium has been considered to be the earth matter with neutron density being equal to electron density, i.e, $N_e = N_n$ and the matter potential term is $A = 2\sqrt{2}G_F N_e E_\nu$ with neutrino energy E_ν and the mass squared differences are given as $\Delta_{ij} = m_j^2 - m_i^2$ where m_i's are mass eigenvalues. This would require diagonalization of the total Hamiltonian to go to the matter mass basis. However, this poses difficulty even in the three flavor case, and one has to resort to approximate methods. A comprehensive review of the various approximations used in the three flavor case has been discussed in [211]. In the context of this work, we have considered the two mass scale dominance(TMSD) approximation with Δ_{21} set as zero, similar to the well known one mass scale dominance(OMSD) approximation[217] in three flavor case. TMSD approximation allows us to obtain compact analytic expressions for the probabilities in the matter, which can facilitate the understanding of the underlying physics in the 3+1 framework.

3.2.1 TMSD approximation

In the TMSD approximation, we choose $\Delta_{21} = 0$ since from the experimental data $\Delta_{21} << \Delta_{31} << \Delta_{41}$. As a consequence, the contribution of the solar angle θ_{12} drops out of mixing matrix U (3.1) as R_{12} commutes with the mass matrix M in this approximation. The $\Delta_{21} = 0$ approximation holds well for $\frac{\Delta_{21} L}{E_\nu} << 1$[217]. In our study, we further assume $\theta_{34} = 0$ which is allowed within current bounds [144, 146]. Thus we have only two additional non-zero mixing angles θ_{14}, θ_{24} and a non-zero phase δ_{14}. This leads to the effective vacuum mixing matrix,

$$\tilde{U} = R_{24}(\theta_{24})\tilde{R}_{14}(\theta_{14}, \delta_{14})R_{23}(\theta_{23})U_{13}^{\delta}R_{13}(\theta_{13})$$
$$= \begin{bmatrix} c_{13}c_{14} & 0 & c_{14}s_{13} & e^{-\iota\delta_{14}}s_{14} \\ -e^{\iota\delta_{13}}c_{24}s_{13}s_{23} - e^{\iota\delta_{14}}c_{13}s_{14}s_{24} & c_{23}c_{24} & e^{\iota\delta_{13}}c_{13}c_{24}s_{23} - e^{\iota\delta_{14}}s_{13}s_{14}s_{24} & c_{14}s_{24} \\ -e^{\iota\delta_{13}}c_{23}s_{13} & -s_{23} & e^{\iota\delta_{13}}c_{13}c_{23} & 0 \\ -e^{\iota\delta_{14}}c_{13}c_{24}s_{14} + e^{\iota\delta_{13}}s_{13}s_{23}s_{24} & -c_{23}s_{24} & -e^{\iota\delta_{14}}c_{24}s_{13}s_{14} - e^{\iota\delta_{13}}c_{13}s_{23}s_{24} & c_{14}c_{24} \end{bmatrix} \tag{3.4}$$

where we have used notations $s_{ij} = \sin\theta_{ij}, c_{ij} = \cos\theta_{ij}$. Since the allowed values of the vacuum mixing angles θ_{13}, θ_{14}, and θ_{24} are of a similar order, these small parameters can be expressed in terms of $\mathcal{O}(\lambda^n)$ with $\lambda \sim 0.15$ as follows;

$$\sin\theta_{13} \simeq \mathcal{O}(\lambda), \sin\theta_{14} \simeq \mathcal{O}(\lambda), \sin\theta_{24} \simeq \mathcal{O}(\lambda), \Delta_{21} \simeq \mathcal{O}(\lambda^5), \Delta_{31} \simeq \mathcal{O}(\lambda^3), A \simeq \mathcal{O}(\lambda^3) \tag{3.5}$$

We can split the total Hamiltonian H into two parts as

$$H = \frac{1}{2E_\nu}(H_0 + H_p) \tag{3.6}$$

where H_p, the perturbed Hamiltonian, is proportional to the order of $\Delta_{31}, A[\mathcal{O}(\lambda^3)]$ whereas the unperturbed Hamiltonian H_0 is proportional to Δ_{41}. These can be written as follows,

$$H_0 = \Delta_{41} \begin{bmatrix} s_{14}^2 & e^{-\iota\delta_{14}} c_{14} s_{14} s_{24} & 0 & e^{-\iota\delta_{14}} c_{24} c_{14} s_{14} \\ e^{\iota\delta_{14}} c_{14} s_{24} s_{14} & c_{14}^2 s_{24}^2 & 0 & c_{14}^2 c_{24} s_{24} \\ 0 & 0 & 0 & 0 \\ e^{\iota\delta_{14}} c_{24} c_{14} s_{14} & c_{14}^2 c_{24} s_{24} & 0 & c_{14}^2 c_{24}^2 \end{bmatrix}, \tag{3.7}$$

$$H_p = \tilde{U} \begin{bmatrix} 0 & 0 & 0 & 0 \\ 0 & 0 & 0 & 0 \\ 0 & 0 & \Delta_{31} & 0 \\ 0 & 0 & 0 & 0 \end{bmatrix} \tilde{U}^\dagger + \begin{bmatrix} A & 0 & 0 & 0 \\ 0 & 0 & 0 & 0 \\ 0 & 0 & 0 & 0 \\ 0 & 0 & 0 & \frac{A}{2} \end{bmatrix} \tag{3.8}$$

The unperturbed and perturbed Hamiltonian can be expressed in terms of the small parameter λ in the following manner,

$$H_0 \sim \begin{bmatrix} \lambda^2 & \lambda^2 & 0 & \lambda \\ \lambda^2 & \lambda^2 & 0 & \lambda \\ 0 & 0 & 0 & 0 \\ \lambda & \lambda & 0 & 1 \end{bmatrix}, H_p \sim \begin{bmatrix} \lambda^5 & \lambda^4 & \lambda^4 & -\lambda^5 \\ \lambda^4 & \lambda^3 & \lambda^3 & -\lambda^4 \\ \lambda^4 & \lambda^3 & \lambda^3 & -\lambda^4 \\ -\lambda^5 & -\lambda^4 & -\lambda^4 & \lambda^5 \end{bmatrix} \tag{3.9}$$

The unperturbed Hamiltonian has the smallest terms proportional to $\mathcal{O}(\lambda^2)$, which is at least an order less than the largest term in H_p, the perturbed Hamiltonian. The eigenvalues of H_0 are $\lambda_{01} = 0$, $\lambda_{02} = 0$, $\lambda_{03} = 0$, $\lambda_{04} = \Delta_{41}$. This implies the need for degenerate perturbation theory to determine the modified energy eigenvalues in the presence of the matter potential. The modified energy eigenvalues evaluated using degenerated perturbation theory in ascending order of energy are as follows,

$$
\begin{aligned}
E_{1m} &= \frac{1}{2E_\nu}[\Delta_{31}\sin^2(\theta_{13}-\theta_{13m}) + A^{'}\cos^2\theta_{13m}(1+\cos^2\theta_{14}+\cos^2\theta_{14}\sin^2\theta_{24}) \\
&\quad - A^{'}\sin^2\theta_{24}\cos 2\theta_{13m} - A\sin 2\theta_{24}\sin\theta_{14}\sin\theta_{23}\sin 2\theta_{13m}\cos\delta/2], \\
E_{2m} &= 0, \\
E_{3m} &= \frac{1}{2E_\nu}[\Delta_{31}\cos^2(\theta_{13}-\theta_{13m}) + A^{'}\sin^2\theta_{13m}(1+\cos^2\theta_{14}+\cos^2\theta_{14}\sin^2\theta_{24}) \\
&\quad + A^{'}\sin^2\theta_{24}\cos 2\theta_{13m} + A\sin 2\theta_{24}\sin\theta_{14}\sin\theta_{23}\sin 2\theta_{13m}\cos\delta/2], \\
E_{4m} &= \frac{1}{2E_\nu}[\Delta_{41} + A^{'}(1+\sin^2\theta_{14}-\cos^2\theta_{14}\sin^2\theta_{24})]
\end{aligned}
\tag{3.10}
$$

where $A^{'} = A/2 = \sqrt{2}G_F N_e$, the modified angle θ_{13m} in the matter is related to the original angles, and the new phase $\delta = (\delta_{13} - \delta_{14})$ as,

$$\sin 2\theta_{13m} = [\Delta_{31}\sin 2\theta_{13} + A^{'}\cos\delta\sin\theta_{14}\sin\theta_{23}\sin 2\theta_{24}]/f, \tag{3.11}$$

$$\cos 2\theta_{13m} = [\Delta_{31}\cos 2\theta_{13} - A^{'}(1+\cos^2\theta_{14}+\cos^2\theta_{14}\sin^2\theta_{24} - 2\sin^2\theta_{24})]/f \tag{3.12}$$

where f is defined as,

$$f = \sqrt{[\Delta_{31}\sin 2\theta_{13} + A's_{14}s_{23}\sin 2\theta_{24}\cos\delta]^2 + [\Delta_{31}\cos 2\theta_{13} - A'(1+c_{14}^2+c_{14}^2 s_{24}^2 - 2s_{24}^2)]^2} \tag{3.13}$$

It is noteworthy that for the 3+1 framework, the modified angle θ_{13m} depends on cp phases, unlike in the three generation framework. Now if we put $\sin 2\theta_{13m} = 1$, i.e., $\cos 2\theta_{13m} = 0$, we will get maximum θ_{13m}, i.e., resonance in this sector for the matter. The corresponding resonance energy is given by,

$$E_{res} = \frac{\Delta_{31}\cos 2\theta_{13}}{\sqrt{2}G_F N_e(1+\cos^2\theta_{14}+\cos^2\theta_{14}\sin^2\theta_{24} - 2\sin^2\theta_{24})} \tag{3.14}$$

The resonance energy for 1300 km and 7000 km are $\sim$ 11 GeV, and 8 GeV respectively corresponding to $\theta_{14} = \theta_{24} = 7^\circ, \theta_{13} = 8.57^\circ, \Delta_{31} = 2.515 \times 10^{-3}\text{eV}^2$. It only changes minimally from the three generation case. The modified active-sterile mixing angles $\theta_{14m}, \theta_{24m}$ are related to the vacuum angles as,

$$\sin\theta_{14m} = \sin\theta_{14}[1 + \frac{A'}{\Delta_{41}}\cos^2\theta_{14}(1+s_{24}^2)], \cos\theta_{14m} = \cos\theta_{14}[1 - \frac{A'}{\Delta_{41}}\sin^2\theta_{14}(1+s_{24}^2)], \tag{3.15}$$

$$\sin\theta_{24m} = \sin\theta_{24}[1 - \frac{A'}{\Delta_{41}}\cos^2\theta_{14}\cos^2\theta_{24}], \cos\theta_{24m} = \cos\theta_{24}[1 + \frac{A'}{\Delta_{41}}\cos^2\theta_{14}\sin^2\theta_{24}] \tag{3.16}$$

The mixing matrix in matter obtained from the modified eigenvectors using degenerate perturbation theory is as follows,

$$\begin{aligned}\tilde{U}_m &= R_{24}^m(\theta_{24m})\tilde{R}_{14}^m(\theta_{14m},\delta_{14})R_{23}(\theta_{23})U_{\delta 13}R_{13}^m(\theta_{13m})R_{12}^m(\theta_{12m}) \\ &= \begin{bmatrix} c_{13m}c_{14m} & (U_m)_{12} & c_{14m}s_{13m} & e^{-\iota\delta_{14}}s_{14m} \\ -e^{\iota\delta_{13}}c_{24m}s_{13m}s_{23} - e^{\iota\delta_{14}}c_{13m}s_{14m}s_{24m} & c_{23}c_{24m} & e^{\iota\delta_{13}}c_{13m}c_{24m}s_{23} - e^{\iota\delta_{14}}s_{13m}s_{14m}s_{24m} & c_{14m}s_{24m} \\ -e^{\iota\delta_{13}}c_{23}s_{13m} & -s_{23} & e^{\iota\delta_{13}}c_{13m}c_{23} & 0 \\ -e^{\iota\delta_{14}}c_{13m}c_{24m}s_{14m} + e^{\iota\delta_{13}}s_{13m}s_{23}s_{24m} & -c_{23}s_{24m} & -e^{\iota\delta_{14}}c_{24m}s_{13m}s_{14m} - e^{\iota\delta_{13}}c_{13m}s_{23}s_{24m} & c_{14m}c_{24m} \end{bmatrix}\end{aligned} \tag{3.17}$$

where the original vacuum angles are replaced by modified angles as given by (3.11), (3.12), (3.15), (3.16) and null value of the element $(\tilde{U})_{12}$ in vacuum mixing matrix $\tilde{U}$(3.4) is modified as $(U_m)_{12} = \frac{A}{\Delta_{41}}e^{-\iota\delta_{14}}c_{14}c_{23}c_{24}s_{14}s_{24} \sim \mathcal{O}(\lambda^5)$. This is due to the fact that the matter effect introduces correction of mixing angle θ_{12}, which was absent before due to the approximation $\Delta_{21} = 0$. The other terms related to θ_{12} don't show up as they are $< \mathcal{O}(\lambda^5)$. Now we can calculate the oscillation(survival) probabilities using the elements of $\tilde{U}_m$ in place of U and $\Delta_{ij}^m = 2E_\nu(E_{im} - E_{jm})$ replacing Δ_{ij} in (3.18) assuming constant matter density,

$$P_{\alpha\beta} = \delta_{\alpha\beta} - 4\sum_{i>j}^{N} Re(U_{\alpha i}^* U_{\beta i} U_{\alpha j} U_{\beta j}^*)\sin^2\frac{1.27\Delta_{ij}L}{E_\nu} + 2\sum_{i>j}^{N} Im(U_{\alpha i}^* U_{\beta i} U_{\alpha j} U_{\beta j}^*)\sin 2\frac{1.27\Delta_{ij}L}{E_\nu} \tag{3.18}$$

On the other hand, the exact numerical probability at constant matter density can be evaluated as,

$$P_{\alpha\beta}^{\text{num}} = |[e^{-\iota HL}]_{\alpha\beta}|^2, \tag{3.19}$$

where H is the total Hamiltonian without any approximation given by (3.3).

$P_{\mu e}$ Channel

The appearance channel, i.e., $\nu_\mu \to \nu_e$ oscillation probability is given by,

$$P_{\mu e} = P^1_{\mu e} + P^2_{\mu e} + P^3_{\mu e} + \mathcal{O}(\lambda^6) \tag{3.20}$$

where the different significant terms of the probability $P_{\mu e}$ are as follows,

$$\begin{aligned} P^1_{\mu e} =& \, 4\cos^2\theta_{13m}\cos^2\theta_{14m}\sin^2\theta_{13m}(\cos^2\theta_{24m}\sin^2\theta_{23} - \sin^2\theta_{14m}\sin^2\theta_{24m})\sin^2\frac{1.27\Delta^m_{31}L}{E} \\ &+ 2\cos^3\theta_{13m}\cos^2\theta_{14m}\sin\theta_{13m}\sin\theta_{14m}\sin 2\theta_{24m}\sin\theta_{23}\sin\frac{1.27\Delta^m_{31}L}{E}\sin(\frac{1.27\Delta^m_{31}L}{E} + \delta) \\ &- 2\cos\theta_{13m}\cos^2\theta_{14m}\sin^3\theta_{13m}\sin\theta_{14m}\sin 2\theta_{24m}\sin\theta_{23}\sin\frac{1.27\Delta^m_{31}L}{E}\sin(\frac{1.27\Delta^m_{31}L}{E} - \delta), \end{aligned} \tag{3.21}$$

$$\begin{aligned} P^2_{\mu e} =& \cos^2\theta_{14m}\sin 2\theta_{13m}\sin\theta_{14m}\sin\theta_{23}\sin 2\theta_{24m}\sin\frac{1.27\Delta^m_{41}L}{E}\sin(\frac{1.27\Delta^m_{41}L}{E} - \delta) \\ &+ \sin^2 2\theta_{14m}\sin^2\theta_{24m}\cos^2\theta_{13m}\sin^2\frac{1.27\Delta^m_{41}L}{E}, \end{aligned} \tag{3.22}$$

$$\begin{aligned} P^3_{\mu e} =& -\cos^2\theta_{14m}\sin 2\theta_{13m}\sin\theta_{14m}\sin\theta_{23}\sin 2\theta_{24m}\sin\frac{1.27\Delta^m_{43}L}{E}\sin(\frac{1.27\Delta^m_{43}L}{E} - \delta) \\ &+ \sin^2 2\theta_{14m}\sin^2\theta_{24m}\sin^2\theta_{13m}\sin^2\frac{1.27\Delta^m_{43}L}{E} \end{aligned} \tag{3.23}$$

The total analytic probability $P_{\mu e}$(orange) and the dominant terms contributing to it are plotted at 1300 km and 7000 km baselines as a function of neutrino energy E_ν in the top panel of fig. 3.1. For the plots, and calculations of $P_{\mu e}, P_{\mu\mu}$ in this section, we have considered $\theta_{12} = 33.44^\circ, \theta_{13} = 8.57^\circ, \theta_{23} = 49^\circ, \theta_{14} = \theta_{24} = 7^\circ, \delta_{13} = 195^\circ, \delta_{14} = 30^\circ, \Delta_{31} = 2.515 \times 10^{-3}\text{eV}^2$, and $\Delta_{41} = 1\text{eV}^2$. The analytic expression of $P_{\mu e}$ consists of three significant terms, although there are other higher order terms $[\mathcal{O}(\lambda^6)]$ that are neglected. The first term in (3.21)(blue curve) that is proportional to the modified mass squared difference Δ^m_{31}, is the most dominant one and provides the average curve of the total probability as seen in fig. 3.1. The fast oscillations seen fig. 3.1 are a manifestation of the terms in (3.22) (green curve), (3.23) (violet curve) which are proportional to the modified mass squared differences related to the sterile neutrino mass states $\Delta^m_{41}, \Delta^m_{43}$ respectively. The fast oscillations are not reflected in experiments, as we can only get the average probability. Also, these terms are relatively much smaller than the $P^1_{\mu e}$ around probability maxima, so in the next section, while discussing the degeneracies, we will only use the term $P^1_{\mu e}$. Putting θ_{14}, θ_{24} angles to zero in equations (3.21), (3.22), (3.23) gives the standard three flavor oscillation probability from the very first term of the (3.21) as the other terms go to zero due to presence of $\sin\theta_{14m}, \sin\theta_{24m}$.

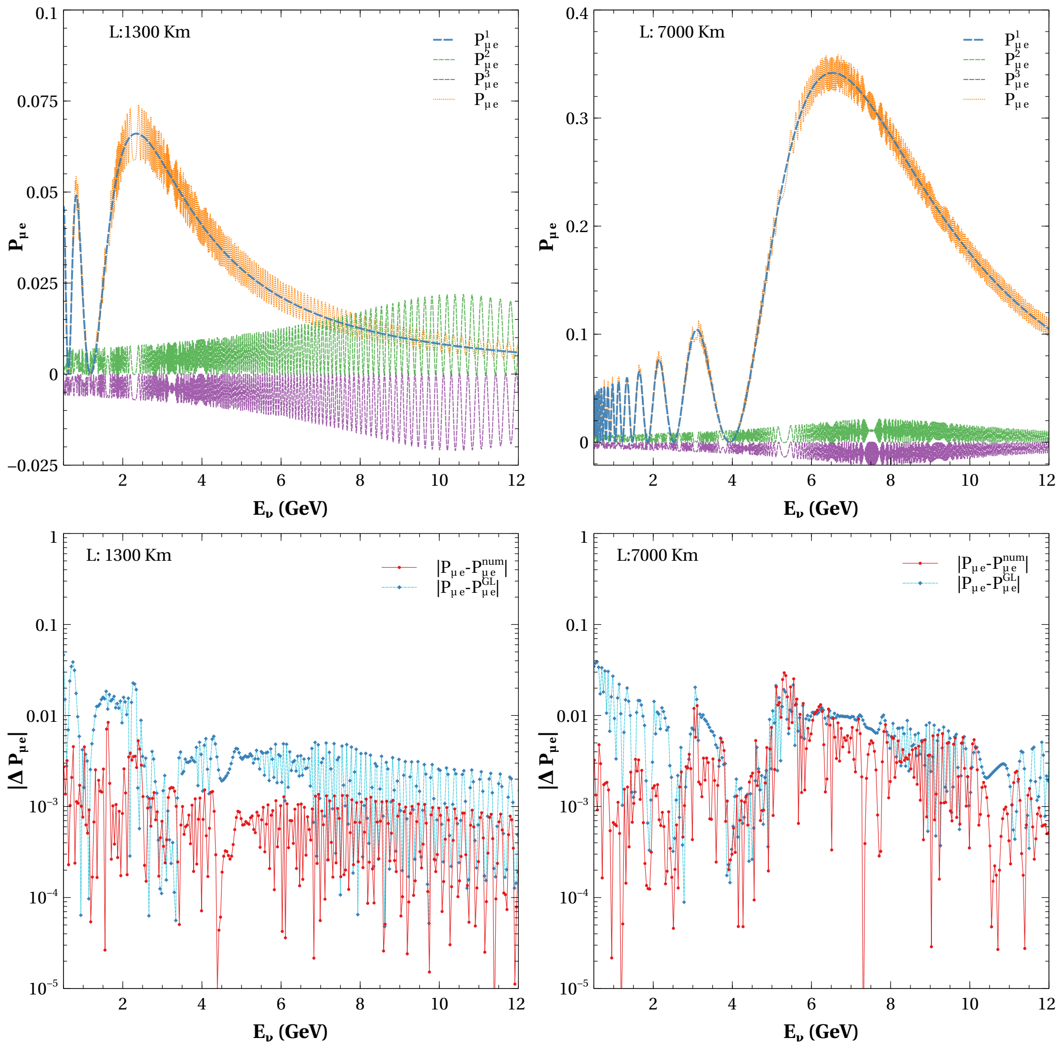

Figure 3.1: The total analytic probability $P_{\mu e}$ (orange) along with its other dominant terms in the top panel and the absolute differences $|P_{\mu e} - P^{\rm num}_{\mu e}|$ (red) and $|P_{\mu e} - P^{\rm GL}_{\mu e}|$ (cyan) in the bottom panel at 1300 km(left), and 7000 km(right) baselines.

We have shown the comparison of the absolute differences $|\Delta P|$ of the analytic probability $P_{\mu e}$ (3.20) with the exact probability $P^{\rm num}_{\mu e}$(3.19) (red) as well as with the probability $P^{\rm GL}_{\mu e}$ (cyan) obtained using GLoBES[103] as a function of neutrino energy at the bottom panel in fig. 3.1. We can see the value of $|\Delta P|$ is around 10^{-3} for most of the energies. $|\Delta P|$ values are smaller around the resonance energy of 11 GeV for 1300 km and 8 GeV for 7000 km. Also, at the energies where the value of probability is smaller, we get smaller values of $|\Delta P|$. Overall, we can conclude that the analytic probability $P_{\mu e}$ using TMSD approximation is in good agreement with both numerical and exact ones, better with the exact one $P_{\mu e}^{\mathrm{num}}$ for all energies (> 0.5 GeV), especially around the resonance. This is similar to probabilities derived using OMSD approximation matching well with numerical ones in the standard three flavor case in the region with significant matter effect[218, 219].

$P_{\mu\mu}$ Channel

The disappearance channel, i.e., $\nu_\mu \to \nu_\mu$ survival probability is given by,

$$P_{\mu\mu} = 1 - P_{\mu\mu}^1 - P_{\mu\mu}^2 - P_{\mu\mu}^3 + \mathcal{O}(\lambda^6) \tag{3.24}$$

where the significant terms of the probability are as follows,

$$\begin{aligned} P_{\mu\mu}^1 &= \cos^4\theta_{24m}\sin^2 2\theta_{13m}\sin^4\theta_{23}\sin^2\frac{1.27\Delta_{31}^m L}{E} + \sin^4\theta_{24m}\sin^4\theta_{14m}\sin^2 2\theta_{13m}\sin^2\frac{1.27\Delta_{31}^m L}{E} \\ &+ \sin 2\theta_{24m}\sin\theta_{14m}\sin 4\theta_{13m}\sin\theta_{23}\cos\delta(\cos^2\theta_{24m}\sin^2\theta_{23} - \sin^2\theta_{24m}\sin^2\theta_{13m})\sin^2\frac{1.27\Delta_{31}^m L}{E} \\ &+ 4\cos^2\theta_{24m}\sin^2\theta_{24m}\sin^2\theta_{14m}\sin^2\theta_{23}(1 - \frac{\sin^2 2\theta_{13m}}{2} - \sin^2 2\theta_{13m}\cos^2\delta)\sin^2\frac{1.27\Delta_{31}^m L}{E}, \end{aligned} \tag{3.25}$$

$$\begin{aligned} P_{\mu\mu}^2 &= \cos^4\theta_{24m}\cos^2\theta_{13m}\sin^2 2\theta_{23}\sin^2\frac{1.27\Delta_{32}^m L}{E} \\ &+ 4\cos^2\theta_{24m}\sin^2\theta_{24m}\sin^2\theta_{14m}\sin^2\theta_{13m}\cos^2\theta_{23}\sin^2\frac{1.27\Delta_{32}^m L}{E} \\ &- 4\cos^3\theta_{24m}\sin\theta_{24m}\sin\theta_{14m}\sin 2\theta_{13m}\cos^2\theta_{23}\sin\theta_{23}\cos\delta\sin^2\frac{1.27\Delta_{32}^m L}{E}, \end{aligned} \tag{3.26}$$

$$\begin{aligned} P_{\mu\mu}^3 &= \cos^4\theta_{24m}\sin^2\theta_{13m}\sin^2 2\theta_{23}\sin^2\frac{1.27\Delta_{21}^m L}{E} \\ &+ 4\cos^2\theta_{24m}\sin^2\theta_{24m}\sin^2\theta_{14m}\cos^2\theta_{13m}\cos^2\theta_{23}\sin^2\frac{1.27\Delta_{21}^m L}{E} \\ &+ 4\cos^3\theta_{24m}\sin\theta_{24m}\sin\theta_{14m}\sin 2\theta_{13m}\cos^2\theta_{23}\sin\theta_{23}\cos\delta\sin^2\frac{1.27\Delta_{21}^m L}{E} \end{aligned} \tag{3.27}$$

We show the total analytic probability $P_{\mu\mu}$ (orange) and the different terms contributing significantly to it at 1300 km and 7000 km baselines in the top panel of fig. 3.2 as a function of neutrino energy. The analytic expression of $P_{\mu\mu}$ consists of three significant terms (3.25), (3.26), and (3.27), although there are three other fast oscillating terms that are neglected. Here, the fast oscillating terms are proportional to the sterile mass squared differences $\Delta_{41}^m, \Delta_{42}^m, \Delta_{43}^m$ and are of higher orders [$\mathcal{O}(\lambda^6)$]. The first term in

(3.25) (blue curve), which is proportional to the modified mass squared difference Δ_{31}^m, has a dependence on octant of θ_{23} in the leading order due to the presence of $\sin^4\theta_{23}$. $P_{\mu\mu}^1$ grows with energy initially and decreases after resonance energy. The second and third terms in (3.26) (green curve), (3.27) (violet curve) which are proportional to the modified mass squared differences $\Delta_{32}^m, \Delta_{21}^m$ respectively, show no octant dependence in the leading order due to the presence of $\sin^2 2\theta_{23}$. The second term is the most dominant one before resonance energy but almost becomes zero after resonance energy, whereas the third term only grows after the resonance energy. In the case of 7000 km at oscillation maxima of 7.5 GeV, $P_{\mu\mu}^1, P_{\mu\mu}^2, P_{\mu\mu}^3$ all have significant contributions. Putting the θ_{14}, θ_{24} angles to zero, we will get back the three flavor oscillation probability from the first term of the equations (3.25), (3.26), and (3.27).

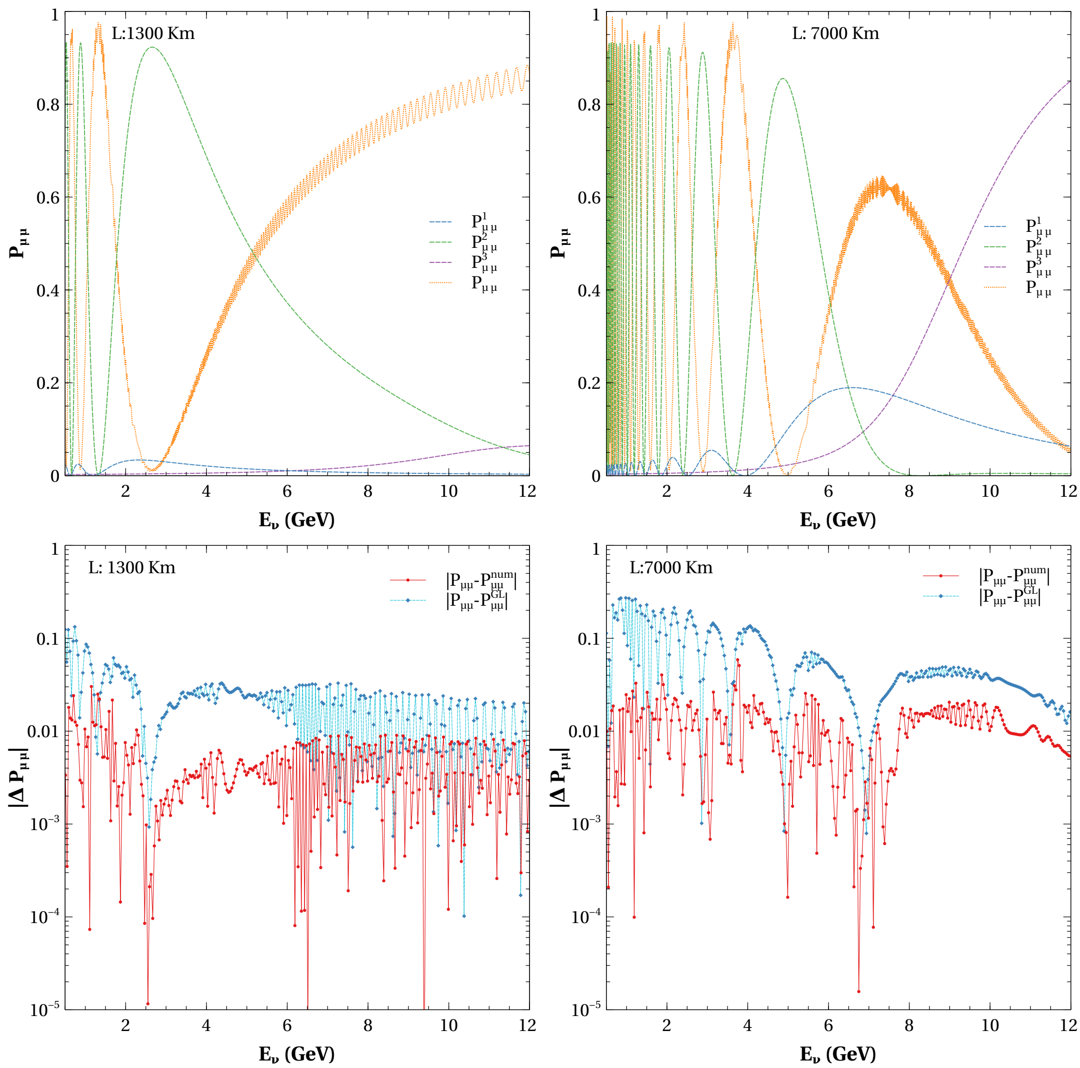

Figure 3.2: The total analytic probability $P_{\mu\mu}$ (orange) along with its other dominant terms in the top panel and the absolute differences $|P_{\mu\mu} - P_{\mu\mu}^{\text{num}}|$ (red) and $|P_{\mu\mu} - P_{\mu\mu}^{\text{GL}}|$ (cyan) in the bottom panel at 1300 km(left), and 7000 km(right).

It has also been shown in the bottom panel of fig. 3.2, the absolute differences $|\Delta P|$ of the analytical probability $P_{\mu\mu}$(3.24) with the exact probability $P_{\mu\mu}^{\rm num}$(3.19) (red) and the probability $P_{\mu\mu}^{\rm GL}$ (cyan) obtained using GLoBES at 1300 km and 7000 km baselines. We observe that value of $|\Delta P|$ is mostly around 10^{-3}. The $|\Delta P|$ values are seen to be lower around resonance energies. We can also see the $|\Delta P|$ value going down at the minima or at the regions where the value of probability is less. The $|\Delta P_{\mu\mu}|$ for 7000 km is increasing after resonance energy as the dominant term in those energies is $P_{\mu\mu}^3$ that is proportional to Δ_{21m} and hence is affected by the $\Delta_{21} = 0$ approximation[1]. Hence, we can conclude that the analytical probability $P_{\mu\mu}$ using TMSD approximation is in agreement with exact and numerical probabilities to a good extent, matching better with the exact one $P_{\mu\mu}^{\rm num}$.

3.3 Octant Degeneracy

The degeneracy in the determination of the octant of θ_{23} can arise from both the survival/oscillation probabilities as follows:

- When the probability is a function of $\sin^2 2\theta_{23}$, it is not possible to differentiate between the probabilities arising due to θ_{23} and $\frac{\pi}{2} - \theta_{23}$. This is called intrinsic octant degeneracy[147].
- When the probability is a function of $\sin^2\theta_{23}$ or $\cos^2\theta_{23}$, the degeneracy of the octant arises due to the uncertainties in the Dirac CP phase δ_{CP}.

$$P(\theta_{23}^{\rm right}, \delta_{13}) = P(\theta_{23}^{\rm wrong}, \delta_{13}') \tag{3.28}$$

- The addition of a light sterile neutrino brings an extra phase δ_{14} which will also affect the determination of octant just like in the above case through additional degeneracies.

$$P(\theta_{23}^{\rm right}, \delta_{14}) = P(\theta_{23}^{\rm wrong}, \delta_{14}') \tag{3.29}$$

- Considering known hierarchy and two unknown phases, there will be a new 8 fold

[1] In the appendix we have shown that with non-zero Δ_{21} in the Cayley Hamilton method we get better fit at these regions as well as at very low energies.

octant-δ_{13}-δ_{14} degeneracy.

$$P(\theta_{23}^{\text{right}}, \delta_{13}, \delta_{14}) = P(\theta_{23}^{\text{wrong}}, \delta_{13}^{'}, \delta_{14}^{'}) \tag{3.30}$$

We consider the normal hierarchy ($\Delta_{31} = 2.515 \times 10^{-3}$ eV^2) for our octant degeneracy study. Therefore, we have a 8-fold *octant*-δ_{13}-δ_{14} degeneracy in presence of a sterile neutrino as depicted in table 3.2. For unknown hierarchy, this will become a 16-fold degeneracy.

Solution with right octant	Solution with wrong octant
RO-Rδ_{13}-Rδ_{14}	WO-Rδ_{13}-Rδ_{14}
RO-Rδ_{13}-Wδ_{14}	WO-Rδ_{13}-Wδ_{14}
RO-Wδ_{13}-Rδ_{14}	WO-Wδ_{13}-Rδ_{14}
RO-Wδ_{13}-Wδ_{14}	WO-Wδ_{13}-Wδ_{14}

Table 3.2: New degeneracies in presence of unknown octant and phases with fixed hierarchy.

In order to understand the degeneracy analytically, we follow the method outlined in [195] and use the TMSD probabilities derived in the earlier section. The current 3σ range of θ_{23} is $[39.7°, 50.9°]$ [144] for normal hierarchy. We can express θ_{23} w.r.t. $\pi/4$ as,

$$\theta_{23} = \frac{\pi}{4} \pm \eta \tag{3.31}$$

where the deviation in value of θ_{23} from current global analysis fit is given by $\eta \sim 0.1$ with the plus and minus sign in (3.31) indicating higher octant(HO), and lower octant (LO) of θ_{23} respectively. The octant sensitivity will be there if there is a difference between probabilities of the two opposite octants even when the phases δ_{13}, δ_{14} vary in the range $[-\pi, \pi]$. The octant sensitivity from the appearance channel probability $P_{\mu e}$ is defined as,

$$\Delta P_{oct,1} \equiv P_{\mu e}^{1HO}(\delta_{13}^{HO}, \delta_{14}^{HO}) - P_{\mu e}^{1LO}(\delta_{13}^{LO}, \delta_{14}^{LO}) > 0 \tag{3.32}$$

As η is small, we can have the following expansion

$$\sin^2\theta_{23} \simeq \frac{1}{2} \pm \eta, \sin\theta_{23} \simeq \frac{1}{\sqrt{2}}(1 \pm \eta), \cos\theta_{23} \simeq \frac{1}{\sqrt{2}}(1 \mp \eta) \tag{3.33}$$

Putting $P_{\mu e}^1$ from (3.21) in (3.32) and using the above expressions of (3.33), we get three contributions to $\Delta P_{oct,1}$ corresponding to the three terms in $P^1_{\mu e}$,

$$\Delta P_0 = 8\eta\cos^2\theta_{13m}\cos^2\theta_{14m}\cos^2\theta_{24m}\sin^2\theta_{13m}\sin^2 D^m_{31},$$
$$\Delta P_1 = X_1[\sin(D^m_{31}+\delta^{HO}) - \sin(D^m_{31}+\delta^{LO})] + \eta X_1[\sin(D^m_{31}+\delta^{HO}) + \sin(D^m_{31}+\delta^{LO})],$$
$$\Delta P_2 = -Y_1[\sin(D^m_{31}-\delta^{HO}) - \sin(D^m_{31}-\delta^{LO})] - \eta Y_1[\sin(D^m_{31}-\delta^{HO}) + \sin(D^m_{31}-\delta^{LO})] \tag{3.34}$$

The contribution of the fast oscillation terms $P^2_{\mu e}, P^3_{\mu e}$ to the octant sensitivity is,

$$\Delta P_{fast} = \sum_{k=1,3} Z_k[\sin(D^m_{4k}-\delta^{HO}) - \sin(D^m_{4k}-\delta^{LO})] + \eta Z_k[\sin(D^m_{4k}-\delta^{HO}) + \sin(D^m_{4k}-\delta^{LO})]$$

Where $D^m_{ij} = \frac{1.27\Delta^m_{ij}}{E}$. Now we can rewrite (3.32) for octant sensitivity as,

$$\Delta P_{oct,1} = \Delta P_0 + \Delta P_1 + \Delta P_2 + \Delta P_{fast} \tag{3.35}$$

Among the terms of $\Delta P_{oct,1}$ (3.34), ΔP_0 has no dependence on phase and is positive whereas the values of $\Delta P_1, \Delta P_2, \Delta P_{fast}$ can be both positive and negative as they contain phases. Thus degeneracy can occur when $\Delta P_1 + \Delta P_2 + \Delta P_{fast}$ is negative and is of the same order as ΔP_0 making ΔP zero. X_1, Y_1 the positive definite amplitudes of ΔP_1, ΔP_2 respectively as well as the amplitudes Z_1, Z_3 of ΔP_{fast} are as follows,

$$\begin{aligned}
X_1 &= \sqrt{2}\cos^3\theta_{13m}\cos^2\theta_{14m}\sin\theta_{13m}\sin\theta_{14m}\sin 2\theta_{24m}\sin D^m_{31},\\
Y_1 &= \sqrt{2}\cos\theta_{13m}\cos^2\theta_{14m}\sin^3\theta_{13m}\sin\theta_{14m}\sin 2\theta_{24m}\sin D^m_{31},\\
Z_1 &= \cos^2\theta_{14m}\sin 2\theta_{13m}\sin\theta_{14m}\sin 2\theta_{24m}\sin D^m_{41}/\sqrt{2},\\
Z_3 &= -\cos^2\theta_{14m}\sin 2\theta_{13m}\sin\theta_{14m}\sin 2\theta_{24m}\sin D^m_{43}/\sqrt{2}
\end{aligned} \tag{3.36}$$

Now, if we inspect the possibility of the octant degeneracy through the probabilities at a baseline of 1300 km. We use the following values of the oscillation parameters: $\theta_{12} = 33.47°, \theta_{13} = 8.54°, \theta_{14} = 7°, \theta_{24} = 7°, \Delta_{31} = 2.515 \times 10^{-3}\text{eV}^2, \Delta_{41} = 1\text{eV}^2$. For 1300 km at oscillation maxima of 2.5 GeV, the values of various terms of $\Delta P_{oct,1}$ are,

$$\Delta P_0 = 0.0279, X_1 = 0.0073, Y_1 = 0.0003, Z_1 = -0.0056, Z_3 = 0.0064 \tag{3.37}$$

Therefore, ΔP_2 is negligible compared to ΔP_0, ΔP_{fast}, and ΔP_1 due to presence of extra $\sin^2\theta_{13m}$ in Y_1(3.36). It can be seen from (3.34) the square bracketed terms multiplying

X_1, Z_1, Z_3 can vary from $-2 : +2$ and therefore, for certain phase choices, cancellation can occur resulting in loss of octant sensitivity in 1300 km baseline when fast oscillations considered. However, in the absence of fast oscillations, there is octant sensitivity.

Next, we use the analytic expressions in (3.35) to understand the octant sensitivity at 7000 km. In the case of 7000 km at oscillation maxima of $E = 6.5$ GeV, the values of the different terms contributing to ΔP are,

$$\Delta P_0 = 0.1453, X_1 = 0.0133, Y_1 = 0.0040, Z_1 = 0.0001, Z_3 = -0.0164 \tag{3.38}$$

It shows that $\Delta P_0, X_1, Z_3$ are the dominant contributions and any combination of phases can not make $\Delta P_{oct,1} = 0$ as the value of P_0 is one order greater than X_1. It shows probabilities ($P_{\mu e}$) corresponding to two different octants will always be well separated from each other, i.e., the octant-δ_{13}-δ_{14} degeneracy will be removed. This suggests unlike in 1300 km here even with the variation of phases in both octants, we can have significant octant sensitivity at higher baselines. This is mainly because at the higher baselines ΔP_0 has much higher values than others due to higher matter effects. Note that if the values of θ_{14}, θ_{24} are decreased, the dominant contribution, ΔP_0 becomes larger whereas other contributions X_1, Y_1, Z_1, Z_3 get smaller. Therefore, octant sensitivity will be higher for smaller values of sterile mixing angles.

The octant sensitivity from the disappearance channel probability $P_{\mu\mu}$ is defined as,

$$\Delta P_{oct,2} \equiv P^{1HO}_{\mu\mu}(\delta^{HO}_{13}, \delta^{HO}_{14}) - P^{1LO}_{\mu\mu}(\delta^{LO}_{13}, \delta^{LO}_{14}) > 0 \tag{3.39}$$

As we have seen earlier, the largest octant sensitive term in $P_{\mu\mu}$ comes from (3.25). We put that in the above (3.39) to get the difference in opposite octant probabilities as,

$$\begin{aligned}\Delta P_{oct,2} = {} & \cos^2\theta_{24m} \sin 2\theta_{24m} \sin\theta_{14m} \sin 4\theta_{13m} (\cos\delta^{HO} - \cos\delta^{LO}) \frac{1+3\eta}{2\sqrt{2}} \sin^2 D^m_{31} \\ & + \cos^2\theta_{24m} 2\eta \cos^2\theta_{24m} \sin^2 2\theta_{13m} \sin^2 D^m_{31}\end{aligned} \tag{3.40}$$

It can be noted from the above expression that the first term has phase dependence while the second term is independent of the phases.

3.3.1 Degeneracy in $\cos\theta_\nu - E_\nu$ Plane

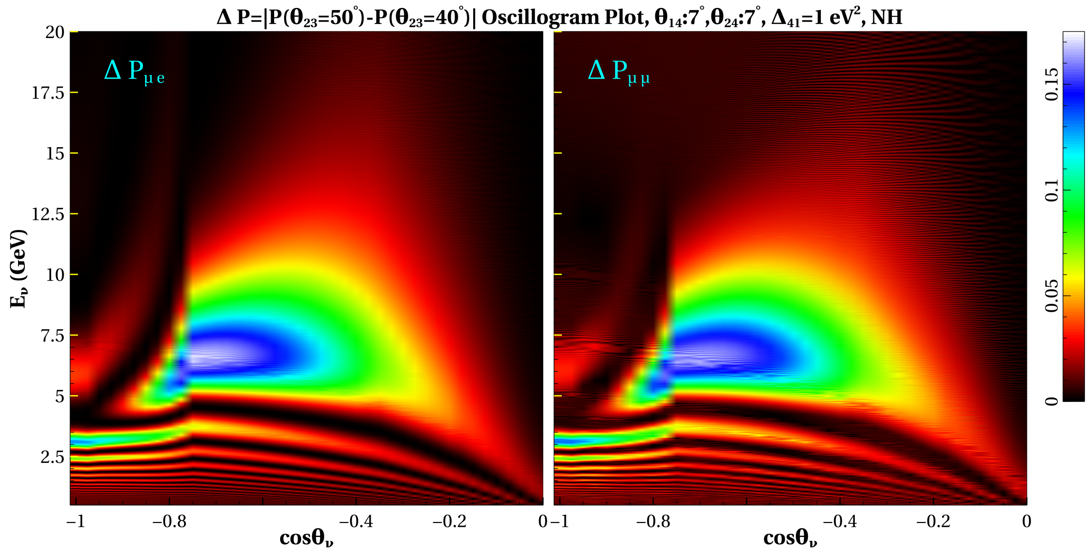

Figure 3.3: $\Delta P_{\mu e}$(left), $\Delta P_{\mu\mu}$(right), i.e, the absolute differences in probabilities for θ_{23} values from opposite octant with fixed value of δ_{13}, δ_{14} in $\cos\theta_\nu - E_\nu$ plane.

To probe the octant sensitivity spanning over all the baselines and energies, we present the oscillogram plots of the differences in probabilities corresponding to the value of $\theta_{23} = 40°$(LO) and $\theta_{23} = 50°$(HO) in $\cos\theta_\nu - E_\nu$ plane for normal hierarchy in fig. 3.3. The phases are kept fixed at same $\delta_{13} = 195°, \delta_{14} = 30°$ for both the octants. From the figure, it can be seen that the maximum difference is obtained at the energy range of $5 : 10$ GeV for $\cos\theta_\nu$ in the range of $-0.5 : -0.8$ which roughly translates to baselines around 5000-10000 km. This figure serves as a reference to show at which baselines and energies the octant sensitivity can be maximum and motivates us to add the contribution from atmospheric neutrinos to obtain better octant sensitivity in our analysis.

3.3.2 Degeneracy with variation of δ_{13}, δ_{14} at fixed baseline

In this section, we study the probabilities (GLoBES) as a function of the phases to understand the dependency of the degeneracy on these parameters. In fig. 3.4, we depict the appearance probability $P_{\mu e}$ for $\theta_{23} = 41°$ (red), and 49°(blue) as a function of neutrino energy at 1300 km and 7000 km baselines. The bands correspond to the variation of δ_{13}, δ_{14}. Two different sets of representative values of θ_{14}, θ_{24} are considered, e.g., $\theta_{14}, \theta_{24} = 4°$, which are allowed after MINOS+[184] bounds, and $\theta_{14}, \theta_{24} = 7°$, which are allowed by an earlier global fit[185] excluding the MINOS+ results. The significant observations are as follows,

- The probability bands of different octants overlap at 1300 km. While at 7000 km difference is observed between opposite octant bands. It shows that at higher baseline, sensitivity for octant will be higher.
- The difference (overlap) between red and blue bands is more (lesser) for 4° than 7°. It is obvious that with smaller sterile mixing angles, we will get better sensitivity.

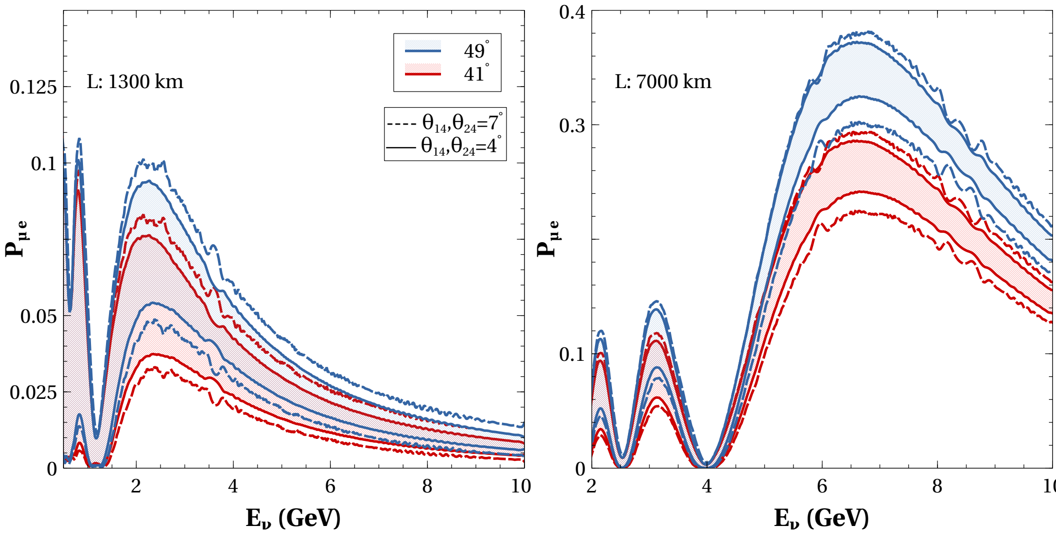

Figure 3.4: $P_{\mu e}$ as a function of energy at 1300 km (left), and 7000 km (right). Blue and red bands are due to variation of δ_{13}, δ_{14} for $\theta_{23} = 49°$, $41°$ using $\theta_{14} = \theta_{24} = 4°$. The regions between blue and red dotted curves are for 49°, 41° respectively, considering $\theta_{14} = \theta_{24} = 7°$.

From the above figures, we can observe that the variation in the phases can lead to overlap in the probabilities from opposite octants giving rise to degenerate solutions. Therefore, it is instructive to study the variation of the probabilities w.r.t. the phases in order to understand for which values of these parameters degenerate solutions can occur. These plots are done at fixed energies. We choose this energy as 2.5 GeV for $P_{\mu e}$, at 1300 km, since first oscillation maxima occur at this energy as can be seen from fig. 3.4. The variation of the probabilities $P_{\mu e}$(left), $P_{\bar{\mu}\bar{e}}$(right) are shown as a function of phases δ_{13} (top), and δ_{14} (bottom) in fig. 3.5 for values of $\theta_{23} = 39°$(grey), 42°(orange), 48°(violet), 51°(blue) spanning over both octants. The curves for other values of θ_{23} will lie in between these ranges. The bands correspond to variation over the non-displayed phase $\delta_{14}(top)/\delta_{13}(bottom)$ over the range $-180° : 180°$ respectively. Three horizontal iso-probability lines are drawn in fig. 3.5 to indicate the values of δ_{13}/δ_{14} for which there are degeneracies (dot-dashed line) and there are no degeneracies (dotted, dashed lines) between the two octants. Note that in the probability vs δ_{13} plots for the three-generation case, there is a single curve for each θ_{23} whereas, in the presence of sterile neutrino, there are bands due to δ_{14} variation for a fixed θ_{23}. We can infer the following

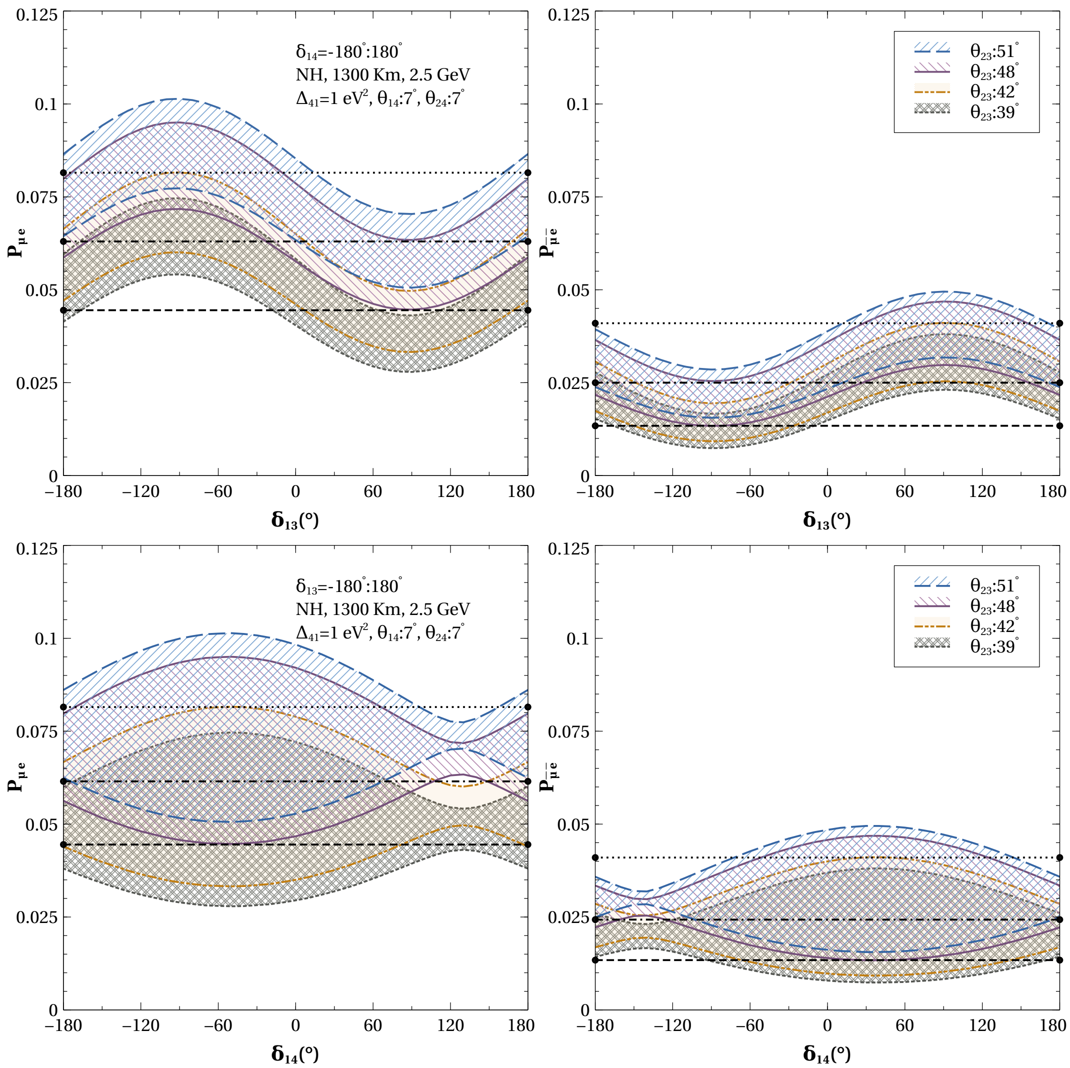

Figure 3.5: $P_{\mu e}$ (left), and $P_{\bar{\mu}\bar{e}}$ (right) as a function of δ_{13} (top), δ_{14} (bottom) for variation of the respective another phase at neutrino energy 2.5 GeV at 1300 km baseline for NH.

points from fig. 3.5,

- The regions above the dotted line in the top panels indicate the values of δ_{13} for which there is no degeneracy in HO. This is around $\delta_{13} = -90°(90°)$ in $P_{\mu e}(P_{\bar{\mu}\bar{e}})$ channel. However, some portions of the blue and violet bands extend below the dotted lines in both figures and sometimes also overlap with the orange and violet bands, indicating that for these values of δ_{13} there are still degeneracies for certain values of δ_{14}.

- Similarly, the regions below the dashed lines in the top panels signify the δ_{13} values devoid of degeneracy for θ_{23} in LO. This region for $P_{\mu e}(P_{\bar{\mu}\bar{e}})$ channel is around $\delta_{13} = 90°(-90°)$. Here also, the portions of grey and orange bands above the dashed lines as well as the portions coinciding with the blue and violet bands, indicate the existence of degeneracies at these values of δ_{13}.

- From the top panels, we can clearly see a synergy between neutrino and anti-neutrino channels for octant degeneracy in both HO and LO. For instance, for HO (LO), the degeneracy is present around $\delta_{13} = 90°(-90°)$ at $P_{\mu e}$ channel but absent for $P_{\bar{\mu}\bar{e}}$.

- In the bottom panels, the regions above the dotted line indicate that the no degeneracy region in HO lies around $\delta_{14} = -60°(60°)$ for $P_{\mu e}(P_{\bar{\mu}\bar{e}})$ channel. Note that the region has a larger spread in δ_{14} over $-180° : 95°(-70° : 140°)$ for $\theta_{23} = 51°$, and over $-180° : 65°(-50° : 120°)$ for $\theta_{23} = 48°$ in $P_{\mu e}(P_{\bar{\mu}\bar{e}})$ channel. Corresponding nondegenerate regions have a smaller spread in δ_{13} as seen from the top panel plots.

- There are regions below the dashed line signifying no degeneracy in LO for the plots in the bottom panels. These regions occur around $\delta_{14} = -60°(60°)$ for $P_{\mu e}(P_{\bar{\mu}\bar{e}})$ channel. However, it is to be noted that unlike in the top panel, the non-degenerate region in LO is over the similar range of δ_{14} w.r.t HO as mentioned in the previous point. Therefore we see in the neutrino (anti-neutrino) channel maximum sensitivity for both HO and LO is around $\delta_{14} = 60°(-60°)$.

- In the bottom panels, the probability bands are wider and the extent of overlap is higher around $-60°(60°)$ in $P_{\mu e}(P_{\bar{\mu}\bar{e}})$ channel. These give rise to WO-Rδ_{14} degeneracies which are hard to resolve using neutrino plus anti-neutrino. The synergy between neutrino and anti-neutrino channels for octant degeneracy is less pronounced here.

- In the bottom panels for $P_{\mu e}$ channel, around $\delta_{14} = 130°$, there is a small region where there is no WO-Rδ_{14} degeneracy between HO and LO for all values of

δ_{13}. For $P_{\bar{\mu}\bar{e}}$ channel there is a similar region with minimum degeneracy around $\delta_{14} = -130°$.

- When the probability bands from HO (blue and violet) coincide with bands from LO (orange and grey) at the same δ_{13}/δ_{14} values, those are examples of WO-Rδ_{13}/Rδ_{14} degeneracies. While the regions of bands from opposite octants connected through iso-probability lines show WO-Wδ_{13}/Wδ_{14} degeneracies.

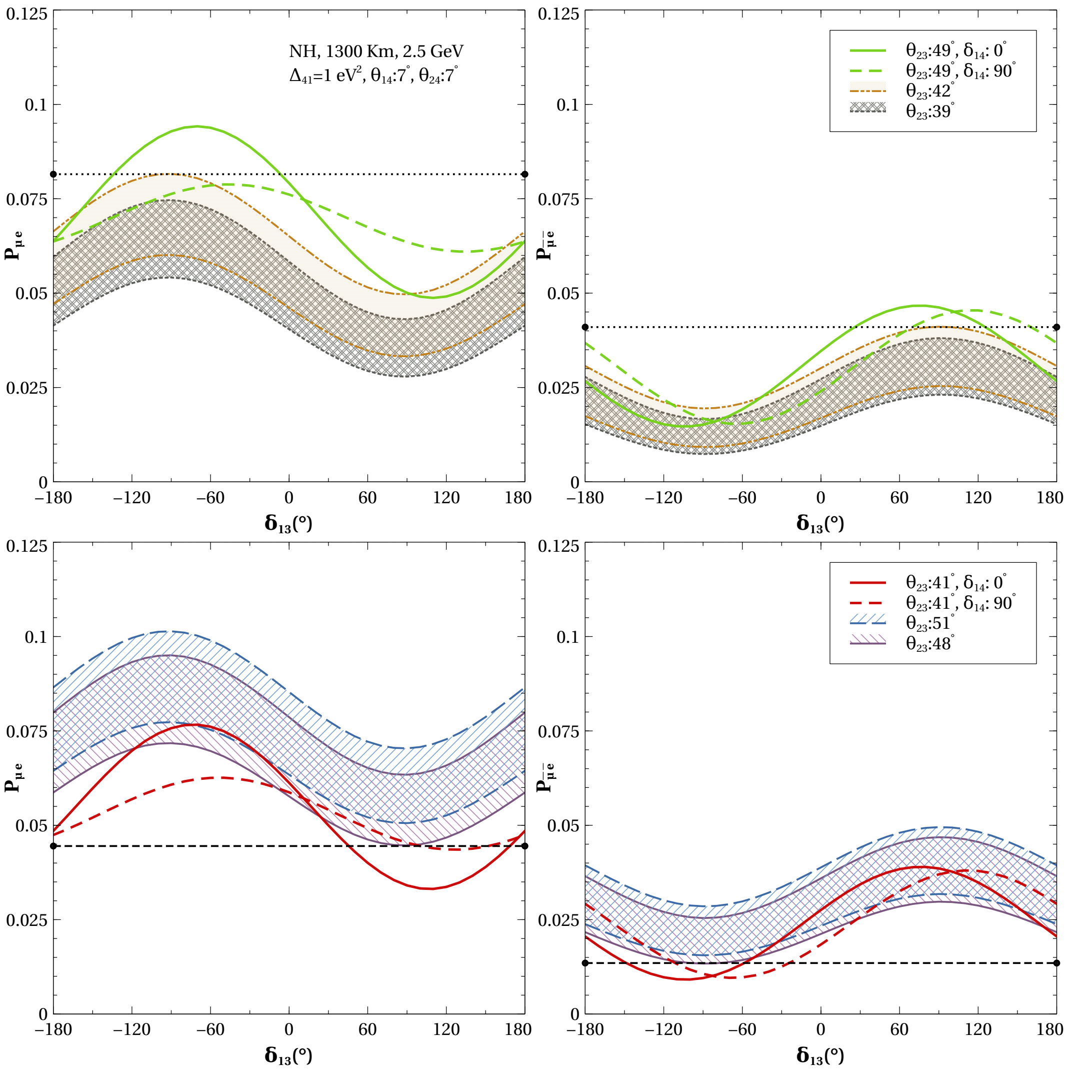

Figure 3.6: $P_{\mu e}$ (left), and $P_{\bar{\mu}\bar{e}}$ (right) as a function of δ_{13} for variation of the phase δ_{14} at neutrino energy 2.5 GeV at 1300 km baseline for NH.

While performing χ^2 analysis, we take fixed true values of parameters in one octant and marginalize χ^2 over the relevant parameters in the opposite octant. Therefore, a better understanding of the octant degeneracy can be achieved if we keep θ_{23}, and the phases constant in one octant and vary them in the opposite one. We replicate this in fig. 3.6 where the probabilities in neutrino (left) and anti-neutrino (right) channels are drawn as a function of phase δ_{13}. In the top [bottom] panel, the green [red] solid(dashed) line corresponds to $\theta_{23} = 49°[41°]$ and $\delta_{14} = 0°(90°)$. The grey and orange [violet and blue] bands correspond to $\theta_{23} = 39°, 42°[48°, 51°]$ in LO[HO] for δ_{14} varying over $-180° : 180°$. The horizontal iso-probability lines in the plots demarcate different degenerate and non-degenerate regions. The important points from fig. 3.6 are as follows,

- In the top panel, the region above the dotted line corresponds to no degeneracy. This region is around $\delta_{13} = -90°(90°)$ at $P_{\mu e}(P_{\bar{\mu}\bar{e}})$ channel for green solid ($\delta_{14} = 0°$) curve. However, the green dashed ($\delta_{14} = 90°$) curve has a non-degenerate region only in $P_{\bar{\mu}\bar{e}}$ channel around $\delta_{13} = 90°$. This suggests that for $\delta_{14} = 0°$, the octant sensitivity comes from both $P_{\mu e}$, and $P_{\bar{\mu}\bar{e}}$ channel around $\delta_{13} \sim 0°$ whereas for $\delta_{14} = 90°$ sensitivity comes only from $P_{\bar{\mu}\bar{e}}$ channel around $\delta_{13} \sim 90°$.

- For the bottom panel, the non-degenerate regions are below the dashed horizontal line. In $P_{\mu e}$ channel this region is around $\delta_{13} = 120°$ for $\delta_{14} = 0°$. A very small region for $\delta_{14} = 90°$ also extends below the dashed line. In $P_{\bar{\mu}\bar{e}}$ channel the region of no degeneracy lies around $\delta_{13} = -120°(-60°)$ for $\delta_{14} = 0°(90°)$.

Now we focus on the disappearance channel probabilities $P_{\mu\mu}$ (left), and $P_{\bar{\mu}\bar{\mu}}$ (right) as a function of phases δ_{13}(top panel), δ_{14}(bottom panel) at 2.5 GeV in fig. 3.7. The following points may be noted,

- The bands due to variation of δ_{13}/δ_{14} are narrower than the ones for appearance channel. Hence these bands are well separated from each other.

- The bands corresponding to $\theta_{23} = 51°$(blue) in HO comes in between the bands corresponding to $\theta_{23} = 39°$(grey) and $\theta_{23} = 42°$(yellow) in LO. On the other hand, the violet band corresponding to $\theta_{23} = 48°$ is outside the whole region of LO between the grey and yellow band. This implies the presence (absence) of the octant degeneracy for $\theta_{23} = 51°(48°)$ in $P_{\mu\mu}$ channel.

- Similarly, $\theta_{23} = 39°$ (grey) in LO demonstrates octant sensitivity since it lies outside the HO region between the blue and violet bands, but $\theta_{23} = 42°$ (yellow) lies within the HO region and therefore is not sensitive to the octant. A similar feature can also be seen from probability vs δ_{14} plots in the bottom panel.

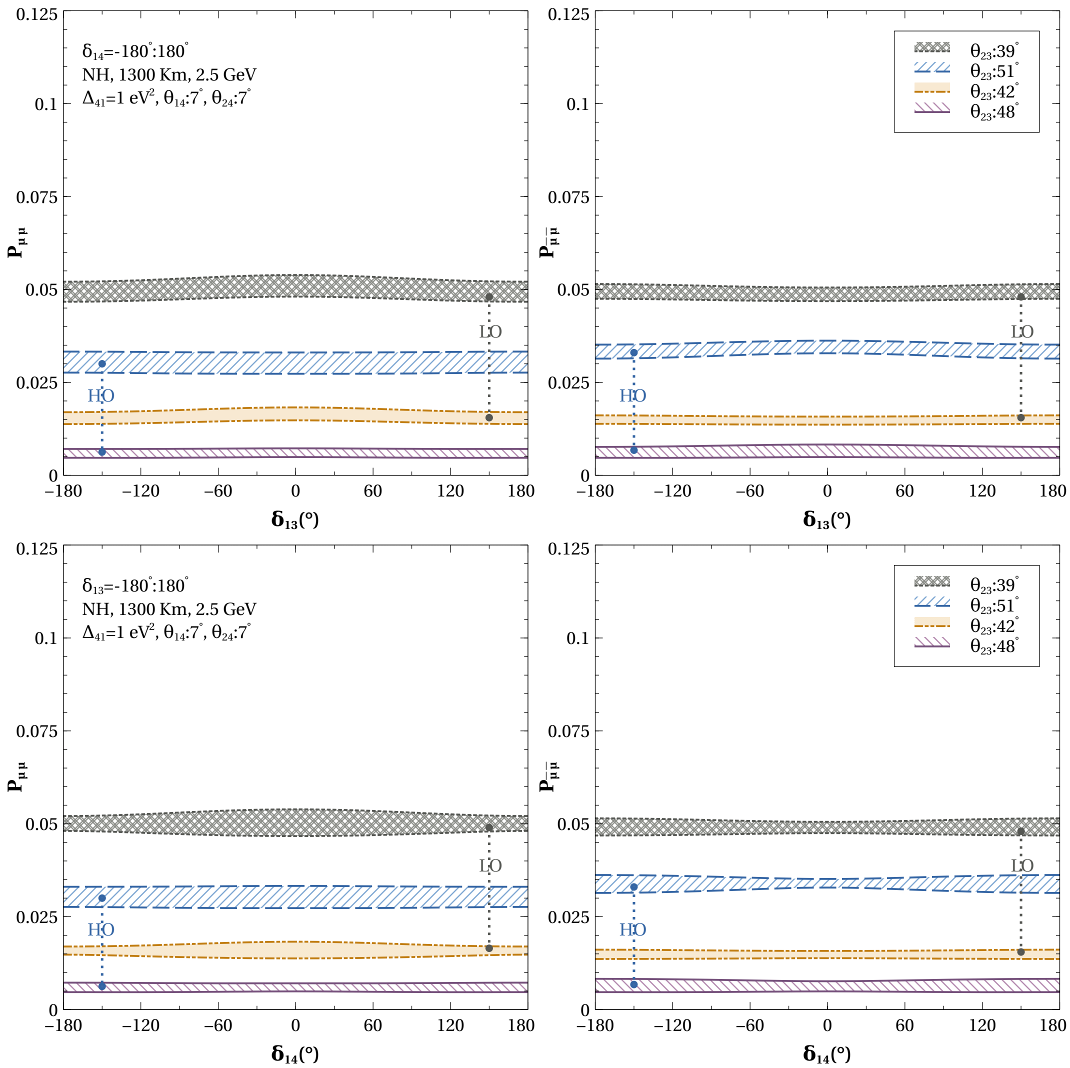

Figure 3.7: $P_{\mu\mu}$ (left), and $P_{\bar{\mu}\bar{\mu}}$ (right) vs δ_{13} (top), δ_{14} (bottom) for variation of the respective another phase at neutrino energy 2.5 GeV at 1300 km baseline for NH.

We can conclude that for certain trues values of θ_{23}, the $P_{\mu\mu}$ channel can contribute to the octant sensitivity at 1300 km.

Next, we study the behavior of the probabilities at a higher baseline of 7000 km where the resonant matter effect comes into play. We observe the appearance probability $P_{\mu e}$ as a function of the phase δ_{13} (left), and δ_{14} while the respective other phase variation creates band at different values of $\theta_{23} = 39°, 42°, 48°, 51°$ spanning over both octants at energy maxima of 6.5 GeV in fig. 3.8. We see similar variations of the disappearance channel probability $P_{\mu\mu}$ at maxima energy of 7 GeV in fig. 3.9. Energies of 6.5 GeV and 7 GeV are chosen as they correspond to the maxima in $P_{\mu e}, P_{\mu\mu}$ channels at this baseline, respectively. The effect of sterile mixing angles and phases on octant sensitivity in the

$P_{\mu e}$ channel at other energies can be seen in 3.4. The following facts can be noted,

- Unlike at 1300 km, the $P_{\mu e}$ probability bands of opposite octant at 7000 km are clearly separated. It suggests that even with the variation of phases and θ_{23} in both octants, the octant degeneracy can be clearly removed at higher baselines.

- In $P_{\mu\mu}$ channel, the LO and HO bands are mostly separated apart from the occurrence of WO-Wδ_{13} (left panel), WO-Rδ_{14}/Wδ_{14} (right panel) degeneracies respectively around δ_{13}, δ_{14} values of $\pm 150°$ in a tiny region. This suggests contributions to the octant sensitivity also come from the $P_{\mu\mu}$ channel. The sensitivity of the octant in $P_{\mu\mu}$ comes from the first term in (3.25), which has a more significant contribution at 7000 km than 1300 km as noted in fig. 3.2 due to larger matter effect.

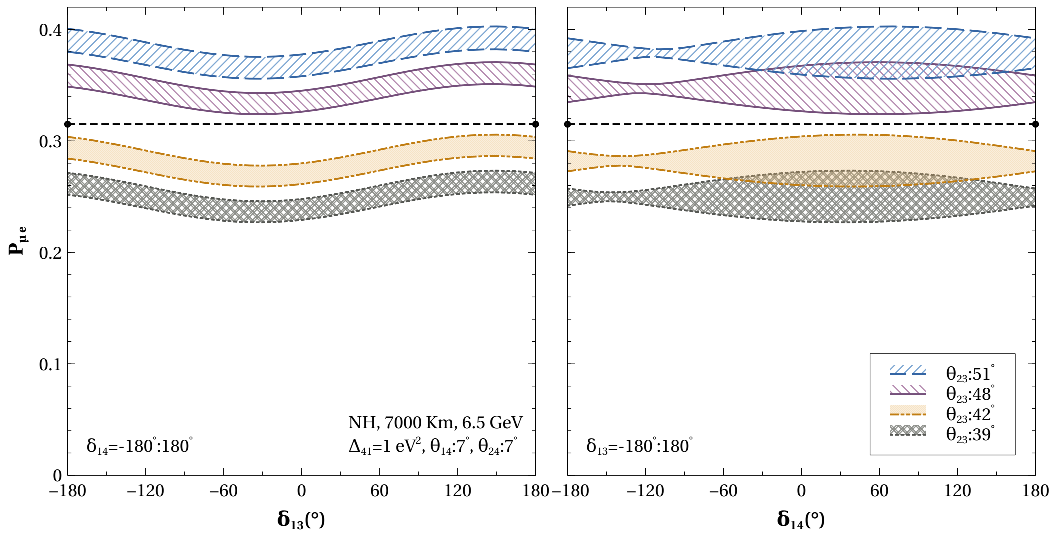

Figure 3.8: $P_{\mu e}$ vs δ_{13}(left), and δ_{14}(right) for variation of the respective another phase at neutrino energy 6.5 GeV at 7000 km baseline for NH.

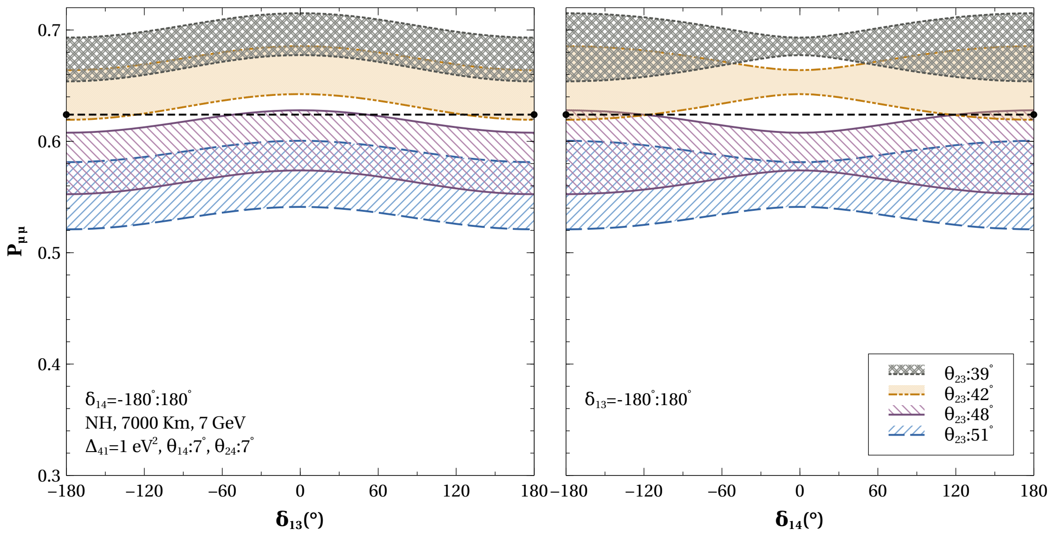

Figure 3.9: $P_{\mu\mu}$ vs δ_{13}(left), and δ_{14}(right) for variation of the respective another phase at energy 7 GeV at 7000 km baseline for NH.

3.4 Hierarchy Degeneracy

Considering $\theta_{34} = 0°$, the sterile parameters affecting the probabilities are $\theta_{14}, \theta_{24}, \delta_{14}$, and Δ_{41}. We investigate how the probabilities depend on those parameters leading to changes in the hierarchy sensitivity of the atmospheric mass squared difference Δ_{31}.

Effect of non-zero θ_{14}, θ_{24}

The dominant term in the $\nu_\mu - \nu_e$ oscillation probability in OMSD approximation valid for $\Delta_{21}L/E << 1$, e.g., at 7000 km baseline around the resonance energy is given by eq. (3.21) as,

$$\begin{aligned} P^1_{\mu e} &= 4\cos^2\theta_{13m}\cos^2\theta_{14m}\sin^2\theta_{13m}(\cos^2\theta_{24m}\sin^2\theta_{23} - \sin^2\theta_{14m}\sin^2\theta_{24m})\sin^2\frac{1.27\Delta^m_{31}L}{E} \\ &+ 2\cos^3\theta_{13m}\cos^2\theta_{14m}\sin\theta_{13m}\sin\theta_{14m}\sin 2\theta_{24m}\sin\theta_{23}\sin\frac{1.27\Delta^m_{31}L}{E}\sin(\frac{1.27\Delta^m_{31}L}{E}+\delta) \\ &- 2\cos\theta_{13m}\cos^2\theta_{14m}\sin^3\theta_{13m}\sin\theta_{14m}\sin 2\theta_{24m}\sin\theta_{23}\sin\frac{1.27\Delta^m_{31}L}{E}\sin(\frac{1.27\Delta^m_{31}L}{E}-\delta) \end{aligned} \tag{3.41}$$

The difference in the probability $P_{\mu e}$ for two different mass orderings as a function of the phases δ_{13}, δ_{14} (varied in the range $-\pi : \pi$) can be expressed as,

$$\Delta P \equiv P_{\mu e}^{1NO}(\delta_{13}^{NO}, \delta_{14}^{NO}) - P_{\mu e}^{1IO}(\delta_{13}^{IO}, \delta_{14}^{IO}) \tag{3.42}$$

Using only the dominant first term of (3.41), we get the difference in probability as

$$\begin{aligned} \Delta P = \Delta P_{np} + A_1[\sin^2(M-N)\cos\delta^{NH} - \sin^2(M+N)\cos\delta^{IH}] + \\ A_2[\sin 2(M-N)\sin\delta^{NH} + \sin 2(M+N)\sin\delta^{IH}] \end{aligned} \tag{3.43}$$

where ΔP_{np} is the part with no phases involved and is given as follows,

$$\begin{aligned} \Delta P_{np} = \cos^2\theta_{14m}\sin^2 2\theta_{13m}(\sin^2\theta_{24m}\sin^2\theta_{14m} - \\ \cos^2\theta_{24m}\sin^2\theta_{23})\sin 2M \sin 2N \end{aligned} \tag{3.44}$$

and the other part containing the phases are defined by the amplitude parameters A_1, A_2 and the frequency parameters M, N defined as,

$$A_1 = \cos^2\theta_{14m}\cos 2\theta_{13m}\sin 2\theta_{13m}\sin\theta_{14m}\sin 2\theta_{24m}\sin\theta_{23} \tag{3.45}$$

$$A_2 = \cos^2\theta_{14m}\sin 2\theta_{13m}\sin\theta_{14m}\sin 2\theta_{24m}\sin\theta_{23} \tag{3.46}$$

$$M = \Delta_{31}\cos 2(\theta_{13} - \theta_{13m}) * 1.27L/E \tag{3.47}$$

$$N = A\cos 2\theta_{13m}(1 + \cos^2\theta_{14} + \cos^2\theta_{14}\sin^2\theta_{24}) * 1.27L/E \tag{3.48}$$

Now if we use $\Delta_{31} = 2.5 \times 10^{-3}$ eV^2, $\theta_{23} = 45°$ and true values of other parameters given in table 5.1 to calculate at 1300 km at 2.5 GeV (maxima), then we have $\Delta P < 0$. At 7000 Km at first oscillation maxima with energy at $E = 7$ GeV if we calculate using $\theta_{24} = 7°, \theta_{14} = 7°, \theta_{23} = 45°$, and $\Delta_{31} = 2.515 \times 10^{-3}$ eV^2 for NH and $\Delta_{31} = -2.515 \times 10^{-3}$ eV^2 for IH, the contributions are $\Delta P_{np} = 0.241$, $A_1 = 0.006$, $A_2 = 0.021$. The phase dependent part multiplied with A_1 and A_2 can vary from -2 to +2 and are suppressed w.r.t. P_{np}. Thus, we can see that at energies around 7 GeV ΔP will always be greater than zero, i.e., hierarchy can be determined even with unknown δ for the 7000 Km baseline.

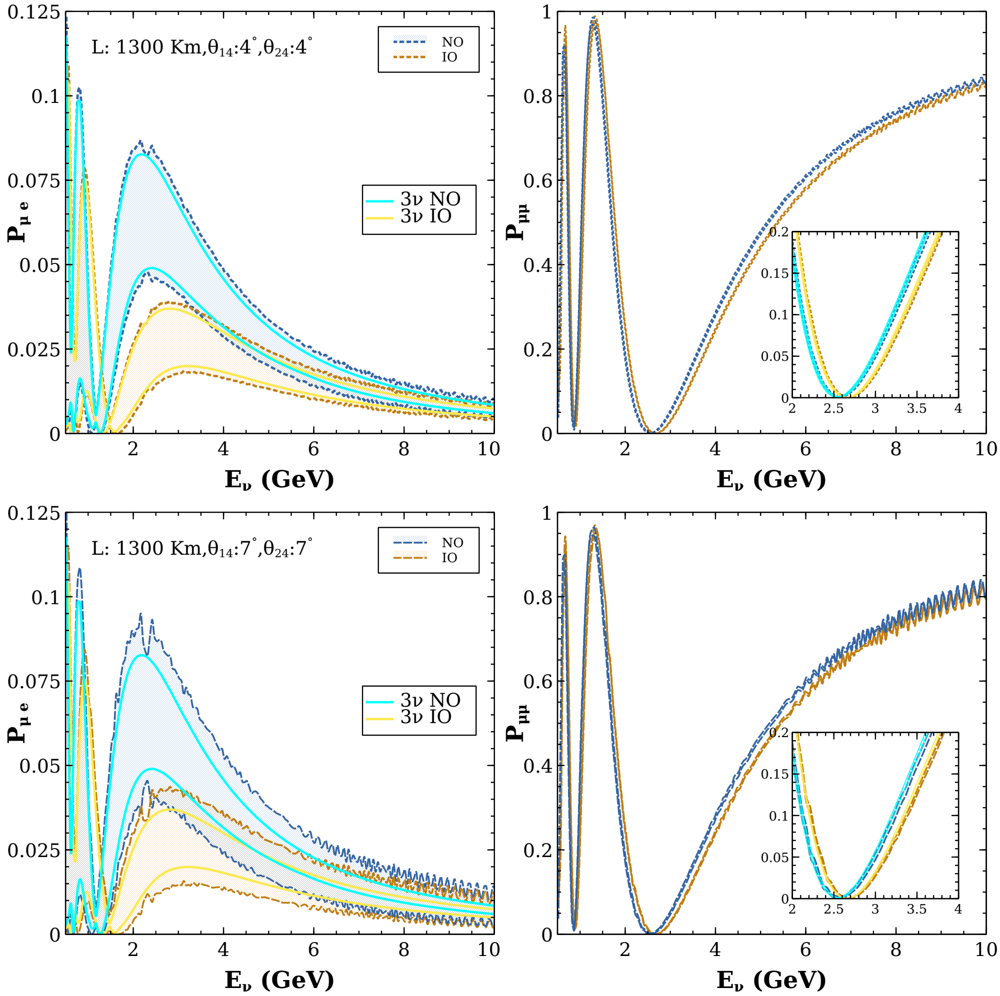

Figure 3.10: Probabilities $P_{\mu e}$(left) and $P_{\mu\mu}$ (right) as a function of energy E_ν due to variation of phases δ_{13}, δ_{14} for NO and IO at 1300 km baseline for $\Delta_{41} = 1$ eV^2. Blue and orange bands in top (bottom) panels refer to varied phases for $\theta_{14} = 4°$ (7°), $\theta_{24} = 4°$ (7°) corresponding to NO and IO respectively. The regions between cyan(yellow) curves are due to variation δ_{13} in 3ν case for NO(IO).

We have plotted the appearance (left), and disappearance (right) probabilities in fig. 3.10 as a function of neutrino energy for varying the respective phase. The blue and orange bands refer at the top (bottom) panels to NO and IO, respectively, corresponding to mixing angles $\theta_{14} = \theta_{24} = 4°(7°)$ in 3+1 framework. The regions between cyan and yellow lines suggest the variation of δ_{13} in three generation framework in NO and IO, respectively. In the right panel, we show $P_{\mu\mu}$ over $2-4$ GeV in a magnified inset. The important observations are as follows,

- In the 3+1 framework, we can observe that the probability regions corresponding to NO and IO are closer than those in the three generation framework. This suggests the hierarchy sensitivity will be reduced in the 3+1 framework.

- The difference between NO and IO bands increases when the values of sterile mixing angles decrease.
- In $P_{\mu e}$ channel, for the 3+1 framework, we observe the difference between the two probability bands of NO and IO in the energy range 1-3 GeV.
- Disappearance channel probability $P_{\mu\mu}$ doesn't depend on the phases as can be seen from the narrow band in NO and IO cases for both three and 3+1 frameworks.
- The $P_{\mu\mu}$ curves for opposite hierarchies are hard to separate from each other at energies lower than 2 GeV. However, some demarcation is visible from opposite hierarchy curves at energies in the range of 2-7 GeV for both three generation cases and 3+1 generation.
- In the disappearance channel, here we don't see a significant effect of variation of sterile-active mixing angles θ_{14}, θ_{24} on the probability bands.

In the context of atmospheric neutrinos, we have depicted in fig. 3.11, the appearance (left) and disappearance (right) probabilities with the variation of phases δ_{13}, δ_{14} in normal(NO) and inverted mass hierarchy (IO) with similar cases as in fig. 3.10 at 7000 km baseline. The important observations are as follows,

- There is a prominent difference between the regions of probabilities due to NH, and IH, implying sensitivity to mass hierarchy even for the 3+1 framework.
- However, the difference decreases for sterile case w.r.t. the standard one.
- Also, with lower θ_{14}, θ_{24} values, the gap between the opposite hierarchy probabilities bands increases further.
- At $P_{\mu\mu}$ channel, a significant gap between opposite hierarchy regions is seen only at energies higher than 4 GeV whereas, in the case of $P_{\mu e}$ channel, the sensitivity is present even at much lower energies of 3 GeV.
- From $P_{\mu e}$ plot at 7 GeV, we find the gap between NH and IH bands is around 0.23, which is similar to what we have calculated earlier using (3.44).

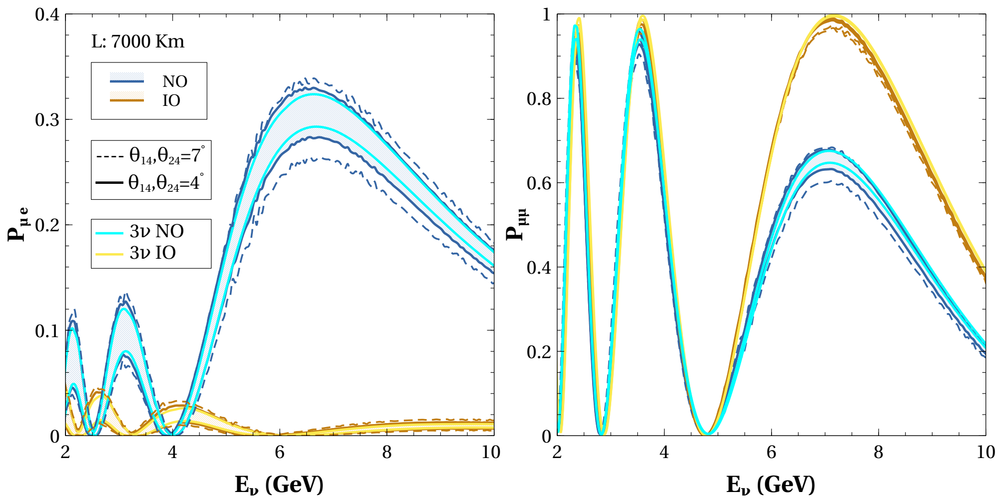

Figure 3.11: Probabilities $P_{\mu e}$(left) and $P_{\mu\mu}$ (right) as a function of energy E_ν due to variation of phases δ_{13}, δ_{14} for NO and IO at 7000 km baseline for $\Delta_{41} = 1$ eV^2. Shaded bands refer to varied phases for $\theta_{14}, \theta_{24} = 4°$. Regions between dashed blue(orange) curves show phase variation for $\theta_{14}, \theta_{24} = 7°$ for NO(IO). Regions between cyan(yellow) curves are due to variation δ_{13} in 3ν case for NO(IO).

Effect of non-zero θ_{34}

In fig. 3.12, the appearance probability is plotted as a function of neutrino energy at 1300 km (left) and 7000 km (right) baseline for both hierarchies with the variation of all the three phases $\delta_{13}, \delta_{14}, \delta_{34}$ for $\theta_{14}, \theta_{24} = 7°$, and $\theta_{34} = 7°, 15°$. The shaded blue (orange) regions correspond to $\theta_{34} = 7°$, whereas the region between the dotted blue (orange) curves are due to $\theta_{34} = 15°$ for NO(IO). The most important observation is a notable decrease in the gap between NH and IH regions at both baselines. Although at 1300 baseline, the regions of NH and IH overlap significantly. However, significant sensitivity can still be achieved when we fix the phases for one hierarchy (true case) and vary it in another hierarchy (test case). In the case of 7000 km, there is still a gap between the opposite hierarchy regions, which gets diminished for a non-zero θ_{34}; however, it's more than what is seen in 1300 km for hierarchy sensitivity.

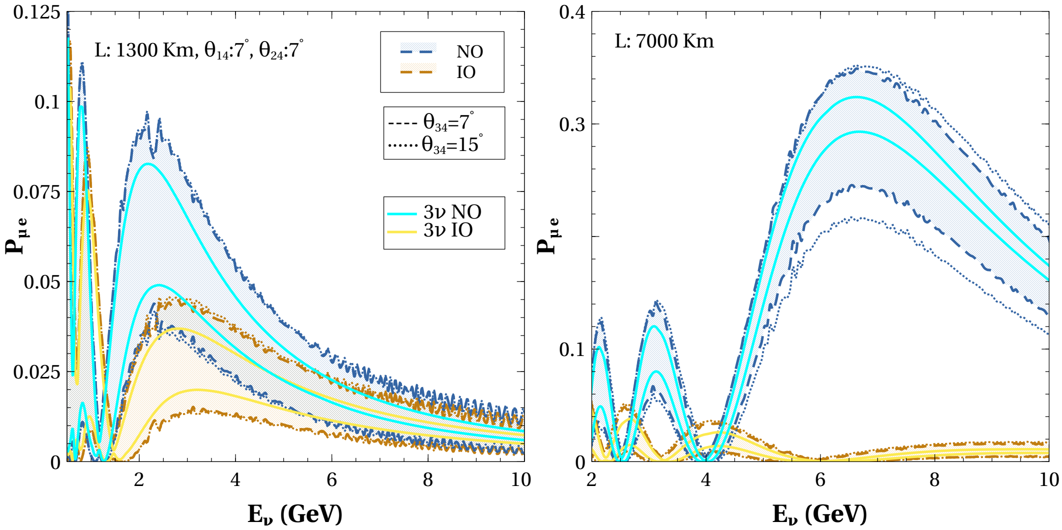

Figure 3.12: Probability $P_{\mu e}$ as a function of energy E_ν with the variation of phases $\delta_{13}, \delta_{14}, \delta_{34}$ for NO (blue) and IO(orange), $\Delta_{41} = 1$ eV^2 at 1300 km (left) and 7000 km (right). Shaded regions refer to $\theta_{14}, \theta_{24} = 7°$, $\theta_{34} = 7°$. Regions between dashed blue(orange) curves show phase variation for $\theta_{14}, \theta_{24} = 7°, \theta_{34} = 15°$ for NO(IO). Regions between cyan(yellow) curves are due to variation δ_{13} in 3ν case for NO(IO).

3.5 Experimental and Simulation Details of the LArTPC detector

As a typical example for the long baseline analysis, we consider an experimental setup consisting of a near detector (ND) and far detector (FD) exposed to a megawatt-scale muon neutrino beam produced by Long Baseline Neutrino Facility (LBNF) at the Fermilab. The ND will be placed close to the source of the beam, while the FD, comprising a LArTPC detector of 40 kton will be installed 1300 km away. The large LArTPC detector at this depth will also collect atmospheric neutrinos. In this analysis, we have used beams coming from the accelerator as well as neutrinos generated in the atmosphere by cosmic ray interactions. The experimental setup considered in our work is similar to that proposed by the DUNE experiment[220][221].

3.5.1 Events from beam neutrinos

We use a beam power of 1.2 MW leading to a total exposure of 10×10^{21} POT. The neutrino beam simulation for the experiment has been carried out using the GLoBES[103] software with the most recent publicly available configuration file[170]. We assume experimental run time for 3.5 years each in the neutrino and the antineutrino mode with a total exposure of 280 kt-yr.

We have plotted the electron and muon events spectrum for 1300 km baseline considering normal hierarchy with sterile mixing angle of $\theta_{14}, \theta_{24} = 7°$ at fixed phases $\delta_{13} = -90°, \delta_{14} = 90°$ in fig. 3.13. There are differences between the spectra of the events for the true value of $\theta_{23} = 41°$(green) in LO with the values of θ_{23} in HO for 46°(orange), 50°(blue). This is indicative of the octant sensitivity. It should be noted that although the green spectrum is closer to the orange one(46°) for electron events (left panels), for muon events (right panels) the green one is closer to the blue one(50°). This indicates that the maximum sensitivity occurs at different θ_{23} values in the opposite octant for electron and muon events. This will lead to the synergy between electron and muon events when we compute the combined octant sensitivity at χ^2 level. The maximum difference in events is observed in the energy region of 2-4 GeV where the spectra of the event have maxima in the case of both electrons and muons. We present bi-events plots in fig. 3.14 considering the total no of electron neutrino and anti-neutrino events obtained by integrating over the full energy range. The elliptic regions are due to variations in the relevant phases over their full range. This figure shows that in the case of three flavor oscillation framework, the ellipses for θ_{23} being in two different octants are well separated, showing no octant degeneracy with combined $\nu_e + \bar{\nu}_e$ events of 3.5+3.5 years with 40 kt LArTPC detector. Now if we add a sterile neutrino, these ellipses turn into blobs, a combination of many ellipses[195]. From this figure, we can see that the separation between the green(LO) and yellow (HO) regions increases with smaller values of sterile mixing angles θ_{14}, θ_{24} leading to an enhanced octant sensitivity.

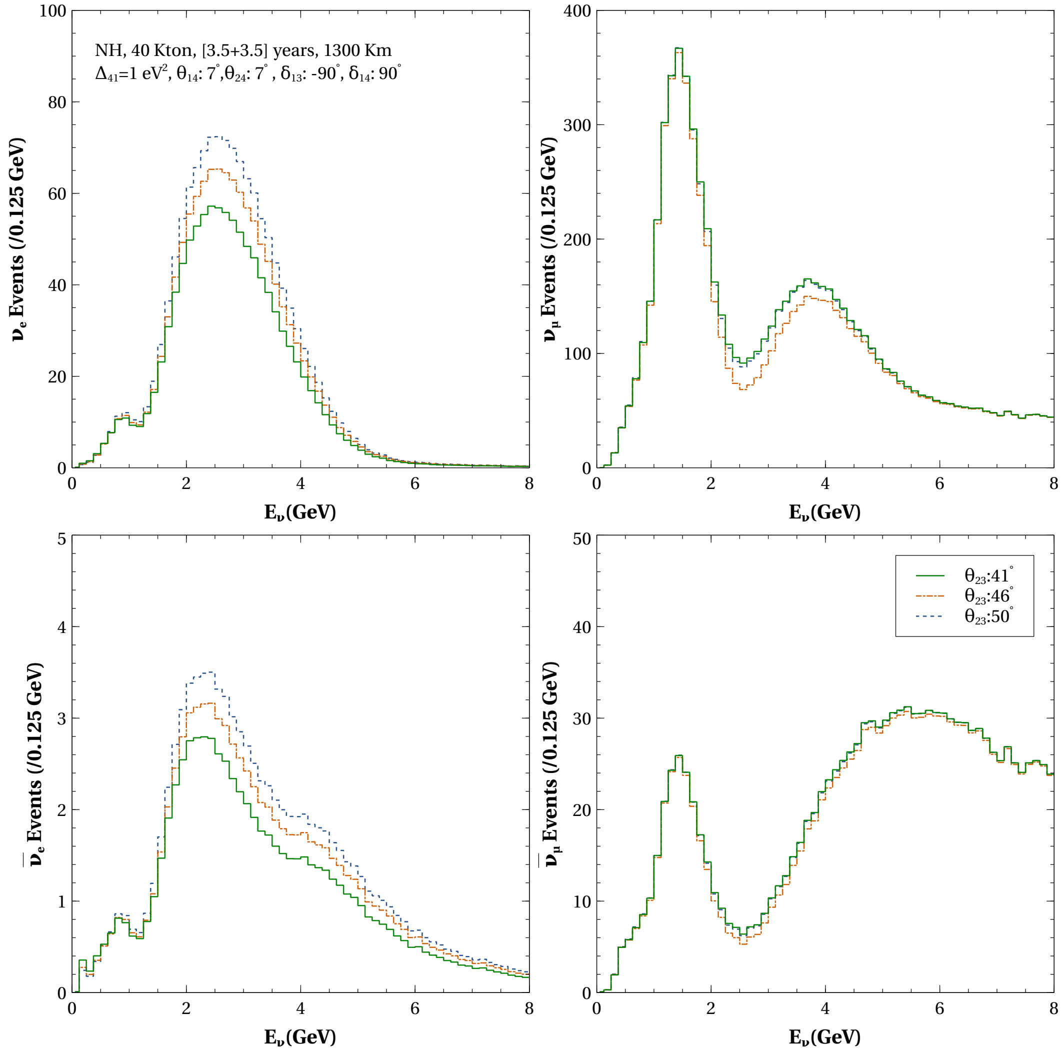

Figure 3.13: Electron (left) and muon neutrino (right) event spectrum for neutrinos (top) and anti-neutrinos (bottom) as a function of energy for true $\theta_{23} = 41°$(green) with true phases $\delta_{13} = -90°, \delta_{14} = 90°$ at 1300 km for test values of $\theta_{23} = 46°$(orange) and $\theta_{23} = 50°$(blue) for NH.

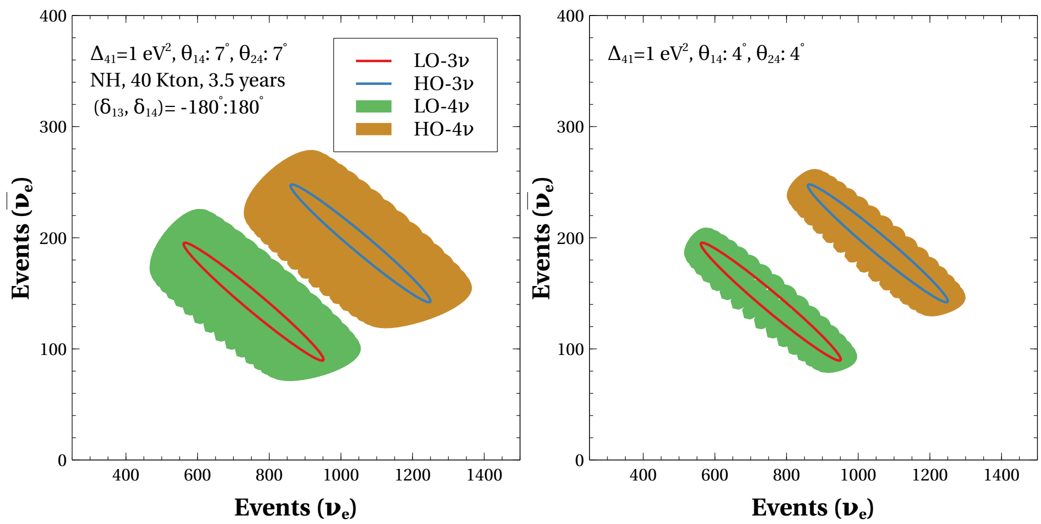

Figure 3.14: Bi-events plot in $\nu_e - \bar{\nu}_e$ plane for $\theta_{23} = 41°$(red, green), 49°(blue, yellow) at 1300 km with variation of phases δ_{13}, δ_{14} corresponding to $\theta_{14}, \theta_{24} = 7°$ (left), 4° (right) for NH.

3.5.2 Events from atmospheric neutrinos

The atmospheric neutrino and anti-neutrino events are obtained by folding the relevant incident fluxes with the appropriate disappearance and appearance probabilities, charge current (CC) cross sections, detector efficiency, resolution, detector mass, and exposure time.

Assumptions of the far detector (LArTPC) parameters are mentioned in table 3.3[169].

Parameter uncertainty	Value
$\mu^{+/-}$ Angular	2.5°
$e^{+/-}$ Angular	3.0°
($\mu^{+/-}$, $e^{+/-}$) Energy	GLB files for each E bin [170]
Detection efficiency	GLB files for each E bin [170]
Flux normalization	20%
Zenith angle dependence	5%
Cross section	10%
Overall systematic	5%
Tilt	5%

Table 3.3: Assumptions of the LArTPC far detector parameters and uncertainties.

Magnetizing the large 40 kt LArTPC detector is difficult and expensive, but the charge id of the muon can be identified using the capture vs decay process of the muon inside the argon as studied previously for the DUNE detector[171]. We have implemented the charge id of the muon as follows: some fraction of the μ^- like events that undergo the capture process are identified using capture fraction efficiency, and the rest of the muons as well as all the μ^+ undergo muon decay. In fig. 3.15, we show the absolute differences of atmospheric events between HO & LO in E_ν-$\cos\theta_\nu$ plane for $\mu^+ + \mu^-$ (left), and $e^+ + e^-$ (right). This clearly shows that the difference is larger at the matter-resonance region as observed from the probability oscillogram plot in fig. 3.3. The electron event spectrum shows a significant difference in the energy range of $2-8$ GeV for $\cos\theta_\nu$ range of $-0.5:-0.9$. The muon events also contribute, especially in a few parts of the energy range $3-8$ GeV for $\cos\theta_\nu$ range of $-0.5:-0.9$. This plot captures the octant sensitivity at different baselines and energies for fixed values of oscillation parameters.

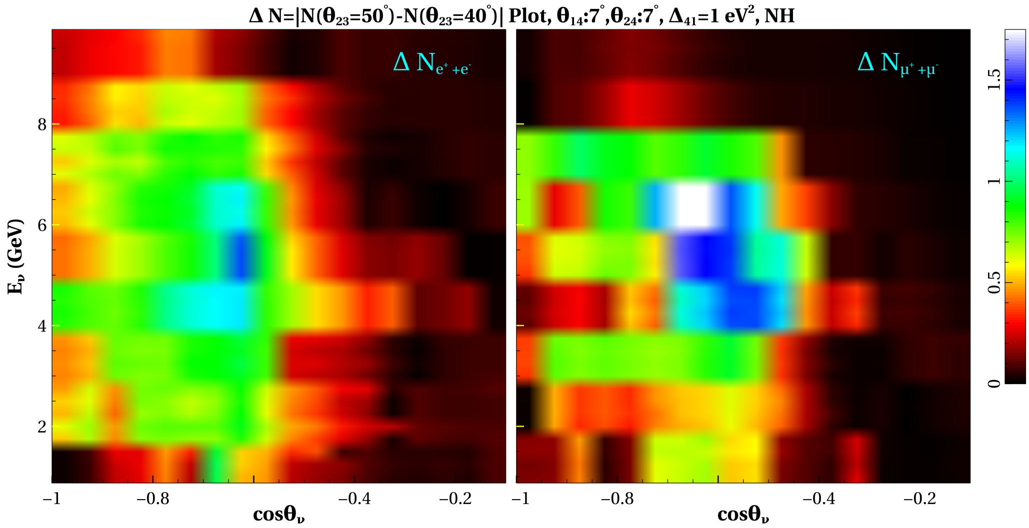

Figure 3.15: The difference of atmospheric events between HO and LO has been plotted in $E_\nu - \cos\theta_\nu$ plane for $e^+ + e^-$(left), and $\mu^+ + \mu^-$(right) events.

3.5.3 χ^2 analysis

The computation of χ^2 is performed using the method of pulls considering various statistical and systematic uncertainties as mentioned in table 3.3. Finally, $\Delta\chi^2$ is marginalized over the oscillation parameters as mentioned in table 5.1.

Parameter	True Value	Marginalization Range
θ_{12}	$33.47°$	N.A.
θ_{13}	$8.54°$	N.A.
θ_{23}	$49°(41°)$	$39° : 44°(46° : 51°)$
θ_{14}, θ_{24} (A)	$7°$	$3° : 9°$
θ_{14}, θ_{24} (B)	$4°$	$0° : 6°$
Δ_{21}	7.42×10^{-5} eV^2	N.A.
Δ_{31}	2.515×10^{-3} eV^2	N.A.
Δ_{41}	1 eV^2	N.A.
δ_{13}, δ_{14}	many	$-180° : 180°$

Table 3.4: True values of all the oscillation parameters and their range of marginalization. Two different sets of θ_{14}, θ_{24} are considered. Set A is according to Global fit. Set B is taken considering MINOS+ bounds.

3.6 Results and Discussion

In this section, we discuss the sensitivity to the octant of θ_{23} and mass ordering in the context of a LArTPC setup, as mentioned in the previous section. We use both accelerator neutrino beam and atmospheric neutrinos for our analysis.

3.6.1 Sensitivity to octant of θ_{23}

The results are demonstrated for beam only, atmospheric only, and a combination of both of these. We also explain the underlying degeneracies through the contour plots of octant sensitivity in $\delta_{13} - \delta_{14}$ test plane. In fig. 3.16, the sensitivity to the octant of θ_{23} degeneracy ($\Delta\chi^2$) has been plotted as a function of true δ_{13} for NH. The marginalised $\Delta\chi^2$ values for true $\theta_{23} = 41°$(blue), $49°$(red) have been shown for true $\delta_{14} = 0°$ (left panel), $90°$ (right panel). The observable points are,

- The sensitivity of θ_{23} is prominently higher for LO as compared to HO for most of the $\delta_{13}^{\text{true}}$ values.
- The $\Delta\chi^2$ vs δ_{13} curve has strikingly different features for different δ_{14}^{true} values as can be seen from the two panels in fig. 3.16.
- For $\delta_{14}^{true} = 0°$ and LO the highest sensitivity comes around $\delta_{13} = \pm 120°$. This feature can be understood from fig. 3.6 which shows that there is no degeneracy in $P_{\mu e}(P_{\bar{\mu}\bar{e}})$ channel at $\delta_{13} = 120°(-120°)$.
- On the other hand for $\delta_{14}^{true} = 90°$ the maximum sensitivity occurs for $\delta_{13} = -90°$. From the red dashed curves depicted in the bottom panels of fig. 3.6, we can see that this sensitivity comes from $P_{\bar{\mu}\bar{e}}$ channel.
- For HO and $\delta_{14}^{true} = 0°$ the octant sensitivity is higher around the range $\delta_{13} = -60° : 60°$. From the solid green curve drawn in the top panels of fig. 3.6, we can see that there is no degeneracy in the range $-120° : 0°(0° : 120°)$ comes from $P_{\mu e}(P_{\bar{\mu}\bar{e}})$ channel with a maximum difference between the HO curve and the LO band occurring at $\delta_{13} = -60°(60°)$.
- In case of $\delta_{14} = 90°$ in HO, the highest sensitivity is at $\delta_{13} = 90°$. From the top panel in fig. 3.6, it can be seen that is no degeneracy in $P_{\bar{\mu}\bar{e}}$ around $\delta_{13} = 90°$.

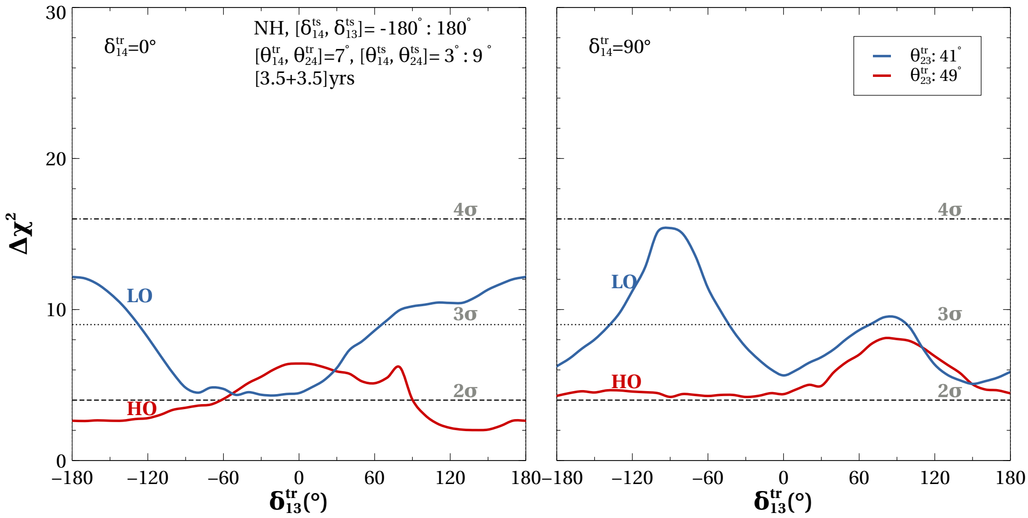

Figure 3.16: Sensitivity to the octant of θ_{23} with beam only analysis as a function of δ_{13}^{true} due to $\theta_{23}^{true} = 41°$ in LO(blue), and 49°in HO(red) for $\delta_{14}^{true} = 0°$ (left), 90° (right).

In the above discussion, we try to explain the salient features of fig. 3.16 in terms of the probabilities plotted in fig. 3.6 for an energy of 2.5 GeV. However, it should be borne in mind that the source has a broadband beam and contributions from other energy bins also influence the $\Delta\chi^2$.

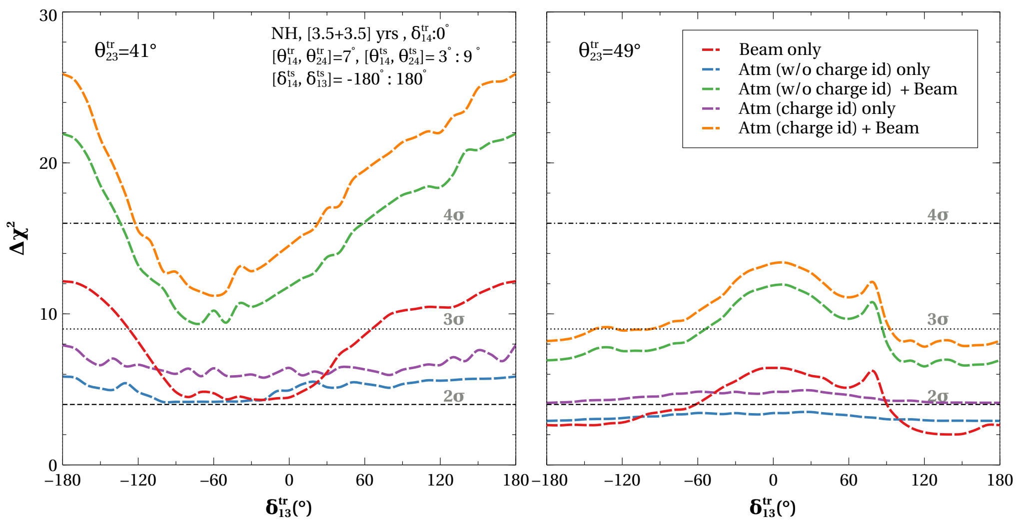

Figure 3.17: Sensitivity to the octant of θ_{23} as a function of $\delta_{13}^{\text{true}}$ at $\delta_{14}^{\text{true}} = 0°$ for $\theta_{23}^{\text{true}} = 41°$ (left) and 49° (right). The representative plots are shown for simulated data from beam only(red), atmospheric only w/o charge-id (blue), atmospheric only with charge-id (violet), beam+atmospheric w/o charge-id(green), and beam+atmospheric with charge-id(yellow) analysis with 280 kt-yr exposure.

In fig. 3.17, we have shown the sensitivity to the octant of θ_{23} for atmospheric neutrinos without and with partial charge id of muon events(blue and violet curves respectively) as well as combining both beam and atmospheric data (green and orange curves) using the 40 kt far detector. In the figure, we also present the $\Delta\chi^2$ for beam only data (red curve). These plots are obtained for true values of $\theta_{23} = 41°$(left), $49°$(right) respectively. Here are the observations from fig. 3.17,

- The sensitivity for atmospheric data is less than 2σ for HO and slightly higher than 2σ for LO for whole $\delta_{13}^{\text{true}}$ parameter space.
- For the case including charge id, the sensitivity increases slightly. In matter $P_{\mu\mu}$, and $P_{\bar{\mu}\bar{\mu}}$ probabilities are very different due to the presence of resonant matter effect in $P_{\mu\mu}$ since we are considering normal hierarchy. This leads to a synergy when neutrino and anti-neutrino χ^2 are added separately, enhancing sensitivity.
- Combining atmospheric and beam data, the sensitivity increases up to more than $4\sigma(3\sigma)$ for LO(HO) depending on the values of δ_{13}^{true}.
- The $\Delta\chi^2$ for atmospheric data has very less dependence on δ_{13}^{true}. Therefore in the combined case, the nature of $\Delta\chi^2$ is mostly dictated by the beam data.

θ_{23}	δ_{14}	Above 2σ	Above 3σ	Above 2σ	Above 3σ
Beam+Atmospheric w/o(with) charge-id				Beam	
True Value		3.5+3.5 Years, $\theta_{14} = 7°, \theta_{24} = 7°$			
41°	0°	100%(100%)	100%(100%)	100%	46%
49°	0°	100%(100%)	38%(53%)	42%	0%
41°	90°	100%(100%)	100%(100%)	100%	32%
49°	90°	100%(100%)	30%(48%)	100%	0%

Table 3.5: The percentages of $\delta_{13}^{\text{true}}$ parameter space that has χ^2 value above $2\sigma, 3\sigma$ for various combination of true values of θ_{23}, δ_{14} and $\theta_{14}, \theta_{24} = 7°$ as seen in fig. 3.16, fig. 3.17.

The percentage of values of $\delta_{13}^{\text{true}}$ for which $\Delta\chi^2$ value of octant sensitivity for true value of $\theta_{14}, \theta_{24} = 7°$ is above 2σ, and 3σ are shown in the above table 3.5.

- The percentage of values of the $\delta_{13}^{\text{true}}$ for which 3σ sensitivity is achieved, is higher for $\theta_{23}^{\text{true}}$ in lower octant than in higher octant.
- The sensitivity for $\theta_{23}^{\text{true}} = 41°$ (LO) is more than 3σ for 46%(32%) values of the $\delta_{13}^{\text{true}}$ for $\delta_{14}^{\text{true}} = 0°(90°)$ with beam only data. However, in case of $\theta_{23}^{\text{true}} = 49°$ (HO)

3σ sensitivity isn't observed for any values of $\delta_{13}^{\rm true}$ as 2σ sensitivity is achieved for 42%(100%) values of the δ_{13}^{true} for $\delta_{14}^{\rm true} = 0°(90°)$.

- For the combination of both the beam and the atmospheric data (w/o charge-id), the sensitivity for $\theta_{23} = 49°$ increases to more than 3σ for 38%(30%) values of the $\delta_{13}^{\rm true}$ while for 41° the whole $\delta_{13}^{\rm true}$ parameter space is allowed.

- When we use the combined data for beam and atmospheric neutrinos with charge-id, the sensitivity improves further to provide more than 3σ for all $\delta_{13}^{\rm true}$ values $\theta_{23} = 41°$ and for 53%(48%) of $\delta_{13}^{\rm true}$ values corresponding to $\delta_{14}^{\rm true} = 0°(90°)$ for $\theta_{23} = 49°$.

In fig. 3.18, the octant sensitivity is depicted as a function of δ_{13}^{true} corresponding to $\theta_{23}^{true} = 41°$ (blue) and 49° (red) for true values of $\theta_{14}, \theta_{24} = 4°$. In the left panel, δ_{14}^{true} is taken as 0°, and in the right panel, it is 90°. The dotted curves denote sensitivity for beam only cases, whereas the dashed ones are for beam + atmospheric(with charge id) cases.

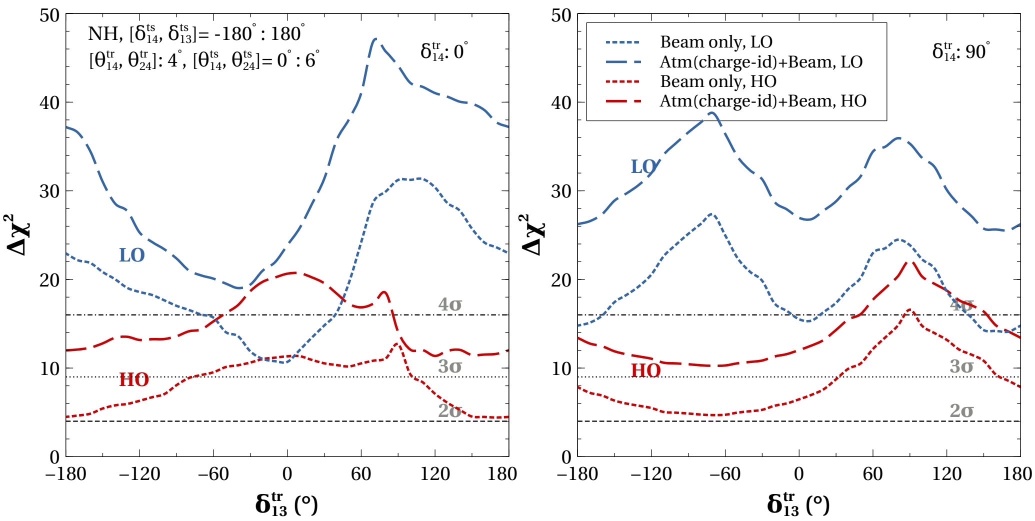

Figure 3.18: Sensitivity to the octant of θ_{23} with beam only (dotted) and beam+atmospheric with charge-id (dashed) analysis as a function of δ_{13}^{true} for true values of $\delta_{14} = 0°$ (left), 90° (right). The representative plots are shown for true values of θ_{23} in HO (red), LO (blue), and $\theta_{14}, \theta_{24} = 4°$.

We observe the following in fig. 3.18,

- An increase in the sensitivity in beam only and beam+atmospheric scenarios compared to the sensitivity obtained for the true value of $\theta_{14}, \theta_{24} = 7°$ (fig. 3.17).

- The sensitivity for $\theta_{23} = 49°$ is more than 3σ irrespective of δ_{13}^{true} values when we consider the beam + atmospheric (with charge-id) analysis.

- For true value of $\theta_{23} = 41°$, the octant sensitivity is greater than 4σ over the full range of δ_{13}^{true}.

The percentage of δ_{13}^{true} values for which more than 2σ, 3σ octant sensitivity for true value of $\theta_{14}, \theta_{24} = 4°$ is achieved have been enlisted in fig. 3.6.

θ_{23}	δ_{14}	Above 2σ	Above 3σ	Above 2σ	Above 3σ
Beam+Atmospheric with charge-id				Beam	
True Value		3.5+3.5 Years, $\theta_{14} = 4°, \theta_{24} = 4°$			
41°	0°	100%	100%	100%	100%
49°	0°	100%	100%	100%	50%
41°	90°	100%	100%	100%	75%
49°	90°	100%	100%	100%	36%

Table 3.6: The percentages of $\delta_{13}^{\mathrm{true}}$ parameter space that has χ^2 value above $2\sigma, 3\sigma$ for various combination of true values of θ_{23}, δ_{14}, and $\theta_{14}, \theta_{24} = 4°$ as seen in fig. 3.18

One of the noteworthy features of a liquid argon detector is its sensitivity to both electron and muon events. In order to explore if there is any synergy between these, we show in fig. 3.19 how the value of χ^2 for octant sensitivity from muon (red) and electron events (blue) varies with $\theta_{23}^{\mathrm{test}}$. These sensitivity curves are obtained using true values of $\theta_{23} = 41°, \delta_{13} = -90°, \delta_{14} = 90°$ for beam (left) and atmospheric (right) neutrinos.

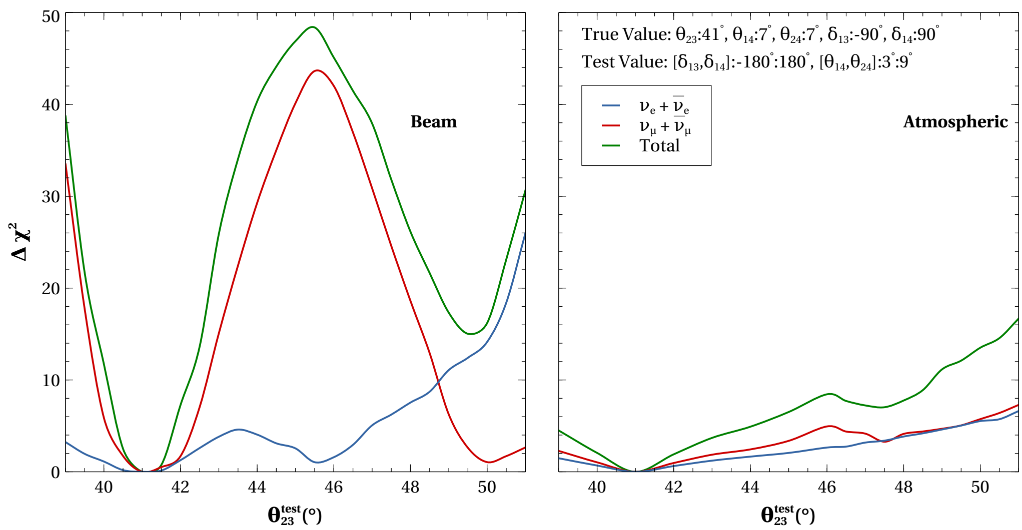

Figure 3.19: Octant sensitivity as a function of $\theta_{23}^{\mathrm{test}}$ from beam (left), and atmospheric (right) neutrinos using 280 kt-yr exposure of LArTPC detector with $\theta_{23}^{tr} = 41°, \delta_{13}^{tr} = -90°, \delta_{14}^{tr} = 90°$.

The observations from fig. 3.19 are as follows,

- In the case of beam neutrinos, the octant sensitivity for appearance channel increases with $\theta_{23}^{\text{test}}$ whereas the sensitivity for disappearance channel mimics the nature of $\sin^2 2\theta_{23}$ with minima at $41°$, and $50°$. This different feature of octant sensitivity for $P_{\mu e}, P_{\mu\mu}$ channels can be seen in fig. 3.13. When we combine these two channels, the position of minimum sensitivity at $\theta_{23}^{\text{test}} = 50°$ is still guided by muon events but due to the rising nature of electron χ^2 a large octant sensitive contribution gets added and increases the overall value of the χ^2.

- For atmospheric neutrinos, both muon and electron χ^2 are similar. The muon χ^2 is dictated by probabilities $P_{\mu\mu}, P_{e\mu}$, and the octant sensitivity coming from these channels is opposite, which dilutes the sensitivity for muons. On the other hand, for electron events, the octant sensitivity comes from only $P_{\mu e}$ since P_{ee} doesn't depend on θ_{23}. Therefore, even though atmospheric ν_μ flux is almost twice as ν_e flux, both muon and electron events can give similar values of χ^2. These features were also noted in three flavor case in [208].

In order to understand the θ_{23}-δ_{13}-δ_{14} degeneracies listed in table 3.2, we have provided the contour plots in δ_{13}-δ_{14} plane showing the regions with octant sensitivity more than 3σ. In fig. 3.20, the 3σ contours are shown for the true value of sterile CP phase $\delta_{14} = 0°$ with four different true values of $\delta_{13} = -90°, 0°, 90°, 150°$. In each panel, the solid (dashed) lines represent the RO (WO) solutions. The blue, yellow (violet, red) correspond to contours from beam only (beam and atmospheric combined) analysis for $\theta_{23}^{true} = 41°, 49°$ respectively.

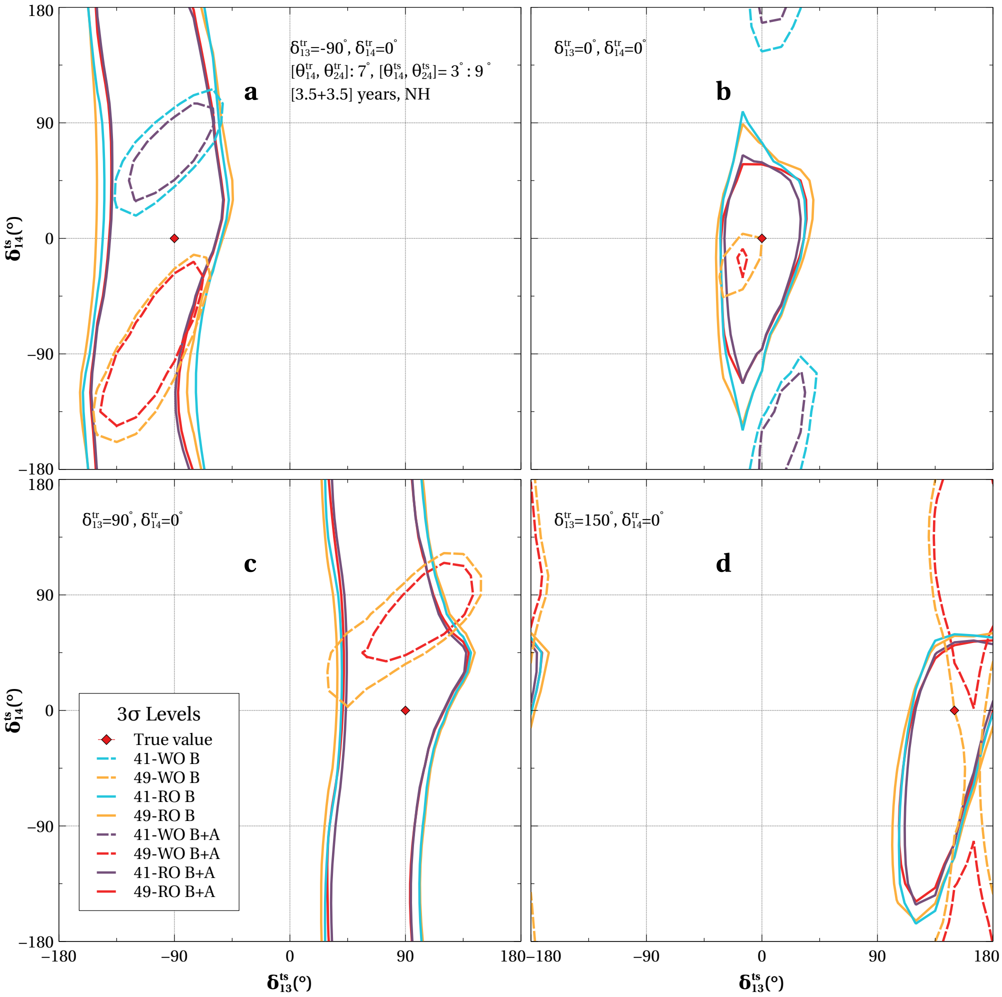

Figure 3.20: 3σ contour plot of sensitivity to the octant of θ_{23} in test $\delta_{13} - \delta_{14}$ plane with 7 years of data for $\delta_{14}^{true} = 0°$ and $\delta_{13}^{true} = -90°, 0°, 90°, 150°$ in panels a,b,c,d respectively. The representative plots are shown for the true value of $\theta_{23} = 41°$ in LO (blue and violet) and 49° in HO (yellow and red) for right octant solutions(solid) and wrong octant solutions(dashed) for simulated beam only (B) and beam+atmospheric (B+A) data.

True δ_{13}	True δ_{14}	Present Degeneracies
$-90°$	$0°$	WO-Rδ_{13}-Wδ_{14}
$0°$	$0°$	WO-Rδ_{13}-Rδ_{14}(49°), WO-Rδ_{13}-Wδ_{14}(41°)
$90°$	$0°$	WO-Rδ_{13}-Wδ_{14}(49°)
$150°$	$0°$	WO-Rδ_{13}-Rδ_{14}(49°), WO-Rδ_{13}-Wδ_{14}(49°)

Table 3.7: The degeneracies for different true value of δ_{13} with true $\delta_{14} = 0°$ as seen in fig. 3.20.

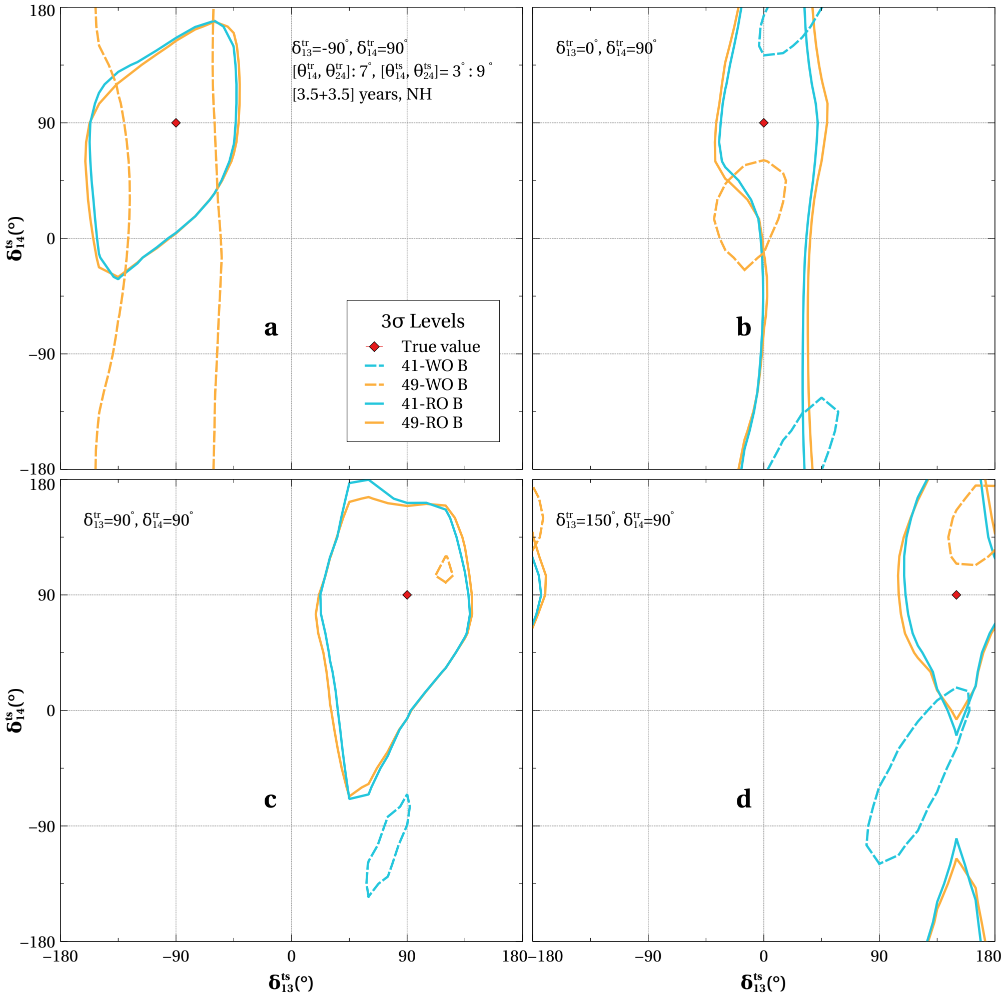

Figure 3.21: 3σ contour plot of sensitivity to the octant of θ_{23} in test $\delta_{13}-\delta_{14}$ plane with 7 years of beam only simulated data for $\delta_{14}^{true} = 90°$ and $\delta_{13}^{true} = -90°, 0°, 90°, 150°$ in panels a,b,c,d respectively. The representative plots are shown for true value of $\theta_{23} = 41°$ in LO (blue) and 49°(yellow) in HO for right octant solutions(solid) and wrong octant solutions(dashed).

True δ_{13}	True δ_{14}	Present Degeneracies
$-90°$	$90°$	WO-Rδ_{13}-Rδ_{14}(49°), WO-Rδ_{13}-Wδ_{14}(49°)
$0°$	$90°$	WO-Rδ_{13}-Wδ_{14}
$90°$	$90°$	WO-Wδ_{13}-Wδ_{14}(49°), WO-Rδ_{13}-Wδ_{14}(41°)
$150°$	$90°$	WO-Rδ_{13}-Wδ_{14}

Table 3.8: The degeneracies for different true value of δ_{13} with true $\delta_{14} = 90°$ as seen in fig. 3.21.

The noteworthy observations from fig. 3.20 are as follows,

- In panel "a", the solid contours spanning the full range of δ_{14} indicate true solutions with poor precision in δ_{14} for both $\theta_{23}^{true} = 41°, 49°$. We also observe dashed contours indicating WO-Rδ_{13}-Wδ_{14} solutions for both θ_{23}^{true}.

- In the panel "b", the precision of the true solutions improves significantly. A small region of WO solutions for $\theta_{23}^{true} = 49°$ occurs adjacent to the true value. We also find WO-Rδ_{13}-Wδ_{14} solutions for $\theta_{23}^{true} = 41°$.

- Comparing the true solutions in panels "c", and "d" but the precision of δ_{14} is notably better in "d". In these panels, WO solutions are present for only $\theta_{23}^{true} = 49°$. For $\theta_{23}^{true} = 41°$, the octant can be determined at more than 3σ sensitivity as seen from the solid blue curve in the left panel of fig. 3.16 and hence WO solutions are not observed. In panel "c" we find WO-Rδ_{13}-Wδ_{14} solution wheres the WO-Rδ_{13} solutions are observed in panel "d".

- Inclusion of atmospheric analysis shrinks all the contours improving octant sensitivity. The choice of δ_{13}^{true} affects the precision of RO solutions as well as the occurrence of degeneracies.

Similarly, we have plotted the 3σ contours in fig. 3.21 showing WO (dashed), and RO (solid) solutions w.r.t. true values of $\theta_{23} = 41°$ (blue), and $49°$ (yellow) for the true value of $\delta_{14} = 90°$ with $\delta_{13} = -90°, 0°, 90°, 150°$ using beam-only analysis. The observations from fig. 3.21 are as follows,

- In panel "a", we see the WO-Rδ_{13} solutions spanning the full range of δ_{14} for only $\theta_{23}^{true} = 49°$. We also find true solutions with notable precision in δ_{14} for both $\theta_{23}^{true} = 41°, 49°$ as compared to panel "a" in fig. 3.20.

- In panel "b", the precision of δ_{14} in true solutions deteriorates w.r.t panel "a" covering the full δ_{14} range. We observe a small region of WO-Rδ_{13}-Wδ_{14} solution for $\theta_{23}^{true} = 49°$, along with a bigger region of WO-Rδ_{13}-Wδ_{14} solution for $\theta_{23}^{true} = 41°$.

- In panels "c" and "d", the true solutions show better precision in δ_{14} as compared to the same panels in fig. 3.20. We can also observe for $\theta_{23}^{true} = 49°$ a tine region of WO-Wδ_{13}-Wδ_{14} in panel "c" while in panel "d" WO-Rδ_{13}-Wδ_{14} solutions occur. There are WO-Rδ_{13}-Wδ_{14} solutions for $\theta_{23}^{true} = 41°$ in both panel "c", and "d" but the region is smaller in "c".

- Overall, we see the precision of the RO true solutions along with the size and type of WO contours depend on δ_{13}^{true} for fixed δ_{14}^{true}.

The most common degeneracies seen in fig. 3.20, fig. 3.21 are WO-Rδ_{13}-Rδ_{14}, WO-Rδ_{13}-Wδ_{14}. It indicates that the presence of δ_{14} creates more problems in precise measurement of the octant of θ_{23}. We also observe true solutions with poor precision in δ_{14}. If we repeat the above analysis for true values of $\theta_{14}, \theta_{24} = 4°$ along with marginalization in the range of $0 - 6°$, the 3σ contours get smaller due to higher octant sensitivity.

The regions under 3σ sensitivity in the contour plots of fig. 3.20, fig. 3.21 can be understood using the difference in the probability plots in $\delta_{13} - \delta_{14}$ plane. We will mainly focus on the dominant $P_{\mu e}$ channel to understand the effect.

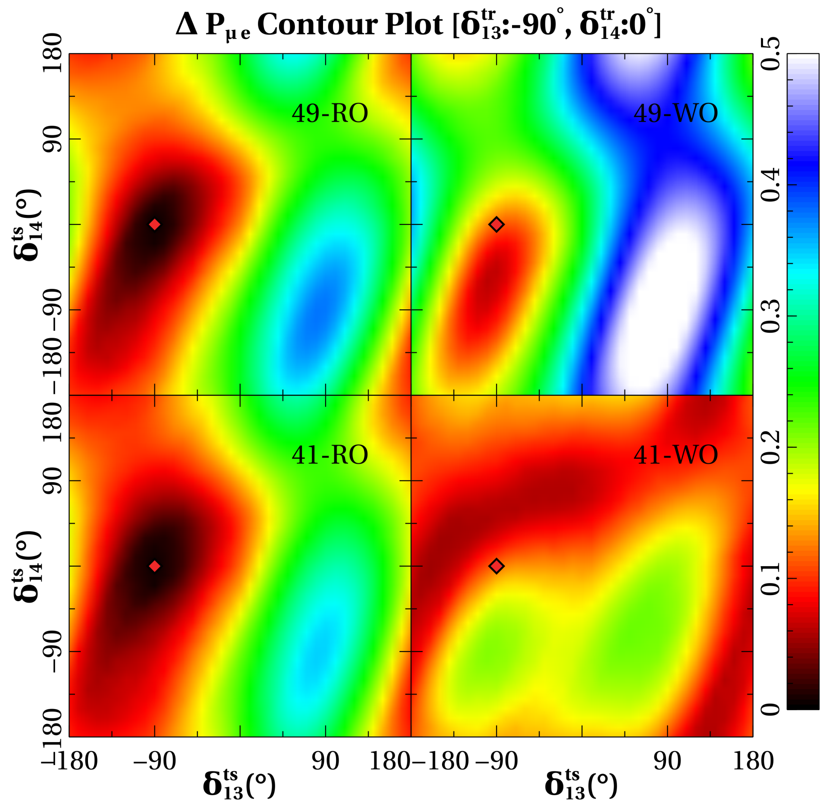

Figure 3.22: Contour plot in test $\delta_{13} - \delta_{14}$ plane showing the difference in probability $\Delta P_{\mu e}$ with θ_{23} being fixed at one octant while θ_{23} varies in the opposite octant for WO solutions (right) and in the same octant for RO solutions (left) at true values of $\delta_{13} = -90°, \delta_{14} = 0°, \theta_{23} = 49°$(top), $41°$(bottom). Black and dark red show the least differences, while blue and white show the highest.

In fig. 3.22, the contour plot in test δ_{13}-δ_{14} plane represents the difference between the probabilities $P_{\mu e}$ of opposite octants while varying the θ_{23} value only in same (left) /opposite (right) octant for the true $\theta_{23} = 49°$(top), $41°$(bottom) with $\delta_{13}^{tr} = -90°, \delta_{14}^{tr} = 0°$ corresponding to panel "*a*" of fig. 3.20. The understandings are as follows,

- First, we consider the right octant solutions in the panels at the left side column. It can be clearly seen that the black and darker red regions around the true value on the left side of $\delta_{13} - \delta_{14}$ plane where the difference in the probability is minimum in fig. 3.22 is similar to the 3σ regions under the *solid* curves in panel "*a*" of fig. 3.20. These darker regions also indicate poor precision of δ_{14}.

- For 49°-WO solution, minima arise in the darker red region, including the true value in the top-right panel of fig. 3.22 similar to the *yellow-dashed* contour in panel "*a*" of fig. 3.20. Similarly, for 41°-WO solutions in the bottom-right panel, the minimum difference is observed in the darker red region just above the true value similar to the *blue-dashed* contour in the panel "*a*" of fig. 3.20. These darker red regions clearly show precise WO-Rδ_{13}-Wδ_{14} degenerate solutions.

3.6.2 Sensitivity to sign of Δ_{31}

Here, we demonstrate the sensitivity to the atmospheric mass ordering in the presence of a sterile neutrino. The sensitivity to the atmospheric mass ordering is probed in the presence of a sterile neutrino corresponding to the mass squared difference of 1 eV^2.

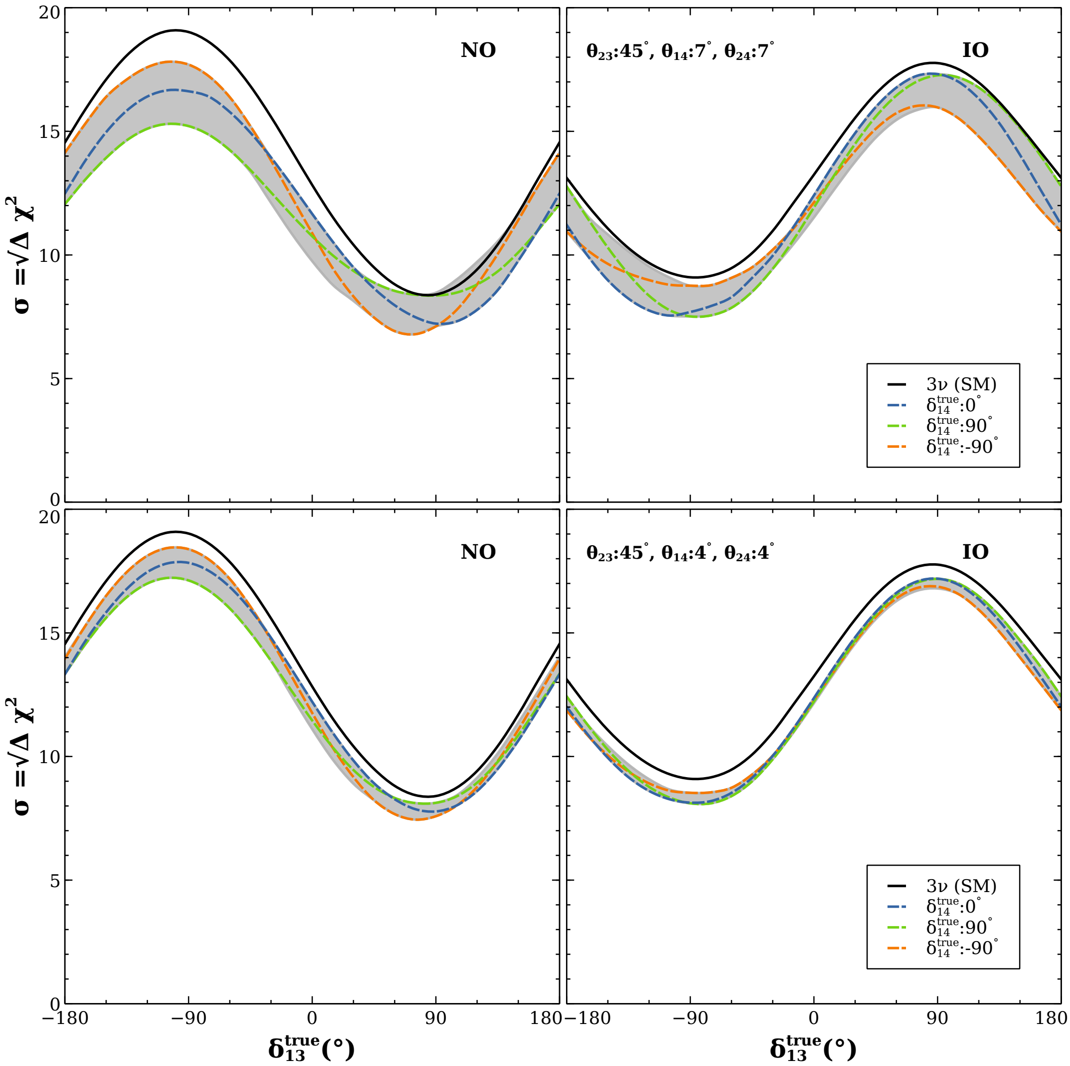

Figure 3.23: The sensitivity to the atmospheric mass ordering as a function of true δ_{13} for various δ_{14}^{true} values at 1300 km baseline considering normal (left), inverted (right) ordering. Grey bands correspond to variation in $\delta_{14}^{\rm true}$.

In fig. 3.23, the sensitivity to the mass ordering (MO),i.e., the sign of Δ_{31}, is presented as a function of δ_{13}^{true} in standard three flavor framework (black) for normal (left) and inverted (right) ordering. We also present the sensitivity in the presence of a sterile neutrino corresponding to SNO-NO (left), and SNO-IO (right) for true values of $\delta_{14} = 0°$(blue), $90°$(green), $-90°$(orange), $180°$(red). We will call $-180° < \delta_{13} \leq 0°$ as the lower half plane and $0° < \delta_{13} \leq 180°$ as the upper half plane throughout this section. The important points to be noted are,

- The sensitivity decreases in the presence of a sterile neutrino compared to the three flavor case.

- The sensitivity for sterile cases depends on the true values of δ_{14}, δ_{13}.
- For $\theta_{14}, \theta_{24} = 4°$, the sensitivity is higher than $\theta_{14}, \theta_{24} = 7°$ and also closer to the standard 3ν case. This is due to the evident fact that the smaller the sterile mixing angles are the 3+1 oscillation framework is more similar to the standard case.
- For NO, in the lower half plane of true δ_{13} the highest sensitivity is observed for $\delta_{14}^{true} = -90°$ (orange) whereas in the upper half plane, same curve gives the lowest sensitivity.
- For IO, $\delta_{14}^{true} = 0°$ (blue) shows the lowest sensitivity in the lower half plane of true δ_{13} and also the highest sensitivity in the upper half-plane.

In fig. 3.24, we present the effect of θ_{34} on sensitivity to the atmospheric mass ordering. In this plot, the sensitivity is shown as a function of true δ_{13} for various combinations of true values of θ_{34}, δ_{34}. We consider $\theta_{34} = 0°$ at $\delta_{34} = 0°$(green dotted), and 7°(blue dot-dashed), 30° (blue solid) at $\delta_{14} = 90°$ along with a sensitivity curve for standard three flavors (black). The observations are as follows,

- The sensitivity decreases more with higher values of θ_{34}.
- The impact of θ_{34} is more in the normal ordering than in the inverted case.
- In the combined analysis of beam and atmospheric data, the sensitivity gets post and provides higher values than standard beam analysis. The decrease in sensitivity due to non-zero θ_{34} then gets compensated.

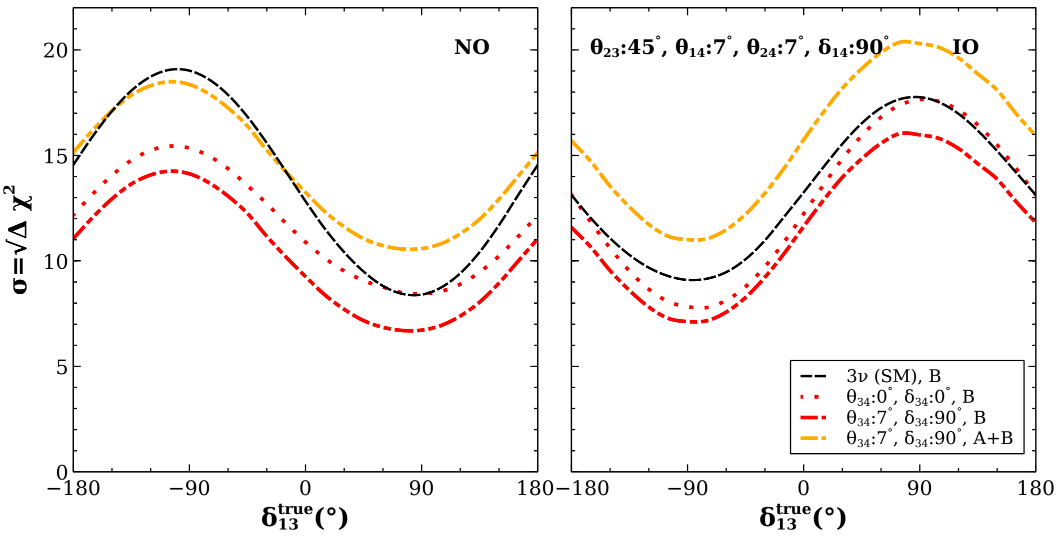

Figure 3.24: The sensitivity to mass ordering as a function of δ_{13}^{true} for various θ_{34}^{true} values for beam neutrinos with 1300 km baseline for normal (left), inverted (right) ordering

Next, we include the atmospheric neutrinos and evaluate the sensitivity of atmospheric mass ordering. In the case of atmospheric neutrinos, we incorporate charge id identification which can partially separate μ^+, μ^- events. In fig. 3.25, the MO sensitivity is shown as a function of true δ_{13} corresponding to the analysis of only atmospheric (blue), only beam neutrinos and a combination of them both (green). The cases with charge identification in both atmospheric only (violet) and combined analysis (orange) are also depicted. The representative sensitivity curves are obtained for $\theta_{14}, \theta_{24} = 7°$, $\delta_{14} = 0°$ corresponding to true hierarchy considered as normal (left) and inverted (right). The observations from fig. 3.25 are following,

- Sensitivity for atmospheric neutrinos doesn't have significant dependence on δ_{13}.
- Although the sensitivity decreases with the inclusion of sterile neutrino w.r.t. standard three flavor (beam only) case, combining atmospheric neutrinos with beam again lifts the sensitivity.
- We observe slightly higher sensitivity when we use partial charge identification for atmospheric neutrinos. This also leads to higher sensitivity for combined analysis.

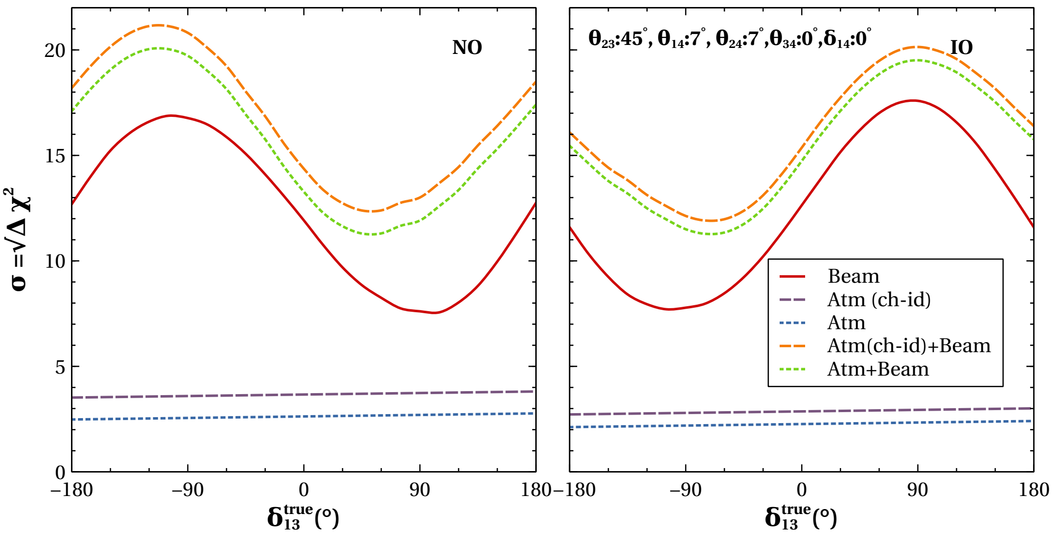

Figure 3.25: Atmospheric mass ordering sensitivity as a function of δ_{13}^{true} corresponding to the analysis of only beam (red), only atmospheric (violet), combined atmospheric+beam (green) neutrinos for normal (left) and inverted (right) hierarchy with 400 kt-yr exposure of LArTPC

3.7 Conclusions

In this work, we expound the possibility of determining the octant of θ_{23}, in the 3+1 framework, assuming the presence of an extra sterile neutrino in addition to the three standard ones. We present our results for a beam based long baseline experiment as well as for atmospheric neutrinos considering a LArTPC detector. We also do a combined analysis of both beam and atmospheric neutrinos and probe the synergies between these two options, which can result in an enhanced sensitivity. For the beam neutrinos, the typical baseline considered in our study is 1300 km which is similar to that proposed by the DUNE collaboration. We provide the analytic expressions for oscillation probabilities in the presence of an extra sterile neutrino using the approximation that the mass squared difference Δ_{21} is zero. We show that these expressions match well with the numerical probabilities, especially in the resonance region.

We study in detail the different parameter degeneracies, emphasizing especially the influence of the phases δ_{13}, δ_{14} in the determination of octant of θ_{23}. This is done by plotting the probability curves for two different θ_{23} values belonging to the opposite octants– (i) as a function of δ_{13}/δ_{14} for fixed energy and baseline, (ii) as a function of energy, for varying δ_{13}, δ_{14} at fixed baselines. We also illustrate (iii) the difference in the appearance and disappearance probabilities for two values θ_{23} belonging to opposite octants in the $\cos\theta_\nu - E$ plane.

We perform a χ^2 analysis and show that for a set of true values of sterile parameters, one can achieve more than 3σ octant sensitivity depending upon the true value of δ_{13} using beam neutrinos. The representative true values of the sterile neutrino parameters considered by us correspond to $\Delta_{41} = 1$ eV^2, $[\theta_{14}, \theta_{24}] = 7°$ and $4°$, $\delta_{14} = 0°$, and $90°$, $\theta_{34} = 0°$. For true values of $\theta_{14}, \theta_{24} = 7°$, $\theta_{23} = 41°(49°)$, and $\delta_{14} = 90°$ one gets more than 3σ sensitivity for 51%(18%) of the δ_{13}^{true} space. On the other hand for true values of $\theta_{14}, \theta_{24} = 4°$, the sensitivity for $\theta_{23} = 41°(49°)$, and $\delta_{14} = 90°$ reaches more than 3σ sensitivity for 75%(36%) of the δ_{13}^{true} space. It can be noted that greater sensitivity is obtained when true values of θ_{14}, θ_{24} are smaller.

In case of $\theta_{14}, \theta_{24} = 7°$, combining the beam and the atmospheric neutrinos (with charge-id), we can obtain 3σ sensitivity in the 100%(48%) of the δ_{13}^{true} space for $\theta_{23} = 41°(49°), \delta_{14} = 90°$. However, the sensitivity for $\theta_{23} = 41°(49°), \delta_{14} = 90°$ is over 3σ for entire range of δ_{13}^{true} when $\theta_{14}, \theta_{24} = 4°$.

At fixed hierarchy, there can be a total of 8-fold degeneracies (Table 3.2) with at least one of the parameters - octant of θ_{23}, δ_{13}, δ_{14} assuming a wrong value. We also identify the extra degeneracies due to the presence of δ_{14} assuming the normal hierarchy and summarise these in table 3.7, and table 3.8. We can conclude that the presence of the phase δ_{14} leads to the occurrence of new degeneracies that hinders the discovery of the octant of θ_{23} precisely.

The sensitivity of atmospheric mass ordering (MO) for $\Delta_{41} = 1$ eV^2 gets diminished w.r.t. to the 3ν case in the presence of a sterile neutrino with the decrement being higher for larger values of θ_{14}, θ_{24} and also dependent on δ_{13}, δ_{14}. The sensitivity to MO decreases further in the presence of non-zero θ_{34}. However, with the combined analysis of beam and atmospheric neutrino, we are able to recover the sensitivity over 10σ irrespective of the choice of true values of δ_{13}, δ_{14}.

In summary, the combination of the beam and the atmospheric neutrinos provides promising results using a LArTPC detector in the presence of an eV scale sterile neutrino.

"Where the mind is without fear and the head is held high;

Where knowledge is free

Where the world has not been broken up into fragments by narrow domestic walls"

Rabindranath Tagore

4

Effect of a very light sterile neutrino on mass ordering and octant of θ_{23}

In this chapter, we explore the effects of very light sterile neutrinos corresponding to $10^{-4}-10^{-1}$ eV^2 on the mass orderings and octant of θ_{23}. We obtain the sensitivity to the sign of Δ_{41} and Δ_{31} along with octant of θ_{23} in a LArTPC using beam neutrinos with the detector at a baseline of 1300 km as well as atmospheric neutrinos. This chapter is based on [222].

4.1 Introduction: a light sterile neutrino

The next-generation experiments open up the door to explore beyond standard model (BSM) physics, which can occur at a sub-leading level. In the previous chapter, we have discussed one such scenario of an eV scale light sterile neutrino scenario motivated by three long-standing anomalies observed in the LSND[142, 223], MiniBooNE experiment [224, 225] and radio-chemical gallium experiments [226–228]. In this chapter, we have considered very light sterile neutrinos at sub-eV energy scales.

A sterile neutrino is a neutral SU(2)×U(1) singlet with no ordinary weak interaction except those induced by the mixing. Very heavy sterile neutrinos ($10^{14} - 10^{16}$ GeV) are proposed as the mediators in the type I seesaw model[229–231] which can give rise to small neutrino masses. They also play a significant role in leptogenesis[232, 233]. Such neutrinos are natural candidates in grand unified theories. Sterile neutrinos of TeV energies have also been studied in the context of low-scale seesaw models[234, 235]. Sterile neutrinos of keV mass are especially interesting because the sterile neutrinos would be a viable dark matter candidate[236].

Can there be sterile neutrinos lighter than the eV scale? In the presence of a sterile neutrino, there is a new mass squared difference $\Delta_{41} = m_4^2 - m_1^2$. A very light sterile neutrino corresponding to the mass-squared difference in ranges $10^{-4} - 0.1$ eV^2 is expected to be consistent with cosmological mass bounds. It was suggested in ref. [237] that the existence of a very light ($\approx 10^{-5} eV^2$) sterile neutrino can provide the explanation for the lack of upturn in the solar neutrino oscillation probability below ≈ 8 MeV. A recent study has probed the possibility of alleviating the tension between the results of the ongoing beam experiments, T2K and NOνA for the value δ_{cp} using very light sterile neutrino with a wide mass difference range of $10^{-5} : 0.1$ eV^2[238].

We focus our study on only one sterile neutrino added to the three light neutrinos, namely the 3+1 framework, and consider a wide mass range for $|\Delta_{41}|$ varying in the range of $10^{-4} - 1$ eV^2. The cosmological constraints on the sum of all the neutrino masses imply that the sign of Δ_{41} can not be negative for $\Delta_{41} > 0.1$ eV^2. However, both signs of Δ_{41} are possible for lower mass squared differences. In this work, we investigate the possibility of determining (i) the sign of Δ_{31} in the presence of a sterile neutrino corresponding to Δ_{41} in the range of $10^{-4} - 0.1$ eV^2; (ii) the sign of Δm_{41}^2 for the mass range $10^{-4} - 0.1$ eV^2. To answer these questions, we use a liquid argon time projection chamber (LArTPC) capable of detecting both beam and atmospheric neutrinos. The typical baseline we have used for the beam neutrinos is $\sim$ 1300 km, similar to the DUNE experiment. We delineate the sensitivities to mass ordering by performing a combined analysis of beam and atmospheric neutrinos, along with a separate study for each. Additionally, we present the results, including the charge tagging capability of muon capture in liquid argon, allowing one to differentiate between μ^+ and μ^- events in the context of atmospheric neutrinos.

The implications of light sterile neutrino in the context of reactor experiments with medium baseline like Double Chooz, Daya Bay, and RENO have been performed in [239]. The mass ordering in the presence of a light sterile neutrino has been studied in ref. [215] with the additional mass squared difference varying in a wide range in the context of a magnetized iron calorimeter detector proposed by the India-based Neutrino Observatory (INO) collaboration. There are other studies related to sterile neutrino with eV scale mass[240–245]. Recently, the sensitivity of the sterile mass ordering in the same mass range has been studied in reference [246] in the context of the DUNE experiment using beam neutrinos. We perform our study in the context of a liquid argon time projection chamber detector as in DUNE, using both beam and atmospheric neutrino events separately as well as in a combined analysis.

The plan of this chapter is as follows. In section 4.2, we present the 3+1 framework which is used for the analysis. In section 4.3 we present the probability level study of $P_{\mu e}$, $P_{\mu\mu}$ in the presence of a sterile neutrino and explore the effect of sterile mixing and point out where these effects will be significant. Simulation procedure used both for the neutrinos coming from the beam and atmosphere, detector specification, and numerical analysis are given in section 4.4. Next, in section 4.5, we present and discuss the results. Finally, we conclude in section 4.6.

4.2 Mass orderings in the 3+1 framework:

The 3+1 oscillation framework has been discussed in the previous chapter. In the presence of a very light sterile neutrino, there is an additional independent mass-squared difference Δ_{41}. The sign of both Δ_{31}, Δ_{41} are unknown. The possible mass orderings, in this case, are shown in Figure 4.1. There can be four possibilities,

(i) SNO-NO: where $\Delta_{41} > 0$ and $\Delta_{31} > 0$. The positioning of the 4th state depends on the value of $|\Delta_{41}|$. For $|\Delta_{41}| > 10^{-3}$ eV^2 the 4th state lies above the 3rd state while if it is $< 10^{-3}$ eV^2 it lies below the 3rd state.

(ii) SNO-IO: in this case $\Delta_{41} > 0$ and $\Delta_{31} < 0$ corresponding to Inverted ordering of the light active neutrinos. In this case, the 4th state lies above the three active states with positioning depending on the value of $|\Delta_{41}|$.

(iii) SIO-NO: this corresponds to $\Delta_{41} < 0$ and $\Delta_{31} > 0$. The 4th state will always lie below the lightest. active states with the placement depending on the value of $|\Delta m^2_{41}|$.

(iv) SIO-IO: for this case both Δ_{41} and Δ_{31} are < 0. For $|\Delta_{41}| < 10^{-3}$ eV^2, the 4th state lies above m_3.

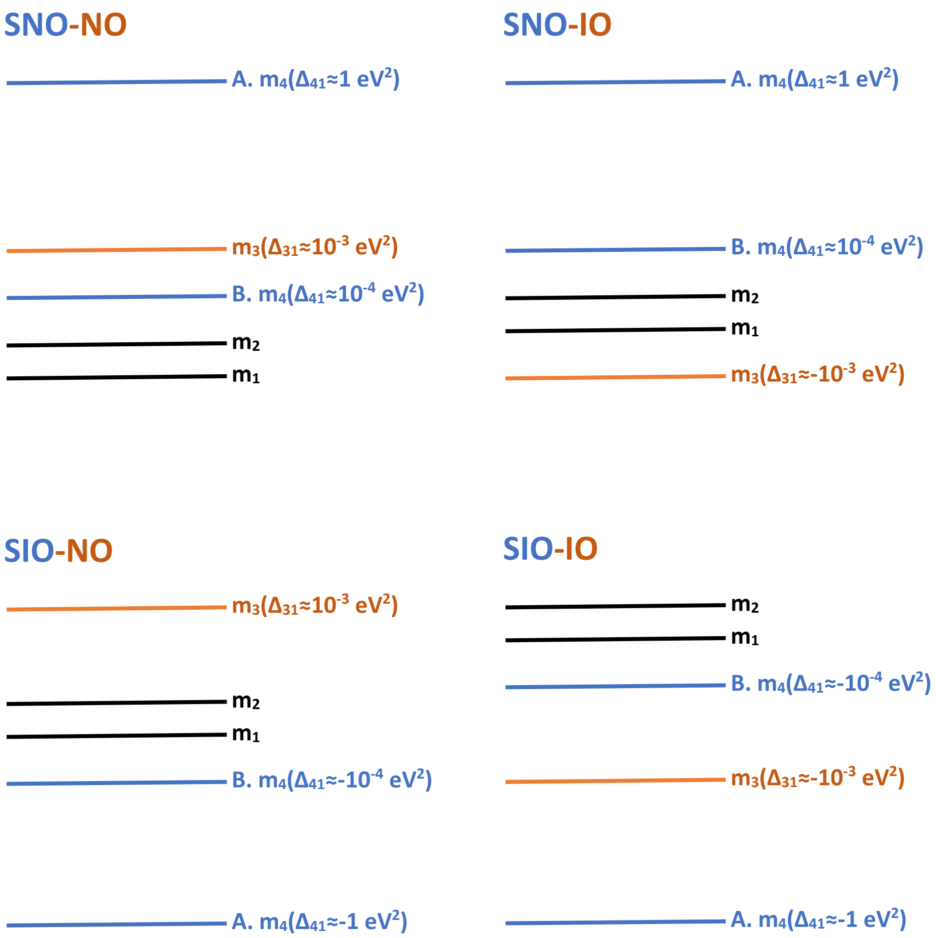

Figure 4.1: The 3+1 mass spectrum: mass ordering in the presence of an extra sterile neutrino state m_4 (blue) corresponding to two different sterile mass squared difference: A. $|\Delta_{41}| \sim 1$ eV^2, B. $|\Delta_{41}| \sim 10^{-4}$ eV^2 when the standard mass ordering Δ_{31} lead by m_3 (red) can be both +ve and -ve.

Note that the usual 3+1 picture corresponds to the cases (i) and (ii) with $\Delta m^2_{41} \sim$ eV^2. The Cases (iii) and (iv) with $\Delta m^2_{41} \sim$ eV^2 are disfavored from cosmology,

4.3 Probability level analysis

The appearance probability calculated using $\alpha - s_{13}$ approximation in [246] is well suited for any Δ_{41} value and at 1300 km and can be expressed as,

$$\begin{aligned} P_{\mu e}^{m} = 4s_{13}^2 s_{23}^2 \frac{\sin^2[(A'-1)\Delta]}{(A'-1)^2} + 8\alpha s_{13}s_{12}c_{12}s_{23}c_{23}\frac{\sin[A\Delta]}{A'}\frac{\sin[(A'-1)\Delta]}{A'-1}\cos(\Delta+\delta_{13}) \\ +4s_{13}s_{14}s_{24}s_{23}\frac{\sin[(A'-1)\Delta]}{A'-1}[P_{14}^{s}\sin\delta'_{14} + P_{14}^{c}\cos\delta'_{14}] \end{aligned}, \tag{4.1}$$

where the terms corresponding to sterile neutrino are,

$$\begin{aligned} P_{14}^{s} &= R[\frac{1}{2}A'c_{23} + (R-1)(1+s_{23}^2)]\frac{\sin[(R-1+\frac{A'}{2})\Delta]}{R-1+\frac{A'}{2}}\frac{\sin[(R-\frac{A'}{2})\Delta]}{R-\frac{A'}{2}} \\ &+ Rc_{23}^2\sin[(R-1-\frac{A'}{2})\Delta]\frac{\sin[(R+\frac{A'}{2})\Delta]}{R+\frac{A'}{2}} \end{aligned} \tag{4.2}$$

$$\begin{aligned} P_{14}^{c} &= \frac{R}{R-\frac{1}{2}}\Bigg([R-\frac{1}{2}s_{23}^2-\frac{1}{2}]\cos[(R-1-\frac{A'}{2})\Delta]\frac{\sin[(R-\frac{A'}{2})\Delta]}{R-\frac{A'}{2}} \\ &+s_{23}^2(R-1)\cos[(R-\frac{A'}{2})\Delta]\frac{\sin[(R-1+\frac{A'}{2})\Delta]}{R-1+\frac{A'}{2}} + s_{23}^2\frac{\sin[(A'-1)\Delta]}{A'-1}\Bigg), \\ &+ Rc_{23}^2\cos[(R-1+\frac{A'}{2}\Delta]\frac{\sin[(R+\frac{A'}{2})\Delta]}{R+\frac{A'}{2}} \end{aligned} \tag{4.3}$$

and $A' = \frac{A}{\Delta_{31}}$, $R = \frac{\Delta_{41}}{\Delta_{31}}$, $\Delta = \frac{1.27\Delta_{31}L}{E}$, $\delta'_{14} = \delta_{13} + \delta_{14}$ and $c_{ij} \sim \cos\theta_{ij}, s_{ij} \sim \sin\theta_{ij}$. at limit $R >> 1$, for $R >> \frac{A'}{2}$, approximately $R - \frac{A'}{2} \simeq R + \frac{A'}{2} \simeq R$, also $R - \frac{1}{2} \simeq R$, $R - \frac{1}{2}s_{23}^2 - \frac{1}{2} \simeq R$

$$P_{14}^{s} \simeq \frac{1}{2}A'c_{23}\frac{\sin[(R-1)\Delta]}{R-1}\sin[R\Delta] + 2\sin[(R-1)\Delta]\sin[R\Delta] \simeq (\frac{1}{2R}A'c_{23}+2)\sin[R\Delta]^2 \tag{4.4}$$

$$\begin{aligned} P_{14}^{c} &\simeq (1+c_{23}^2)\cos[(R-1)\Delta]\sin[R\Delta] + s_{23}^2\cos[R\Delta]\sin[(R-1)\Delta] + s_{23}^2\frac{\sin[(A'-1)\Delta]}{A'-1} \\ &\simeq \sin[2R\Delta] + s_{23}^2\frac{\sin[(A'-1)\Delta]}{A'-1} \end{aligned} \tag{4.5}$$

4.3.1 Effect of sterile parameters on sign of Δ_{31}

In this subsection, the sensitivity for the sign of Δ_{31} has been looked into at various values of the sterile mass squared difference Δ_{41}, considered over a range of 10^{-4} : 1 eV^2. To understand the effect of Δ_{41} on sensitivity to atmospheric mass ordering, we check the difference in appearance probability $\Delta P_{\mu e}$. We consider the minimum difference $\Delta P_{\mu e}$ by fixing $P_{\mu e}$ for a particular sign of Δ_{31} with constant δ_{13}, δ_{14} and varying the phases and Δ_{31} for the probability for the opposite sign of Δ_{31}. The phases are varied over their full range, and for Δ_{31}, the current 3σ range is considered.

$$\Delta P_{\mu e} = |P_{\mu e}^{true}(\Delta_{31}, \delta_{13}, \delta_{14}) - P_{\mu e}^{test}(-\Delta'_{31}, \delta'_{13}, \delta'_{14})|_{min} \tag{4.6}$$

In fig. 4.2, we illustrate the difference $\Delta P_{\mu e}$ (using GLoBES) due to the change in sign of Δ_{31} in the $\Delta_{41} - E_\nu$ plane at 1300 km. In the panels of this figure, the label SNO-NO refers to the true value with $\Delta_{41} = +ve$, $\Delta_{31} = +ve$. The observations are as follows,

- Around $\Delta_{41} = 2.5 \times 10^{-3}$ eV^2, we see either very high or low values of $\Delta P_{\mu e}$
- We observe an oscillating pattern of $\Delta P_{\mu e}$ along Δ_{41} for a fixed energy. This oscillation becomes rapid at higher Δ_{41} values.
- Significant contribution to $\Delta P_{\mu e}$ is seen for energies in the range of $1.5 - 4$ GeV.
- For the SNO-NO case (top panels), the occurrence for maxima and minima reverses for $\delta_{13} = 90°$, and $-90°$.
- However, for the SNO-IO case, the maxima and minima occur at the same Δ_{41} for $\delta_{13} = 90°, -90°$. Although, the magnitude is higher for $\delta_{13} = 90°$.

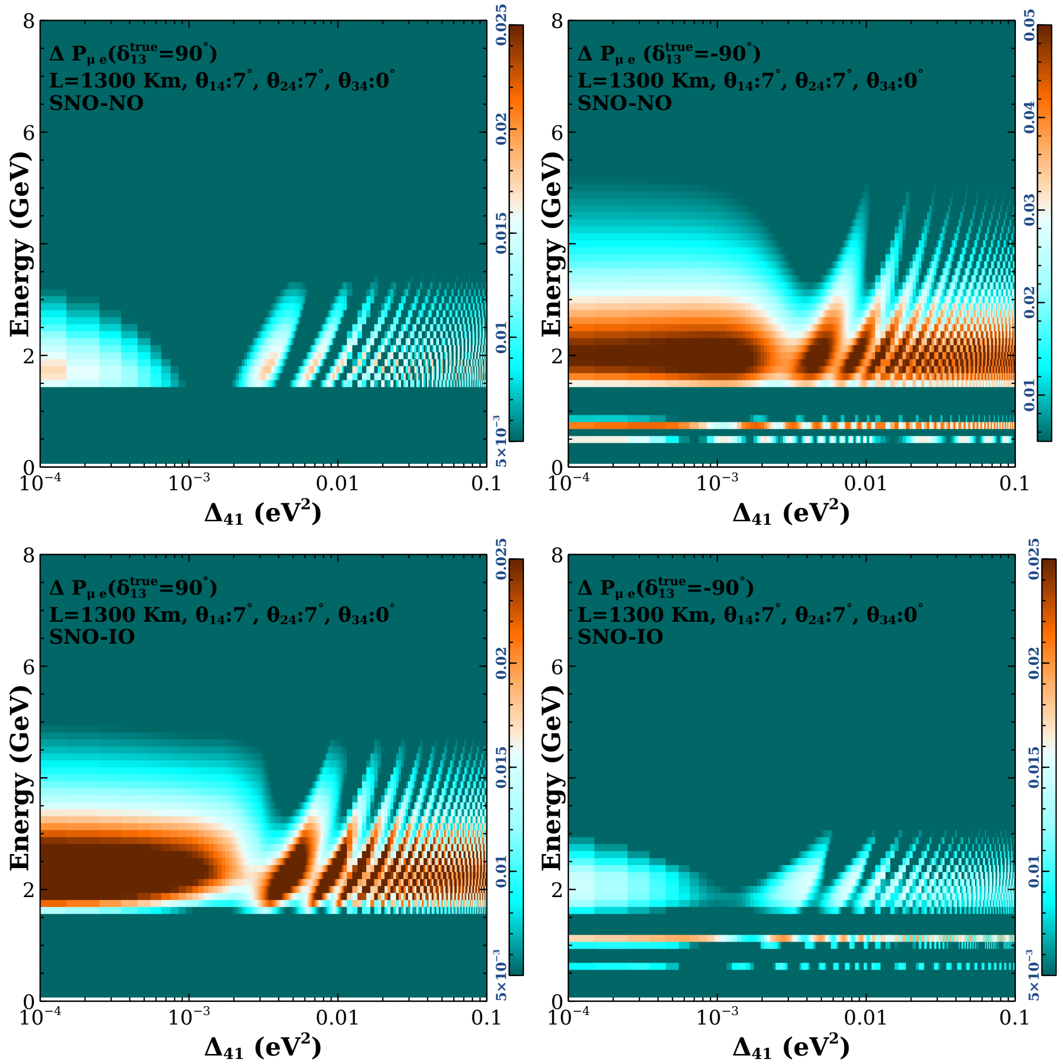

Figure 4.2: Difference in appearance channel probability $\Delta P_{\mu e}$ for different atmospheric mass orderings as a function of Δ_{41}^{true} and E_ν at 1300 km baseline for SNO-NO (above) and SNO-IO (below).

4.3.2 Effect on sign of Δ_{41} in $P_{\mu e}$ channel

As we consider Δ_{41} in the rage 5×10^{-4} : 10^{-1} eV^2, the sterile mass ordering also becomes unknown, giving us four possibilities depending on the ordering of the three active states as discussed in section 2 from fig. 4.1. Therefore, in this section, we study how to determine the sterile mass ordering. We define the difference in the probability for different signs of the sterile mass squared difference $|delta_{41}$ with the probability being fixed for one sign of Δ_{41} and varies for the other sign as,

$$\Delta P_s = |P_{\mu\alpha}^{true}(+\Delta_{41}, \delta_{13}, \delta_{14}) - P_{\mu\alpha}^{test}(-\Delta_{41}', \delta_{13}', \delta_{14}')|_{min} \quad (4.7)$$

The value of ΔP_s marginalized over phase δ_{14} with other oscillation parameters fixed gives us an idea about the sensitivity to the sterile mass hierarchy coming from the appearance channel. We investigate the difference in probability ΔP_s for appearance (left) and disappearance channel(right) over a wide range of the sterile mass squared difference and neutrino energy in fig. 4.3 for $\theta_{14}, \theta_{24} = 7°$, $\delta_{13} = -90°$ at 1300 km baseline (top) and 7000 km (bottom). It can be observed that the high values of ΔP_s are mostly concentrated in the mass square range of $10^{-3} : 10^{-2}$ eV^2 range. In $P_{\mu e}$ channel, the contribution is lower than $P_{\mu\mu}$. The difference is observed to be larger at higher baselines.

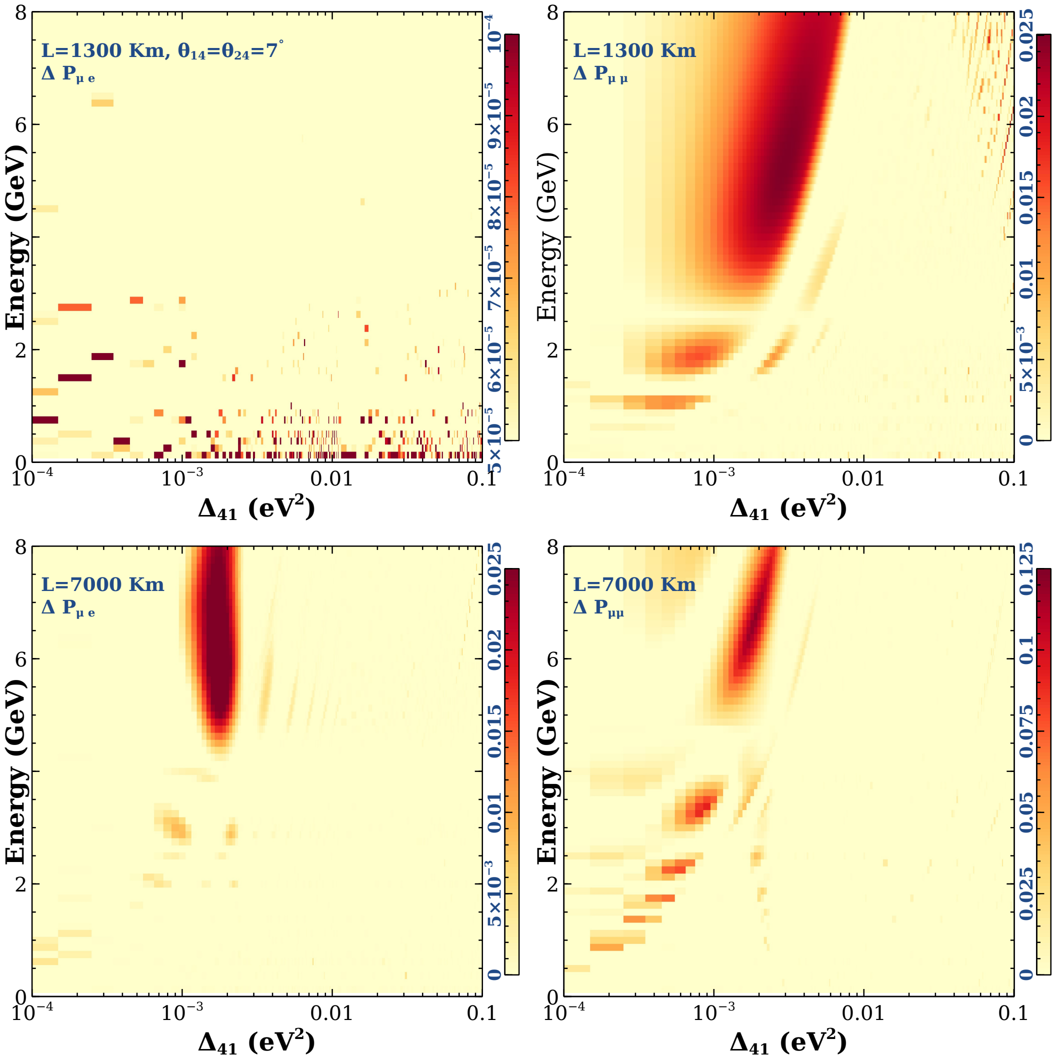

Figure 4.3: Difference in appearance probability $\Delta P_{\mu e}$ (left), and disappearance probability $\Delta P_{\mu\mu}$ (right) for different sterile mass ordering in the $\Delta_{41} - E_\nu$ plane at 1300 km (top), 7000 km(bottom).

Higher difference is observed around $\Delta_{41} = 1 - 2 \times 10^{-3}$ eV^2 while a dip is found immediately after around $\Delta_{41} = 2.5 - 3 \times 10^{-3}$ eV^2 in $P_{\mu e}$ channel. In $P_{\mu\mu}$ channel below 4 GeV, a similar pattern is observed. However, at higher energies, we observe a region of high ΔP value in the range $1 - 6$ eV^2 for 1300 km, and $1 - 3$ eV^2 at 7000 km. For 1300 km, above 4 GeV, the no of beam events is low, leading to a smaller contribution towards sensitivity. In the case of a higher baseline of 7000 km, the atmospheric events are significant at higher energies and contribute to sensitivity.

4.4 Simulation procedure and the experimental details

The experimental setup under consideration consists of a megawatt-scale muon neutrino beam source accompanied by a near detector (ND) and a far detector(FD). The ND will be placed close to the source of the beam, while the FD, comprising a 40 Kton LArTPC detector, is placed at a distance of 1300 km away from the neutrino source. The large LArTPC at an underground observatory is also capable of observing atmospheric neutrinos. The proposed DUNE experiment has a similar experimental configuration[170]. In this analysis, both neutrino beams coming from the accelerator and the atmospheric neutrinos have been considered.

A beam-power of 1.2MW leading to a total exposure of 10×10^{21} pot has been implemented for the numerical analysis. The neutrino beam simulation has been carried out using the GLoBES[103] software. We assume the experiment to be running for 3.5 years each in the neutrino mode and the antineutrino mode.

We use the pull method to calculate χ^2 using the systemic uncertainties specified in table 3.3. Finally, we marginalize the χ^2 over the allowed range of the oscillation parameters as mentioned in table 4.1. For the combined analysis, we add the chi-square for beam and atmospheric and then marginalize over the oscillation parameters. The marginalization has been performed in $\theta_{23}, \theta_{14}, \theta_{24}, \delta_{13}, \delta_{14}$ over the range specified in table 4.1 for all cases unless otherwise mentioned.

Parameter	True Values	Marginalization Range
θ_{12}	$33.47°$	N.A.
θ_{13}	$8.54°$	N.A.
θ_{23}	$45°$	$39° : 51°$
θ_{14}, θ_{24}	$7°$	$0° : 10°$
θ_{34}	$0°, 7°, 15°$	$0° : 17°$
Δ_{21}	7.42×10^{-5} eV^2	N.A.
Δ_{31}(NO)	2.5×10^{-3} eV^2	$-(2.42 : 2.62) \times 10^{-3}$ eV^2
Δ_{31}(IO)	-2.5×10^{-3} eV^2	$(2.42 : 2.62) \times 10^{-3}$ eV^2
Δ_{41} (for MO)	1 eV^2	N.A.
Δ_{41} (for SMO)	$0.0005 : 0.01$ eV^2	$\pm 15\%$ of $-\Delta_{41}$
δ_{13}	many	$-180° : 180°$
δ_{14}	$0°, 90°, -90°$	$-180° : 180°$

Table 4.1: The table depicts true values of all the parameters and their range of marginalization as used in our analysis.

4.5 Numerical Results and Discussions

In this section, we present the results for the analysis of beam only, a combination of beam and atmospheric data in the following scenarios,

- determination of the sign of Δ_{31} in the range of $\Delta_{41} = 5 \times 10^{-4} : 0.1$ eV^2
- determination the sign of Δ_{41} when it's value lies in the range of $5 \times 10^{-4} : 0.1$ eV^2
- probing the octant sensitivity when the range of $\Delta_{41} = 5 \times 10^{-4} : 0.1$ eV^2.

Sensitivity of the sign of Δ_{31} for $\Delta_{41} = 10^{-4} : 10^{-1}$ eV^2

In this section, we study how the sensitivity to the sign of Δ_{31} behaves with Δ_{41} where the latter varies in the range of $10^{-4} : 10^{-1}$ eV^2. Note that for $\Delta_{41} \sim 1$ eV^2, only SNO-NO, and SNO-IO cases are cosmologically allowed. However, for $\Delta_{41} = 10^{-4} : 10^{-1}$ eV^2 all the four possibilities depicted in fig. 4.1 are allowed. Hence, we analyze the sensitivity for all four cases.

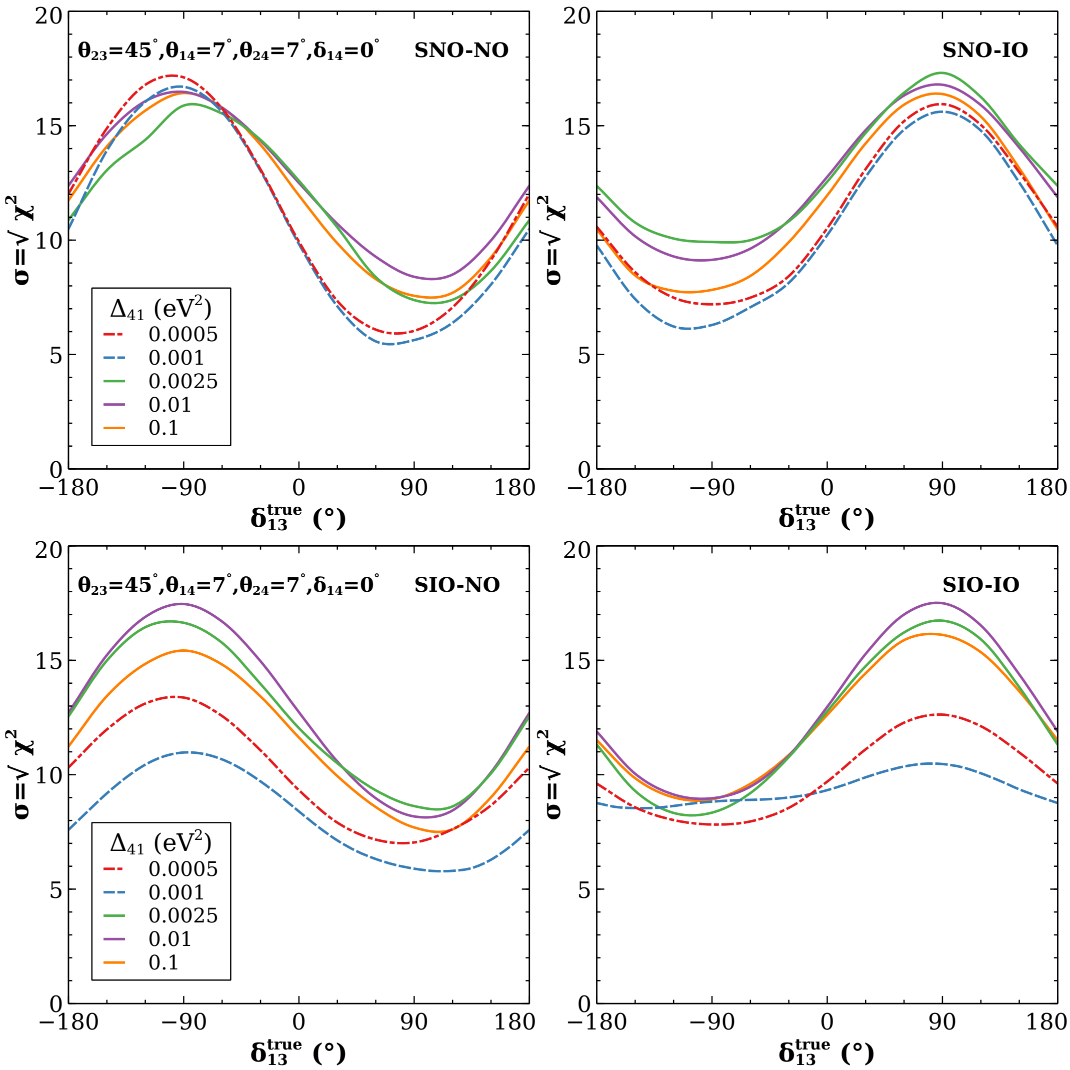

Figure 4.4: Sensitivity to atmospheric mass ordering as a function of δ_{13}^{true} in SNO(top), SIO (bottom) scenarios with true Δ_{31} for different values of Δ_{41}^{true} at 1300 km baseline

In fig. 4.4, the MO sensitivity is shown as a function of δ_{13}^{true} at various true values of Δ_{41}. The upper(lower) panels correspond to the true value in SNO (SIO) cases, while the left (right) panels are for NO(IO). During the computation of χ^2, the $|\Delta_{41}|$ is fixed in true and test cases for this plot. The observations of significance in fig. 4.4 are as follows,

- The nature of variation of sensitivity with δ_{13}^{true} doesn't change significantly for different true values of Δ_{41}.
- Sensitivity gets notably reduced for $\Delta_{41} = 0.001$ eV^2(blue) at the most of values of δ_{13}^{true} in the upper half plane (UHP) [0° : 180°] in SNO-NO and SIO-IO case. In

SNO-IO and SIO-NO cases, blue curves give minimum sensitivity over full range of δ_{13}

- However, sensitivity for $\Delta_{41} = 0.001$ eV^2 is very high in the lower half plane (LHP) $[-180° : 0°]$ of δ_{13}^{true} in SNO-NO, SIO-IO.
- The maximum sensitivity is observed for $\Delta_{41} = 0.01$ eV^2(violet) in SIO-NO and SIO-IO case for most of the δ_{13}^{true} values.
- For SIO-IO case $\Delta_{41} = 2.5 \times 10^{-3}$ eV^2 shows the maximum sensitivity over full range of δ_{13}^{true}.

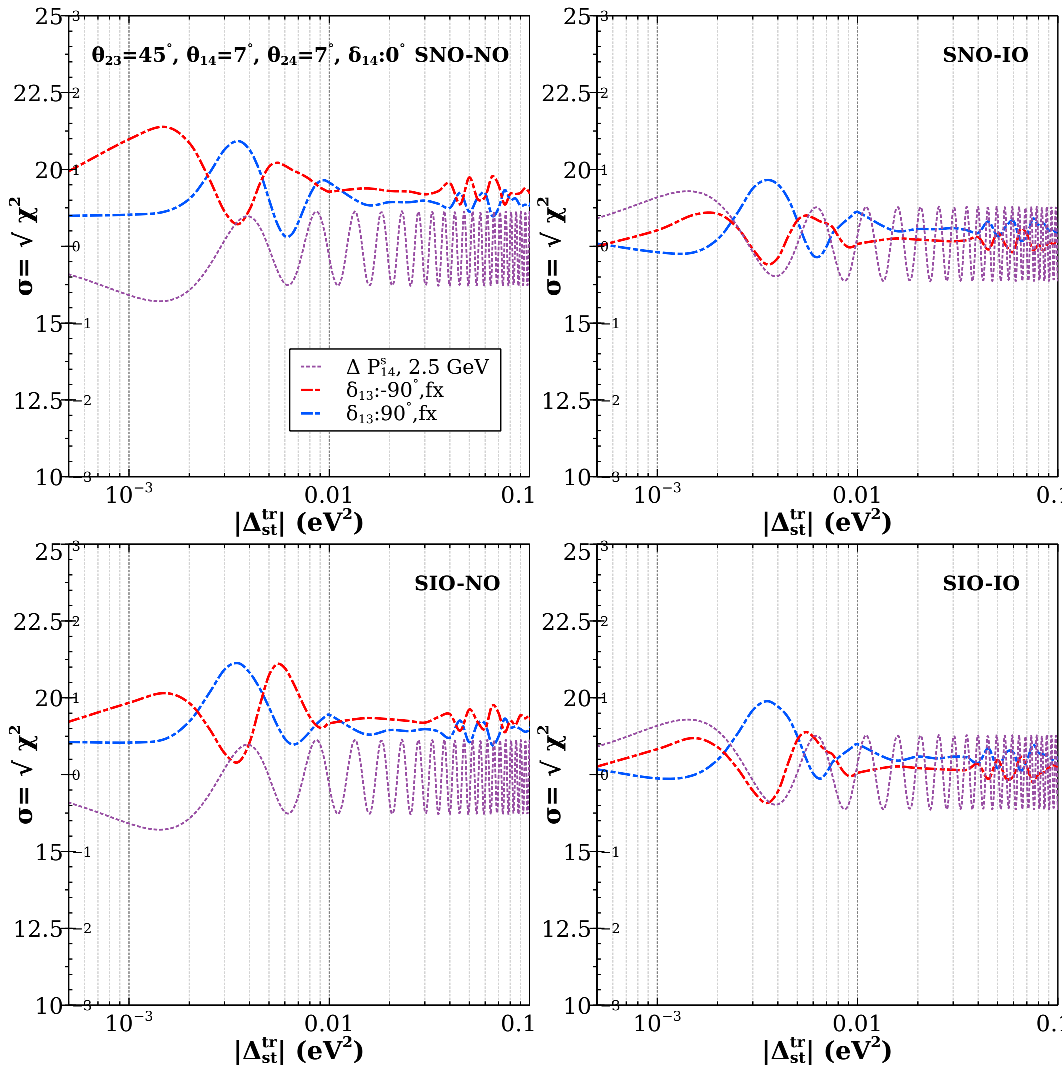

Figure 4.5: Sensitivity to atmospheric mass ordering as a function of Δ_{41}^{true} with marginalisation in Δ_{31} for $\theta_{23}^{true} = 45°$, $\delta_{14}^{true} = 0°$, $\delta_{13}^{true} = -90°$(red), $90°$(blue) at 1300 km baseline. The violet curve shows ΔP_{14}^{s} at 2.5 GeV.

We note that for the difference in the probability for the opposite MO, the dependence on Δ_{41} will come from the last term in eq. (4.1) and can be represented as (for fixed $\theta_{13}, \theta_{23}, \theta_{14}, \theta_{24}, \delta_{13}, \delta_{14}$),

$$\Delta P_{\mu e}^{st} \propto 4 s_{13} s_{14} s_{24} s_{23} [\Delta P_{14}^{s} \sin \delta_{14}' + \Delta P_{14}^{c} \cos \delta_{14}'], \tag{4.8}$$

where for difference considered between SNO-NO and SNO-IO, we define;

$$\Delta P_{14}^{s,c} = \frac{\sin[(A'-1)\Delta]}{(A'-1)} P_{14}^{s,c}(+\Delta_{31}) - \frac{\sin[(A'+1)\Delta]}{-(A'+1)} P_{14}^{s,c}(-\Delta_{31}) \tag{4.9}$$

In fig. 4.5, we have depicted the sensitivity to MO with marginalization performed only over Δ_{31} with all other parameters being fixed as a function of $|\Delta_{41}|$. The red (blue) curve refers to $\delta_{13} = -90°(90°)$. We also show the difference in probability term ΔP_{14}^{s}(4.9) evaluated at 2.5 GeV by the violet curve. The understandings from fig. 4.5 are as follows,

- Since we have chosen $\delta_{14} = 0°$ for $\delta_{13} = 90°$ and $-90°$, the sign of $\sin \delta_{14}' = \sin[\delta_{13} + \delta_{14}]$ is +1, -1 respectively and $\cos \delta_{14}' = 0$. If we take the phases and mixing angles fixed for both true and test cases, then the difference in probability(4.8) between NO and IO will only depend on ΔP_{14}^{s}.
- In the case of SNO-NO, the analytic difference in probability (4.8) is given as,

$$\Delta P_{\mu e} = B \sin \delta_{14}' \tag{4.10}$$

  where $B = 4 s_{13} s_{14} s_{24} s_{23} \Delta P_{14}^{s}$ doesn't depend on phases. This means $\Delta P_{\mu e}^{st}$ will be opposite for $\delta_{13} = 90°$ and $-90°$ leading to the opposite nature of chi-square. This can be seen from the top-left panel where in the range of $\Delta_{41} : 5 \times 10^{-4} : 10^{-2}$, the nature of the blue and violet curves are similar as it is proportional to $\Delta P_{\mu e}^{st}$. Similarly, the nature of the red curve is opposite to violet as it is proportional to $-\Delta P_{\mu e}^{st}$.
- The sensitivity is almost constant at $R >> 1$, i.e., $\Delta_{41} >> \Delta_{31}$. The difference in $P_{\mu e}$ for fixed energy and phases will only depend on ΔP_{14}^{s} and can be evaluated

using eq. (4.9) for $\Delta_{41} >> 1$ limit as,

$$\Delta P_{14}^{s} = \left(\frac{\sin[(A'-1)\Delta]}{(A'-1)} + \frac{\sin[(A'+1)\Delta]}{(A'+1)}\right) \times \left(\frac{A'}{2R}c_{23} + 2\right)\sin[R\Delta]^2 \quad (4.11)$$

At $R >> 1$ the term $\sin[R\Delta]$ shows fast oscillation. Summing over all the energies, i.e., values of Δ, A' in the term ΔP_{14}^{s} and averaging over $\sin[R\Delta]$, will give constant value.

- The sensitivity for SIO-NO is just opposite in nature to SNO-IO. Therefore, the violet curve is similar to the red one here.
- In SIO-NO, and SIO-IO cases, we also observe that the sensitivity is opposite for $\delta_{13} = 90°$, $-90°$.

In fig. 4.6, we depict the sensitivity to the sign of Δ_{31} as a function of true Δ_{41} for $\delta_{13} = -90°(\text{red}), 90°(\text{blue})$, and $\delta_{14} = 0°$ at 1300 km. Some interesting features of sensitivity to the MO as seen from fig. 4.6 are as follows,

- For SNO-NO and SIO-IO cases we observe a contrasting nature of the sensitivity between $\delta_{13} = 90°$ and $-90°$. For instance, in SNO-NO, at $\Delta_{41} = 3 \times 10^{-3}$ eV^2 a maxima of sensitivity occurs for $\delta_{13} = 90°$ whereas minima occurs for $\delta_{13} = -90°$. Note that a similar contrasting nature has been observed in the top two panels of fig. 4.2 showing the oscillogram of $\Delta P_{\mu e}$.
- However, the nature of sensitivity curves, for $\delta_{13} = 90°$ and $-90°$ is similar in SNO-IO and SIO-NO cases. We observe the same in the bottom panels of fig. 4.2 for SNO-IO case.
- In SNO-IO, and SIO-NO cases, maxima of sensitivity is around 2.5×10^{-3} eV^2. In SIO-NO, there is also a maxima for $\delta_{13} = -90°$ at $\Delta_{41} = 0.005$ eV^2.
- In all the cases, the minima and maxima are observed in the range of $0.001 - 0.01$ eV^2. Beyond that, the sensitivity is relatively flat with Δ_{41}.

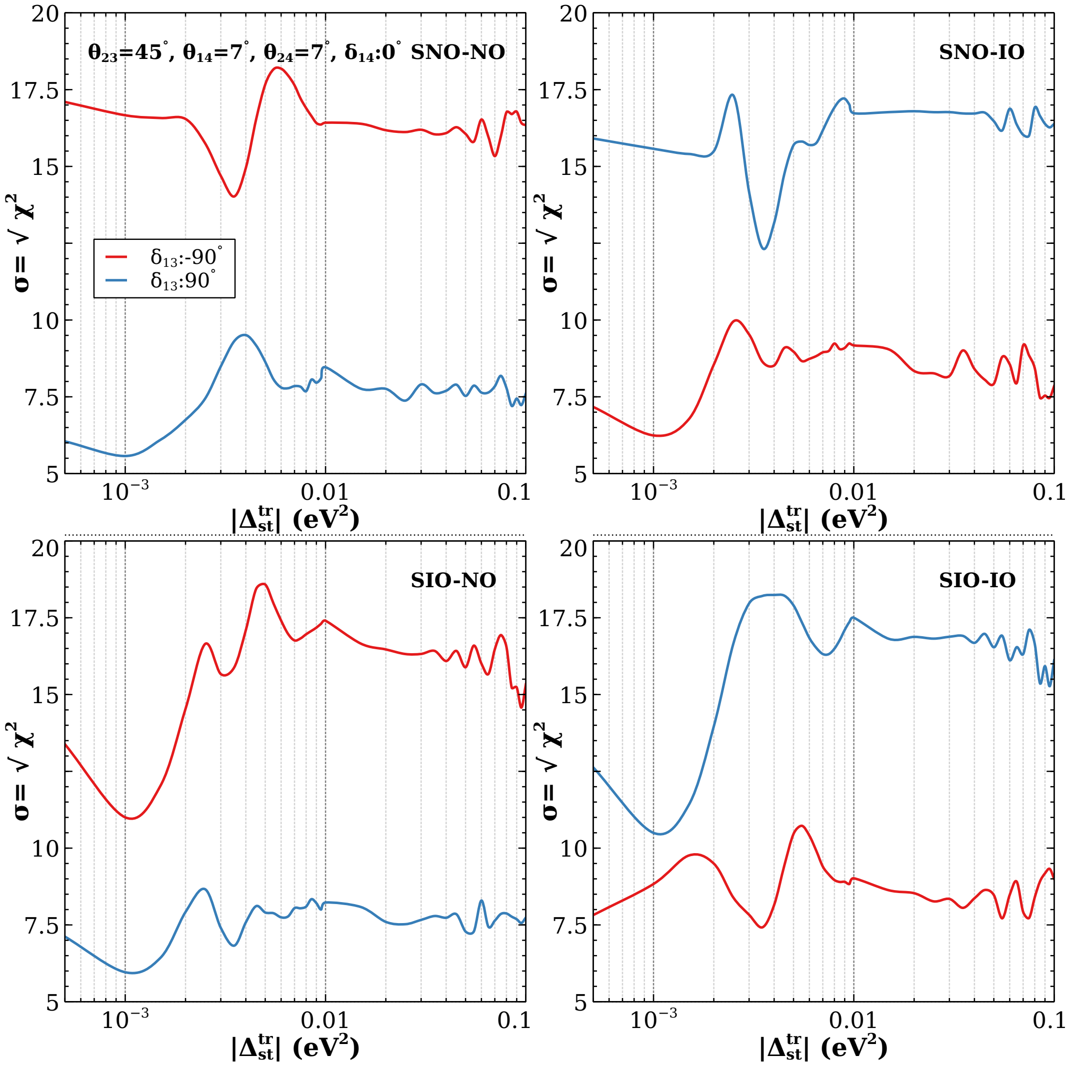

Figure 4.6: Sensitivity to atmospheric mass ordering as a function of Δ_{41}^{true} for $\theta_{23}^{true} = 45°$, $\delta_{14}^{true} = 0°$, $\delta_{13}^{true} = -90°$ (red), 90°(blue) at 1300 km baseline

4.5.1 Sensitivity to sign of Δ_{41} (SMO)

In this section, we present the sensitivity of the sign of Δ_{41} considering values to be in the range of $[5 \times 10^{-4} : 10^{-1}]$ eV^2 for which all four possibilities depicted in figure 1 will be viable. In fig. 4.7, the sensitivity of the sign of sterile mass squared differences are depicted as a function of the true value of Δ_{41} for various true values of δ_{13}, δ_{14}[1]. We observe following features in fig. 4.7,

- Sensitivity curve shows two prominent maxima around true values of $\Delta_{41} = 1 \times 10^{-3}$ eV^2, 5×10^{-3} eV^2 for SNO-NO and SIO-IO cases. There is a dip in sensitivity

[1]This plot has been presented in ref [246] at fixed values of $\delta_{13} = 0°, \delta_{14} = 0°$

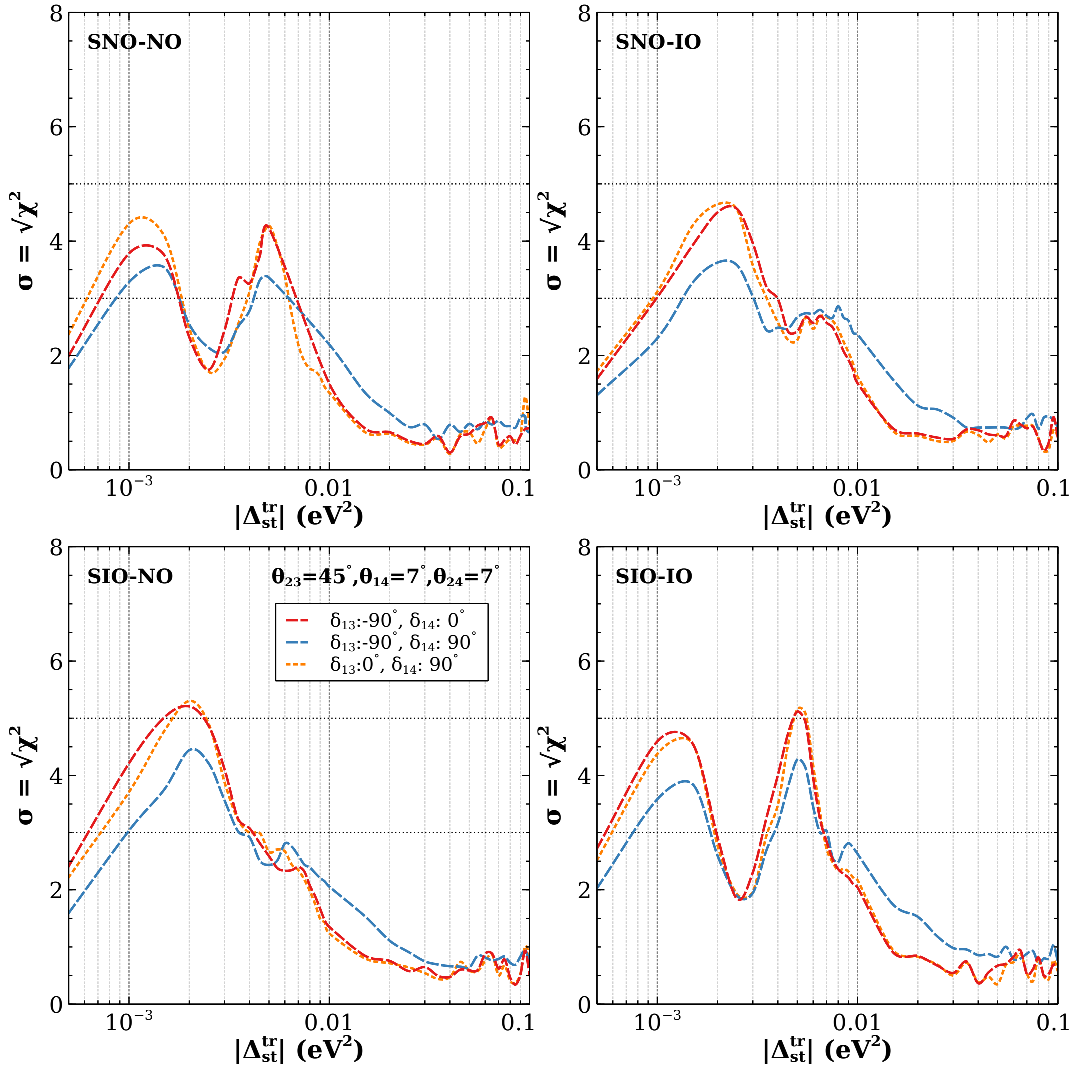

Figure 4.7: Sensitivity to sterile mass ordering as a function of Δ_{41}^{true} for $\Delta_{31} = +ve$(left), $-ve$(right) and $\Delta_{41} = +ve$(top), $-ve$(bottom) using different values of δ_{14}^{true}, δ_{13}^{true} at 1300 km.

when true Δ_{41} is around 2.5×10^{-3} eV^2 due to its proximity to atmospheric mass squared difference[246].

- In the case of SNO-IO and SIO-NO, the maxima occurs around $\Delta_{41} = 2.5 \times 10^{-3}$ eV^2, i.e., when the sterile mass squared difference is equal to the atmospheric mass squared difference Δ_{31}.
- The SNO-IO and SIO-IO cases provide relatively higher sensitivity than the SNO-NO and SIO-IO cases.
- We also observe a variation of 1σ in sensitivity at a fixed Δ_{41} for different values of the phases δ_{13}, δ_{14}.
- The features of sensitivity in SNO-NO can also be seen from the plot of probability difference in top panels of fig. 4.3.

In fig. 4.8, we have used the simulated data from atmospheric neutrino analysis to perform a combined analysis of beam and atmospheric neutrinos and get the sensitivity of the sterile mass ordering as a function of the true value of Δ_{41} for the true value of phases $\delta_{13} = -90°$(left), $\delta_{14} = 90°$(right). In these four panels, it is observed that the sensitivity to SMO is better in combined analysis than in beam neutrinos. The nature of the sensitivity is almost similar for beam and atmospheric analysis. This can be understood from the similar profile of difference in probabilities $\Delta P_{\nu e}, \Delta P_{\mu\mu}$ at 1300 km and 7000 km as shown in fig. 4.2. The combined sensitivity is above 3σ for most of the parameter space up to $\Delta_{41} = 10^{-2}$ eV^2. For Δ_{41} value greater than that, even with the addition of atmospheric neutrinos, we get a fixed sensitivity of 1.5σ.

4.5.2 Impact of very light sterile neutrino on octant sensitivity

In this section, we study the dependence of octant sensitivity with various mass ordering scenarios in the presence of a light sterile neutrino. We show the results for SNH-NH, SIH-NH, and SIH-IH scenarios. In computing the octant sensitivity we marginalize over θ_{23} in opposite octant as well as over $\delta_{13}, \delta_{14}, \theta_{14}, \theta_{24}$, and Δ_{41} as given in table 4.1. We demonstrate in fig. 4.9 the sensitivity of octant as a function of true Δ_{41} for $\theta_{23}^{true} = 49°$ (left) and $41°$ (right) in SNH-NH scenario at 1300 km baseline with different combinations of true values of phases.

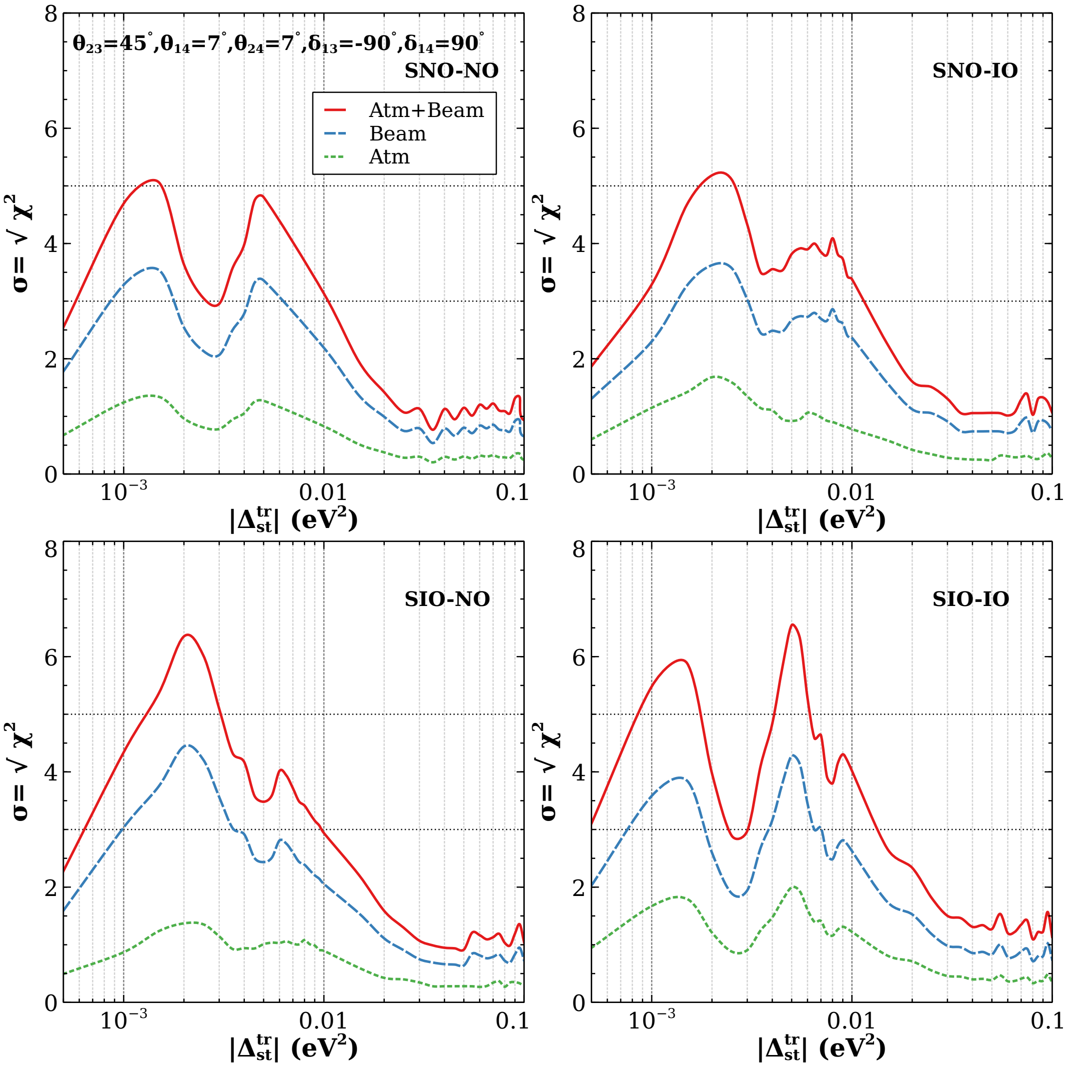

Figure 4.8: Sensitivity to sterile mass hierarchy as a function of Δ_{41}^{true} using combined beam and atmospheric neutrinos at 1300 km baseline.

The important features of fig. 4.9 are as follows,

- Similar to the SNO case, we see a drop of sensitivity to the octant of θ_{23} around $\Delta_{41} = 2.5 \times 10^{-3}$ eV^2.
- The sensitivity is observed to increase for values greater than $\Delta_{41} = 2.5^{-3}$ eV^2 and reach a maximum around 10^{-2} eV^2. The maximum sensitivity for the true value of $\theta_{23} = 49°$ is around 4σ, whereas for lower octant true value of 41° the maximum sensitivity reaches 5σ.
- At higher values of Δ_{41} the sensitivity falls to be around 2σ range which is also the sensitivity for sterile neutrino with $\Delta_{41} = 1$ eV^2.

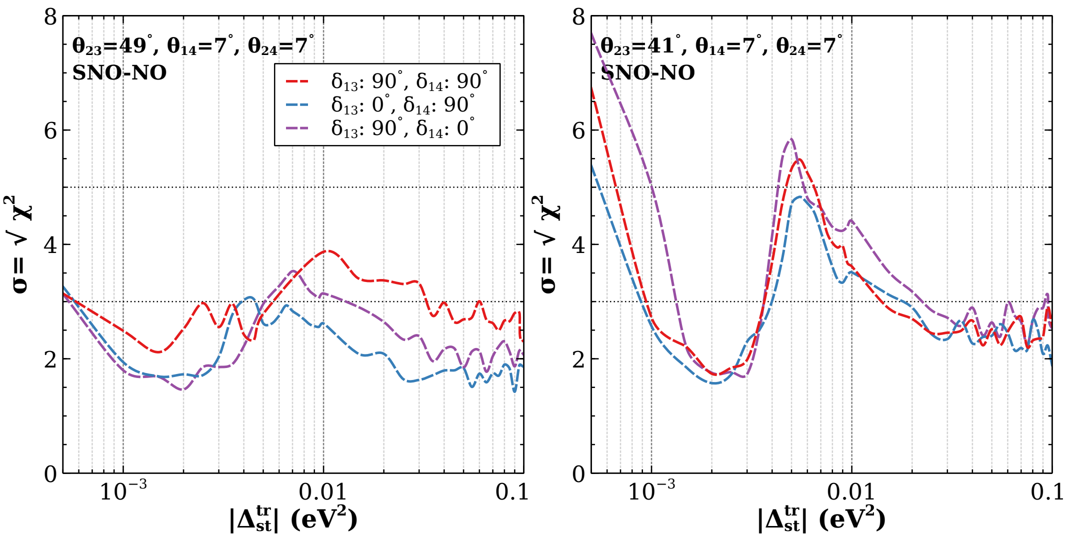

Figure 4.9: Sensitivity to octant as a function of Δ_{41}^{true} for $\theta_{23}^{true} = 49°$(left), 41°(right) using different values of δ_{14}^{true}, δ_{13}^{true} in SNO-NO case at 1300 km.

In fig. 4.10, the octant sensitivity for combined analysis of beam and atmospheric neutrinos has been illustrated as a function of Δ_{41}^{ture} in the SNO-NO scenario. Due to the addition of atmospheric analysis, the sensitivity to octant for $\theta_{23} = 49°, 41°$ gets boosted by more than 1σ w.r.t. the beam analysis results with a minimum sensitivity of 3σ.

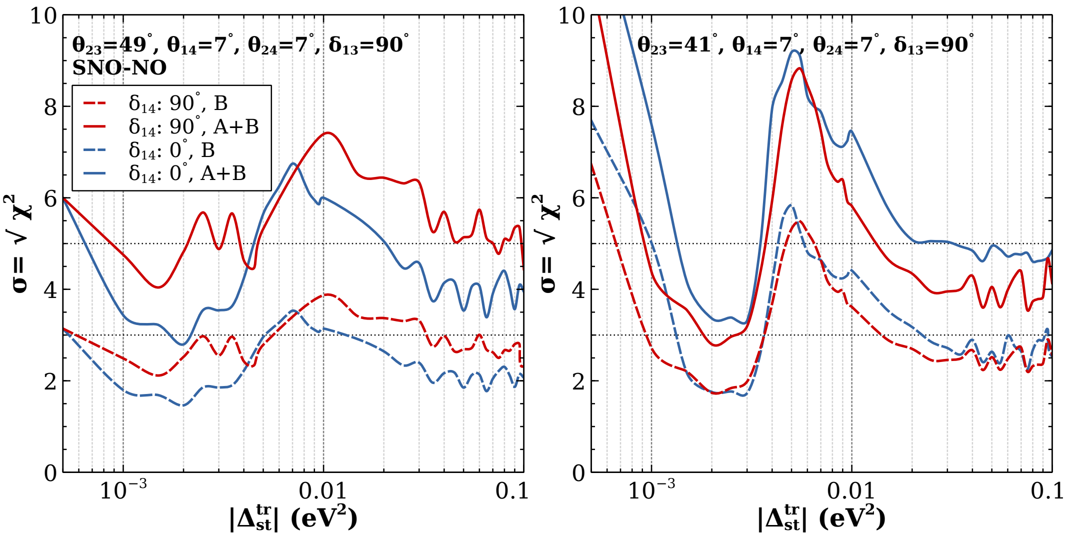

Figure 4.10: Sensitivity to octant as a function of Δ_{41}^{true} for $\theta_{23}^{true} = 49°$(left), $41°$(right) using $\delta_{14}^{true} = 0°(blue), 90°(red)$, $\delta_{13}^{true} = 90°$ at 1300 km baseline from beam [B] analysis (dashed), and combined beam plus atmospheric [A+B] analysis (solid)

4.6 Conclusions

Our work focuses on the effect of an additional light sterile neutrino corresponding to the sterile mass squared difference in the range of $10^{-4} : 0.1$ eV^2 on the determination of atmospheric mass ordering, and sterile mass ordering. This study demonstrates for the first time the dependence of sensitivity to MO on the absolute value of Δ_{41} as well as the on the true scenario of 3+1 mass spectrum (SNO-NO, SNO-IO, SIO-NO, SIO-IO). The MO sensitivity shows significant decrements/ increments for Δ_{41} in the range of $10^{-3} : 10^{-2}$ eV^2.

The presence of a light sterile neutrino gives a possibility of both positive and negative values of Δ_{41}. In our study, we observe the sensitivity to sterile mass ordering (SMO) for the $\Delta_{41} = 5 \times 10^{-4} : 0.1$ eV^2 in different scenarios of the 3+1 mass spectrum. The sensitivity gets reduced when Δ_{41} is in proximity of Δ_{31}. The addition of atmospheric neutrinos boosts the sensitivity over 3σ for $\Delta_{41} < 10^{-2}$ eV^2. However, for higher values of Δ_{41}, the sensitivity falls off $\sim 1 - 1.5\sigma$.

We have also probed the effect of Δ_{41} on the octant of θ_{23}. The sensitivity is suppressed below 2σ for values of $\Delta_{41} = 1 - 4 \times 10^{-3}$ eV^2 in the vicinity of Δ_{31}. However, the inclusion of atmospheric neutrinos helps us reinforce the sensitivity above

3σ irrespective of values of Δ_{41}.

"He who can listen to the music in the midst of noise can achieve great things"

Vikram Sarabhai

5

Implications of DLMA solutions at IceCube

In this chapter, we study the implication of the IceCube data in the measurement of the neutrino oscillation parameters, namely θ_{23} and δ_{13} in light of Dark Large Mixing Angle (DLMA) solution of θ_{12} for different astrophysical sources. This chapter is based on [247].

The solar mixing angle θ_{12} has been precisely measured in the standard neutrino oscillation framework. However, an interesting problem in the neutrino oscillation sector is the existence of the Dark Large Mixing Angle (DLMA) solution of the solar mixing angle θ_{12}. The DLMA solution is related to the standard Large Mixing Angle (LMA) solution of θ_{12} as $\theta_{12}^{DLMA} = 90^\circ - \theta_{12}^{LMA}$, referring to $\theta_{12}^{DLMA} > 45^\circ$. This solution was shown initially to be existing in ref. [248]. However, the presence of solar matter effects disfavoured [249] this solution. But, the inclusion of NSI made this solution resurface [250]. In ref. [251], it was shown that the tension between the solar and KamLAND data regarding the measurement of Δ_{21} can be resolved if one introduces non-standard interaction (NSI) in neutrino propagation [252]. However, due to the introduction of NSI, the values of θ_{12} greater than 45°, i.e., the DLMA solution also became allowed. It has been shown that the DLMA solution is manifested from a generalized degeneracy appearing with the sign of Δ_{31} when first order correction from NSI is added to the standard three flavor NC neutrino-quark interactions [253]. Note that, in vacuum, the total Hamiltonian for neutrino is invariant under a CPT transformation that can be translated into a symmetry given as follows[253],

$$\Delta_{31} \rightarrow -\Delta_{32} \tag{5.1}$$

$$\sin\theta_{12} \rightarrow \cos\theta_{12} \tag{5.2}$$

$$\delta_{13} \rightarrow 180^\circ - \delta_{13} \tag{5.3}$$

In the presence of NSI, the Hamiltonian will be CPT invariant by following the additional transformation; along with the above ones,

$$\epsilon_{ee} - \epsilon_{\mu\mu} \rightarrow -(\epsilon_{ee} - \epsilon_{\mu\mu}) - 2 \tag{5.4}$$

$$\epsilon_{\tau\tau} - \epsilon_{\mu\mu} \rightarrow -(\epsilon_{\tau\tau} - \epsilon_{\mu\mu}) \tag{5.5}$$

$$\epsilon_{\alpha\beta} \rightarrow \epsilon^*_{\alpha\beta} \tag{5.6}$$

Since $\epsilon_{\alpha\beta}$ depends on the matter potential, the degeneracy becomes exact only when the matter dependence vanishes. This degeneracy implies that the neutrino mass ordering and the true nature of θ_{12} can not simultaneously be determined from the neutrino oscillation experiment. It was concluded that this degeneracy can only be solved if one of the quantities i.e., either the neutrino mass ordering or the true nature of θ_{12} can be measured from a non-oscillation experiment [254, 255]. The non-oscillation neutrino-nucleus scattering experiment COHERENT constrained the DLMA parameter space severely [256]. However, these bounds are model dependent and depend on the mass of the light mediator [257, 258]. From the previous global analysis [259], it has been shown that the DLMA solution can be allowed at 3σ when the NSI parameters have a smaller range of values and with light mediators of mass ≥ 10 MeV. The latest global analysis shows that the DLMA solution is allowed at 97% C.L. or above [260].

IceCube [50] is an ongoing experiment at the South Pole that studies neutrinos from astrophysical sources. These astrophysical sources can be active galactic nuclei (AGN), gamma-ray bursts (GRB), etc. The astrophysical sources are located at a distance of several kpc to Mpc from Earth, while the energies of these neutrinos are around TeV to PeV. In AGNs and GRBs, neutrinos are produced via three basic mechanisms. The accelerated protons (p) can interact either with photons (γ) or the matter to produce pions ($\pi^{\pm}$). These pions decay to produce muons ($\mu^{\pm}$) and muon neutrinos ($\nu_\mu/\bar{\nu}_\mu$). Then the muons decay to produce electrons/ positrons along with electron antineutrinos/neutrinos ($\bar{\nu}_e/\nu_e$) and muon neutrinos/antineutrinos. This process is known as the πS process which produces a neutrino flux of $\nu_e : \nu_\mu : \nu_\tau = 1 : 2 : 0$ [261]. We label this the π source. Some of the muons in the above process, due to their light mass, can get cooled in the magnetic field, resulting in a neutrino flux ratio of $0 : 1 : 0$. This is known as the μDS process [262]. We call this the μ source. The interaction between the protons and the photons also produces high-energy neutrons (n), which would decay to produce a neutrino flux ratio of $1 : 0 : 0$. This process is known as nS process [263]. This is labeled as the n source. Neutrinos produced in these three sources oscillate among their flavors before reaching Earth. It has been shown that if one assumes the tri-bi-maximal (TBM) scheme of mixing, then the final flux ratio of the neutrinos at Earth for the π source is 1:1:1 [264–266]. However, as the current neutrino mixing is different from the TBM, the flux ratios at Earth will be different from that of TBM [267]. Note that one of the authors in ref. [268] carried on a study of constraining δ_{13} using the first 3 years of the IceCube data for different astrophysical sources.

In this chapter, we study the implications of the measurement of the oscillation parameters θ_{23} and δ_{13} in the IceCube data in light of the DLMA solution of θ_{12}. Because of the large distance of the astrophysical sources, the oscillatory terms in the neutrino oscillation probabilities are averaged out, and as a result, the neutrino oscillation probabilities become independent of the mass square differences. Therefore, the IceCube experiment gives us an opportunity to measure the currently unknown parameters i.e., θ_{23} and δ_{13} by analyzing its data. These measurements can be complementary to the measurements of the other neutrino oscillation experiments. Further, as the oscillation probabilities are independent of Δ_{31}, they are free from the generalized degeneracy that appears between the neutrino mass ordering and the two different solutions of θ_{12}. However, as the oscillation of the astrophysical neutrinos is mostly in vacuum, the two solutions of θ_{12} become degenerate with δ_{13}.

The chapter will be organized as follows. In section 5.1, the expressions for the different probabilities corresponding to the oscillation of the astrophysical neutrinos relevant to IceCube are evaluated. In this section, we will locate the degeneracies associated with the parameters. In the following section 5.2, we will lay out our analysis method and present our results. Finally, we will summarize the important conclusions from our study.

5.1 Oscillation of the astrophysical neutrinos

If we denote the flux of neutrinos of flavour α at the source by ϕ^0_α and the final oscillated flux at Earth by ϕ_α, then the relation between ϕ^0_α and ϕ_α can be written as:

$$\begin{pmatrix} \phi_e \\ \phi_\mu \\ \phi_\tau \end{pmatrix} = \begin{pmatrix} P_{ee} & P_{\mu e} & P_{\tau e} \\ P_{e\mu} & P_{\mu\mu} & P_{\tau\mu} \\ P_{e\tau} & P_{\mu\tau} & P_{\tau\tau} \end{pmatrix} \begin{pmatrix} \phi^0_e \\ \phi^0_\mu \\ \phi^0_\tau \end{pmatrix}, \tag{5.7}$$

where $P_{\alpha\beta}$ is the oscillation probability for $\nu_\alpha \to \nu_\beta$, with α and β being e, μ and τ. From eq. 5.7, we can understand that the probabilities $P_{\tau e}$, $P_{\tau\mu}$ and $P_{\tau\tau}$ don't enter in the calculation for the final fluxes, as $\phi^0_\tau = 0$ for all the three sources i.e, π source, μ source, and n source. The final flux depends upon $P_{\mu e}$, $P_{\mu\mu}$, and $P_{\mu\tau}$ for the μ source ($\phi^0_e = \phi^0_\tau = 0$) whereas the final flux depends only on P_{ee}, $P_{e\mu}$ and $P_{e\tau}$ for the n source ($\phi^0_\mu = \phi^0_\tau = 0$). Therefore, when analyzing a particular source, it will be sufficient to look at the relevant probabilities to understand the numerical results. For the energy and baselines related to IceCube, the probabilities can be calculated using the formula:

$$P_{\alpha\beta} = \sum_{i=1}^{3} |U_{\alpha i}|^2 |U_{\beta i}|^2 \tag{5.8}$$

where U is the PMNS matrix having the parameters θ_{12}, θ_{13}, θ_{23} and δ_{13}. It is easy to obtain the expressions for the different probabilities by expanding eq. 5.8:

$$P_{ee} = \cos^4\theta_{12}\cos^4\theta_{13} + \sin^4\theta_{12}\cos^4\theta_{13} + \sin^4\theta_{13} \tag{5.9}$$

$$\begin{aligned} P_{e\mu} = {} & [\sin^2\theta_{13}\sin^2\theta_{23}(2 - \frac{1}{2}\sin^2 2\theta_{12}) + \frac{1}{2}\sin 2\theta_{23}\sin\theta_{13}\sin 2\theta_{12}\cos 2\theta_{12}\cos\delta_{13} \\ & + \frac{1}{2}\sin^2 2\theta_{12}\cos^2\theta_{23} +]\cos^2\theta_{13} \end{aligned} \tag{5.10}$$

$$\begin{aligned} P_{e\tau} = {} & [\sin^2\theta_{13}\cos^2\theta_{23}(2 - \frac{1}{2}\sin^2 2\theta_{12}) - \frac{1}{2}\sin 2\theta_{23}\sin\theta_{13}\sin 2\theta_{12}\cos 2\theta_{12}\cos\delta_{13} \\ & + \frac{1}{2}\sin^2 2\theta_{12}\sin^2\theta_{23} +]\cos^2\theta_{13} \end{aligned} \tag{5.11}$$

$$\begin{aligned} P_{\mu\mu} = {} & [\sin^2\theta_{12}\cos^2\theta_{23} + \cos^2\theta_{12}\sin^2\theta_{13}\sin^2\theta_{23} + \frac{1}{2}\sin 2\theta_{12}\sin 2\theta_{23}\sin\theta_{13}\cos\delta_{13}]^2 \\ & + [\cos^2\theta_{12}\cos^2\theta_{23} + \sin^2\theta_{12}\sin^2\theta_{13}\sin^2\theta_{23} - \frac{1}{2}\sin 2\theta_{12}\sin 2\theta_{23}\sin\theta_{13}\cos\delta_{13}]^2 \\ & + \cos^4\theta_{13}\sin^4\theta_{23} \end{aligned} \tag{5.12}$$

$$\begin{aligned} P_{\mu\tau} = {} & \frac{1}{2}\cos\delta_{13}\cos 2\theta_{12}\cos 2\theta_{23}\sin 2\theta_{12}\sin 2\theta_{23}\sin\theta_{13}(1 + \sin^2\theta_{13}) \\ & + \frac{1}{4}\sin^2 2\theta_{23}(1 - \frac{1}{2}\sin^2 2\theta_{12})(1 + \sin^4\theta_{13})\frac{1}{2}\sin^2 2\theta_{12}\sin^2\theta_{13}(1 - \frac{1}{2}\sin^2 2\theta_{23}) \end{aligned} \tag{5.13}$$

$$\begin{aligned} P_{\tau\tau} = {} & [\sin^2\theta_{12}\sin^2\theta_{23} + \cos^2\theta_{12}\sin^2\theta_{13}\cos^2\theta_{23} - \frac{1}{2}\sin 2\theta_{12}\sin 2\theta_{23}\sin\theta_{13}\cos\delta_{13}]^2 \\ & + [\cos^2\theta_{12}\sin^2\theta_{23} + \sin^2\theta_{12}\sin^2\theta_{13}\cos^2\theta_{23} + \frac{1}{2}\sin 2\theta_{12}\sin 2\theta_{23}\sin\theta_{13}\cos\delta_{13}]^2 \\ & + \cos^4\theta_{13}\cos^4\theta_{23} \end{aligned} \tag{5.14}$$

From eq.5.9, we see that the probability expression P_{ee} is independent of θ_{23} and δ_{13} and also is invariant under θ_{12} and $90^\circ - \theta_{12}$. Therefore we study only probability plots of $P_{\mu e}(P_{e\mu})$, $P_{\mu\mu}$, $P_{\mu\tau}$, and $P_{e\tau}$

In fig.5.1, we have plotted the probabilities which are relevant for the IceCube energy

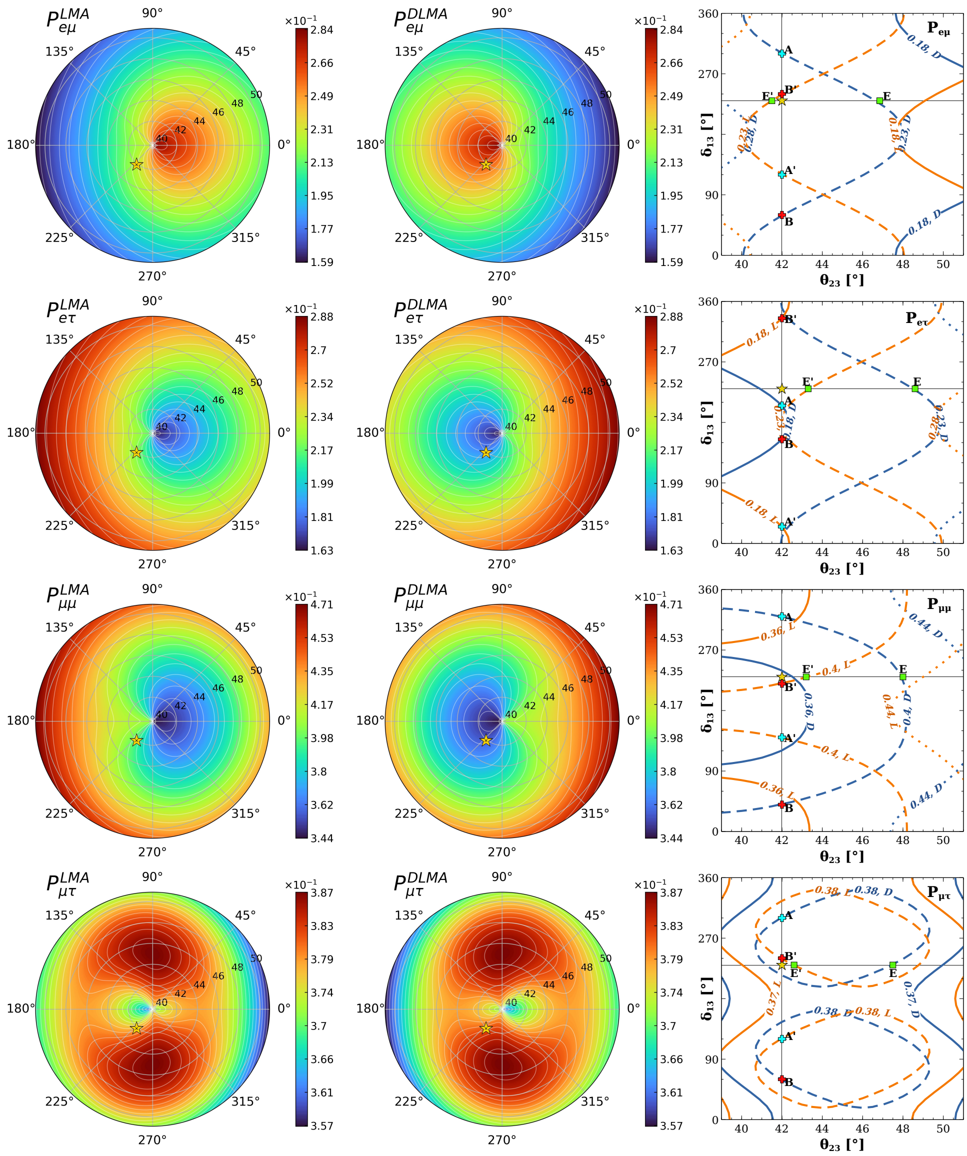

Figure 5.1: First two columns show contour plots of probabilities in $\delta_{13} - \theta_{23}$ plane in polar projection. Best-fit values were taken for θ_{12} and θ_{13}. The polar radius represents θ_{23}, and the polar angle represents $\delta_{\rm CP}$. Values of probabilities are represented by colors shown next to the corresponding plot. The left column is for the LMA solution, and the middle is for the DLMA solution. The third column shows iso-probability curves for LMA (orange) and DLMA (blue) in conjunction. $P_{e\mu}$, $P_{e\tau}$, $P_{\mu\mu}$ and $P_{\mu\tau}$ are shown in the panels of the first, second, third, and fourth row respectively.

Parameter	Best Fit	Marginalization Range
θ_{12}	$33.4°(56.6°)$	$31.27°(54.13°) : 35.87°(58.73°)$
θ_{13}	$8.62°$	$8.25° : 8.98°$
θ_{23}	$42.1°$	$39° : 51°$
δ_{13}	$230°$	$0° : 360°$

Table 5.1: The table depicts the best-fit values of all the parameters and their range of marginalization which are taken from NuFit 5.1 [101].

and baselines i.e., all the four probabilities except P_{ee} and $P_{\tau\tau}$. In the left and middle columns, we have presented the polar plots of probabilities in θ_{23} and $\delta_{\rm CP}$ plane. The circle's radius represents θ_{23}, and the polar angle represents $\delta_{\rm CP}$. The different color shades correspond to different values of the probability, as shown in the z-axis. The left column is for the LMA solution, and the middle is for the DLMA solution. Rows represent different probabilities written next to the panels. In the right column, we show the iso-probability curves in the θ_{23} - δ_{13} plane for both LMA and DLMA values of θ_{12}. The orange curves are for LMA solution and the blue curves are for DLMA solution. The values of the oscillation probabilities are written on the curves. In all panels, the current best-fit value of the θ_{23} and δ_{13} are marked by a STAR. We have used the current best-fit values of θ_{12} and θ_{13} to generate this figure. These values are listed in table 5.1.

From the figure, the following observations can be made regarding the measurement of θ_{23}, δ_{13} and LMA and DLMA solution of θ_{12} at IceCube:

- Parameter degeneracy defined by $P_{\alpha\beta}(\theta_{12}^{LMA}, \delta_{13}) = P_{\alpha\beta}(\theta_{12}^{DLMA}, 180° \pm \delta_{13})$ for a fixed value of θ_{23} exists. This can be observed from the panels in the left and the middle column in the following way. Imagine rotating the DLMA solution panels around the central horizontal axis by 180° clockwise or anti-clockwise. These panels now look the same as the ones for the LMA solution. This transformation represents $\delta_{\rm CP} \to 180° \pm \delta_{\rm CP}$ degeneracy between the two solutions. This can also be seen by drawing an imaginary vertical line on panels in the right column. For example, this is shown by the vertical line at $\theta_{23} = 42°$. Here, one can see that the probability for point A' (LMA) is the same as the probability in points A and B (DLMA), where the δ_{13} values are related by $\delta_{\rm CP}^{A} = 180° + \delta_{\rm CP}^{A'}$ and $\delta_{\rm CP}^{B} = 180° - \delta_{\rm CP}^{A'}$. Similarly, for B (DLMA) there are two degenerate solutions B' and A'. Here, we also see that points A (A') and B (B') are also degenerate with each other. We will discuss this later. The origin of degeneracy discussed above stems at the Hamiltonian level as the Hamiltonian of neutrino oscillation in vacuum is invariant for the transformations shown in equations (5.1),(5.2),(5.3).

This can also be viewed from eq. 5.10 to eq. 5.13 in the following way. The difference between the probabilities due to the LMA and DLMA solutions while keeping other parameters constant can be calculated as $\Delta P_{\alpha\beta} = P_{\alpha\beta}(\theta_{12}) - P_{\alpha\beta}(90° - \theta_{12})$. Then the differences are given as follows,

$$\Delta P_{e\mu} = \sin 2\theta_{12} \cos 2\theta_{12} \sin\theta_{13} \cos^2\theta_{13} \sin 2\theta_{23} \cos\delta_{13} \tag{5.15}$$

$$\Delta P_{e\tau} = -\sin 2\theta_{12} \cos 2\theta_{12} \sin\theta_{13} \cos^2\theta_{13} \sin 2\theta_{23} \cos\delta_{13} \tag{5.16}$$

$$\Delta P_{\mu\mu} = 2\sin 2\theta_{12} \cos 2\theta_{12} \sin\theta_{13} \cos^2\theta_{13} \sin 2\theta_{23} \cos\delta_{13} (\sin^2\theta_{23} \sin^2\theta_{13} - \cos^2\theta_{23}) \tag{5.17}$$

$$\Delta P_{\mu\tau} = \sin 2\theta_{12} \cos 2\theta_{12} \sin\theta_{13} \cos^2\theta_{13} \sin 2\theta_{23} \cos\delta_{13} (1 + \sin^2\theta_{13}) \cos 2\theta_{23} \tag{5.18}$$

It can be observed that $\Delta P_{\alpha\beta} = 0$ when $\delta_{13} = 90°$ and $270°$. We identify that the terms $\sin 2\theta_{23}$ and $\cos\delta_{13}$ are the reason behind degeneracies of LMA and DLMA solutions with θ_{23} and δ_{13}. If we equate the probabilities for LMA and DLMA at fixed θ_{23} then the relation between different δ_{13} values for LMA and DLMA is given as,

$$\cos\delta_{13}^{LMA} = -\cos\delta_{13}^{DLMA} = \cos[180° \pm \delta_{13}^{DLMA}] \tag{5.19}$$

Therefore from the IceCube experiment alone, it will not be possible to separate the LMA solution from the DLMA solution. However, if δ_{13} can be measured from a different experiment, then IceCube gives the opportunity to break the generalized mass ordering degeneracy as the oscillation probabilities are independent of Δ_{31} in IceCube.

- In these probabilities, there also exists a degeneracy between θ_{23} and the two solutions of θ_{12} for a given value of δ_{13}. This can be viewed from the right column by drawing an imaginary horizontal line in the right panels. To show this we have drawn a horizontal line at $\delta_{13} = 230°$. This line intersects blue curves and orange curves having equal probabilities, showing the degeneracy between θ_{23} and the two solutions of θ_{12} for a given value of δ_{13}. This degeneracy can also be seen on polar plots. Here, fixing the value of $\delta_{\rm CP}$ is equivalent to drawing a line that comes out of the center at a polar angle that is equal to the value of $\delta_{\rm CP}$. Next, we pick a certain shade of color, which corresponds to fixing a value of the probability. By reading the value of the radius where the line and this colored patch intersect, we get θ_{23}, which doesn't necessarily have to be the same for the LMA and DLMA solutions. However, unlike the degeneracy mentioned in the earlier item, this degeneracy is not intrinsic.

The degenerate values of θ_{23} corresponding to LMA and DLMA solutions for a particular probability depend on the value of δ_{13}. Let us show this explicitly in the case of $P_{e\mu}$. This degeneracy for $P_{e\mu}$ is defined by $P_{e\mu}(\theta_{12}^{LMA}, \theta_{23}^{L}) = P_{e\mu}(\theta_{12}^{DLMA}, \theta_{23}^{D})$ which gives,

$$(\sin\theta_{23}^{L} + \sin\theta_{23}^{D})\Big\{-\frac{M_2}{2}\cos\delta_{13}(\sin^2\theta_{23}^{L} - \sin\theta_{23}^{L}\sin\theta_{23}^{D} + \sin^2\theta_{23}^{D}) \tag{5.20}$$

$$+M_1(\sin\theta_{23}^{L} - \sin\theta_{23}^{D}) + M_2\cos\delta_{13}\Big\} = 0 \tag{5.21}$$

$$\tag{5.22}$$

This implies that

$$\sin\theta_{23}^{L} + \sin\theta_{23}^{D} = 0\ \text{, or} \tag{5.23}$$

$$-\frac{M_2}{2}\cos\delta_{13}(\sin^2\theta_{23}^{L} - \sin\theta_{23}^{L}\sin\theta_{23}^{D} + \sin^2\theta_{23}^{D}) + M_1(\sin\theta_{23}^{L} - \sin\theta_{23}^{D}) + M_2\cos\delta_{13} = 0 \tag{5.24}$$

where $M_1 = \sin^2\theta_{13}(2 - \frac{1}{2}\sin^2 2\theta_{12}) - \frac{1}{2}\sin^2 2\theta_{12}$ and $M_2 = \sin\theta_{13}\sin 2\theta_{12}\cos 2\theta_{12}$ are constants.

The solution $(\sin\theta_{23}^{L} + \sin\theta_{23}^{D}) = 0$ suggest that degenerate solution is given by $\theta_{23}^{L} = 360° - \theta_{23}^{D}$. But this can't be observed in fig. 5.1 as $360° - \theta_{23}^{D}$ don't lie in the range of $39° - 51°$. For the other solution, with $\delta_{13} = 90°$ and $270°$, it gives simply $\sin\theta_{23}^{L} - \sin\theta_{23}^{D} = 0$, i.e., $\theta_{23}^{L} = \theta_{23}^{D}$ as seen from fig. 5.1. In the case of other values of δ_{13}, angles θ_{23}^{L} and θ_{23}^{D} are connected by a quadratic equation, i.e., two degenerate solutions. For $\delta_{13} = 230°$ and $\theta_{23}^{L} = 41.5°$, we obtain $\theta_{23}^{D} = 46.95°$ which is consistent with what we see in fig. 5.1. This gives a $P_{e\mu}$ value of 0.23.

- One more degeneracy defined by $\delta_{13} \to -\delta_{13}$ is easily visible in left and middle columns. It can be seen from all probability expressions as they are degenerate for $\cos\delta_{13} = \cos[-\delta_{13}] = \cos[360^\circ - \delta_{13}]$. This degeneracy within each of the LMA and DLMA solutions can be seen if the plots are flipped around a horizontal line going through the center. Each plot looks the same if it is flipped around that line. As mentioned earlier, when discussing $\delta_{\rm CP} \to 180^\circ - \delta_{\rm CP}$ degeneracy, this degeneracy is the reason why points A (A') and B (B') in the right column are degenerate.

In the next section, we will see how these degeneracies manifest in the analysis of the IceCube data.

5.2 Analysis and Results

We analyze the IceCube data in terms of track by shower ratio. The advantage of using this ratio is that one does not need the fluxes of the astrophysical neutrinos and the exact cross-sections to analyze the data of IceCube.

Category	$E < 60$ TeV	$E > 60$ TeV	Total
Total Events	42	60	102
Cascade	30	41	71
Track	10	17	27
Double Cascade	2	2	4

Table 5.2: The observed events are categorized and presented. The left-most column indicates the event category, while the right-most column displays the total number of events observed in each category. The intermediate columns separate the events based on the reconstructed deposited energy, distinguishing between those with less than 60 TeV and those with greater than 60 TeV [269].

At IceCube, the muon event produces a track, whereas the electron and tau events produce a shower. In table 5.2, we have listed the number of events from the 7.5 years of IceCube data. From this data, we calculate the experimental track by shower ratio for the neutrinos having deposited energy greater than 60 TeV as:

$$R_{exp} = \frac{17-1}{41+2} = \frac{16}{43} \approx 0.372.$$

In the above equation, we have subtracted 1 from the numerator because this is the number of events arising due to the atmospheric muons, and we treat this as a background. From the total number of tracks, we subtract the expected number of tracks produced by muons, which rounds down to 1. In the denominator, we have added the events corresponding to cascade and double cascade to obtain the total number of shower events. Cascade events refer to a series of decays or interactions that produce a large number of secondary particles, and these events typically have a spherical topology. A double cascade event occurs when an additional cascade event is created from showering particles, and the topology of these events resembles a distorted sphere.

Morphology	Cascade	Track	Double Cascade
Total	72.7 %	23.4 %	3.9 %
ν_e	56.7%	9.8%	21.1%
ν_μ	15.7%	72.8%	14.2%
ν_τ	27.6%	10.5%	64.7%
μ	0.0%	6.9%	0.0%

Table 5.3: Expected events by category for best-fit parameters above 60 TeV are presented in tabular form. Each column represents the reconstructed event morphology, while each row corresponds to a specific particle. The top table displays the percentage of events expected in each morphology relative to the total number of events. The bottom table illustrates the percentage of events in each category for a specific morphology, where the percentages were calculated with respect to the total number of expected events for that particular morphology. When addressing background noise, the contribution of track events from muons will be taken into account. The percentages have been rounded to one decimal point [269].

To define a theoretical track by shower ratio, we refer to table 5.3. This table shows the event morphology, i.e., the fraction of events from different neutrino flavors that can cause a track or a shower event at IceCube for deposited neutrino energy greater than 60 TeV. Using this information, one can define the theoretical track by shower ratio as

$$R = \frac{P_t \sum_\alpha p_t^\alpha \phi_\alpha}{P_c \sum_\alpha p_c^\alpha \phi_\alpha + P_{dc} \sum_\alpha p_{dc}^\alpha \phi_\alpha}. \tag{5.25}$$

where $P_t/P_c/P_{dc}$ is the probability of getting a track/cascade/double cascade event at IceCube. These probabilities are given in the first row of table 5.3. The above equation defines the probabilities for each neutrino flavor α leaving a track/cascade/double cascade signal (denoted by i) at IceCube by p_i^α. The term ϕ_α is the flux of the oscillated neutrinos at Earth.

To compare these two R_{exp} and R, which we constructed above, we define a simple Gaussian χ^2 in the following way:

$$\chi^2 = \left(\frac{R_{exp} - R(\theta_{ij}, \delta_{13})}{\sigma_R}\right)^2, \tag{5.26}$$

where σ_R is given by,

$$\sigma_R = \sqrt{\frac{(1 - R_{exp})R_{exp}}{N}}, \tag{5.27}$$

where N is the total number of events. As the total number of events is not very high, we have not considered any systematic uncertainty in our analysis. We do not expect to have a major impact of systematic uncertainties on our results.

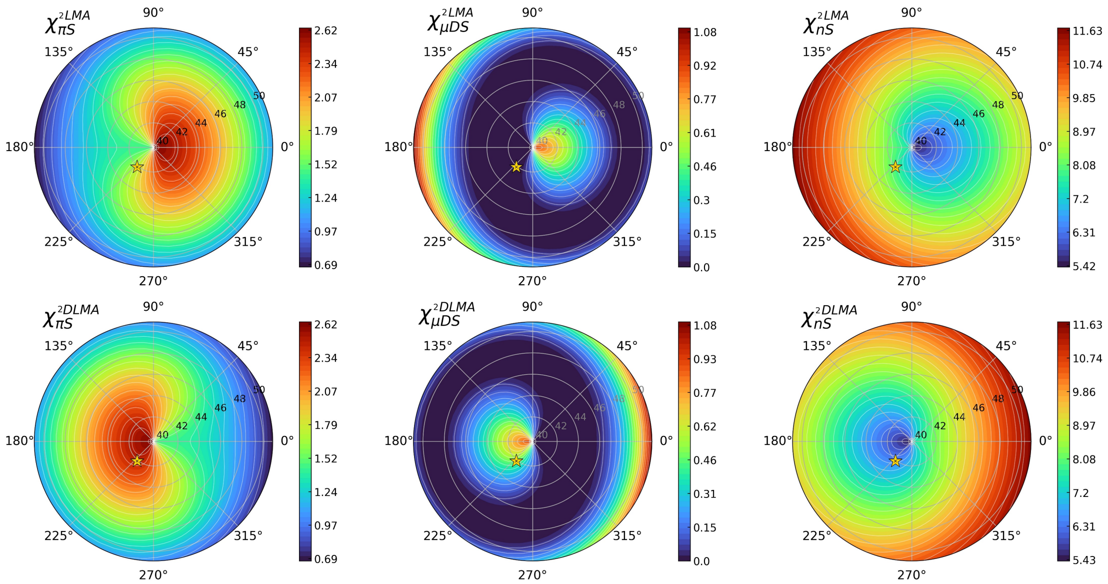

Figure 5.2: χ^2 polar contour plots in dependence of $\delta_{\rm CP}$ and θ_{23} marginalized over θ_{13} and θ_{12}. The polar radius represents θ_{23}, and the polar angle represents $\delta_{\rm CP}$. Values of χ^2 are represented by colors shown next to the corresponding plot. The upper row shows calculations for the LMA solution, and the lower row for the DLMA solution. Columns represent the pion, muon, and neutron sources, respectively. Current best-fit value for θ_{23} and $\delta_{\rm CP}$ is marked by a star at coordinates (42.1°, 230°).

In fig. 5.2, we have plotted the polar plots of this χ^2 for the three different astrophysical sources in θ_{23} and $\delta_{\rm CP}$ plane. In generating this plot, we have minimized over θ_{12} and θ_{13} over their 3σ allowed ranges as listed in table 5.1. In these panels, the different color shades correspond to different values of χ^2, which are given in the z-axis. The top row is for the LMA solution of θ_{12} whereas the bottom row is for the DLMA solution of θ_{12}. In each row, the left panel is for π source, the middle panel is for μ source, and the right panel is for n source. To understand the χ^2 results, in fig. 5.3, we have plotted the same as in fig. 5.2 but for theoretical track by shower ratio i.e., R. This figure is generated using the best-fit values of θ_{12} and θ_{13}. From figures 5.2 and 5.3, the following can be concluded:

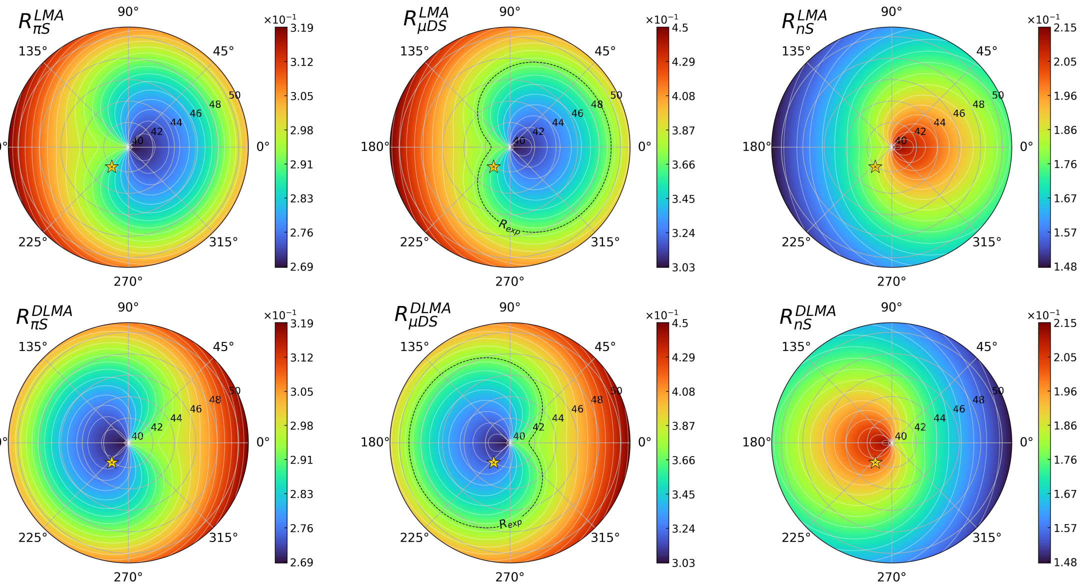

Figure 5.3: Track by shower ratio contour plots in dependence of δ_{CP} and θ_{23}. Best-fit values were taken for θ_{12} and θ_{13}. The polar radius represents θ_{23}, and the polar angle represents δ_{CP}. Values of χ^2 are represented by colors shown next to the corresponding plot. The upper row shows calculations for the LMA solution, and the lower row for the DLMA solution. Columns represent the pion, muon, and neutron sources, respectively. The black dashed line represents the experimental value of the ratio measured at IceCube. The current best-fit value for θ_{23} and δ_{CP}, and the corresponding value of the ratio for a given source, is marked by a star at coordinates (42.1°, 230°).

- The variation of the color shading between the figures 5.2 and 5.3 are consistent. This shows the information of R is correctly reflected in the χ^2 plots.

- The existence of degeneracy defined by $\chi^2(\theta_{12}^{LMA}, \delta_{13}) = \chi^2(\theta_{12}^{DLMA}, 180° - \delta_{13})$ and $R(\theta_{12}^{LMA}, \delta_{13}) = R(\theta_{12}^{DLMA}, 180° - \delta_{13})$ for a given value of θ_{23} is clearly visible in figures 5.2 and 5.3, respectively. We can consider any point in these figures and take a 180° transformation we will get the degenerate solutions. The same arguments from the previous discussion also apply here.

- The degeneracy between $\delta_{13} \to -\delta_{13}$ for a given LMA/DLMA solution is also visible in figures 5.2 and 5.3.

- Degeneracy between θ_{23} and the two solutions of θ_{12} for a given value of δ_{13} is carried over from probabilities and is still present in figures 5.2 and 5.3.

- Among the three sources, the μ source is the most preferred source by the IceCube data as for this source, we obtain a χ^2 value of 0 (middle column of fig. 5.2). From the panels, we see that the data does not prefer a particular value of θ_{23} and δ_{13}, rather it is consistent with a region in the θ_{23} - δ_{13} plane. The best-fit regions of the θ_{23} - δ_{13} plane can be understood by looking at the middle column of fig. 5.3. In these panels, the value of R_{exp} is drawn over R. This shows the values of θ_{23} - δ_{13} for which the prediction of track by shower ratio matches exactly with the data. Note that though R_{exp} in the middle column of fig. 5.3 is a curve, the best-fit region in the middle column of fig. 5.2 is not a curve, rather it is a plane. The reason is two fold: (i) In fig. 5.2 we have marginalized over the parameters θ_{13} and θ_{12}. Because of this, there can be many more combinations of θ_{23} and δ_{13} which can give the exact value of R_{exp} as compared to fig. 5.3 which is generated for a fixed value of θ_{13} and θ_{12}. (ii) In polar plots, we don't have the precision to shade a region corresponding to exactly $\chi^2 = 0$. In these plots, $\chi^2 = 0$ is defined by a large set of very small numbers. This is why the best-fit region appears as a large black area. As we mentioned earlier, with the help of the χ^2 plots, we can infer the true nature of θ_{12} given δ_{13} is measured from the other experiments. According to the current-best fit scenario, it can be said that IceCube data prefers the LMA solution of θ_{12} because at this best-fit value (denoted by the star), we obtain the non-zero χ^2 for the DLMA solution of θ_{12}.

- The second most favored source, according to the IceCube data, is the π source. For this source, the minimum χ^2 is 0.7. As the minimum χ^2 value is much less, one can say that the π source and the μ source are almost equally favored. In this case, the best-fit region in the θ_{23} - δ_{13} plane is smaller than the μ source. For this source, the upper octant of θ_{23} is preferred for both LMA and DLMA solutions of θ_{23}. Regarding δ_{13}, the best-fit value is around 180° for LMA solution of θ_{12} whereas for DLMA solution of θ_{12}, the best-fit value is around 0°/360°. For this source, the current best-fit value (denoted by a star) is excluded at $\chi^2 = 1.7(2.4)$ for the LMA (DLMA) solution of θ_{12}.

- The n source is excluded by IceCube at more than 2σ C.L., as the minimum χ^2 in this case is 5.4. In this case, the region with lowest χ^2 value in the θ_{23} - δ_{13} plane is smaller than the μ source. The n source prefers the lower octant of θ_{23} for both LMA and DLMA solutions of θ_{12}. Regarding δ_{13}, the best-fit value is around 180° for DLMA solution of θ_{12} whereas for LMA solution of θ_{12}, the best-fit value is around 0°/360°. For this source, the current best-fit value (denoted by a star) is excluded at $\chi^2 = 7.9(6.5)$ for the LMA (DLMA) solution of θ_{12}.

5.3 Summary and Conclusion

In this paper, we have studied the implications of measurement of θ_{23} and δ_{13} in IceCube data in the light of the DLMA solution of θ_{12}. IceCube is an ongoing neutrino experiment at the South Pole that studies neutrinos from astrophysical sources. In the astrophysical sources, neutrinos are produced via three mechanisms: πS process, μDS process, and neutrino decay. As the neutrinos coming from the astrophysical sources change their flavor during propagation, it is possible to measure the neutrino oscillation parameters by analyzing the IceCube data. Because of the large distance of the astrophysical sources and high energy of the astrophysical neutrinos, the oscillatory terms in the neutrino oscillation probabilities get averaged out. As a result, the neutrino oscillation probabilities become independent of the mass square differences.

In our work, we first identify the oscillation probability channels responsible for the conversion of the neutrino fluxes for the three different sources mentioned above. Then we identified the degeneracies in neutrino oscillation parameters relevant to IceCube. We have shown the existence of an intrinsic degeneracy between the two solutions of the θ_{12} and δ_{13}. As this degeneracy stems at the Hamiltonian level, it is impossible for IceCube alone to simultaneously measure δ_{13} and the true nature of θ_{12}. However, if δ_{13} can be measured from other experiments, it might be possible for IceCube to pinpoint the true nature of θ_{12}. Apart from this, we also identified a degeneracy between θ_{23} and two possible solutions of θ_{12} for a fixed value of δ_{13}. In addition, we also identified a degeneracy defined by $\delta_{13} \rightarrow 360^\circ - \delta_{13}$ within LMA and DLMA solution of θ_{12}.

Taking the track by shower as an observable, we analyze the 7.5 years of IceCube data. Our results show that the IceCube data prefers the μ source among the three sources. However, in this case, the data does not prefer a particular best-fit of θ_{23} and δ_{13} rather, the data is consistent with a large region in the θ_{23} - δ_{13} plane. After the μ source, the next favorable source of the astrophysical neutrinos, according to the IceCube data, is the π source. However, as both μ and π sources are allowed within 1σ, one can say that both sources are almost equally favored by IceCube. The n source is excluded at 2σ by IceCube. Unlike, μ source, the allowed region in the θ_{23} - δ_{13} plane is smaller for both π and n source. π (n) source prefers higher (lower) octant for θ_{23} for both LMA and DLMA solution of θ_{12}. Regarding δ_{13}, the best-fit value is around

$180°$ ($0°/360°$) for LMA (DLMA) solution of θ_{12} whereas for DLMA (LMA) solution of θ_{12}, the best-fit value is around $0°/360°$ ($180°$) for π (n) source. If we assume the current best-fit value of θ_{23} and δ_{13} to be true, then the μ and π source prefers the LMA solution of θ_{12} whereas the n source prefers the DLMA solution of θ_{12}.

In conclusion, we can say that analysis of IceCube data in terms of track by shower ratio can give important information regarding the measurement of θ_{23}, δ_{13} and the true nature of θ_{12}. However, we find that the current statistics of IceCube are too low to make any concrete statements regarding the above measurements.

"The true laboratory is the mind, where behind illusions we uncover the laws of truth."

Sir Jagadish Chandra Bose

6

Sensitivity to CP discovery at T2HKK and T2HK in presence of LIV

Lorentz invariance is one of the cornerstones of the local relativistic field theories. Violation of the same will indicate the existence of new physics beyond the SM. The minimal Standard-Model Extension (SME) introduces the Lorentz invariance and CPT violation through spontaneous symmetry breaking. This can have sub-leading effects on neutrino propagation. In this chapter, we explore the implications of CPT violating LIV phases on CP discovery potential in the context of the T2HK/T2HKK experiment. This chapter is based on [270].

In this chapter, we explore the effects of CPT violating LIV parameters on the detection of CP phase in the upcoming T2HK[271]/T2HKK[167] detector. A recent study has been performed to give bounds on LIV parameters using INO-ICAL, T2HK, and DUNE in [272]. There has been a study in NOνA and T2K in [273]. Efforts have been made to separately understand the effects of LIV interactions and non-standard interactions (NSI) at long baseline experiments in [274, 275]. Other recent studies related to CPT violation and LIV interactions in neutrinos can be found in [276–284].

The structure of this chapter is as follows. At first, an insight into the formalism of LIV in the neutrino sector is provided in section 6.1. It's followed by a discussion on the dependence of the neutrino oscillation probabilities on LIV parameters in section 6.2. We present the numerical analysis for CP discovery in the presence of non-diagonal CPT violating NSI parameters in section 6.3.

6.1 Theory of Lorentz invariance violation

LIV in the neutrino sector has been introduced in the subsection 1.6.3. The total Hamiltonian for neutrino propagation in the presence of CPT violating LIV parameters, including the standard MSW matter effect, is given by,

$$H_{tot} = \frac{1}{2E}\begin{pmatrix} m_1^2 & 0 & 0 \\ 0 & m_2^2 & 0 \\ 0 & 0 & m_3^2 \end{pmatrix} + \begin{pmatrix} \sqrt{2}G_F N_e & 0 & 0 \\ 0 & 0 & 0 \\ 0 & 0 & 0 \end{pmatrix} + \begin{pmatrix} a_{ee} & a_{e\mu} & a_{e\tau} \\ a_{e\mu}^\star & a_{\mu\mu} & a_{\mu\tau} \\ a_{e\tau}^\star & a_{\mu\tau}^\star & a_{\tau\tau} \end{pmatrix} \tag{6.1}$$

Here, we only consider CPT-violating LIV parameters $a_{\alpha\beta}$ whose constraints are drawn from Super-Kamiokande[285]. The non-diagonal parameters are complex and given by $a_{\alpha\beta} = |a_{\alpha\beta}|e^{\iota\phi_{\alpha\beta}}$ where as diagonal parameters $a_{\alpha\alpha}$ are real. There is an established correlation between CPT-violation LIV parameters and matter NSI parameters given by,

$$\epsilon_{\alpha\beta}^m \equiv \frac{a_{\alpha\beta}}{\sqrt{2}G_F N_e} \tag{6.2}$$

Irrespective of their correlation, their origins are very different as well as the effect, e.g, the matter NSI produces in neutrino propagation is just an extra exotic matter effect similar to the MSW matter effect, whereas CPT-violating LIV has an intrinsic effect on neutrino propagation even in vacuum. Current bounds on LIV parameters are given below in table 6.1 [285, 286].

Parameter	SK Bound	IceCube Bound
$a_{e\mu}$	1.8×10^{-23} GeV	N.A.
$a_{e\tau}$	4.1×10^{-23} GeV	N.A.
$a_{\mu\tau}$	0.65×10^{-23} GeV	0.29×10^{-23} GeV

Table 6.1: The table depicts 95% C.L. bounds of CPT violating non-diagonal LIV parameters from SK and IceCube experiments

6.2 Probabilities in presence of LIV parameters

In our study, we probe the effects of the CPT violating NSI parameters $a_{e\mu}, a_{e\tau}, a_{\mu\tau}$ on the discovery of CP at proposed long baseline experiment configuration of Tokai to hyper Kamiokande (T2HK). The setup of T2HK provides a muon beam, which can be observed at detector hyper Kamiokande, 295 Km away from the source, 1100 km away from the source. At the leading order of $\alpha = \Delta_{21}/\Delta_{31}$, the appearance probability $P_{\mu e}$ depends only on parameters $a_{e\mu}, a_{e\tau}, \phi_{e\mu}, \phi_{e\tau}$ whereas, the disappearance probability depends on $a_{\mu\tau}, \phi_{\mu\tau}$. The probabilities are calculated in ref. [287, 288] as follows,

$$P_{\mu e} = P_{\mu e}^{3\nu} + P_{\mu e}^{a_{e\mu}} + P_{\mu e}^{a_{e\tau}} \tag{6.3}$$

$$P_{\mu\mu} = P_{\mu\mu}^{3\nu} + P_{\mu\mu}^{a_{\mu\tau}}, \tag{6.4}$$

where $P_{\mu e}^{3\nu}, P_{\mu\mu}^{3\nu}$ are the three flavor oscillation probabilities in the matter, and the LIV-induced part of the probabilities are given as,

$$P_{\mu e}^{3\nu} = 4s_{13}^2 s_{23}^2 \frac{\sin^2[(\hat{A}-1)\Delta]}{(\hat{A}-1)^2} + 2\alpha s_{13} \sin 2\theta_{12} \sin 2\theta_{23} \frac{\sin[\hat{A}\Delta]}{\hat{A}} \frac{\sin[(\hat{A}-1)\Delta]}{\hat{A}-1} \cos(\Delta + \delta_{13}) \tag{6.5}$$

$$P_{\mu e}^{a_{e\mu}} \simeq \frac{4|a_{e\mu}|\hat{A}\Delta s_{13} \sin 2\theta_{23} \sin\Delta}{\sqrt{2}G_F N_e}[Z_{e\mu}\sin(\delta_{13}+\phi_{e\mu}) + W_{e\mu}\cos(\delta_{13}+\phi_{e\mu})] \tag{6.6}$$

$$P_{\mu e}^{a_{e\tau}} \simeq \frac{4|a_{e\tau}|\hat{A}\Delta s_{13} \sin 2\theta_{23} \sin\Delta}{\sqrt{2}G_F N_e}[Z_{e\tau}\sin(\delta_{13}+\phi_{e\tau}) + W_{e\tau}\cos(\delta_{13}+\phi_{e\tau})] \tag{6.7}$$

$$P_{\mu\mu}^{a_{\mu\tau}} = \frac{4|a_{\mu\tau}|\hat{A}\Delta \sin 2\theta_{23} \sin\Delta}{\sqrt{2}G_F N_e}[Z_{\mu\tau}\cos\phi_{\mu\tau} + W_{\mu\tau}\cos\phi_{\mu\tau}] \tag{6.8}$$

where $\Delta = \frac{\Delta_{31}L}{4E}$, $\alpha = \Delta_{21}/\Delta_{31}$, $\hat{A} = \frac{2\sqrt{2}G_F N_e E}{\Delta_{31}}$, $A = 2\sqrt{2}G_F N_e E$, $s_{ij} = \sin\theta_{ij}$, $c_{ij} = \cos\theta_{ij}$,

$$Z_{e\mu} = -\cos\theta_{23}\sin\Delta, \quad Z_{e\tau} = \sin\theta_{23}\sin\Delta, \quad Z_{\mu\tau} = -\sin^2 2\theta_{23}\cos\Delta \tag{6.9}$$

$$W_{e\mu} = c_{23}(\frac{s_{23}^2\sin\Delta}{\Delta.c_{23}^2} + \cos\Delta), W_{e\tau} = s_{23}(\frac{\sin\Delta}{\Delta} - \cos\Delta), W_{\mu\tau} = \frac{-\cos^2 2\theta_{23}\sin\Delta}{\Delta} \tag{6.10}$$

6.2.1 Variation in $P_{\mu e}$ with phases at fixed $a_{e\mu}, a_{e\tau}, a_{\mu\tau}$

In the presence of the LIV parameters, the appearance channel probability depends on the parameters $a_{e\mu}, a_{e\tau}$, and $a_{\mu\tau}$. This also shows dependence on the LIV phases $\phi_{e\mu}, \phi_{e\tau}$ in conjunction with δ_{13}. The modifications in $P_{\mu e}$ due to LIV parameters are probed in this section at 1100 and 295 km baselines. In the following plots, the values of the oscillation parameters being chosen are, $\theta_{12} = 33.44°, \theta_{13} = 8.57°, \theta_{23} = 49°, \Delta_{21} = 7.42 \times 10^{-5}$ eV^2, and $|\Delta_{31}| = 2.515 \times 10^{-3}$ eV^2. $P_{\mu e}$ is plotted as a function of δ_{13} at 0.6 GeV in fig. 6.1 for normal (top panel) and inverted (bottom panel) mass orderings in case of 295 km (red), and 1100 km (blue) baseline while the values of the non-diagonal LIV parameters are kept fixed at 10^{-23} GeV. The bands refer to the variation of LIV phases. The significant points to be noted are as follows,

- It can be observed from both top and bottom panels that the effect of $\phi_{e\mu}, \phi_{e\tau}$ is larger than $\phi_{\mu\tau}$ as the width of the red and blue bands are narrower in the right panels than the left and middle ones. This can be understood from the eq. (6.6), (6.7) as $P_{\mu e}$ has no contribution from $\phi_{\mu\tau}$ at the leading order. However, a weak dependence is present in the numerical plots in the right-hand column.

- In the case of NO(upper panels), the variation of $P_{\mu e}$ with δ_{13} for 1100 km is sharper as 0.6 GeV is adjacent to the second oscillation maxima(0.7 GeV). However, in 295 km the variation is less due to the first oscillation maxima occurring at 0.6 GeV. Thus, probabilities at CP conserving values $0°, \pm180°$ are more separated from probabilities at other CP violating values at 1100 km than at 295 km.

- Also, in the case of NO, the maxima and minima of $P_{\mu e}$ happen at different δ_{13} values for 295 km and 1100 km. For instance, the probabilities at $\delta_{13} = \pm 90°$

have a maximum difference from probabilities at CP conserving values for 295 km. However, in the case of 1100 km, the probabilities at $\delta_{13} = \pm 90°$ are very close to probability values at $\pm 180°$. Therefore, while evaluating the sensitivity to CP discovery at $\delta_{13} = \pm 90°$, there will be a higher sensitivity for 295+1100 km configuration than individual 295 km and 1100 km due to the synergy.

- For IO, The variation with δ_{13} is very flat at 1100 km while the variation at 295 km remains similar. This leads to poor sensitivity for CP discovery for the T2HKK configuration.

The disappearance probability $P_{\mu\mu}$ doesn't depend on the CP phase. Therefore, in the case of $P_{\mu\mu}$, dependence on $\phi_{\mu\tau}$ isn't linked with δ_{13}.

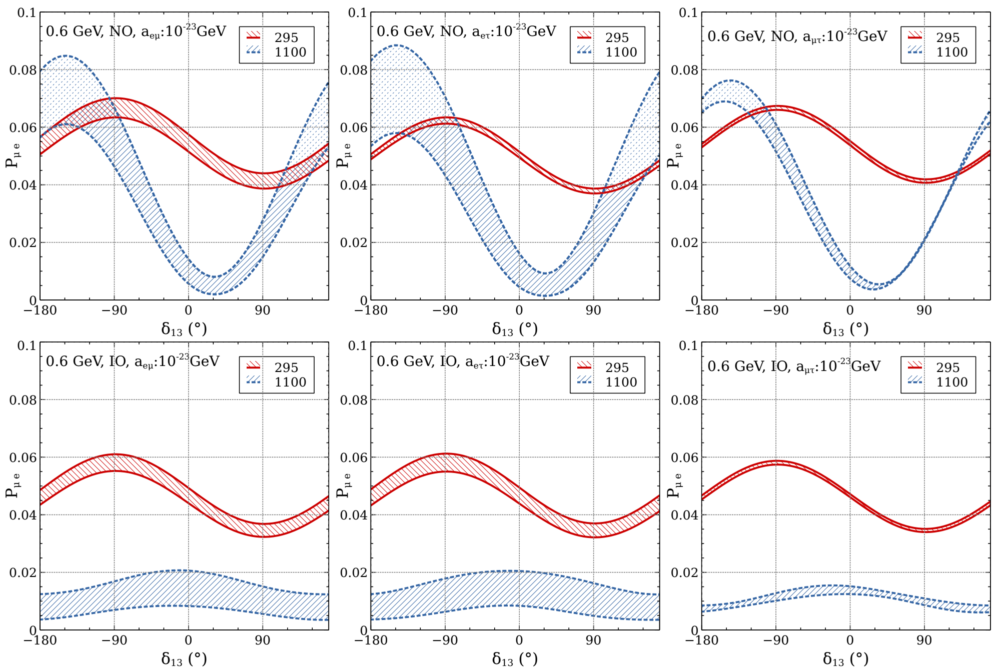

Figure 6.1: $P_{\mu e}$ as a function of δ_{13} for $\theta_{23} = 49°$, $a_{e\mu} = 10^{-23}$ GeV (left), $a_{e\tau} = 10^{-23}$ GeV (middle), and $a_{\mu\tau} = 10^{-23}$ GeV (right) due to variation of respective phases $\phi_{e\mu}, \phi_{e\tau}, \phi_{\mu\tau}$ for NO(top), IO(bottom) at 0.6 GeV in 295 km (red), 1100 km(blue)

In fig. 6.2, the oscillation probabilities $P_{\mu e}, P_{\bar{\mu}\bar{e}}$ are plotted as a function of δ_{13} at fixed energy of 0.6 GeV corresponding to 295 km and 1100 km baselines for NO, IO considering $\theta_{23} = 49°$ and $a_{e\mu} = 10^{-23}$ GeV. We observe the following features,

- In 1100 km, the $P_{\mu e}$ probabilities have larger values than $P_{\bar{\mu}\bar{e}}$ in NO. However, in IO that order reverses.

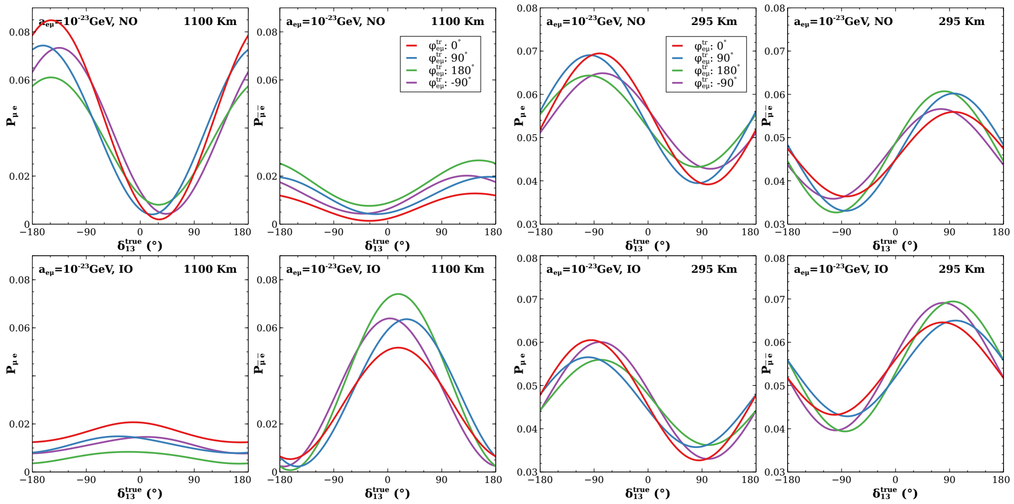

Figure 6.2: $P_{\mu e}$, $P_{\bar{\mu}\bar{e}}$ as a function of δ_{13}^{true} for true values of $\theta_{23} = 49°$, $a_{e\mu} = 10^{-23}$ GeV. Two panels on the left(right) refer to 295 km (1100 km) for NO(top) and IO(bottom). Violet, red, green, blue refer to $\phi_{e\mu}^{true} = -90°, 0°, 90°, 180°$ respectively.

- In NO, the $P_{\mu e}$ curves show a peak at the lower half plane (LHP)[$-180°$: $0°$] in the range $-160°$: $-130°$. The peaks of $P_{\bar{\mu}\bar{e}}$ curves occur at the upper half plane (UHP)[$0°$: $180°$] in the range $130°$: $170°$.
- In the case of IO for 1100 km, both the $P_{\mu e}$, $P_{\bar{\mu}\bar{e}}$ has maxima around $0°$.
- In 295 km, various probabilities for different values of $\phi_{e\mu}$ vary over a small region while being very close to each other.
- In 295 km, the maxima of $P_{\mu e}$, $P_{\bar{\mu}\bar{e}}$ curves occur around $\pm 90°$ for both NO and IO.
- In the case of both 295 km and 1100 km, the red (green) curves give the maximum (minimum) variation in $P_{\mu e}$. In $P_{\bar{\mu}\bar{e}}$, this order reveres.

6.3 χ^2 Analysis of CP discovery

In this section, we study the potential of the T2HKK/T2HK experiments for CP discovery. The configurations for the proposed experiments are as follows, (i) T2HK (Tokai to Hyper-Kamiokande): two detectors of 187 kton at 295 km, (ii)T2HKK (Tokai to Hyper-Kamiokande and Korea): one detector of 187 kton at 295 km and another similar detector at 1100 km away in Korea[289]. For our study, we consider the first detector at an off-axis angle of 2.5° and the second detector of T2HKK at an off-axis angle of 1.5°

Parameter	True Value	Marginalization Range
θ_{12}	$33.4°$	N.A.
θ_{13}	$8.62°$	N.A.
θ_{23}	$49°$	$39° : 51°$
δ_{13}	$-180° : 180°$	$0°, 180°$
Δ_{21}	7.4×10^{-5} eV^2	N.A.
$\lvert\Delta_{31}\rvert$	2.5×10^{-3} eV^2	$2.4 : 2.6 \times 10^{-3}$ eV^2
$a_{\alpha\beta}$	10^{-23} GeV	$10^{-22} : 10^{-24}$ GeV
$\phi_{\alpha\beta}$	$-180° : 180°$	$0°, 180°$

Table 6.2: True values[101] of all the parameters and their range of marginalization

from the source at the J-PARC facility in Tokai[167]. The T2HKK experiment offers us the advantage of a large matter effect at 1100 km. For our numerical analysis with GLoBES[103, 104], we use a proposed beam of energy 1.3 MW considering 2.5 years of neutrino mode and 7.5 years of anti-neutrino mode run time with an exposure of 27×10^{21} proton on target (POT). The detector configuration and systematic errors are taken from [167].

The final value of χ^2 is derived after marginalization over pull variables ξ, and variables of oscillation ω as follows,

$$\Delta\chi^2 = Min[\chi^2_{stat}(\omega, \xi) + \chi^2_{pull}(\xi)], \tag{6.11}$$

where χ^2_{pull} includes the symmetric errors and the Poissonian χ^2_{stat} is defined in terms of total true no of events N_i^{true} and events generated by theoretical model N_i^{test} in the i^{th} energy beam.

$$\chi^2_{stat}(\omega, \xi) = 2\sum_i [N_i^{test} - N_i^{true} + N_i^{true} \ln \frac{N_i^{true}}{N_i^{test}}];\ \chi^2_{pull} = \sum_{r=1}^{4} \xi_r^2 \tag{6.12}$$

The systematic uncertainties are included through the method of pull in terms of variables: signal normalization error, background normalization error, energy calibration error on signal, and background (tilt). We have seen in table 6.1 the current bound for NSI parameters are $\sim 10^{-23}$ GeV. Therefore, we have considered true values of $a_{e\mu}, a_{e\tau}, a_{\mu\tau} = 10^{-23}$ GeV throughout our study. For numerical analysis for CP discovery in standard three flavor case, the test values are considered as $\delta_{13} = 0°, 180°$. Similarly, in the presence of an extra LIV phase, we consider test values of $\delta_{13}, \phi_{\alpha\beta}$ as combinations of $0°, 180°$. While performing chi-square(χ^2) analysis in the presence of

Channel	295 km	1100 km
ν_e Appearance	3.2%(5%)	3.8%(5%)
ν_μ Disappearance	3.6%(5%)	3.8%(5%)
$\bar{\nu}_e$ Appearance	3.9%(5%)	4.1%(5%)
$\bar{\nu}_\mu$ Disappearance	3.6%(5%)	3.8%(5%)

Table 6.3: The signal (background) normalization uncertainties of the experiments for different channels

LIV, we consider one parameter to be non-zero at a time. Apart from phases, we have marginalized the chi-square over θ_{23} and $|\Delta_{31}|$. The true values and the marginalization ranges of the parameters are given in table 6.2. The run time in neutrino and anti-neutrino mode is 2.5 years and 7.5 years, respectively.

6.3.1 Single detector analysis

In this section, the sensitivity to CP discovery is probed with a single detector at 295 km and 1100 km. This helps in understanding the features of these individual baselines. The total event rates get equal contributions from neutrinos and anti-neutrinos because of the chosen run time. Therefore, studying sensitivity for individual channels will help in understanding the total sensitivity. In this section, we study the effect of only the NSI parameter $a_{e\mu}$ as a representative case.

The χ^2 in ν_e, $\bar{\nu}_e$, neutrino $(\nu_e + \nu_\mu)$, anti-neutrino $(\bar{\nu}_e + \bar{\nu}_\mu)$ modes, and the total χ^2, is plotted from first to fifth row, respectively, corresponding to 1100 km (295 km) in fig. 6.3 (fig. 6.4). The left(right) panels of the figures refer to the NO (IO). The different true values of $\phi_{e\mu} = -90°, 0°, 90°, 180°$ have been shown by violet, red, blue, and green curves, respectively. The features of significance in fig. 6.3 are as follows,

- In the ν_e mode (NO), the red curve $\phi_{e\mu} = 0°$ has the maximum sensitivity in both half-planes but in LHP the magnitude at the peak is significantly larger. The green curve $\phi_{e\mu} = 180°$ has the lowest sensitivity. This is consistent with the features seen from the plot of $P_{\mu e}$ in the left panels of fig. 6.2.

- In the case of IO in the ν_e mode, the red (green) shows the maximum (minimum) sensitivity and the value of χ^2 is higher in UHP than LHP.

- In the $\bar{\nu}_e$ mode (NO), the highest sensitivity is achieved for the green $\phi_{e\mu} = -90°$

and blue curve $\phi_{e\mu} = 180°$ in both UHP and LHP but the peak value in UHP is higher.

- In the context of IO for $\bar{\nu}_e$ mode, the green (red) curve reaches the maximum (minimum) value of χ^2. The green curve's maximum value of χ^2 is predominantly the highest in UHP. The other curves also have maxima of higher value in UHP.

- The third and fourth row shows the χ^2 in $\nu_e + \nu_\mu$ and $\bar{\nu}_e + \bar{\nu}_\mu$ channels. Here, a significant increase in sensitivity is observed due to the synergistic effect between the appearance and disappearance channel. This is discussed further in fig. 6.5.

- In the case of total sensitivity (NO), the red curve ($\phi_{e\mu} = 0°$) has the highest sensitivity in the UHP, and the blue curve ($\phi_{e\mu} = 180°$) reaches the maximum sensitivity in the LHP. While marginalizing, the minimum of χ^2 occurs at different values of the parameters for neutrino and anti-neutrino, leading to a synergistic effect in total sensitivity.

- In the case of IO for the total sensitivity, the green curve ($\phi_{e\mu} = 0°$) has the maximum χ^2 in both LHP and UHP with the latter case having significantly higher value.

- The sensitivity curves for $\phi_{e\mu} = -90°, 90°$ show non-zero sensitivity at $\delta_{13}^{true} = 0°, \pm 180°$. This happens as the test values $\phi_{e\mu}, \delta_{13}$ don't add to give a CP conserving values of $0°, 180°$.

The main observations of fig. 6.4 are as follows,

- In the case of both NO and IO, in the ν_e mode, the red ($\phi_{e\mu} = 0°$) curves show the maximum sensitivity in LHP. However, in UHP, all curves have very low and similar sensitivity. In the $\bar{\nu}_e$ mode, the sensitivity for all the curves in both UHP and LHP is almost similar and very low.

- In both NO and IO, we observe higher sensitivity in neutrino mode. This is due to the fact that $P_{\mu e}$ curves have a higher range of variation than $P_{\bar{\mu}\bar{e}}$ ones as was seen in fig. 6.2.

- The addition of $\nu_\mu(\bar{\nu}_\mu)$ has led to a rise in the sensitivity in neutrino (anti-neutrino) mode as seen from figures in the third (fourth) row.

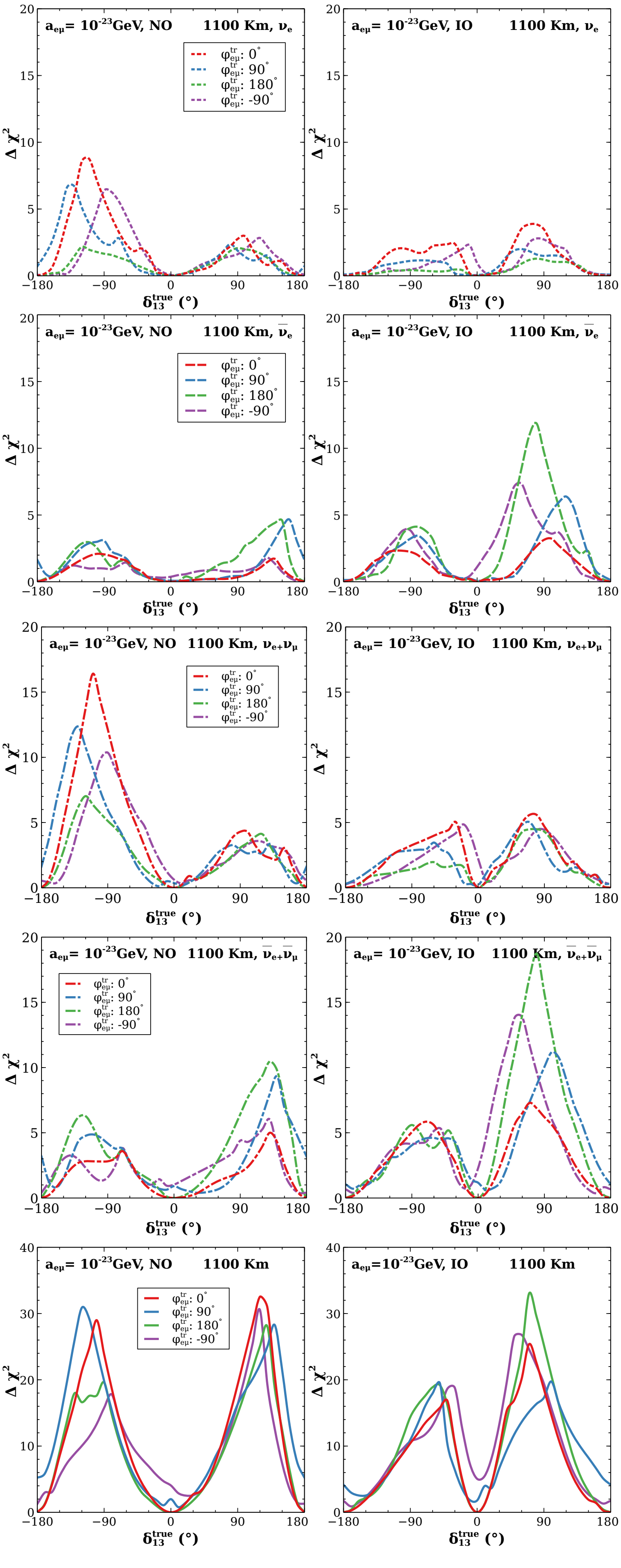

Figure 6.3: χ^2 in ν_e (first), $\bar{\nu}_e$ (second), $\nu_e + \nu_\mu$ (third), $\bar{\nu}_e + \bar{\nu}_\mu$ (fourth) modes and total χ^2 (bottom) as a function of δ_{13}^{true} for true values of $\theta_{23} = 49°$ with $a_{e\mu} = 10^{-23}$ GeV at 1100 km for NO (left), IO(right).

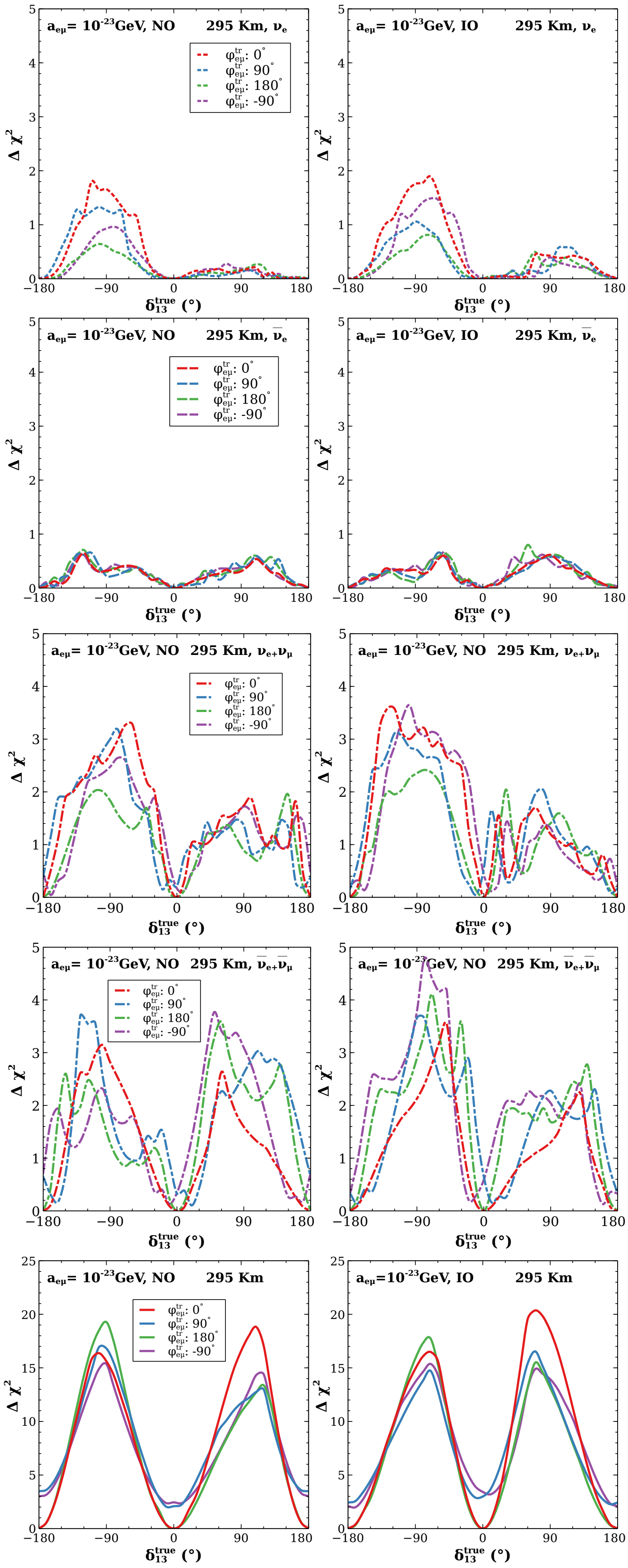

Figure 6.4: χ^2 in ν_e (first), $\bar{\nu}_e$ (second), $\nu_e+\nu_\mu$ (third), $\bar{\nu}_e+\bar{\nu}_\mu$ (fourth) modes and total χ^2 (bottom) as a function of δ_{13}^{true} for true values of $\theta_{23}=49°$ with $a_{e\mu}=10^{-23}$ GeV at 295 km for NO (left), IO(right).

- In the case of total sensitivity, all the curves have similar sensitivity except for the red curve ($\phi_{e\mu}^{tr} = 0°$) and green curve ($\phi_{e\mu}^{tr} = 180°$) showing highest χ^2 in UHP and LHP respectively.

- The total sensitivity is significantly higher than the sensitivity of ν_e and $\bar{\nu}_e$ channels. This is due to the synergy between the two channels, which is depicted in fig. 6.5 where we plot the χ^2 as a function of θ_{23}^{test}.

The synergy between various channels in the test θ_{23} is depicted in fig. 6.5 for 1100 km (right panel) and 295 km (left panel). It is observed that the shape of the total chi-square is dictated by the $\nu_\mu, \bar{\nu}_\mu$ channels. Therefore, minima of the total sensitivity are obtained near the minima of the $\nu_\mu, \bar{\nu}_\mu$ channels with $\theta_{23} = 49°$ giving the lowest χ^2. At the minima, the $\chi^2 \sim 0$ for $\nu_\mu, \bar{\nu}_\mu$ channels. However, the non-zero contribution from the $\nu_e, \bar{\nu}_e$ channels boosts the total chi-square. At 1100 km, the $\bar{\nu}_e$ channel contributes more at minima, whereas, in 295 km, both $\nu_e, \bar{\nu}_e$ give equal contribution at minima. Due to the opposite nature w.r.t θ_{23}^{test}, further synergy is observed between ν_e and $\bar{\nu}_e$ channels, elevating the total sensitivity.

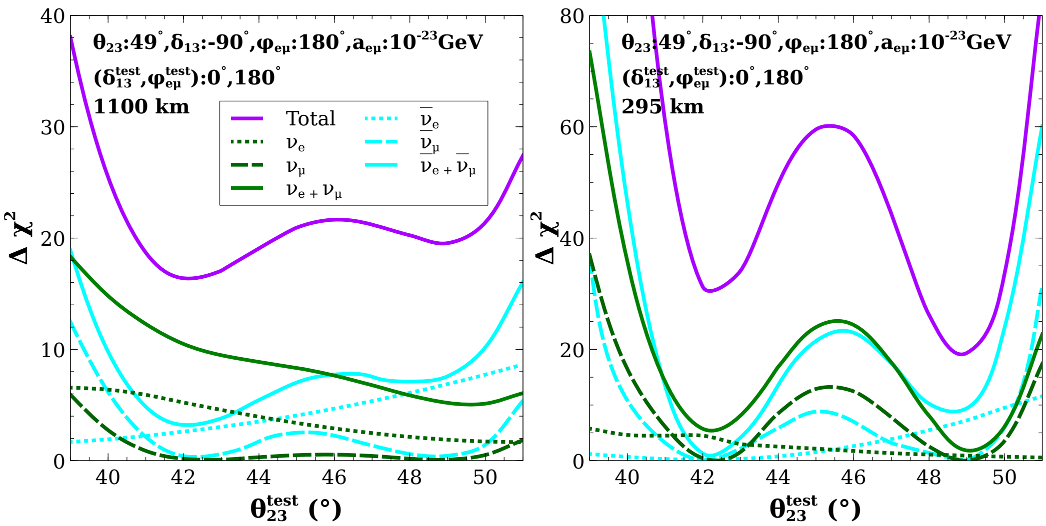

Figure 6.5: χ^2 as a function of θ_{23}^{test} at 295 km (left), 1100 km (right). Green (blue) refers to $\nu(\bar{\nu})$ channels and violet gives total χ^2. The dotted, dashed, and dashed curves signify electron, muon, and both channels together, respectively.

6.3.2 Comparative analysis between T2HKK and T2HK

In this section, we compare and contrast the CP discovery potential of the proposed T2HKK and T2HK configurations. This study is performed for the LIV parameters $a_{e\mu}, a_{e\tau}, a_{\mu\tau}$ taking one to be non-zero at a time. In fig. 6.6, we present the sensitivity as a function of δ_{13}^{true} for T2HKK (left) and T2HK (right) for NO (top) and IO(bottom) for $a_{e\mu}^{true} = 10^{-23}$ GeV. Different curves correspond to the different values of $\phi_{e\mu}^{true}$.

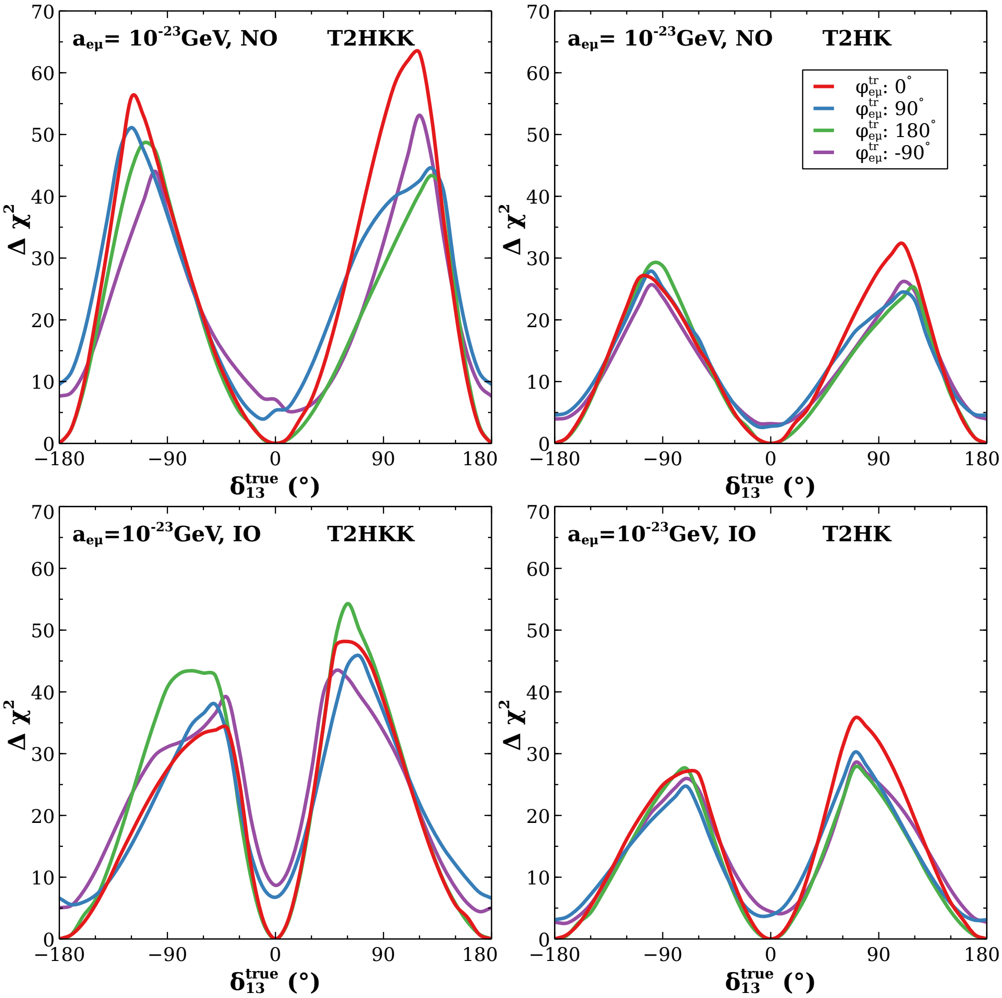

Figure 6.6: χ^2 as a function of δ_{13}^{true} for true values of $\theta_{23} = 49°$, $a_{e\mu} = 10^{-23}$ GeV in T2HKK (left) and T2HK (right) configurations for NO (top), and IO(bottom). Violet, red, green, and blue curves refer to $\phi_{e\mu}^{true} = -90°, 0°, 90°, 180°$ respectively.

It can be observed from fig. 6.6 that;

- T2HKK offers the best sensitivity for all values of the LIV phase $\phi_{e\mu}$. This is due to the synergistic effect between 1100 km and 295 km baselines. This will be explained later in the context of fig. 6.7.

- The highest sensitivity is obtained at $\delta_{13} = 90°$ for both T2HK and T2HKK. The corresponding values of $\phi_{e\mu}$ are $0°(180°)$ for NO(IO) case in T2HKK, and $0°$ in T2HK. This can be understood from fig. 3 and 4, which shows that for individual baseline, the maxima comes at $\phi_{e\mu} = 0°$ around $\delta_{13} = 90°$.

In order to understand the synergy between 295km and 1100 km baselines, in fig. 6.7, we have shown the χ^2 as a function of test $a_{e\mu}$ (left), and θ_{23} (right) for a set of true parameters keeping other test parameters fixed.

- From the left panel, we show that minimum χ^2 for 295 km and 1100 km occurs at different test values of LIV parameter $a_{e\mu}$. Whereas in T2HKK, both baselines are analyzed together, the minimum occurs at a different value of $a^{ts}_{e\mu}$, thus enhancing the $\Delta\chi^2$.

- In the right panel, the enhancement in χ^2 for T2HKK is due to the increased statistics. However, when marginalizing the χ^2 over other test parameters, the synergy is also observed in θ_{23}.

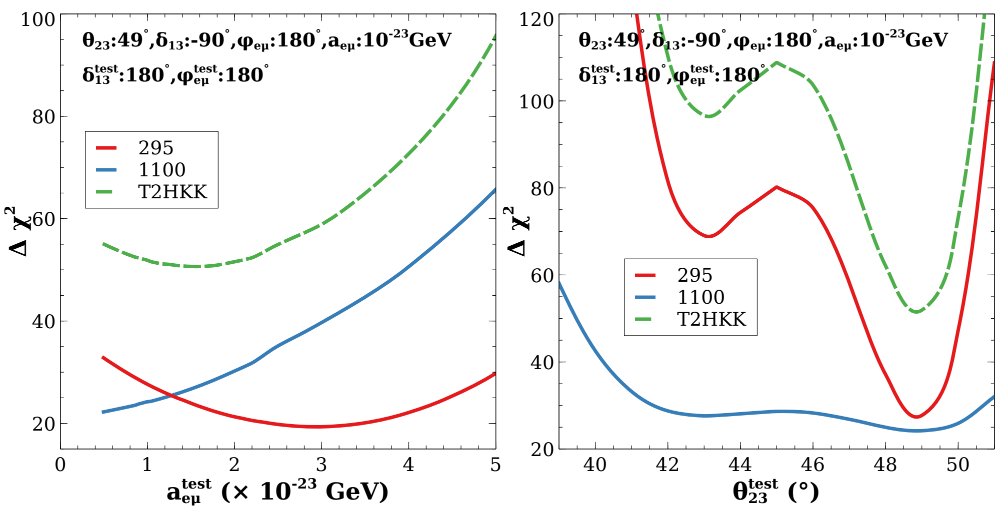

Figure 6.7: χ^2 as a function of $a^{test}_{e\mu}$(left), θ^{test}_{23}(right) for true values of $\theta_{23} = 49°$, $\delta_{13} = -90°$, $\phi_{e\mu} = 180°$, $a_{e\mu} = 10^{-23}$GeV. The red, blue, and green curves correspond to 295 km, 1100 km, and T2HKK, respectively.

In fig. 6.8, we present the values of χ^2 as a function of δ^{true}_{13} for $a^{true}_{e\tau} = 10^{-23}$ GeV in the T2HKK and T2HK configurations corresponding to NO (IO) in the top (bottom) column. The results for the true values of phase $\phi_{e\tau}$ as $-90°$(violet), $0°$(red), $90°$(blue), $180°$(green) using different colours as mentioned in the parenthesis. The major observations are as follows,

- Similar to in fig. 6.6, the sensitivity at T2HKK is quiet higher than T2HK configurations.
- We observe the maximum sensitivity in T2HKK around $\delta_{13} = 90°$ $(-90°)$ which is influenced by the maxima of $P_{\mu e}$ $(P_{\bar{\mu}\bar{e}})$ curves in 295 km occurring at $90°$ $(-90°)$. Although most of the curves show sensitivity in a similar range, the red one reaches the highest at UHP of δ_{13}^{true}.

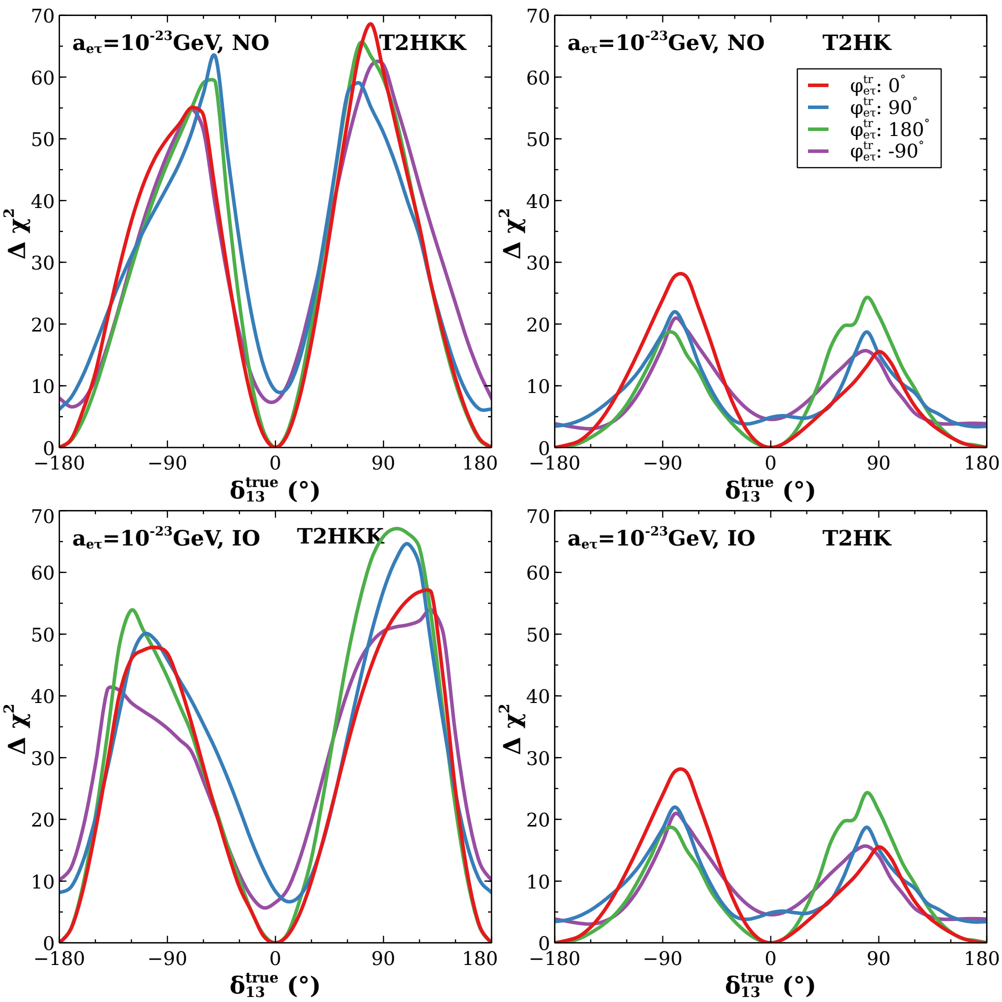

Figure 6.8: χ^2 as a function of δ_{13}^{true} for true values of $\theta_{23} = 49°$ with $a_{e\tau} = 10^{-23}$ GeV for T2HKK (left) and T2HK (right) configurations in NO (top), and IO (bottom). Violet, red, green, and blue refer to $\phi_{e\mu}^{true} = -90°, 0°, 90°, 180°$ respectively.

We show the χ^2 as a function of true δ_{13} in the 6.9 for effects of $a_{\mu\tau}$ for T2HKK and

T2HK configurations in NO(top) and IO(bottom). The noteworthy points from these two figures are as follows,

- The best sensitivity is observed in T2HKK, but the sensitivity of T2HK is also very close. The reason behind this is that there is no significant effect of $a_{\mu\tau}$ in $P_{\mu e}$.
- Also, there is no significant variation of sensitivity w.r.t phase $\phi_{\mu\tau}$. This is due to the narrow band of due to $\phi_{\mu\tau}$ as also seen from probability plots in fig. 6.1.

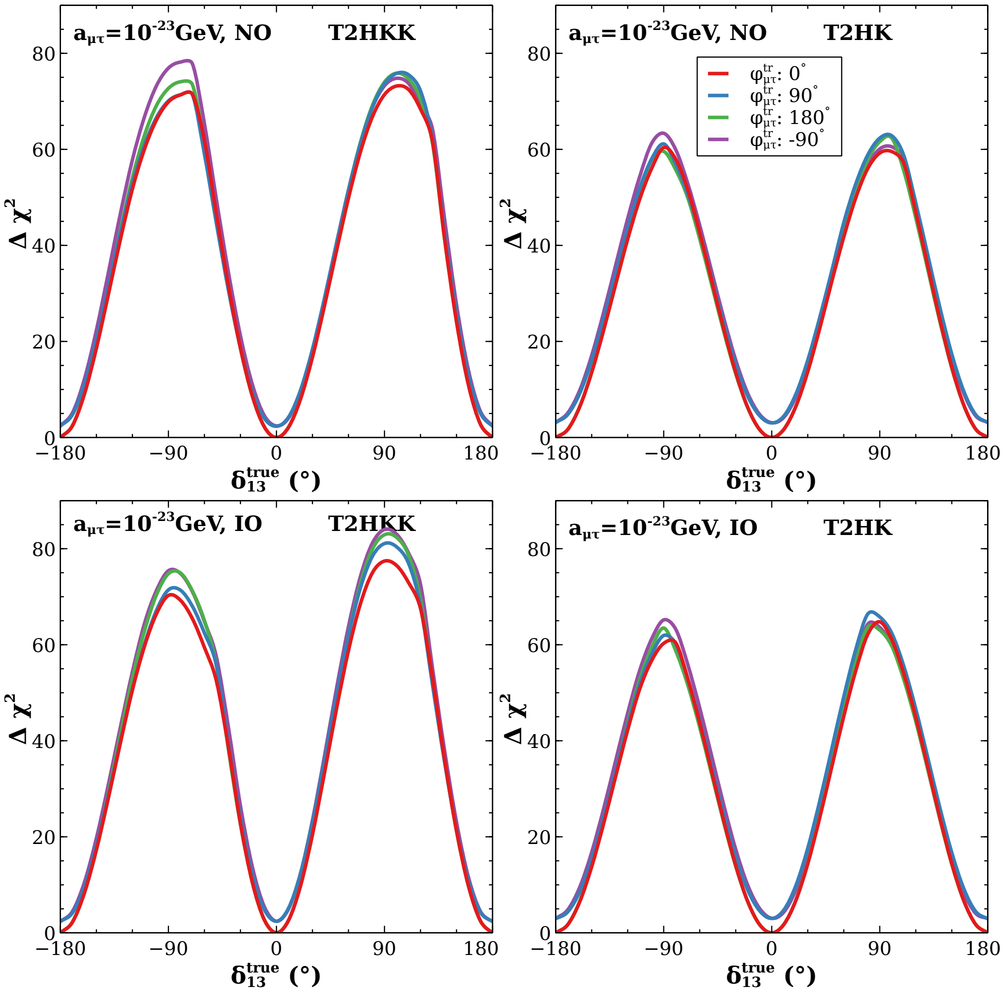

Figure 6.9: χ^2 as a function of δ_{13}^{true} for true values of $\theta_{23} = 49°$ with $a_{\mu\tau} = 10^{-23}$ GeV for T2HKK (left) and T2HK (right) configurations for NO (top), and IO (bottom). Violet, red, green and blue refer to $\phi_{\mu\tau}^{true} = -90°, 0°, 90°, 180°$ respectively.

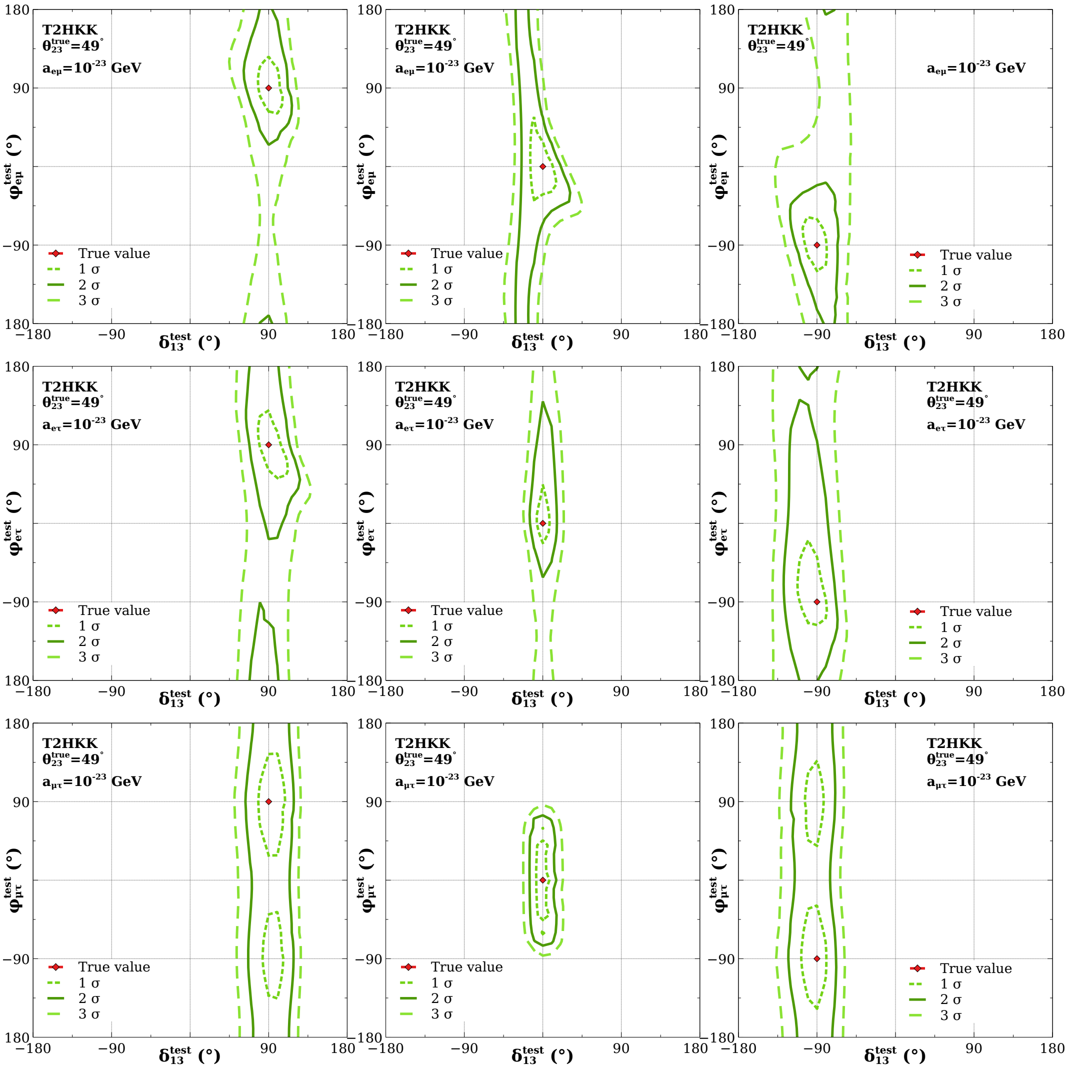

Figure 6.10: 1σ(dotted), 2σ(solid), 3σ(dashed) contours[2 d.o.f.] corresponding to three different true values of δ_{13}, ϕ_{jk} for true LIV parameters $a_{e\mu}$ (top), $a_{e\tau}$ (middle) and $a_{\mu\tau}$ (bottom) having value of 10^{-23} GeV for T2HKK configuration

6.4 Precision χ^2 analysis of $\delta_{13}, \phi_{\alpha\beta}$'s

In this section, we analyze the precision of δ_{13} and LIV phases $\phi_{\alpha\beta}$'s for T2HKK, T2HK in the figures 6.10 and 6.11 respectively. These are presented in terms of contours in $\phi_{\alpha\beta} - \delta_{13}$ test plane of various combinations of true values of $\phi_{\alpha\beta}, \delta_{13} = 0°, 90°, -90°$. We consider the true values of LIV parameters as 10^{-23} GeV, $\theta_{23} = 49°$. we can observe the following points from fig. 6.10,

- In the topmost panels corresponding to $a_{e\mu}$, we observe closed 2σ contours for $\delta_{13}, \phi_{e\mu} = 90°, -90°$ but not for $\delta_{13}, \phi_{e\mu} = 0°$(middle panel).

- On the other hand, in the middle panels corresponding to $a_{e\tau}$, the 2σ precision is better for $\delta_{13}, \phi_{e\tau} = 0°$ but worse for $90°, -90°$

- In the lowest panel corresponding to $a_{\mu\tau}$, we observe that 2σ contours for $\delta_{13} = 90°, \phi_{\mu\tau} = 90°$ and $\delta_{13} = -90°, \phi_{\mu\tau} = -90°$ stretch over full range of $\phi_{\mu\tau}$. However, in the middle panel, very good precision is obtained for $\delta_{13} = 0°, \phi_{\mu\tau} = 0°$ with a closed 3σ contour.

In fig. 6.11, we plot similar contours for T2HK. We can observe that the 2σ contours widen, i.e., δ_{13} precision is poorer. This is expected as at 295 km, the δ_{13} sensitivity is less.

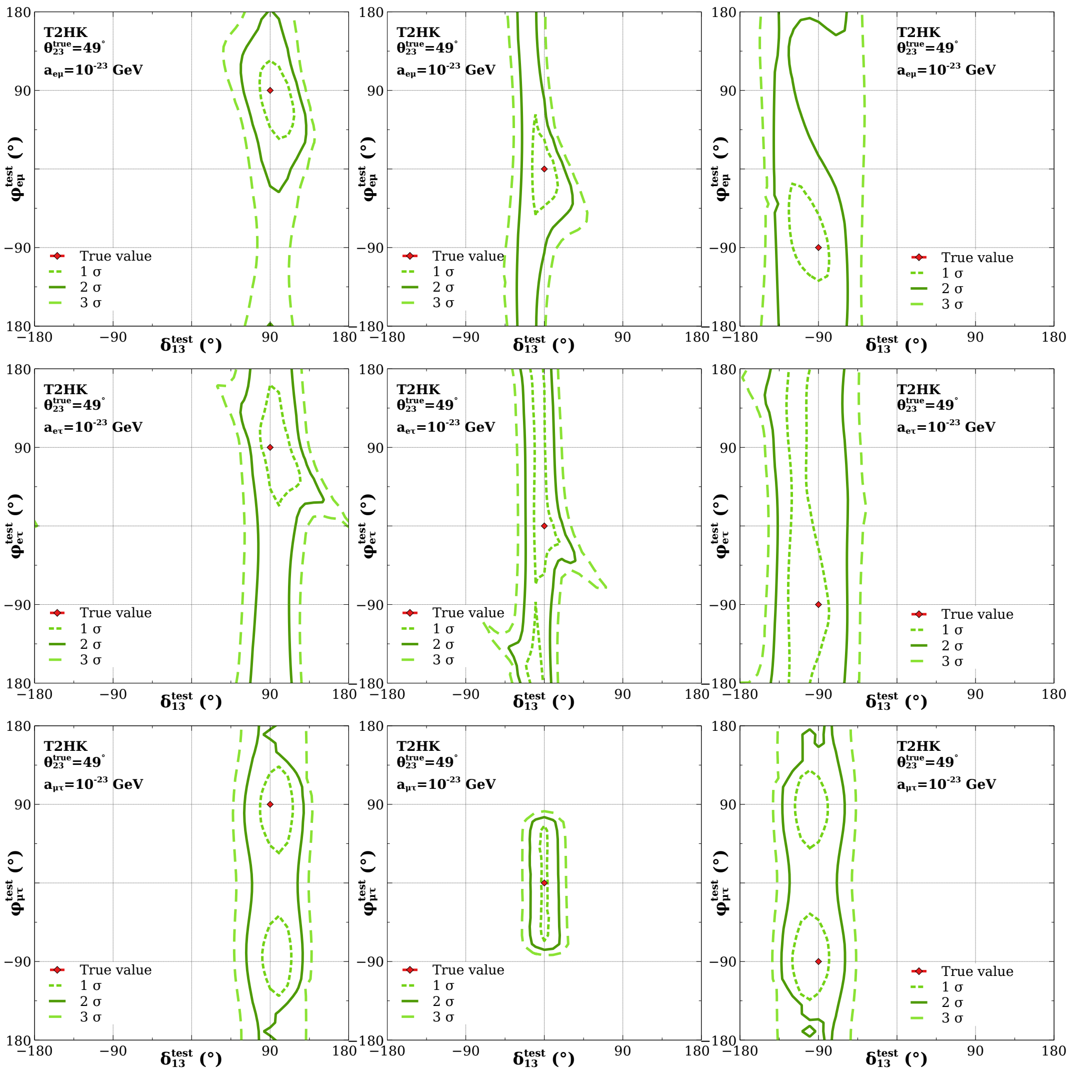

Figure 6.11: 1σ(dotted), 2σ(solid), 3σ(dashed) contours[2 d.o.f.] corresponding to three different true values of δ_{13}, ϕ_{jk} for true LIV parameters $a_{e\mu}$ (top), $a_{e\tau}$ (middle) and $a_{\mu\tau}$ (bottom) having value of 10^{-23} GeV for T2HK configuration

6.5 Discussions

The main focus of our work is to investigate the CP sensitivity in the future T2HK/T2HKK experiment in the presence of the CPT violating LIV parameters. We first study the CP discovery potential for individual baselines of 295km and 1100 km in the presence of LIV phases and ascertain the role of neutrino and anti-neutrino contributions to the total χ^2. Next, we obtain the sensitivity for T2HK and T2HKK configurations. This study inferred that at a fixed baseline, the sensitivity increases due to synergy between the electron appearance and muon disappearance channels as well as between the neutrino and anti-neutrino channels. We find that T2HKK gives a better sensitivity because of the synergistic effects of 295 km and 1100 km for LIV in the $e-\mu$ and $e-\tau$ sectors. We have identified synergy in parameters of $a_{\alpha\beta}, \theta_{23}, \phi_{\alpha\beta}, \delta_{13}$. However, for LIV in the $\mu-\tau$ sector, both configurations give similar sensitivity. This is because of the weak dependence of $P_{\mu e}$ on $\phi_{\mu\tau}$.

We also obtain the precision of $\delta_{13}, \phi_{\alpha\beta}$ for various true values of these phases in T2HK, T2HKK. We have found that the sensitivity of δ_{13} is better for T2HKK configuration in the presence of $a_{e\mu}, a_{e\tau}$. The 2σ sensitivity of $\phi_{e\mu}, \phi_{e\tau}$ becomes worse for T2HK but the 3σ sensitivity is very poor in both T2HK and T2HKK. In the case of $a_{\mu\tau}$, the sensitivity is best for $\delta_{13}=0°, \phi_{\mu\tau}=0°$.

"I am not a perfectionist, but I like to feel that things are done well. More important than that, I feel an endless need to learn, to improve, to evolve".

Cristiano Ronaldo

7 Summary

This chapter summarises the work done and the main results obtained in this thesis.

The paradigm of three flavor neutrino oscillations is well established as the leading solution to the solar and atmospheric neutrino anomalies. This was further corroborated by accelerator and reactor experiments, and the majority of the parameters governing oscillation were determined with considerable precision. The unknown parameters of the standard three flavor neutrino oscillation are the sign of mass squared difference Δ_{31}, the octant of the mixing angle θ_{23}, and the value of leptonic CP phase δ_{13}. The current and future high-precision and high-statistics experiments aim to determine these unknown parameters precisely. These experiments can also probe the sub-leading effects of BSM physics. This thesis explores three BSM scenarios: sterile neutrinos, non-standard interactions (NSIs), and Lorentz invariance violation (LIV) in the context of current and future experiments. Our study considers three experimental setups: a liquid argon time. projection detector capable of observing both beam and atmospheric neutrinos (e.g., DUNE) and Cerenkov detectors (e.g., T2HK/T2HKK, IceCube). My doctoral thesis mainly comprises the following topics;

- Probing the sensitivity to octant of θ_{23}, and the sign of Δ_{31} in the presence of an eV scale sterile neutrino in the context of a liquid argon detector using beam and atmospheric neutrinos,
- Investigation of the sensitivity to the sign of Δ_{31}, Δ_{41} and the octant of θ_{23} for very light sterile neutrinos corresponding to $\Delta_{41} : 10^{-4} - 10^{-1}\text{eV}^2$ in the context of a liquid argon detector using beam and atmospheric neutrinos,
- Study the implications of Dark Large Mixing Angle (DLMA) solutions of θ_{12} from IceCube data in the context of various astrophysical sources,
- Exploring the synergy between 295 and 1100 km baselines in the study of CP discovery in the presence of LIV parameters at the T2HKK experiment and comparing the results with that of T2HK using a water Cherenkov detector.

In the presence of an eV scale sterile neutrino, we calculate the oscillation probabilities using $\Delta_{21} = 0$ approximation while considering $\theta_{34} = 0$. In this 3+1 framework, increased parameters create unfavorable conditions for determining the parameters because of degeneracies. The analytic expressions help us to understand how the sensitivity to the octant of θ_{23} and the sign of Δ_{31} depend on various parameters. Numerical analysis of beam and atmospheric neutrinos in combination provided more than 3σ sensitivity for the octant of θ_{23} for $\theta_{23}^{true} = 49°, 41°$. At fixed hierarchy, we identified that the wrong octant solutions are mainly due to the phase δ_{14}. The combined analysis achieved over 10σ sensitivity for the sign of Δ_{31}, i.e., atmospheric mass ordering. Higher values of sterile mixing angles lead to lower sensitivity.

The presence of a very light sterile neutrino corresponding to $\Delta_{41} : 10^{-4} - 10^{-1}\text{eV}^2$ opens us few possibilities of the mass spectrum of the neutrinos as the sign of both Δ_{31}, Δ_{41}(sterile mass ordering) is unknown. We study the sensitivity of determining the signs of these mass-squared differences as a function of the sterile mass-squared difference Δ_{41} and phase δ_{13}^{true}. We observed the sensitivity to atmospheric mass ordering vary significantly between minima and maxima for $\Delta_{41} : 10^{-3} - 10^{-2}\text{eV}^2$ as $|\Delta_{41}|$ is adjacent to $|\Delta_{31}| = 2.5 \times 10^{-3}\text{eV}^2$. The sterile mass ordering sensitivity also shows a significant rise or dip for $|\Delta_{41}|$ close to $|\Delta_{31}|$. In the combined analysis, 3σ sensitivity has been attained for the sterile mass ordering when $|\Delta_{41}| > 10^{-2}\text{eV}^2$. We also achieve 3σ sensitivity to the octant of θ_{23} for $\Delta_{41} : 10^{-4} : 10^{-1}\text{eV}^2$ in combined analysis.

The introduction of non-standard interactions of neutrinos invokes the possibility of a degenerate solution of the standard MSW LMA solution of θ_{12}. This degenerate solution is defined as $\theta_{12}^{DLMA} = \frac{\pi}{2} - \theta_{12}$, known as the DLMA solution[250]. We explore the implications of this solution in the context of high energy astrophysical neutrinos observed in the IceCube detector. The oscillation probabilities of astrophysical neutrinos only depend on the mixing angles and cp phase. From these probabilities, we have studied the degeneracies related to θ_{12}. The degeneracy between two solutions of θ_{12} and δ_{CP}, also present in the Hamiltonian level, was seen in the probability level. We identified a new degeneracy that manifests the same probability at fixed value of δ_{CP} for different sets of θ_{12} and θ_{23}, i.e., $P(\theta_{12}^{LMA}, \theta_{23}) = P(\theta_{12}^{DLMA}, \theta'_{23})$. This degeneracy suggests that the octant of θ_{23} and LMA/DLMA nature of θ_{12} can't be identified simultaneously for known δ_{CP}. We analyzed the sensitivity of LMA and DLMA solutions using the 7.5 years of IceCube data for high-energy neutrinos with energy greater than 60 TeV. Considering the track by shower ratio of the events as an observable, we evaluated the sensitivity for three different possible astrophysical sources w.r.t. the experimental ratio. Due to the presence of degeneracy of θ_{12} with θ_{23}, δ_{CP}; the data prefers a region in the $\theta_{23} - \delta_{CP}$ plane rather than a best-fit value. The LMA and DLMA solutions are allowed in a large portion of $\theta_{23} - \delta_{CP}$ plane for μ source; however, the current best fit shows a preference for the LMA solution. For the π source, the LMA and DLMA solutions are allowed in smaller regions than the μ source. In the case of μ source, the best fit is excluded at $\chi^2 = 1.7(2.4)$ for LMA(DLMA), suggesting slight favor for LMA. However, The n source doesn't fit the IceCube data for both LMA and DLMA solutions.

The sub-leading effect of Lorentz invariance violation can be probed in future neutrino oscillation experiments. As the off-diagonal LIV parameters $a_{\alpha\beta}$ come with a phase $\phi_{\alpha\beta}$ that are extra sources for the CP violation. In the presence of these parameters, the cp conservation is achieved when the phases $\delta_{CP}, \phi_{\alpha\beta}$ occur in combinations of $0°, 180°$. We consider the proposed T2HK/T2HKK experiments for probing the CP sensitivity in the presence of LIV parameters. By analyzing the CP discovery potential for individual baselines of 295km and 1100 km in the presence of LIV phases, we ascertain the role of neutrino and anti-neutrino contributions to the total χ^2. T2HKK is found to have a better sensitivity because of the synergistic effects of 295 km and 1100 km due to parameters $a_{\alpha\beta}, \theta_{23}, \phi_{\alpha\beta}, \delta_{13}$ for LIV in the $e-\mu$ and $e-\tau$ sectors. However, both configurations give similar sensitivity for LIV in the $\mu-\tau$ sector as $P_{\mu e}$ has very mild dependence on $\phi_{\mu\tau}$. The precision of $\delta_{CP}, \phi_{\alpha,\beta}$ is evaluated for various true values of these phases in T2HK, T2HKK. We have found that the sensitivity of δ_{13} is better for T2HKK configuration in the presence of $a_{e\mu}, a_{e\tau}$ whereas the sensitivity of $\phi_{e\mu}, \phi_{e\tau}$ is much worse as compared to δ_{13}. Among the two setups, T2HKK gives better precision. In the case of $a_{\mu\tau}$, the sensitivity of $\delta_{13}, \phi_{\mu\tau}$ is best for $\delta_{13} = 0°, \phi_{\mu\tau} = 0°$.

In this thesis, we have considered three BSM scenarios. We wish to explore other BSM scenarios like various NSI, Non-unitary mixing, etc, emphasizing the aspect of combined beam and atmospheric analysis. In the future, we also want to investigate if there are some unique signatures of BSM physics possible in future experiments that can help in differentiating between the different scenarios.

A

Probability calculation using Cayley Hamilton formalism

A.1 Cayley Hamilton formalism

We will now find out the analytic probability using the Cayley-Hamilton formalism[290–292]. We calculate the time evolution operator and do not introduce auxiliary matter mixing angles.

The flavour eigenstates ψ_α and mass eigenstates ψ_i are related as

$$\psi_i = \sum_{j=e,\mu,\tau,s} U^\star_{\alpha j}\psi_j \tag{A.1}$$

where $U_{\alpha j}$ is component of unitary mixing matrix corresponding to mixing between ψ_α, ψ_j,

$$U = \tilde{R}_{34}(\theta_{34}, \delta_{34})R_{24}(\theta_{24})\tilde{R}_{14}(\theta_{14}, \delta_{14})R_{23}(\theta_{23})\tilde{R}_{13}(\theta_{13}, \delta_{13})R_{12}(\theta_{12}) \tag{A.2}$$

The Schrodinger equation in mass basis is given as,

$$\iota\frac{d}{dt}\psi_m(t) = \mathcal{H}_m\psi_m(t) \tag{A.3}$$

where total Hamiltonian $\mathcal{H}_m$ in mass basis, and interaction Hamiltonian V_f in flavour basis are given as follows,

$$\mathcal{H}_m = H_m + U^{-1}V_f U \tag{A.4}$$

$$V_f = H_{int} = diag(2A', 0, 0, A') \tag{A.5}$$

Equation (A.3) gives the solution with time evolution operator $e^{-\iota\mathcal{H}_m t}$ as,

$$\psi_m(t) = e^{-\iota\mathcal{H}_m t}\psi_m(0) \tag{A.6}$$

We get the solution in terms of distance L traveled by neutrinos in time t as,

$$\psi_m(L) = \psi_m(t = L) = e^{-\iota\mathcal{H}_m t}\psi_m(0) \equiv U_m(L)\psi_m(0) \tag{A.7}$$

Solution in flavour state ψ_f is expressed at $t = L$ as,

$$\psi_f(L) = U\phi_m(L) = Ue^{-\iota\mathcal{H}_m t}U^{-1}U\psi_m(0) = Ue^{-\iota\mathcal{H}_m t}U^{-1}\psi_f(0) \equiv U_f(L)\psi_f(0) \quad \text{(A.8)}$$

We will calculate the time evolution operator, i.e., the exponential of the matrix $\mathcal{H}_m$ using the Cayley-Hamilton theorem. We construct a traceless matrix out of $\mathcal{H}_m$ as ,

$$\mathcal{H}_m = T + \frac{1}{4}(tr\mathcal{H}_m)I \quad \text{(A.9)}$$

The time evolution operator is then redefined as,

$$U_m(L) = e^{-\iota\mathcal{H}_m L} = \phi e^{-\iota TL} \quad \text{(A.10)}$$

The elements of the traceless matrix T in mass basis are as follows,

$$\begin{aligned}
T_{11} &= A\left[-\cos^2\theta_{12}\left(2\sin\theta_{13}\cos\theta_{13}\sin\theta_{14}\sin\theta_{23}\sin\theta_{24}\cos\theta_{24}\cos(\delta_{13}-\delta_{14}) + \cos 2\theta_{23}\sin^2\theta_{24}\right)\right. \\
&+2\sin\theta_{12}\cos\theta_{12}\cos\theta_{23}\sin\theta_{24}(\cos\delta_{13}\sin\theta_{13}\sin\theta_{23}\sin\theta_{24} - \cos\delta_{14}\cos\theta_{13}\sin\theta_{14}\cos\theta_{24}) \\
&+\cos^2\theta_{12}\cos^2\theta_{13}\left(2-\sin^2\theta_{24}\left(\sin^2\theta_{14}+\sin^2\theta_{23}\right)-\sin^2\theta_{14}\right) \\
&\left.+\cos^2\theta_{23}\sin^2\theta_{24}\right] - \frac{3A}{4} + \frac{1}{4}(-\Delta_{21}-\Delta_{31}-\Delta_{41}) \qquad \text{(A.11)} \\
T_{12} &= A\left[-\sin\theta_{12}\cos\theta_{12}\left(2\sin\theta_{13}\cos\theta_{13}\sin\theta_{14}\sin\theta_{23}\sin\theta_{24}\cos\theta_{24}\cos(\delta_{13}-\delta_{14}) + \cos 2\theta_{23}\sin^2\theta_{24}\right)\right. \\
&-\sin\theta_{13}\sin\theta_{23}\cos\theta_{23}\sin^2\theta_{24}\left(e^{-i\delta_{13}}\cos^2\theta_{12} - e^{i\delta_{13}}\sin^2\theta_{12}\right) \\
&+\cos\theta_{13}\sin\theta_{14}\cos\theta_{23}\sin\theta_{24}\cos\theta_{24}\left(e^{-i\delta_{14}}\cos^2\theta_{12} - e^{i\delta_{14}}\sin^2\theta_{12}\right) \\
&\left.+\sin\theta_{12}\cos\theta_{12}\cos^2\theta_{13}\left(2-\sin^2\theta_{24}\left(\sin^2\theta_{14}+\sin^2\theta_{23}\right)-\sin^2\theta_{14}\right)\right] \qquad \text{(A.12)} \\
T_{13} &= A\left[-e^{i\delta_{14}-2i\delta_{13}}\cos\theta_{12}\sin^2\theta_{13}\sin\theta_{14}\sin\theta_{23}\sin\theta_{24}\cos\theta_{24}\right. \\
&-e^{i\delta_{14}-i\delta_{13}}\sin\theta_{12}\sin\theta_{13}\sin\theta_{14}\cos\theta_{23}\sin\theta_{24}\cos\theta_{24} \\
&+e^{-i\delta_{14}}\cos\theta_{12}\cos^2\theta_{13}\sin\theta_{14}\sin\theta_{23}\sin\theta_{24}\cos\theta_{24} \\
&\left.+e^{-i\delta_{13}}\cos\theta_{12}\sin\theta_{13}\cos\theta_{13}\left(2-\sin^2\theta_{24}\left(\sin^2\theta_{14}+\sin^2\theta_{23}\right)-\sin^2\theta_{14}\right)\right] \\
&-A\sin\theta_{12}\cos\theta_{13}\sin\theta_{23}\cos\theta_{23}\sin^2\theta_{24} \qquad \text{(A.13)} \\
T_{14} &= A\left[e^{-i\delta_{13}}\cos\theta_{12}\sin\theta_{13}\cos\theta_{14}\sin\theta_{23}\sin\theta_{24}\cos\theta_{24}\right. \\
&\left.+e^{-i\delta_{14}}\cos\theta_{12}\cos\theta_{13}\sin\theta_{14}\cos\theta_{14}\left(2-\cos^2\theta_{24}\right) + \sin\theta_{12}\cos\theta_{14}\cos\theta_{23}\sin\theta_{24}\cos\theta_{24}\right] \qquad \text{(A.14)}
\end{aligned}$$

$$
\begin{aligned}
T_{22} &= A\left[-\sin^2\theta_{12}\left(2\sin\theta_{13}\cos\theta_{13}\sin\theta_{14}\sin\theta_{23}\sin\theta_{24}\cos\theta_{24}\cos(\delta_{13}-\delta_{14})+\cos 2\theta_{23}\sin^2\theta_{24}\right)\right.\\
&\quad +2\sin\theta_{12}\cos\theta_{12}\cos\theta_{23}\sin\theta_{24}(\cos\delta_{14}\cos\theta_{13}\sin\theta_{14}\cos\theta_{24}-\cos\delta_{13}\sin\theta_{13}\sin\theta_{23}\sin\theta_{24})\\
&\quad +\sin^2\theta_{12}\cos^2\theta_{13}\left(2-\sin^2\theta_{24}\left(\sin^2\theta_{14}+\sin^2\theta_{23}\right)-\sin^2\theta_{14}\right)\\
&\quad \left.+\cos^2\theta_{23}\sin^2\theta_{24}\right]-\frac{3A}{4}+\frac{1}{4}(3\Delta_{21}-\Delta_{31}-\Delta_{41}) \qquad \text{(A.15)}\\
T_{23} &= A\left[-e^{i\delta_{14}-2i\delta_{13}}\sin\theta_{12}\sin^2\theta_{13}\sin\theta_{14}\sin\theta_{23}\sin\theta_{24}\cos\theta_{24}\right.\\
&\quad +e^{i\delta_{14}-i\delta_{13}}\cos\theta_{12}\sin\theta_{13}\sin\theta_{14}\cos\theta_{23}\sin\theta_{24}\cos\theta_{24}\\
&\quad +e^{-i\delta_{14}}\sin\theta_{12}\cos^2\theta_{13}\sin\theta_{14}\sin\theta_{23}\sin\theta_{24}\cos\theta_{24}\\
&\quad \left.+e^{-i\delta_{13}}\sin\theta_{12}\sin\theta_{13}\cos\theta_{13}\left(2-\sin^2\theta_{24}\left(\sin^2\theta_{14}+\sin^2\theta_{23}\right)-\sin^2\theta_{14}\right)\right]\\
&\quad +A\cos\theta_{12}\cos\theta_{13}\sin\theta_{23}\cos\theta_{23}\sin^2\theta_{24} \qquad \text{(A.16)}\\
T_{24} &= A\left[e^{-i\delta_{13}}\sin\theta_{12}\sin\theta_{13}\cos\theta_{14}\sin\theta_{23}\sin\theta_{24}\cos\theta_{24}\right.\\
&\quad +e^{-i\delta_{14}}\sin\theta_{12}\cos\theta_{13}\sin\theta_{14}\cos\theta_{14}\left(2-\cos^2\theta_{24}\right)\\
&\quad \left.-\cos\theta_{12}\cos\theta_{14}\cos\theta_{23}\sin\theta_{24}\cos\theta_{24}\right] \qquad \text{(A.17)}
\end{aligned}
$$

$$
\begin{aligned}
T_{33} &= A\left[2\sin\theta_{13}\cos\theta_{13}\sin\theta_{14}\sin\theta_{23}\sin\theta_{24}\cos\theta_{24}\cos(\delta_{13}-\delta_{14})\right.\\
&\quad \left.+\sin^2\theta_{13}\left(2-\sin^2\theta_{24}\left(\sin^2\theta_{14}+\sin^2\theta_{23}\right)-\sin^2\theta_{14}\right)+\sin^2\theta_{23}\sin^2\theta_{24}\right]\\
&\quad -\frac{3A}{4}+\frac{1}{4}(-\Delta_{21}+3\Delta_{31}-\Delta_{41}) \qquad \text{(A.18)}\\
T_{34} &= A\left[e^{i\delta_{13}-i\delta_{14}}\sin\theta_{13}\sin\theta_{14}\cos\theta_{14}\left(2-\cos^2\theta_{24}\right)\right.\\
&\quad \left.-\cos\theta_{13}\cos\theta_{14}\sin\theta_{23}\sin\theta_{24}\cos\theta_{24}\right] \qquad \text{(A.19)}\\
T_{44} &= A\left[\cos^2\theta_{14}\cos^2\theta_{24}+2A\sin^2\theta_{14}\right]-\frac{3A}{4}+\frac{1}{4}(-\Delta_{21}-\Delta_{31}+3\Delta_{41}) \qquad \text{(A.20)}
\end{aligned}
$$

Cayley-Hamilton theorem is used to get the form of the time evolution operator $e^{-\iota TL}$. We need to solve the characteristic equation of matrix T given by,

$$\lambda^4+c_3\lambda^3+c_2\lambda^2+c_1\lambda+c_0=0 \qquad \text{(A.21)}$$

to obtain the energy eigenvalues λ where the constants are defined as follows,

$$\begin{aligned} c_0 \;=\; & \frac{A^2}{128}\Delta_{41}^2\left(8\sin^2\theta_{14}+29\right)+ \\ & \frac{A}{64}\Big[\left(-\Delta_{31}^3+2\Delta_{31}^2\Delta_{41}+3\Delta_{31}\Delta_{41}^2\right)\sin 2\theta_{13}\sin\theta_{14}\sin\theta_{23}\sin 2\theta_{24}\cos(\delta_{13}-\delta_{14}) \\ & +\Delta_{31}^3\left(3-4\cos^2\theta_{13}\sin^2\theta_{23}\sin^2\theta_{24}-4Q\sin^2\theta_{13}\right) \\ & +\Delta_{31}^2\Delta_{41}\left(8\cos^2\theta_{13}\sin^2\theta_{23}\sin^2\theta_{24}+12\cos^2\theta_{24}-4Q\left(2\cos^2\theta_{13}+1\right)+9\right) \\ & +\Delta_{31}\Delta_{41}^2\left(12\cos^2\theta_{13}\sin^2\theta_{23}\sin^2\theta_{24}+8\cos^2\theta_{24}+4Q\left(1-3\cos^2\theta_{13}\right)+1\right) \\ & -\Delta_{41}^3\left(4\cos^2\theta_{24}-4Q+5\right)\Big]+\frac{\Delta_{21}}{64}\left(\Delta_{31}^3-5\Delta_{31}^2\Delta_{41}-5\Delta_{31}\Delta_{41}^2+\Delta_{41}^3\right) \\ & +\left(-\frac{3\Delta_{31}^4}{256}+\frac{\Delta_{31}^3\Delta_{41}}{64}+\frac{7\Delta_{31}^2\Delta_{41}^2}{128}+\frac{\Delta_{31}\Delta_{41}^3}{64}-\frac{3\Delta_{41}^4}{256}\right) \end{aligned} \tag{A.22}$$

$$\begin{aligned} c_1 \;=\; & \frac{1}{8}A^2\Delta_{41}\left(5-7\sin^2\theta_{14}\right)+\frac{A}{8}\Delta_{31}^2\left(3-4\sin^2\theta_{23}\sin^2\theta_{24}\cos^2\theta_{13}-4Q\sin^2\theta_{13}\right) \\ & -\frac{A}{8}\Delta_{41}^2\left(5+4\cos^2\theta_{24}-4Q\right)+\frac{A}{16}\Delta_{31}\Delta_{41}\left(4+8\cos^2\theta_{24}-5P\cos^2\theta_{13}\right) \\ & +\frac{A}{4}\left(-\Delta_{31}{}^2+\Delta_{31}\Delta_{41}\right)\sin 2\theta_{13}\sin\theta_{14}\sin\theta_{23}\sin 2\theta_{24}\cos(\delta_{13}-\delta_{14}) \\ & +\frac{\Delta_{21}}{8}\left(\Delta_{41}-\Delta_{31}\right)^2+\frac{1}{8}\left(-\Delta_{31}^3+\Delta_{31}^2\Delta_{41}+\Delta_{31}\Delta_{41}^2-\Delta_{41}^3\right) \end{aligned} \tag{A.23}$$

$$\begin{aligned} c_2 \;=\; & \frac{A}{4}\Delta_{31}\left(3-4\sin^2\theta_{23}\sin^2\theta_{24}\cos^2\theta_{13}-4Q\sin^2\theta_{13}\right)-\frac{A}{4}\Delta_{41}\left(5+4\cos^2\theta_{24}-4Q\right) \\ & -\frac{11}{8}A^2-\frac{A}{2}\Delta_{31}\sin 2\theta_{13}\sin\theta_{14}\sin\theta_{23}\sin 2\theta_{24}\cos(\delta_{13}-\delta_{14}) \\ & +\frac{\Delta_{21}}{4}\left(\Delta_{41}+\Delta_{31}\right)+\frac{1}{8}\left(-3\Delta_{31}^2+2\Delta_{31}\Delta_{41}-3\Delta_{41}^2\right) \end{aligned} \tag{A.24}$$

$$c_3 = \mathrm{Trace(T)} = 0 \tag{A.25}$$

$$P = 2-\sin^2\theta_{14}-\sin^2\theta_{24}\left(\sin^2\theta_{14}+\sin^2\theta_{23}\right) \tag{A.26}$$

$$Q = 2-\sin^2\theta_{14}-\sin^2\theta_{24}\sin^2\theta_{14} \tag{A.27}$$

The energy eigenvalues are as follows,

$$\lambda_{1,2} = -\frac{1}{2}\left[\sqrt{-c_2+t_0} \pm \sqrt{-c_2-t_0-2\sqrt{-4c_0+t_0^2}}\right] \tag{A.28}$$

$$\lambda_{3,4} = -\frac{1}{2}\left[-\sqrt{-c_2+t_0} \pm \sqrt{-c_2-t_0+2\sqrt{-4c_0+t_0^2}}\right] \tag{A.29}$$

where t_0 is a real root of the following equation,

$$t^3 - c_2 t^2 - 4c_0 t + 4c_0 c_2 - c_1^2 = 0 \tag{A.30}$$

The general form of probability is given by

$$P_{\alpha\beta} = \sum_{a=1}^{4}\sum_{b=1}^{4}(\tilde{B}_a)_{\alpha\beta}(\tilde{B}_b)^{\star}_{\alpha\beta}e^{-\iota L(\lambda_a-\lambda_b)} \tag{A.31}$$

where,

$$(\tilde{B}_a)_{\alpha\beta} = \frac{(c_1+c_2\lambda_a+\lambda_a^3)\delta_{\alpha\beta}+(c_2+\lambda_a^2)\tilde{T}_{\alpha\beta}+\lambda_a\tilde{T}^2_{\alpha\beta}+\tilde{T}^3_{\alpha\beta}}{4\lambda_a^3+c_1+2c_2\lambda_a} \tag{A.32}$$

where components of T, T^2, T^3 in flavour basis are given as following,

$$\tilde{T}_{\alpha\beta} =< \alpha|UTU^{-1}|\beta >, \tilde{T^2}_{\alpha\beta} =< \alpha|UT^2U^{-1}|\beta >, \tilde{T^3}_{\alpha\beta} =< \alpha|UT^3U^{-1}|\beta > \tag{A.33}$$

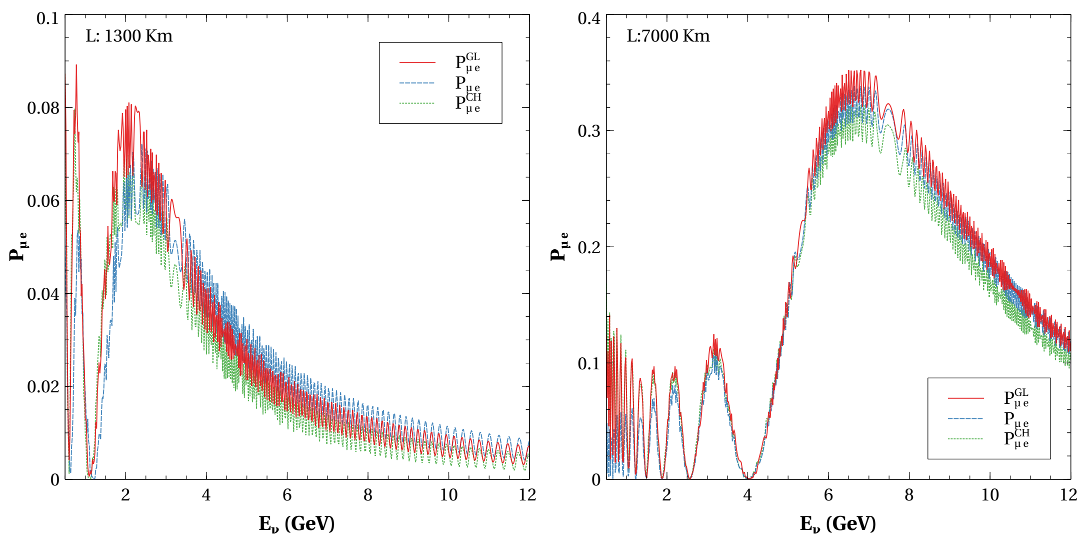

Figure A.1: Comparison of the probability using GLoBES $P^{GL}_{\mu e}$ (red), the Cayley Hamilton probability $P^{CH}_{\mu e}$ (green), and TMSD probability $P_{\mu e}$ (blue) at 1300 km(left), 7000 km(right) baseline.

In Figure A.1, we see that the Cayley Hamilton probabilities at lower energies show a better match with numerical probabilities evaluated using GLoBES, whereas at higher energies especially at resonance region the TMSD probabilities match better as was also seen in Figure 3.1, and Figure 3.2.

Publications

1. Chatterjee, A. and Goswami, S. and Pan, S. "Matter effect in the presence of a sterile neutrino and resolution of the octant degeneracy using a liquid argon detector". *Physical Review D* 108, 095050 (2023), DOI: 10.1103/PhysRevD.108.095050, arXiv:2212.02949

2. Chatterjee, A. and Goswami, S. and Pan, S. "Probing mass hierarchies in presence of a very light sterile neutrino in a liquid argon detector". *Nuclear Physics B, 996, 116370* (2023), DOI: 10.1016/j.nuclphysb.2023.116370, arXiv:2307.12885.

3. Ghosh, M. and Goswami, S. and Pan, S. and Pavlovic, B. "Implications of the DLMA solution of θ_{12} for IceCube data using different astrophysical sources". *Universe*, 9(9), 380 (2023), DOI: 10.3390/universe9090380, arXiv:2306.11653

4. Chakraborty, K. and Goswami, S. and Pan, S. "Sensitivity for CP in the presence of Lorentz invariance violating potential at T2HK/T2HKK". *Accepted in EPJC* (2024), DOI: arXiv:2308.07566.

References

[1] Wolfgang Pauli. "Pauli letter collection: letter to Lise Meitner". Typed copy. URL: https://cds.cern.ch/record/83282.

[2] Henri Becquerel. "On the rays emitted by phosphorescence". In: *Compt. Rend. Hebd. Seances Acad. Sci.* 122.8 (1896), pp. 420–421.

[3] Ernest Rutherford. "VIII. Uranium radiation and the electrical conduction produced by it". In: *The London, Edinburgh, and Dublin Philosophical Magazine and Journal of Science* 47.284 (1899), pp. 109–163. DOI: 10.1080/14786449908621245.

[4] MM Villard. "Sur le rayonnement du radium". In: *CR Acad. Sci. Paris* 130 (1900), p. 1178.

[5] William Henry Bragg and Richard Kleeman. "LXXIV. On the ionization curves of radium". In: *The London, Edinburgh, and Dublin Philosophical Magazine and Journal of Science* 8.48 (1904), pp. 726–738. URL: https://api.semanticscholar.org/CorpusID:121482700.

[6] A. Franklin. "The road to the neutrino". In: *Phys. Today* 53N2 (2000), pp. 22–28. DOI: 10.1063/1.882961.

[7] William Wilson. "On the Absorption of Homogeneous β-Rays by Matter, and on the Variation of the Absorption of the Rays with Velocity". In: *Proceedings of the Royal Society of London. Series A, Containing Papers of a Mathematical and Physical Character* 82.558 (1909), pp. 612–628. DOI: 10.1098/rspa.1909.0067.

[8] J. Chadwick. "The intensity distribution in the magnetic spectrum of beta particles from radium (B + C)". In: *Verh. Phys. Gesell.* 16 (1914), pp. 383–391.

[9] C. L. Cowan et al. "Detection of the free neutrino: A Confirmation". In: *Science* 124 (1956), pp. 103–104. DOI: 10.1126/science.124.3212.103.

[10] Seth H Neddermeyer and Carl D Anderson. "Note on the nature of cosmic-ray particles". In: *Physical Review* 51.10 (1937), p. 884.

[11] G. Danby et al. "Observation of High-Energy Neutrino Reactions and the Existence of Two Kinds of Neutrinos". In: *Phys. Rev. Lett.* 9 (1 July 1962), pp. 36–44. DOI: 10.1103/PhysRevLett.9.36.

[12] Martin L. Perl et al. "Evidence for Anomalous Lepton Production in $e^+ - e^-$ Annihilation". In: *Phys. Rev. Lett.* 35 (1975), pp. 1489–1492. DOI: 10.1103/PhysRevLett.35.1489.

[13] K. Kodama et al. "Observation of tau neutrino interactions". In: *Phys. Lett. B* 504 (2001), pp. 218–224. DOI: 10.1016/S0370-2693(01)00307-0. arXiv: hep-ex/0012035.

[14] S.L. Glashow. "Partial Symmetries of Weak Interactions". In: *Nucl. Phys.* 22 (1961), pp. 579–588. DOI: 10.1016/0029-5582(61)90469-2.

[15] Steven Weinberg. "A Model of Leptons". In: *Phys. Rev. Lett.* 19 (1967), pp. 1264–1266. DOI: 10.1103/PhysRevLett.19.1264.

[16] Abdus Salam. "Weak and Electromagnetic Interactions". In: *Conf. Proc. C* 680519 (1968), pp. 367–377. DOI: 10.1142/9789812795915_0034.

[17] Georges Aad et al. "Observation of a new particle in the search for the Standard Model Higgs boson with the ATLAS detector at the LHC". In: *Phys. Lett. B* 716 (2012), pp. 1–29. DOI: 10.1016/j.physletb.2012.08.020. arXiv: 1207.7214 [hep-ex].

[18] Serguei Chatrchyan et al. "Observation of a New Boson at a Mass of 125 GeV with the CMS Experiment at the LHC". In: *Phys. Lett. B* 716 (2012), pp. 30–61. DOI: 10.1016/j.physletb.2012.08.021. arXiv: 1207.7235 [hep-ex].

[19] T. D. Lee and Chen-Ning Yang. "Question of Parity Conservation in Weak Interactions". In: *Phys. Rev.* 104 (1956), pp. 254–258. DOI: 10.1103/PhysRev.104.254.

[20] M. Goldhaber, L. Grodzins, and A. W. Sunyar. "Helicity of Neutrinos". In: *Phys. Rev.* 109 (1958), pp. 1015–1017. DOI: 10.1103/PhysRev.109.1015.

[21] Brent Follin et al. "First Detection of the Acoustic Oscillation Phase Shift Expected from the Cosmic Neutrino Background". In: *Phys. Rev. Lett.* 115.9 (2015), p. 091301. DOI: 10.1103/PhysRevLett.115.091301. arXiv: 1503.07863 [astro-ph.CO].

[22] M. G. Betti et al. "Neutrino physics with the PTOLEMY project: active neutrino properties and the light sterile case". In: *JCAP* 07 (2019), p. 047. DOI: 10.1088/1475-7516/2019/07/047. arXiv: 1902.05508 [astro-ph.CO].

[23] Steven Weinberg. "Universal Neutrino Degeneracy". In: *Phys. Rev.* 128 (1962), pp. 1457–1473. DOI: 10.1103/PhysRev.128.1457.

[24] Raymond Davis Jr., Don S. Harmer, and Kenneth C. Hoffman. "Search for neutrinos from the sun". In: *Phys. Rev. Lett.* 20 (1968), pp. 1205–1209. DOI: 10.1103/PhysRevLett.20.1205.

[25] Y. Fukuda et al. "Solar neutrino data covering solar cycle 22". In: *Phys. Rev. Lett.* 77 (1996), pp. 1683–1686. DOI: 10.1103/PhysRevLett.77.1683.

[26] W. Hampel et al. "GALLEX solar neutrino observations: Results for GALLEX IV". In: *Phys. Lett. B* 447 (1999), pp. 127–133. DOI: 10.1016/S0370-2693(98)01579-2.

[27] M. Altmann et al. "GNO solar neutrino observations: Results for GNO I". In: *Phys. Lett. B* 490 (2000), pp. 16–26. DOI: 10.1016/S0370-2693(00)00915-1. arXiv: hep-ex/0006034.

[28] J. N. Abdurashitov et al. "Solar neutrino flux measurements by the Soviet-American Gallium Experiment (SAGE) for half the 22 year solar cycle". In: *J. Exp. Theor. Phys.* 95 (2002), pp. 181–193. DOI: 10.1134/1.1506424. arXiv: astro-ph/0204245.

[29] S. N. Ahmed et al. "Measurement of the total active B-8 solar neutrino flux at the Sudbury Neutrino Observatory with enhanced neutral current sensitivity". In: *Phys. Rev. Lett.* 92 (2004), p. 181301. DOI: 10.1103/PhysRevLett.92.181301. arXiv: nucl-ex/0309004.

[30] Hans-Thomas Janka. "Neutrino Emission from Supernovae". In: *Handbook of Supernovae*. Ed. by Athem W. Alsabti and Paul Murdin. Cham: Springer International Publishing, 2017, pp. 1575–1604. ISBN: 978-3-319-21846-5. DOI: 10.1007/978-3-319-21846-5_4.

[31] K. Hirata et al. "Observation of a Neutrino Burst from the Supernova SN 1987a". In: *Phys. Rev. Lett.* 58 (1987). Ed. by K. C. Wali, pp. 1490–1493. DOI: 10.1103/PhysRevLett.58.1490.

[32] E. N. Alekseev et al. “Detection of the Neutrino Signal From SN1987A in the LMC Using the Inr Baksan Underground Scintillation Telescope”. In: *Phys. Lett. B* 205 (1988), pp. 209–214. DOI: 10.1016/0370-2693(88)91651-6.

[33] R. M. Bionta et al. “Observation of a Neutrino Burst in Coincidence with Supernova SN 1987a in the Large Magellanic Cloud”. In: *Phys. Rev. Lett.* 58 (1987), p. 1494. DOI: 10.1103/PhysRevLett.58.1494.

[34] A. Burrows. “Neutrinos From Supernova Explosions”. In: *Ann. Rev. Nucl. Part. Sci.* 40 (1990), pp. 181–212. DOI: 10.1146/annurev.ns.40.120190.001145.

[35] H. A. Bethe. “Supernova mechanisms”. In: *Rev. Mod. Phys.* 62 (1990), pp. 801–866. DOI: 10.1103/RevModPhys.62.801.

[36] Steve Dye. “Geo-neutrinos and the Radioactive Power of the Earth”. In: *Rev. Geophys.* 50 (2012), p. 3007. DOI: 10.1029/2012RG000400. arXiv: 1111.6099 [nucl-ex].

[37] Lawrence M. Krauss, Sheldon L. Glashow, and David N. Schramm. “Anti-neutrinos Astronomy and Geophysics”. In: *Nature* 310 (1984), pp. 191–198. DOI: 10.1038/310191a0.

[38] T. Araki et al. “Experimental investigation of geologically produced antineutrinos with KamLAND”. In: *Nature* 436 (2005), pp. 499–503. DOI: 10.1038/nature03980.

[39] A. Gando et al. “Partial radiogenic heat model for Earth revealed by geoneutrino measurements”. In: *Nature Geo.* 4 (2011), pp. 647–651. DOI: 10.1038/ngeo1205.

[40] G. Bellini et al. “Observation of Geo-Neutrinos”. In: *Phys. Lett. B* 687 (2010), pp. 299–304. DOI: 10.1016/j.physletb.2010.03.051. arXiv: 1003.0284 [hep-ex].

[41] M. Agostini et al. “Spectroscopy of geoneutrinos from 2056 days of Borexino data”. In: *Phys. Rev. D* 92.3 (2015), p. 031101. DOI: 10.1103/PhysRevD.92.031101. arXiv: 1506.04610 [hep-ex].

[42] M. Honda et al. “Calculation of the flux of atmospheric neutrinos”. In: *Phys. Rev. D* 52 (1995), pp. 4985–5005. DOI: 10.1103/PhysRevD.52.4985. arXiv: hep-ph/9503439.

[43] Vivek Agrawal et al. “Atmospheric neutrino flux above 1-GeV”. In: *Phys. Rev. D* 53 (1996), pp. 1314–1323. DOI: 10.1103/PhysRevD.53.1314. arXiv: hep-ph/9509423.

[44] M. G. Aartsen et al. “Observation and Characterization of a Cosmic Muon Neutrino Flux from the Northern Hemisphere using six years of IceCube data”. In: *Astrophys. J.* 833.1 (2016), p. 3. DOI: 10.3847/0004-637X/833/1/3. arXiv: 1607.08006 [astro-ph.HE].

[45] E. Richard et al. “Measurements of the atmospheric neutrino flux by Super-Kamiokande: energy spectra, geomagnetic effects, and solar modulation”. In: *Phys. Rev. D* 94.5 (2016), p. 052001. DOI: 10.1103/PhysRevD.94.052001. arXiv: 1510.08127 [hep-ex].

[46] C. V. Achar et al. “Detection of muons produced by cosmic ray neutrinos deep underground”. In: *Phys. Lett.* 18 (1965), pp. 196–199. DOI: 10.1016/0031-9163(65)90712-2.

[47] F. Reines et al. “Evidence for high-energy cosmic ray neutrino interactions”. In: *Phys. Rev. Lett.* 15 (1965), pp. 429–433. DOI: 10.1103/PhysRevLett.15.429.

[48] Y. Fukuda et al. "Atmospheric muon-neutrino electron-neutrino ratio in the multiGeV energy range". In: *Phys. Lett. B* 335 (1994), pp. 237–245. DOI: 10.1016/0370-2693(94)91420-6.

[49] Y. Ashie et al. "Evidence for an oscillatory signature in atmospheric neutrino oscillation". In: *Phys. Rev. Lett.* 93 (2004), p. 101801. DOI: 10.1103/PhysRevLett.93.101801. arXiv: hep-ex/0404034.

[50] M. G. Aartsen et al. "Evidence for High-Energy Extraterrestrial Neutrinos at the IceCube Detector". In: *Science* 342 (2013), p. 1242856. DOI: 10.1126/science.1242856. arXiv: 1311.5238 [astro-ph.HE].

[51] M. G. Aartsen et al. "Observation of High-Energy Astrophysical Neutrinos in Three Years of IceCube Data". In: *Phys. Rev. Lett.* 113 (2014), p. 101101. DOI: 10.1103/PhysRevLett.113.101101. arXiv: 1405.5303 [astro-ph.HE].

[52] M. G. Aartsen et al. "Multimessenger observations of a flaring blazar coincident with high-energy neutrino IceCube-170922A". In: *Science* 361.6398 (2018), eaat1378. DOI: 10.1126/science.aat1378. arXiv: 1807.08816 [astro-ph.HE].

[53] Yoshikazu Nagai. "Hadron Production Experiments". In: *Prospects in Neutrino Physics*. May 2017. arXiv: 1705.00532 [hep-ex].

[54] Y. Itow et al. "The JHF-Kamioka neutrino project". In: *3rd Workshop on Neutrino Oscillations and Their Origin (NOON 2001)*. June 2001, pp. 239–248. arXiv: hep-ex/0106019.

[55] B. Pontecorvo. "Mesonium and anti-mesonium". In: *Sov. Phys. JETP* 6 (1957), p. 429.

[56] B. Pontecorvo. "Inverse beta processes and nonconservation of lepton charge". In: *Zh. Eksp. Teor. Fiz.* 34 (1957), p. 247.

[57] Ziro Maki, Masami Nakagawa, and Shoichi Sakata. "Remarks on the unified model of elementary particles". In: *Prog. Theor. Phys.* 28 (1962), pp. 870–880. DOI: 10.1143/PTP.28.870.

[58] B. Pontecorvo. "Neutrino Experiments and the Problem of Conservation of Leptonic Charge". In: *Soviet Journal of Experimental and Theoretical Physics* 26 (1968), pp. 984–988.

[59] C. Athanassopoulos et al. "Candidate events in a search for anti-muon-neutrino —> anti-electron-neutrino oscillations". In: *Phys. Rev. Lett.* 75 (1995), pp. 2650–2653. DOI: 10.1103/PhysRevLett.75.2650. arXiv: nucl-ex/9504002.

[60] A. A. Aguilar-Arevalo et al. "Updated MiniBooNE neutrino oscillation results with increased data and new background studies". In: *Phys. Rev. D* 103.5 (2021), p. 052002. DOI: 10.1103/PhysRevD.103.052002. arXiv: 2006.16883 [hep-ex].

[61] Carlo Giunti and Marco Laveder. "Statistical Significance of the Gallium Anomaly". In: *Phys. Rev. C* 83 (2011), p. 065504. DOI: 10.1103/PhysRevC.83.065504. arXiv: 1006.3244 [hep-ph].

[62] Mario A. Acero, Carlo Giunti, and Marco Laveder. "The Gallium and reactor neutrinos anomaly". In: *Nucl. Phys. B Proc. Suppl.* 188 (2009), pp. 211–213. DOI: 10.1016/j.nuclphysbps.2009.02.050.

[63] V. V. Barinov et al. "Results from the Baksan Experiment on Sterile Transitions (BEST)". In: *Phys. Rev. Lett.* 128.23 (2022), p. 232501. DOI: 10.1103/PhysRevLett.128.232501. arXiv: 2109.11482 [nucl-ex].

[64] Patrick Huber. "Determination of antineutrino spectra from nuclear reactors". In: *Physical Review C* 84.2 (Aug. 2011). DOI: 10.1103/physrevc.84.024617.

[65] Th. A. Mueller et al. "Improved predictions of reactor antineutrino spectra". In: *Physical Review C* 83.5 (May 2011). DOI: 10.1103/physrevc.83.054615.

[66] Dimirty Svirida et al. "Searches for sterile neutrinos at the DANSS experiment". In: *PoS* NOW2018 (2019). Ed. by Antonio Marrone, Alessandro Mirizzi, and Daniele Montanino, p. 066. DOI: 10.22323/1.337.0066.

[67] Mikhail Danilov and Nataliya Skrobova. *New results from the DANSS experiment.* 2021. DOI: 10.48550/ARXIV.2112.13413.

[68] Y. J. Ko et al. "Sterile Neutrino Search at the NEOS Experiment". In: *Phys. Rev. Lett.* 118 (12 Mar. 2017), p. 121802. DOI: 10.1103/PhysRevLett.118.121802.

[69] H. Almazán et al. "Improved sterile neutrino constraints from the STEREO experiment with 179 days of reactor-on data". In: *Phys. Rev. D* 102 (5 Sept. 2020), p. 052002. DOI: 10.1103/PhysRevD.102.052002. URL: https://link.aps.org/doi/10.1103/PhysRevD.102.052002.

[70] M. Andriamirado et al. "Improved short-baseline neutrino oscillation search and energy spectrum measurement with the PROSPECT experiment at HFIR". In: *Phys. Rev. D* 103 (3 Feb. 2021), p. 032001. DOI: 10.1103/PhysRevD.103.032001. URL: https://link.aps.org/doi/10.1103/PhysRevD.103.032001.

[71] Alessandro Minotti. "Status of the search for light sterile neutrinos at short baselines". In: *PoS* NuFact2021 (2022), p. 246. DOI: 10.22323/1.402.0246.

[72] Carlo Giunti and T. Lasserre. "eV-scale Sterile Neutrinos". In: *Ann. Rev. Nucl. Part. Sci.* 69 (2019), pp. 163–190. DOI: 10.1146/annurev-nucl-101918-023755. arXiv: 1901.08330 [hep-ph].

[73] G. S. Abrams et al. "Measurements of Z Boson Resonance Parameters in e^+e^- Annihilation". In: *Phys. Rev. Lett.* 63 (1989), p. 2173. DOI: 10.1103/PhysRevLett.63.2173.

[74] Sebastian Böser et al. "Status of light sterile neutrino searches". In: *Progress in Particle and Nuclear Physics* 111 (Mar. 2020), p. 103736. DOI: 10.1016/j.ppnp.2019.103736.

[75] N. Aghanim et al. "Planck 2018 results. VI. Cosmological parameters". In: *Astron. Astrophys.* 641 (2020). [Erratum: Astron.Astrophys. 652, C4 (2021)], A6. DOI: 10.1051/0004-6361/201833910. arXiv: 1807.06209 [astro-ph.CO].

[76] Adam G. Riess et al. "New Parallaxes of Galactic Cepheids from Spatially Scanning theiHubble Space Telescope/i: Implications for the Hubble Constant". In: *The Astrophysical Journal* 855.2 (Mar. 2018), p. 136. DOI: 10.3847/1538-4357/aaadb7.

[77] D. M. Scolnic et al. "The Complete Light-curve Sample of Spectroscopically Confirmed SNe Ia from Pan-STARRS1 and Cosmological Constraints from the Combined Pantheon Sample". In: *Astrophys. J.* 859.2 (2018), p. 101. DOI: 10.3847/1538-4357/aab9bb. arXiv: 1710.00845 [astro-ph.CO].

[78] Robert Foot and R. R. Volkas. "Reconciling sterile neutrinos with big bang nucleosynthesis". In: *Phys. Rev. Lett.* 75 (1995), p. 4350. DOI: 10.1103/PhysRevLett.75.4350. arXiv: hep-ph/9508275.

[79] Basudeb Dasgupta and Joachim Kopp. "Cosmologically Safe eV-Scale Sterile Neutrinos and Improved Dark Matter Structure". In: *Phys. Rev. Lett.* 112.3 (2014), p. 031803. DOI: 10.1103/PhysRevLett.112.031803. arXiv: 1310.6337 [hep-ph].

[80] Xiaoyong Chu et al. "Sterile neutrinos with secret interactions—cosmological discord?" In: *JCAP* 11 (2018), p. 049. DOI: 10.1088/1475-7516/2018/11/049. arXiv: 1806.10629 [hep-ph].

[81] Carlos E. Yaguna. "Sterile neutrino production in models with low reheating temperatures". In: *JHEP* 06 (2007), p. 002. DOI: 10.1088/1126-6708/2007/06/002. arXiv: 0706.0178 [hep-ph].

[82] Srubabati Goswami et al. "Leptogenesis and eV scale sterile neutrino". In: *Phys. Rev. D* 105.9 (2022), p. 095040. DOI: 10.1103/PhysRevD.105.095040. arXiv: 2111.14719 [hep-ph].

[83] L. Wolfenstein. "Neutrino Oscillations in Matter". In: *Phys. Rev. D* 17 (1978), pp. 2369–2374. DOI: 10.1103/PhysRevD.17.2369.

[84] M. M. Guzzo and S. T. Petcov. "On the matter-enhanced transitions of solar neutrinos in the absence of neutrino mixing in vacuum". In: *Phys. Lett. B* 271 (1991), pp. 172–178. DOI: 10.1016/0370-2693(91)91295-7.

[85] M. Guzzo et al. "Status of a hybrid three neutrino interpretation of neutrino data". In: *Nucl. Phys. B* 629 (2002), pp. 479–490. DOI: 10.1016/S0550-3213(02)00139-6. arXiv: hep-ph/0112310.

[86] M. C. Gonzalez-Garcia and Michele Maltoni. "Atmospheric neutrino oscillations and new physics". In: *Phys. Rev. D* 70 (2004), p. 033010. DOI: 10.1103/PhysRevD.70.033010. arXiv: hep-ph/0404085.

[87] V. Alan Kostelecky and Stuart Samuel. "Spontaneous Breaking of Lorentz Symmetry in String Theory". In: *Phys. Rev. D* 39 (1989), p. 683. DOI: 10.1103/PhysRevD.39.683.

[88] V. Alan Kostelecký and Stuart Samuel. "Phenomenological gravitational constraints on strings and higher-dimensional theories". In: *Phys. Rev. Lett.* 63 (3 July 1989), pp. 224–227. DOI: 10.1103/PhysRevLett.63.224.

[89] V. Alan Kostelecky and Stuart Samuel. "Gravitational Phenomenology in Higher Dimensional Theories and Strings". In: *Phys. Rev. D* 40 (1989), pp. 1886–1903. DOI: 10.1103/PhysRevD.40.1886.

[90] V. Alan Kostelecky and Stuart Samuel. "Photon and Graviton Masses in String Theories". In: *Phys. Rev. Lett.* 66 (1991), pp. 1811–1814. DOI: 10.1103/PhysRevLett.66.1811.

[91] Don Colladay and V. Alan Kostelecky. "CPT violation and the standard model". In: *Phys. Rev. D* 55 (1997), pp. 6760–6774. DOI: 10.1103/PhysRevD.55.6760. arXiv: hep-ph/9703464.

[92] V. Alan Kostelecky and Robertus Potting. "CPT and strings". In: *Nucl. Phys. B* 359 (1991), pp. 545–570. DOI: 10.1016/0550-3213(91)90071-5.

[93] V. Alan Kostelecky and Robertus Potting. "CPT, strings, and meson factories". In: *Phys. Rev. D* 51 (1995), pp. 3923–3935. DOI: 10.1103/PhysRevD.51.3923. arXiv: hep-ph/9501341.

[94] Don Colladay and V. Alan Kostelecky. "Tests of direct and indirect CPT violation at a B factory". In: *Phys. Lett. B* 344 (1995), pp. 259–265. DOI: 10.1016/0370-2693(94)01600-H. arXiv: hep-ph/9501372.

[95] Don Colladay and V. Alan Kostelecky. "Testing CPT with the neutral D system". In: *Phys. Rev. D* 52 (1995), pp. 6224–6230. DOI: 10.1103/PhysRevD.52.6224. arXiv: hep-ph/9510365.

[96] Don Colladay and V. Alan Kostelecký. "CPT violation and the standard model". In: *Phys. Rev. D* 55 (11 June 1997), pp. 6760–6774. DOI: 10.1103/PhysRevD.55.6760. URL: https://link.aps.org/doi/10.1103/PhysRevD.55.6760.

[97] J. Linder. "Derivation of neutrino matter potentials induced by earth". In: (Apr. 2005). arXiv: hep-ph/0504264.

[98] S. P. Mikheyev and A. Yu. Smirnov. "Resonance Amplification of Oscillations in Matter and Spectroscopy of Solar Neutrinos". In: *Sov. J. Nucl. Phys.* 42 (1985), pp. 913–917.

[99] Gabriela Barenboim et al. "Neutrino Oscillation Probabilities through the Looking Glass". In: *Phys. Lett. B* 791 (2019), pp. 351–360. DOI: 10.1016/j.physletb.2019.03.002. arXiv: 1902.00517 [hep-ph].

[100] Sandhya Choubey and Probir Roy. "Testing whether muon neutrino flavor mixing is maximal". In: *arXiv preprint hep-ph/0310316* (2003).

[101] Ivan Esteban et al. "The fate of hints: updated global analysis of three-flavor neutrino oscillations". In: *JHEP* 09 (2020), p. 178. DOI: 10.1007/JHEP09(2020)178. arXiv: 2007.14792 [hep-ph].

[102] Evgeny K Akhmedov et al. "Series expansions for three-flavor neutrino oscillation probabilities in matter". In: *Journal of High Energy Physics* 2004.04 (2004), p. 078.

[103] Patrick Huber, M. Lindner, and W. Winter. "Simulation of long-baseline neutrino oscillation experiments with GLoBES (General Long Baseline Experiment Simulator)". In: *Comput. Phys. Commun.* 167 (2005), p. 195. DOI: 10.1016/j.cpc.2005.01.003. arXiv: hep-ph/0407333.

[104] Patrick Huber et al. "New features in the simulation of neutrino oscillation experiments with GLoBES 3.0: General Long Baseline Experiment Simulator". In: *Comput. Phys. Commun.* 177 (2007), pp. 432–438. DOI: 10.1016/j.cpc.2007.05.004. arXiv: hep-ph/0701187.

[105] John N Bahcall. "Solar neutrinos. i. theoretical". In: *Physical Review Letters* 12.11 (1964), p. 300.

[106] P. Anselmann et al. "Solar neutrinos observed by GALLEX at Gran Sasso." In: *Phys. Lett. B* 285 (1992), pp. 376–389. DOI: 10.1016/0370-2693(92)91521-A.

[107] J. N. Abdurashitov et al. "Results from SAGE". In: *Phys. Lett. B* 328 (1994), pp. 234–248. DOI: 10.1016/0370-2693(94)90454-5.

[108] H. H. Chen. "Direct Approach to Resolve the Solar Neutrino Problem". In: *Phys. Rev. Lett.* 55 (1985), pp. 1534–1536. DOI: 10.1103/PhysRevLett.55.1534.

[109] Q. R. Ahmad et al. "Measurement of the rate of $\nu_e + d \to p + p + e^-$ interactions produced by ^{8}B solar neutrinos at the Sudbury Neutrino Observatory". In: *Phys. Rev. Lett.* 87 (2001), p. 071301. DOI: 10.1103/PhysRevLett.87.071301. arXiv: nucl-ex/0106015.

[110] Q. R. Ahmad et al. "Direct evidence for neutrino flavor transformation from neutral current interactions in the Sudbury Neutrino Observatory". In: *Phys. Rev. Lett.* 89 (2002), p. 011301. DOI: 10.1103/PhysRevLett.89.011301. arXiv: nucl-ex/0204008.

[111] K. S. Hirata et al. "Experimental Study of the Atmospheric Neutrino Flux". In: *Phys. Lett. B* 205 (1988). Ed. by J. Tran Thanh Van, p. 416. DOI: 10.1016/0370-2693(88)91690-5.

[112] Maury C. Goodman. "The Atmospheric neutrino anomaly in Soudan-2". In: *Nucl. Phys. B Proc. Suppl.* 38 (1995), pp. 337–342. DOI: 10.1016/0920-5632(94)00766-O.

[113] D. Casper et al. "Measurement of atmospheric neutrino composition with IMB-3". In: *Phys. Rev. Lett.* 66 (1991), pp. 2561–2564. DOI: 10.1103/PhysRevLett.66.2561.

[114] R. Becker-Szendy et al. "The Electron-neutrino and muon-neutrino content of the atmospheric flux". In: *Phys. Rev. D* 46 (1992), pp. 3720–3724. DOI: 10.1103/PhysRevD.46.3720.

[115] Christoph Berger et al. "Study of Atmospheric Neutrino Interactions with the Frejus Detector". In: *Phys. Lett. B* 227 (1989), p. 489. DOI: 10.1016/0370-2693(89)90968-4.

[116] Christoph Berger et al. "A Study of atmospheric neutrino oscillations in the FREJUS experiment". In: *Phys. Lett. B* 245 (1990), pp. 305–310. DOI: 10.1016/0370-2693(90)90150-5.

[117] M. Aglietta et al. "Experimental study of atmospheric neutrino flux in the NUSEX experiment". In: *EPL* 8 (1989), pp. 611–614. DOI: 10.1209/0295-5075/8/7/005.

[118] Y. Fukuda et al. "Evidence for oscillation of atmospheric neutrinos". In: *Phys. Rev. Lett.* 81 (1998), pp. 1562–1567. DOI: 10.1103/PhysRevLett.81.1562. arXiv: hep-ex/9807003.

[119] Y. Fukuda et al. "Measurement of the flux and zenith angle distribution of upward through going muons by Super-Kamiokande". In: *Phys. Rev. Lett.* 82 (1999), pp. 2644–2648. DOI: 10.1103/PhysRevLett.82.2644. arXiv: hep-ex/9812014.

[120] H. Kwon et al. "Search for Neutrino Oscillations at a Fission Reactor". In: *Phys. Rev. D* 24 (1981), pp. 1097–1111. DOI: 10.1103/PhysRevD.24.1097.

[121] V. Zacek et al. "Improved Limits on Oscillation Parameters From $\bar{\nu}_e$ Disappearance Measurements at the Gosgen Power Reactor". In: *Phys. Lett. B* 164 (1985), pp. 193–198. DOI: 10.1016/0370-2693(85)90059-0.

[122] A. A. Kuvshinnikov et al. "Measuring the anti-electron-neutrino $p^+ \to n + e^+$ cross-section and beta decay axial constant in a new experiment at Rovno NPP reactor. (In Russian)". In: *Yad. Fiz.* 52 (1990), pp. 472–479.

[123] G. S. Vidyakin et al. "Limitations on the characteristics of neutrino oscillations". In: *JETP Lett.* 59 (1994), pp. 390–393.

[124] Y. Declais et al. "Search for neutrino oscillations at 15-meters, 40-meters, and 95-meters from a nuclear power reactor at Bugey". In: *Nucl. Phys. B* 434 (1995), pp. 503–534. DOI: 10.1016/0550-3213(94)00513-E.

[125] Z. D. Greenwood et al. “Results of a two position reactor neutrino oscillation experiment”. In: *Phys. Rev. D* 53 (1996), pp. 6054–6064. DOI: 10.1103/PhysRevD.53.6054.

[126] M. Apollonio et al. “Initial results from the CHOOZ long baseline reactor neutrino oscillation experiment”. In: *Phys. Lett. B* 420 (1998), pp. 397–404. DOI: 10.1016/S0370-2693(97)01476-7. arXiv: hep-ex/9711002.

[127] M. Apollonio et al. “Limits on neutrino oscillations from the CHOOZ experiment”. In: *Phys. Lett. B* 466 (1999), pp. 415–430. DOI: 10.1016/S0370-2693(99)01072-2. arXiv: hep-ex/9907037.

[128] F. Boehm et al. “Search for neutrino oscillations at the Palo Verde nuclear reactors”. In: *Phys. Rev. Lett.* 84 (2000), pp. 3764–3767. DOI: 10.1103/PhysRevLett.84.3764. arXiv: hep-ex/9912050.

[129] F. Boehm et al. “Results from the Palo Verde neutrino oscillation experiment”. In: *Phys. Rev. D* 62 (2000), p. 072002. DOI: 10.1103/PhysRevD.62.072002. arXiv: hep-ex/0003022.

[130] K. Eguchi et al. “First results from KamLAND: Evidence for reactor anti-neutrino disappearance”. In: *Phys. Rev. Lett.* 90 (2003), p. 021802. DOI: 10.1103/PhysRevLett.90.021802. arXiv: hep-ex/0212021.

[131] F. Ardellier et al. “Double Chooz: A Search for the neutrino mixing angle theta(13)”. In: (June 2006). arXiv: hep-ex/0606025.

[132] Soo-Bong Kim. “RENO: Reactor experiment for neutrino oscillation at Yonggwang”. In: *AIP Conf. Proc.* 981.1 (2008). Ed. by Kunio Inoue, Atsuto Suzuki, and Tadao Mitsui, pp. 205–207. DOI: 10.1063/1.2898934.

[133] Xinheng Guo et al. “A Precision measurement of the neutrino mixing angle θ_{13} using reactor antineutrinos at Daya-Bay”. In: (Jan. 2007). arXiv: hep-ex/0701029.

[134] P. Adamson et al. “Improved search for muon-neutrino to electron-neutrino oscillations in MINOS”. In: *Phys. Rev. Lett.* 107 (2011), p. 181802. DOI: 10.1103/PhysRevLett.107.181802. arXiv: 1108.0015 [hep-ex].

[135] M. H. Ahn et al. “Measurement of Neutrino Oscillation by the K2K Experiment”. In: *Phys. Rev. D* 74 (2006), p. 072003. DOI: 10.1103/PhysRevD.74.072003. arXiv: hep-ex/0606032.

[136] K. Abe et al. “Measurements of neutrino oscillation in appearance and disappearance channels by the T2K experiment with 6.6×10^{20} protons on target”. In: *Phys. Rev. D* 91.7 (2015), p. 072010. DOI: 10.1103/PhysRevD.91.072010. arXiv: 1502.01550 [hep-ex].

[137] K. Abe et al. “Measurement of neutrino and antineutrino oscillations by the T2K experiment including a new additional sample of ν_e interactions at the far detector”. In: *Phys. Rev. D* 96.9 (2017). [Erratum: Phys.Rev.D 98, 019902 (2018)], p. 092006. DOI: 10.1103/PhysRevD.96.092006. arXiv: 1707.01048 [hep-ex].

[138] K. Abe et al. “Combined Analysis of Neutrino and Antineutrino Oscillations at T2K”. In: *Phys. Rev. Lett.* 118.15 (2017), p. 151801. DOI: 10.1103/PhysRevLett.118.151801. arXiv: 1701.00432 [hep-ex].

[139] P. Adamson et al. “First measurement of electron neutrino appearance in NOvA”. In: *Phys. Rev. Lett.* 116.15 (2016), p. 151806. DOI: 10.1103/PhysRevLett.116.151806. arXiv: 1601.05022 [hep-ex].

[140] M. A. Acero et al. “New constraints on oscillation parameters from ν_e appearance and ν_μ disappearance in the NOvA experiment”. In: *Phys. Rev. D* 98 (2018), p. 032012. DOI: 10.1103/PhysRevD.98.032012. arXiv: 1806.00096 [hep-ex].

[141] M. A. Acero et al. “First Measurement of Neutrino Oscillation Parameters using Neutrinos and Antineutrinos by NOvA”. In: *Phys. Rev. Lett.* 123.15 (2019), p. 151803. DOI: 10.1103/PhysRevLett.123.151803. arXiv: 1906.04907 [hep-ex].

[142] A. Aguilar et al. “Evidence for neutrino oscillations from the observation of $\bar{\nu}_e$ appearance in a $\bar{\nu}_\mu$ beam”. In: *Phys. Rev. D* 64 (2001), p. 112007. DOI: 10.1103/PhysRevD.64.112007. arXiv: hep-ex/0104049.

[143] A. A. Aguilar-Arevalo et al. “Improved Search for $\bar{\nu}_\mu \to \bar{\nu}_e$ Oscillations in the MiniBooNE Experiment”. In: *Phys. Rev. Lett.* 110 (2013), p. 161801. DOI: 10.1103/PhysRevLett.110.161801. arXiv: 1303.2588 [hep-ex].

[144] Ivan Esteban et al. “Updated fit to three neutrino mixing: exploring the accelerator-reactor complementarity”. In: *JHEP* 01 (2017), p. 087. DOI: 10.1007/JHEP01(2017)087. arXiv: 1611.01514 [hep-ph].

[145] P. F. de Salas et al. “2020 global reassessment of the neutrino oscillation picture”. In: *JHEP* 02 (2021), p. 071. DOI: 10.1007/JHEP02(2021)071. arXiv: 2006.11237 [hep-ph].

[146] Francesco Capozzi et al. “Addendum to “Global constraints on absolute neutrino masses and their ordering””. In: *Physical Review D* 101.11 (June 2020). DOI: 10.1103/physrevd.101.116013.

[147] Gian Luigi Fogli, E. Lisi, and D. Montanino. “A comprehensive analysis of solar, atmospheric, accelerator and reactor neutrino experiments in a hierarchical three generation scheme”. In: *Phys. Rev. D* 49 (1994), pp. 3626–3642. DOI: 10.1103/PhysRevD.49.3626.

[148] Monojit Ghosh et al. “New look at the degeneracies in the neutrino oscillation parameters, and their resolution by T2K, NOνA and ICAL”. In: *Phys. Rev. D* 93.1 (2016), p. 013013. DOI: 10.1103/PhysRevD.93.013013. arXiv: 1504.06283 [hep-ph].

[149] Patrick Huber and Walter Winter. “Neutrino factories and the ’magic’ baseline”. In: *Phys. Rev. D* 68 (2003), p. 037301. DOI: 10.1103/PhysRevD.68.037301. arXiv: hep-ph/0301257.

[150] A. Yu. Smirnov. “Neutrino oscillations: What is ’magic’ about the magic baseline?” In: (Oct. 2006). arXiv: hep-ph/0610198.

[151] Amol Dighe, Srubabati Goswami, and Shamayita Ray. “2540 km: Bimagic Baseline for Neutrino Oscillation Parameters”. In: *Physical review letters* 105 (Dec. 2010), p. 261802. DOI: 10.1103/PHYSREVLETT.105.261802.

[152] Hisakazu Minakata and Hiroshi Nunokawa. “Exploring neutrino mixing with low-energy superbeams”. In: *JHEP* 10 (2001), p. 001. DOI: 10.1088/1126-6708/2001/10/001. arXiv: hep-ph/0108085.

[153] K. Abe et al. “Constraint on the matter–antimatter symmetry-violating phase in neutrino oscillations”. In: *Nature* 580.7803 (2020). [Erratum: Nature 583, E16 (2020)], pp. 339–344. DOI: 10.1038/s41586-020-2177-0. arXiv: 1910.03887 [hep-ex].

[154] D. S. Ayres et al. “The NOvA Technical Design Report”. In: (Oct. 2007). DOI: 10.2172/935497.

[155] Babak Abi et al. “Deep Underground Neutrino Experiment (DUNE), Far Detector Technical Design Report, Volume II: DUNE Physics”. In: (Feb. 2020). arXiv: 2002.03005 [hep-ex].

[156] A. Alekou et al. “The European Spallation Source neutrino super-beam conceptual design report”. In: (June 2022). DOI: 10.1140/epjs/s11734-022-00664-w. arXiv: 2206.01208 [hep-ex].

[157] K. Abe et al. “Physics potential of a long-baseline neutrino oscillation experiment using a J-PARC neutrino beam and Hyper-Kamiokande”. In: *PTEP* 2015 (2015), p. 053C02. DOI: 10.1093/ptep/ptv061. arXiv: 1502.05199 [hep-ex].

[158] Jürgen Brunner. “KM3NeT - ORCA”. In: *PoS* NEUTEL2017 (2018), p. 057. DOI: 10.22323/1.307.0057.

[159] M. G. Aartsen et al. “PINGU: A Vision for Neutrino and Particle Physics at the South Pole”. In: *J. Phys. G* 44.5 (2017), p. 054006. DOI: 10.1088/1361-6471/44/5/054006. arXiv: 1607.02671 [hep-ex].

[160] Shakeel Ahmed et al. “Physics Potential of the ICAL detector at the India-based Neutrino Observatory (INO)”. In: *Pramana* 88.5 (2017), p. 79. DOI: 10.1007/s12043-017-1373-4. arXiv: 1505.07380 [physics.ins-det].

[161] R. Acciarri et al. “Long-Baseline Neutrino Facility (LBNF) and Deep Underground Neutrino Experiment (DUNE)”. In: (2015). arXiv: 1512.06148 [physics.ins-det].

[162] B. Abi et al. “The DUNE Far Detector Interim Design Report Volume 1: Physics, Technology and Strategies”. In: (July 2018). arXiv: 1807.10334 [physics.ins-det].

[163] R. Abbasi et al. “The IceCube data acquisition system: Signal capture, digitization, and timestamping”. In: *Nuclear Instruments and Methods in Physics Research Section A: Accelerators, Spectrometers, Detectors and Associated Equipment* 601.3 (Apr. 2009), pp. 294–316. DOI: 10.1016/j.nima.2009.01.001.

[164] R. Abbasi et al. “Detection of astrophysical tau neutrino candidates in IceCube”. In: *Eur. Phys. J. C* 82.11 (2022), p. 1031. DOI: 10.1140/epjc/s10052-022-10795-y. arXiv: 2011.03561 [hep-ex].

[165] M. G. Aartsen et al. “Detection of a particle shower at the Glashow resonance with IceCube”. In: *Nature* 591.7849 (2021). [Erratum: Nature 592, E11 (2021)], pp. 220–224. DOI: 10.1038/s41586-021-03256-1. arXiv: 2110.15051 [hep-ex].

[166] R. Abbasi et al. “Observation of high-energy neutrinos from the Galactic plane”. In: *Science* 380.6652 (2023), adc9818. DOI: 10.1126/science.adc9818. arXiv: 2307.04427 [astro-ph.HE].

[167] K. Abe et al. “Physics potentials with the second Hyper-Kamiokande detector in Korea”. In: *PTEP* 2018.6 (2018), p. 063C01. DOI: 10.1093/ptep/pty044. arXiv: 1611.06118 [hep-ex].

[168] M. Honda et al. “Atmospheric neutrino flux calculation using the NRLMSISE-00 atmospheric model”. In: *Phys. Rev. D* 92 (2 July 2015), p. 023004. DOI: 10.1103/PhysRevD.92.023004. URL: https://link.aps.org/doi/10.1103/PhysRevD.92.023004.

[169] Vernon Barger et al. “Optimal configurations of the Deep Underground Neutrino Experiment”. In: *Int. J. Mod. Phys. A* 31.07 (2016), p. 1650020. DOI: 10.1142/S0217751X16500202. arXiv: 1405.1054 [hep-ph].

[170] T. Alion et al. “Experiment Simulation Configurations Used in DUNE CDR”. In: (June 2016). arXiv: 1606.09550 [physics.ins-det].

[171] Christoph A. Ternes et al. "Neutrino mass ordering at DUNE: An extra ν bonus". In: *Phys. Rev. D* 100 (9 Nov. 2019), p. 093004. DOI: 10.1103/PhysRevD.100.093004. URL: https://link.aps.org/doi/10.1103/PhysRevD.100.093004.

[172] T. Suzuki, D. F. Measday, and J. P. Roalsvig. "Total nuclear capture rates for negative muons". In: *Phys. Rev. C* 35 (6 June 1987), pp. 2212–2224. DOI: 10.1103/PhysRevC.35.2212. URL: https://link.aps.org/doi/10.1103/PhysRevC.35.2212.

[173] A.V. Klinskikh, S. Brianson, V.B Brudanin, et al. "Muon capture in Ar. The muon lifetime and yields of Cl isotopes". In: *Bull. Russ. Acad. Sci. Phys.* 72 (2008). DOI: 10.3103.

[174] Animesh Chatterjee, Srubabati Goswami, and Supriya Pan. "Matter effect in presence of a sterile neutrino and resolution of the octant degeneracy using a liquid argon detector". In: *Phys. Rev. D* 108.9 (2023), p. 095050. DOI: 10.1103/PhysRevD.108.095050. arXiv: 2212.02949 [hep-ph].

[175] Srubabati Goswami. "Accelerator, reactor, solar and atmospheric neutrino oscillation: Beyond three generations". In: *Phys. Rev. D* 55 (1997), pp. 2931–2949. DOI: 10.1103/PhysRevD.55.2931. arXiv: hep-ph/9507212.

[176] Mona Dentler et al. "Updated Global Analysis of Neutrino Oscillations in the Presence of eV-Scale Sterile Neutrinos". In: *JHEP* 08 (2018), p. 010. DOI: 10.1007/JHEP08(2018)010. arXiv: 1803.10661 [hep-ph].

[177] K. N. Abazajian et al. "Light Sterile Neutrinos: A White Paper". In: (Apr. 2012). arXiv: 1204.5379 [hep-ph].

[178] P. Adamson et al. "Search for sterile neutrinos in MINOS and MINOS+ using a two-detector fit". In: *Phys. Rev. Lett.* 122.9 (2019), p. 091803. DOI: 10.1103/PhysRevLett.122.091803. arXiv: 1710.06488 [hep-ex].

[179] K. Abe et al. "Search for light sterile neutrinos with the T2K far detector Super-Kamiokande at a baseline of 295 km". In: *Phys. Rev. D* 99.7 (2019), p. 071103. DOI: 10.1103/PhysRevD.99.071103. arXiv: 1902.06529 [hep-ex].

[180] David Vannerom et al. "Search for sterile neutrinos in low-energy double-cascade events with the IceCube Neutrino Observatory: a first expected sensitivity". In: *PoS* PANIC2021 (2022), p. 299. DOI: 10.22323/1.380.0299.

[181] C. A. Argüelles et al. "MicroBooNE and the Interpretation of the MiniBooNE Low-Energy Excess". In: *Phys. Rev. Lett.* 128.24 (2022), p. 241802. DOI: 10.1103/PhysRevLett.128.241802. arXiv: 2111.10359 [hep-ph].

[182] Harry Hausner. "Sterile Neutrino Search with the NOvA Detectors". PhD thesis. Wisconsin U., Madison, SAL, 2022.

[183] Zhuojun Hu. "Improved Limits on Sterile Neutrino Mixing from a Joint Search of the MINOS, MINOS+, Daya Bay, and Bugey-3 Experiments". In: *PoS* ICHEP2020 (2021), p. 201. DOI: 10.22323/1.390.0201.

[184] P. Adamson et al. "Improved Constraints on Sterile Neutrino Mixing from Disappearance Searches in the MINOS, MINOS+, Daya Bay, and Bugey-3 Experiments". In: *Phys. Rev. Lett.* 125.7 (2020), p. 071801. DOI: 10.1103/PhysRevLett.125.071801. arXiv: 2002.00301 [hep-ex].

[185] S. Gariazzo et al. "Updated Global 3+1 Analysis of Short-BaseLine Neutrino Oscillations". In: *JHEP* 06 (2017), p. 135. DOI: 10.1007/JHEP06(2017)135. arXiv: 1703.00860 [hep-ph].

[186] MicroBooNE Collaboration and P. et.al.. Abratenko. *Search for an Excess of Electron Neutrino Interactions in MicroBooNE Using Multiple Final State Topologies*. 2021. DOI: 10.48550/ARXIV.2110.14054.

[187] P. Abratenko et al. “First constraints on light sterile neutrino oscillations from combined appearance and disappearance searches with the MicroBooNE detector”. In: (Oct. 2022). arXiv: 2210.10216 [hep-ex].

[188] C. A. Argüelles et al. *MicroBooNE and the ν_e Interpretation of the MiniBooNE Low-Energy Excess*. 2021. DOI: 10.48550/ARXIV.2111.10359.

[189] Arevalo Aguilar et al. *MiniBooNE and MicroBooNE Joint Fit to a 3+1 Sterile Neutrino Scenario*. 2022. DOI: 10.48550/ARXIV.2201.01724. URL: https://arxiv.org/abs/2201.01724.

[190] M. Aker et al. “Search for keV-scale Sterile Neutrinos with first KATRIN Data”. In: (July 2022). arXiv: 2207.06337 [nucl-ex].

[191] M. Antonello et al. “A Proposal for a Three Detector Short-Baseline Neutrino Oscillation Program in the Fermilab Booster Neutrino Beam”. In: (Mar. 2015). arXiv: 1503.01520 [physics.ins-det].

[192] S. Ajimura et al. “The JSNS2 detector”. In: *Nucl. Instrum. Meth. A* 1014 (2021), p. 165742. DOI: 10.1016/j.nima.2021.165742. arXiv: 2104.13169 [physics.ins-det].

[193] K. S. Babu et al. “Addressing the short-baseline neutrino anomalies with energy-dependent mixing parameters”. In: *Phys. Rev. D* 107.1 (2023), p. 015017. DOI: 10.1103/PhysRevD.107.015017. arXiv: 2209.00031 [hep-ph].

[194] J. M. Hardin et al. “New Clues About Light Sterile Neutrinos: Preference for Models with Damping Effects in Global Fits”. In: (Nov. 2022). arXiv: 2211.02610 [hep-ph].

[195] Sanjib Kumar Agarwalla, Sabya Sachi Chatterjee, and Antonio Palazzo. “Octant of θ_{23} in danger with a light sterile neutrino”. In: *Phys. Rev. Lett.* 118.3 (2017), p. 031804. DOI: 10.1103/PhysRevLett.118.031804. arXiv: 1605.04299 [hep-ph].

[196] Sanjib Kumar Agarwalla, Suprabh Prakash, and S. Uma Sankar. “Exploring the three flavor effects with future superbeams using liquid argon detectors”. In: *JHEP* 03 (2014), p. 087. DOI: 10.1007/JHEP03(2014)087. arXiv: 1304.3251 [hep-ph].

[197] Monojit Ghosh et al. “Study of parameter degeneracy and hierarchy sensitivity of NOνA in presence of sterile neutrino”. In: *Phys. Rev. D* 96.7 (2017), p. 075018. DOI: 10.1103/PhysRevD.96.075018. arXiv: 1704.04771 [hep-ph].

[198] Sandhya Choubey, Debajyoti Dutta, and Dipyaman Pramanik. “Exploring fake solutions in the sterile neutrino sector at long-baseline experiments”. In: *The European Physical Journal C* 79.11 (Nov. 2019). DOI: 10.1140/epjc/s10052-019-7479-8.

[199] Debajyoti Dutta et al. “Capabilities of long-baseline experiments in the presence of a sterile neutrino”. In: *JHEP* 11 (2016), p. 122. DOI: 10.1007/JHEP11(2016)122. arXiv: 1607.02152 [hep-ph].

[200] Dinesh Kumar Singha et al. “Study of light sterile neutrino at the long-baseline experiment options at KM3NeT”. In: (Nov. 2022). arXiv: 2211.01816 [hep-ph].

[201] Jeffrey M. Berryman et al. “Sterile neutrino at the Deep Underground Neutrino Experiment”. In: *Phys. Rev. D* 92.7 (2015), p. 073012. DOI: 10.1103/PhysRevD.92.073012. arXiv: 1507.03986 [hep-ph].

[202] Raj Gandhi et al. “The impact of sterile neutrinos on CP measurements at long baselines”. In: *JHEP* 11 (2015), p. 039. DOI: 10.1007/JHEP11(2015)039. arXiv: 1508.06275 [hep-ph].

[203] Sanjib Kumar Agarwalla, Sabya Sachi Chatterjee, and Antonio Palazzo. “Physics Reach of DUNE with a Light Sterile Neutrino”. In: *JHEP* 09 (2016), p. 016. DOI: 10.1007/JHEP09(2016)016. arXiv: 1603.03759 [hep-ph].

[204] Yakefu Reyimuaji and Chun Liu. “Prospects of light sterile neutrino searches in long-baseline neutrino oscillations”. In: *JHEP* 06 (2020), p. 094. DOI: 10.1007/JHEP06(2020)094. arXiv: 1911.12524 [hep-ph].

[205] Peter B. Denton, Alessio Giarnetti, and Davide Meloni. “How to Identify Different New Neutrino Oscillation Physics Scenarios at DUNE”. In: (Sept. 2022). arXiv: 2210.00109 [hep-ph].

[206] Sandhya Choubey, Debajyoti Dutta, and Dipyaman Pramanik. “Imprints of a light Sterile Neutrino at DUNE, T2HK and T2HKK”. In: *Phys. Rev. D* 96.5 (2017), p. 056026. DOI: 10.1103/PhysRevD.96.056026. arXiv: 1704.07269 [hep-ph].

[207] C. Rubbia. “The Liquid Argon Time Projection Chamber: A New Concept for Neutrino Detectors”. In: (May 1977).

[208] Animesh Chatterjee et al. “Octant sensitivity for large theta(13) in atmospheric and long baseline neutrino experiments”. In: *JHEP* 06 (2013), p. 010. DOI: 10.1007/JHEP06(2013)010. arXiv: 1302.1370 [hep-ph].

[209] Vernon Barger et al. “Configuring the Long-Baseline Neutrino Experiment”. In: *Phys. Rev. D* 89.1 (2014), p. 011302. DOI: 10.1103/PhysRevD.89.011302. arXiv: 1307.2519 [hep-ph].

[210] Raj Gandhi et al. “Resolving the Mass Hierarchy with Atmospheric Neutrinos using a Liquid Argon Detector”. In: *Phys. Rev. D* 78 (2008), p. 073001. DOI: 10.1103/PhysRevD.78.073001. arXiv: 0807.2759 [hep-ph].

[211] Stephen J Parke and Xining Zhang. “Compact Perturbative Expressions for Oscillations with Sterile Neutrinos in Matter”. In: *Phys. Rev. D* 101.5 (2020), p. 056005. DOI: 10.1103/PhysRevD.101.056005. arXiv: 1905.01356 [hep-ph].

[212] Wei Li et al. “Matter effect of light sterile neutrino: an exact analytical approach”. In: *Journal of High Energy Physics* 2018.10 (Oct. 2018). DOI: 10.1007/jhep10(2018)021.

[213] S. P. Behera et al. “Search for the sterile neutrino mixing with the ICAL detector at INO”. In: *Eur. Phys. J. C* 77.5 (2017), p. 307. DOI: 10.1140/epjc/s10052-017-4851-4. arXiv: 1605.08607 [hep-ph].

[214] Raj Gandhi and Pomita Ghoshal. “Atmospheric neutrinos as a probe of eV^2-scale active-sterile oscillations”. In: *Phys. Rev. D* 86 (2012), p. 037301. DOI: 10.1103/PhysRevD.86.037301. arXiv: 1108.4360 [hep-ph].

[215] Tarak Thakore et al. “Active-sterile neutrino oscillations at INO-ICAL over a wide mass-squared range”. In: *JHEP* 08 (2018), p. 022. DOI: 10.1007/JHEP08(2018)022. arXiv: 1804.09613 [hep-ph].

[216] M. A. Acero et al. “White Paper on Light Sterile Neutrino Searches and Related Phenomenology”. In: (Mar. 2022). arXiv: 2203.07323 [hep-ex].

[217] M. C. Banuls, G. Barenboim, and J. Bernabeu. “Medium effects for terrestrial and atmospheric neutrino oscillations”. In: *Phys. Lett. B* 513 (2001), pp. 391–400. DOI: 10.1016/S0370-2693(01)00723-7. arXiv: hep-ph/0102184.

[218] Raj Gandhi et al. “Mass Hierarchy Determination via future Atmospheric Neutrino Detectors”. In: *Phys. Rev. D* 76 (2007), p. 073012. DOI: 10.1103/PhysRevD.76.073012. arXiv: 0707.1723 [hep-ph].

[219] Sandhya Choubey and Probir Roy. “Probing the deviation from maximal mixing of atmospheric neutrinos”. In: *Phys. Rev. D* 73 (2006), p. 013006. DOI: 10.1103/PhysRevD.73.013006. arXiv: hep-ph/0509197.

[220] Babak Abi et al. “Deep Underground Neutrino Experiment (DUNE), Far Detector Technical Design Report, Volume I Introduction to DUNE”. In: *JINST* 15.08 (2020), T08008. DOI: 10.1088/1748-0221/15/08/T08008. arXiv: 2002.02967 [physics.ins-det].

[221] R. Acciarri et al. “Long-Baseline Neutrino Facility (LBNF) and Deep Underground Neutrino Experiment (DUNE): Conceptual Design Report, Volume 1: The LBNF and DUNE Projects”. In: (Jan. 2016). arXiv: 1601.05471 [physics.ins-det].

[222] Animesh Chatterjee, Srubabati Goswami, and Supriya Pan. “Probing mass orderings in presence of a very light sterile neutrino in a liquid argon detector”. In: *Nucl. Phys. B* 996 (2023), p. 116370. DOI: 10.1016/j.nuclphysb.2023.116370. arXiv: 2307.12885 [hep-ph].

[223] B. Armbruster et al. “Upper limits for neutrino oscillations muon-anti-neutrino —> electron-anti-neutrino from muon decay at rest”. In: *Phys. Rev. D* 65 (2002), p. 112001. DOI: 10.1103/PhysRevD.65.112001. arXiv: hep-ex/0203021.

[224] A. A. Aguilar-Arevalo et al. “The MiniBooNE Detector”. In: *Nucl. Instrum. Meth. A* 599 (2009), pp. 28–46. DOI: 10.1016/j.nima.2008.10.028. arXiv: 0806.4201 [hep-ex].

[225] A. A. Aguilar-Arevalo et al. “A Search for Electron Neutrino Appearance at the $\Delta m^2 \sim 1eV^2$ Scale”. In: *Phys. Rev. Lett.* 98 (2007), p. 231801. DOI: 10.1103/PhysRevLett.98.231801. arXiv: 0704.1500 [hep-ex].

[226] W. Hampel et al. “Final results of the Cr-51 neutrino source experiments in GALLEX”. In: *Phys. Lett. B* 420 (1998), pp. 114–126. DOI: 10.1016/S0370-2693(97)01562-1.

[227] J. N. Abdurashitov et al. “Measurement of the response of the Russian-American gallium experiment to neutrinos from a Cr-51 source”. In: *Phys. Rev. C* 59 (1999), pp. 2246–2263. DOI: 10.1103/PhysRevC.59.2246. arXiv: hep-ph/9803418.

[228] V. V. Barinov et al. “Search for electron-neutrino transitions to sterile states in the BEST experiment”. In: *Phys. Rev. C* 105.6 (2022), p. 065502. DOI: 10.1103/PhysRevC.105.065502. arXiv: 2201.07364 [nucl-ex].

[229] Peter Minkowski. “$\mu \to e\gamma$ at a Rate of One Out of 10^9 Muon Decays?” In: *Phys. Lett. B* 67 (1977), pp. 421–428. DOI: 10.1016/0370-2693(77)90435-X.

[230] Rabindra N. Mohapatra and Goran Senjanovic. “Neutrino Mass and Spontaneous Parity Nonconservation”. In: *Phys. Rev. Lett.* 44 (1980), p. 912. DOI: 10.1103/PhysRevLett.44.912.

[231] J. Schechter and J. W. F. Valle. “Neutrino Masses in SU(2) x U(1) Theories”. In: *Phys. Rev. D* 22 (1980), p. 2227. DOI: 10.1103/PhysRevD.22.2227.

[232] M. Fukugita and T. Yanagida. “Baryogenesis Without Grand Unification”. In: *Phys. Lett. B* 174 (1986), pp. 45–47. DOI: 10.1016/0370-2693(86)91126-3.

[233] Sacha Davidson, Enrico Nardi, and Yosef Nir. “Leptogenesis”. In: *Phys. Rept.* 466 (2008), pp. 105–177. DOI: 10.1016/j.physrep.2008.06.002. arXiv: 0802.2962 [hep-ph].

[234] Thomas Appelquist and Robert Shrock. “Neutrino masses in theories with dynamical electroweak symmetry breaking”. In: *Phys. Lett. B* 548 (2002), pp. 204–214. DOI: 10.1016/S0370-2693(02)02854-X. arXiv: hep-ph/0204141.

[235] Thomas Appelquist and Robert Shrock. “Dynamical symmetry breaking of extended gauge symmetries”. In: *Phys. Rev. Lett.* 90 (2003), p. 201801. DOI: 10.1103/PhysRevLett.90.201801. arXiv: hep-ph/0301108.

[236] Scott Dodelson and Lawrence M. Widrow. “Sterile-neutrinos as dark matter”. In: *Phys. Rev. Lett.* 72 (1994), pp. 17–20. DOI: 10.1103/PhysRevLett.72.17. arXiv: hep-ph/9303287.

[237] P. C. de Holanda and A. Yu. Smirnov. “Solar neutrino spectrum, sterile neutrinos and additional radiation in the Universe”. In: *Phys. Rev. D* 83 (2011), p. 113011. DOI: 10.1103/PhysRevD.83.113011. arXiv: 1012.5627 [hep-ph].

[238] André de Gouvêa, Giancarlo Jusino Sánchez, and Kevin J. Kelly. “Very light sterile neutrinos at NOvA and T2K”. In: *Phys. Rev. D* 106.5 (2022), p. 055025. DOI: 10.1103/PhysRevD.106.055025. arXiv: 2204.09130 [hep-ph].

[239] Arman Esmaili et al. “Probing light sterile neutrinos in medium baseline reactor experiments”. In: *Phys. Rev. D* 88 (2013), p. 073012. DOI: 10.1103/PhysRevD.88.073012. arXiv: 1308.6218 [hep-ph].

[240] Antonio Palazzo. “Constraints on very light sterile neutrinos from θ_{13}-sensitive reactor experiments”. In: *JHEP* 10 (2013), p. 172. DOI: 10.1007/JHEP10(2013)172. arXiv: 1308.5880 [hep-ph].

[241] Ivan Girardi et al. “Constraining Sterile Neutrinos Using Reactor Neutrino Experiments”. In: *JHEP* 08 (2014), p. 057. DOI: 10.1007/JHEP08(2014)057. arXiv: 1405.6540 [hep-ph].

[242] F. P. An et al. “Search for a Light Sterile Neutrino at Daya Bay”. In: *Phys. Rev. Lett.* 113 (2014), p. 141802. DOI: 10.1103/PhysRevLett.113.141802. arXiv: 1407.7259 [hep-ex].

[243] Feng Peng An et al. “Improved Search for a Light Sterile Neutrino with the Full Configuration of the Daya Bay Experiment”. In: *Phys. Rev. Lett.* 117.15 (2016), p. 151802. DOI: 10.1103/PhysRevLett.117.151802. arXiv: 1607.01174 [hep-ex].

[244] David O. Caldwell, George M. Fuller, and Yong-Zhong Qian. “Sterile neutrinos and supernova nucleosynthesis”. In: *Phys. Rev. D* 61 (2000), p. 123005. DOI: 10.1103/PhysRevD.61.123005. arXiv: astro-ph/9910175.

[245] Irene Tamborra et al. “Impact of eV-mass sterile neutrinos on neutrino-driven supernova outflows”. In: *JCAP* 01 (2012), p. 013. DOI: 10.1088/1475-7516/2012/01/013. arXiv: 1110.2104 [astro-ph.SR].

[246] Dibya S. Chattopadhyay et al. “Sterile neutrinos: propagation in matter and sensitivity to sterile mass ordering”. In: *JHEP* 02 (2023), p. 044. DOI: 10.1007/JHEP02(2023)044. arXiv: 2211.03473 [hep-ph].

[247] Monojit Ghosh et al. “Implications of the DLMA Solution of θ_{12} for IceCube Data Using Different Astrophysical Sources”. In: *Universe* 9.9 (2023), p. 380. DOI: 10.3390/universe9090380. arXiv: 2306.11653 [hep-ph].

[248] Andre de Gouvea, Alexander Friedland, and Hitoshi Murayama. “The Dark side of the solar neutrino parameter space”. In: *Phys. Lett. B* 490 (2000), pp. 125–130. DOI: 10.1016/S0370-2693(00)00989-8. arXiv: hep-ph/0002064.

[249] Sandhya Choubey et al. “SNO and the solar neutrino problem”. In: *Conference on Physics Beyond the Standard Model: Beyond the Desert 02*. Sept. 2002, pp. 291–305. arXiv: hep-ph/0209222.

[250] O. G. Miranda, M. A. Tortola, and J. W. F. Valle. “Are solar neutrino oscillations robust?” In: *JHEP* 10 (2006), p. 008. DOI: 10.1088/1126-6708/2006/10/008. arXiv: hep-ph/0406280.

[251] M. C. Gonzalez-Garcia and Michele Maltoni. “Determination of matter potential from global analysis of neutrino oscillation data”. In: *JHEP* 09 (2013), p. 152. DOI: 10.1007/JHEP09(2013)152. arXiv: 1307.3092 [hep-ph].

[252] *Neutrino Non-Standard Interactions: A Status Report*. Vol. 2. 2019, p. 001. DOI: 10.21468/SciPostPhysProc.2.001. arXiv: 1907.00991 [hep-ph].

[253] Pilar Coloma and Thomas Schwetz. “Generalized mass ordering degeneracy in neutrino oscillation experiments”. In: *Phys. Rev. D* 94.5 (2016). [Erratum: Phys.Rev.D 95, 079903 (2017)], p. 055005. DOI: 10.1103/PhysRevD.94.055005. arXiv: 1604.05772 [hep-ph].

[254] Sandhya Choubey and Dipyaman Pramanik. “On Resolving the Dark LMA Solution at Neutrino Oscillation Experiments”. In: *JHEP* 12 (2020), p. 133. DOI: 10.1007/JHEP12(2020)133. arXiv: 1912.08629 [hep-ph].

[255] K. N. Vishnudath, Sandhya Choubey, and Srubabati Goswami. “New sensitivity goal for neutrinoless double beta decay experiments”. In: *Phys. Rev. D* 99.9 (2019), p. 095038. DOI: 10.1103/PhysRevD.99.095038. arXiv: 1901.04313 [hep-ph].

[256] Pilar Coloma et al. “COHERENT Enlightenment of the Neutrino Dark Side”. In: *Phys. Rev. D* 96.11 (2017), p. 115007. DOI: 10.1103/PhysRevD.96.115007. arXiv: 1708.02899 [hep-ph].

[257] Peter B. Denton, Yasaman Farzan, and Ian M. Shoemaker. “Testing large non-standard neutrino interactions with arbitrary mediator mass after COHERENT data”. In: *JHEP* 07 (2018), p. 037. DOI: 10.1007/JHEP07(2018)037. arXiv: 1804.03660 [hep-ph].

[258] Pilar Coloma et al. “Curtailing the Dark Side in Non-Standard Neutrino Interactions”. In: *JHEP* 04 (2017), p. 116. DOI: 10.1007/JHEP04(2017)116. arXiv: 1701.04828 [hep-ph].

[259] Ivan Esteban et al. “Updated constraints on non-standard interactions from global analysis of oscillation data”. In: *JHEP* 08 (2018). [Addendum: JHEP 12, 152 (2020)], p. 180. DOI: 10.1007/JHEP08(2018)180. arXiv: 1805.04530 [hep-ph].

[260] Pilar Coloma et al. "Global constraints on non-standard neutrino interactions with quarks and electrons". In: (May 2023). arXiv: 2305.07698 [hep-ph].

[261] Eli Waxman and John N. Bahcall. "High-energy neutrinos from astrophysical sources: An Upper bound". In: *Phys. Rev. D* 59 (1999), p. 023002. DOI: 10.1103/PhysRevD.59.023002. arXiv: hep-ph/9807282.

[262] Svenja Hummer, Philipp Baerwald, and Walter Winter. "Neutrino Emission from Gamma-Ray Burst Fireballs, Revised". In: *Phys. Rev. Lett.* 108 (2012), p. 231101. DOI: 10.1103/PhysRevLett.108.231101. arXiv: 1112.1076 [astro-ph.HE].

[263] Reetanjali Moharana and Nayantara Gupta. "Tracing Cosmic accelerators with Decaying Neutrons". In: *Phys. Rev. D* 82 (2010), p. 023003. DOI: 10.1103/PhysRevD.82.023003. arXiv: 1005.0250 [astro-ph.HE].

[264] H. Athar, M. Jezabek, and O. Yasuda. "Effects of neutrino mixing on high-energy cosmic neutrino flux". In: *Phys. Rev. D* 62 (2000), p. 103007. DOI: 10.1103/PhysRevD.62.103007. arXiv: hep-ph/0005104.

[265] Werner Rodejohann. "Neutrino Mixing and Neutrino Telescopes". In: *JCAP* 01 (2007), p. 029. DOI: 10.1088/1475-7516/2007/01/029. arXiv: hep-ph/0612047.

[266] Davide Meloni and Tommy Ohlsson. "Leptonic CP violation and mixing patterns at neutrino telescopes". In: *Phys. Rev. D* 86 (2012), p. 067701. DOI: 10.1103/PhysRevD.86.067701. arXiv: 1206.6886 [hep-ph].

[267] Olga Mena, Sergio Palomares-Ruiz, and Aaron C. Vincent. "Flavor Composition of the High-Energy Neutrino Events in IceCube". In: *Phys. Rev. Lett.* 113 (2014), p. 091103. DOI: 10.1103/PhysRevLett.113.091103. arXiv: 1404.0017 [astro-ph.HE].

[268] Animesh Chatterjee et al. "Probing CP violation with the first three years of ultrahigh energy neutrinos from IceCube". In: *Phys. Rev. D* 90.7 (2014), p. 073003. DOI: 10.1103/PhysRevD.90.073003. arXiv: 1312.6593 [hep-ph].

[269] R. Abbasi et al. "The IceCube high-energy starting event sample: Description and flux characterization with 7.5 years of data". In: *Phys. Rev. D* 104 (2021), p. 022002. DOI: 10.1103/PhysRevD.104.022002. arXiv: 2011.03545 [astro-ph.HE].

[270] Supriya Pan, Kaustav Chakraborty, and Srubabati Goswami. "Sensitivity to CP Discovery in the Presence of Lorentz Invariance Violating Potential at T2HK/T2HKK". In: (Aug. 2023). arXiv: 2308.07566 [hep-ph].

[271] "Hyper-Kamiokande Design Report". In: (Feb. 2016).

[272] Deepak Raikwal, Sandhya Choubey, and Monojit Ghosh. "Comprehensive study of LIV in atmospheric and long-baseline experiments". In: (Mar. 2023). arXiv: 2303.10892 [hep-ph].

[273] Ushak Rahaman. "Looking for Lorentz invariance violation (LIV) in the latest long baseline accelerator neutrino oscillation data". In: *Eur. Phys. J. C* 81.9 (2021), p. 792. DOI: 10.1140/epjc/s10052-021-09598-4. arXiv: 2103.04576 [hep-ph].

[274] Rudra Majhi et al. "Distinguishing nonstandard interaction and Lorentz invariance violation at the Protvino to super-ORCA experiment". In: *Phys. Rev. D* 107.7 (2023), p. 075036. DOI: 10.1103/PhysRevD.107.075036. arXiv: 2212.07244 [hep-ph].

[275] Sadashiv Sahoo et al. “Discriminating between Lorentz violation and non-standard interactions using core-passing atmospheric neutrinos at INO-ICAL”. In: *Phys. Lett. B* 841 (2023), p. 137949. DOI: 10.1016/j.physletb.2023.137949.

[276] M. Aker et al. “Search for Lorentz-invariance violation with the first KATRIN data”. In: *Phys. Rev. D* 107.8 (2023), p. 082005. DOI: 10.1103/PhysRevD.107.082005. arXiv: 2207.06326 [nucl-ex].

[277] Nishat Fiza, Nafis Rezwan Khan Chowdhury, and Mehedi Masud. “Investigating Lorentz Invariance Violation with the long baseline experiment P2O”. In: *JHEP* 01 (2023), p. 076. DOI: 10.1007/JHEP01(2023)076. arXiv: 2206.14018 [hep-ph].

[278] Chengyi Li and Bo-Qiang Ma. “Lorentz- and CPT-violating neutrinos from string/D-brane model”. In: *Phys. Lett. B* 835 (2022), p. 137543. DOI: 10.1016/j.physletb.2022.137543. arXiv: 2211.00900 [hep-ph].

[279] Barbara Skrzypek and Carlos A. Argüelles. “Lorentz Violation in Neutrino Oscillations using IceCube Atmospheric Neutrino Interferometry”. In: (Feb. 2023). arXiv: 2302.08998 [hep-ph].

[280] Chengyi Li and Bo-Qiang Ma. “Lorentz and CPT breaking in gamma-ray burst neutrinos from string theory”. In: *JHEP* 03 (2023), p. 230. DOI: 10.1007/JHEP03(2023)230. arXiv: 2303.04765 [hep-ph].

[281] Sanjib Kumar Agarwalla and Mehedi Masud. “Can Lorentz invariance violation affect the sensitivity of deep underground neutrino experiment?” In: *Eur. Phys. J. C* 80.8 (2020), p. 716. DOI: 10.1140/epjc/s10052-020-8303-1. arXiv: 1912.13306 [hep-ph].

[282] Rudra Majhi, Soumya Chembra, and Rukmani Mohanta. “Exploring the effect of Lorentz invariance violation with the currently running long-baseline experiments”. In: *Eur. Phys. J. C* 80.5 (2020), p. 364. DOI: 10.1140/epjc/s10052-020-7963-1. arXiv: 1907.09145 [hep-ph].

[283] J. B. Albert et al. “First Search for Lorentz and CPT Violation in Double Beta Decay with EXO-200”. In: *Phys. Rev. D* 93.7 (2016), p. 072001. DOI: 10.1103/PhysRevD.93.072001. arXiv: 1601.07266 [nucl-ex].

[284] B. Aharmim et al. “Tests of Lorentz invariance at the Sudbury Neutrino Observatory”. In: *Phys. Rev. D* 98.11 (2018), p. 112013. DOI: 10.1103/PhysRevD.98.112013. arXiv: 1811.00166 [hep-ex].

[285] K. Abe et al. “Test of Lorentz invariance with atmospheric neutrinos”. In: *Phys. Rev. D* 91.5 (2015), p. 052003. DOI: 10.1103/PhysRevD.91.052003. arXiv: 1410.4267 [hep-ex].

[286] M. G. Aartsen et al. “Neutrino Interferometry for High-Precision Tests of Lorentz Symmetry with IceCube”. In: *Nature Phys.* 14.9 (2018), pp. 961–966. DOI: 10.1038/s41567-018-0172-2. arXiv: 1709.03434 [hep-ex].

[287] Mehedi Masud, Samiran Roy, and Poonam Mehta. “Correlations and degeneracies among the NSI parameters with tunable beams at DUNE”. In: *Phys. Rev. D* 99.11 (2019), p. 115032. DOI: 10.1103/PhysRevD.99.115032. arXiv: 1812.10290 [hep-ph].

[288] Joachim Kopp et al. “Non-standard neutrino interactions in reactor and superbeam experiments”. In: *Phys. Rev. D* 77 (2008), p. 013007. DOI: 10.1103/PhysRevD.77.013007. arXiv: 0708.0152 [hep-ph].

[289] Kaoru Hagiwara, Naotoshi Okamura, and Ken-ichi Senda. "Physics potential of T2KK: An Extension of the T2K neutrino oscillation experiment with a far detector in Korea". In: *Phys. Rev. D* 76 (2007), p. 093002. DOI: 10.1103/PhysRevD.76.093002. arXiv: hep-ph/0607255.

[290] Tommy Ohlsson and Hakan Snellman. "Three flavor neutrino oscillations in matter". In: *J. Math. Phys.* 41 (2000). [Erratum: J.Math.Phys. 42, 2345 (2001)], pp. 2768–2788. DOI: 10.1063/1.533270. arXiv: hep-ph/9910546.

[291] Yuki Kamo et al. "Analytical calculations of four neutrino oscillations in matter". In: *Eur. Phys. J. C* 28 (2003), pp. 211–221. DOI: 10.1140/epjc/s2003-01138-0. arXiv: hep-ph/0209097.

[292] Evgeny K. Akhmedov et al. "Series expansions for three flavor neutrino oscillation probabilities in matter". In: *JHEP* 04 (2004), p. 078. DOI: 10.1088/1126-6708/2004/04/078. arXiv: hep-ph/0402175.

[293] M. G. Aartsen et al. "First observation of PeV-energy neutrinos with IceCube". In: *Phys. Rev. Lett.* 111 (2013), p. 021103. DOI: 10.1103/PhysRevLett.111.021103. arXiv: 1304.5356 [astro-ph.HE].

[294] C. S. Wu et al. "Experimental Test of Parity Conservation in β Decay". In: *Phys. Rev.* 105 (1957), pp. 1413–1414. DOI: 10.1103/PhysRev.105.1413.

[295] G. Bellini et al. "Measurement of geo-neutrinos from 1353 days of Borexino". In: *Phys. Lett. B* 722 (2013), pp. 295–300. DOI: 10.1016/j.physletb.2013.04.030. arXiv: 1303.2571 [hep-ex].

[296] Stephen M. Barr et al. "Ratio of ν_e/ν_μ in Atmospheric Neutrinos". In: *Phys. Lett. B* 214 (1988), pp. 147–150. DOI: 10.1016/0370-2693(88)90468-6.

[297] Monojit Ghosh. "Present Aspects and Future Prospects of Neutrino Mass and Oscillation". In: *arXiv preprint arXiv:1603.04514* (2016).

[298] Ma Concepción Gonzalez-Garcia and Michele Maltoni. "Atmospheric neutrino oscillations and new physics". In: *Physical Review D* 70.3 (2004), p. 033010.

[299] P. M. Mathews and K. Venkatesan. *A Textbook of Quantum Mechanics*. McGraw-Hill Book Co, 1978.

[300] Mohan Narayan et al. "Solar and atmospheric neutrino oscillations with three flavors". In: *Phys. Rev. D* 53 (5 Mar. 1996), pp. 2809–2819. DOI: 10.1103/PhysRevD.53.2809. URL: https://link.aps.org/doi/10.1103/PhysRevD.53.2809.

[301] James E. Hill. "Results from the LSND neutrino oscillation search for anti-muon-neutrino —> anti-electron-neutrino". In: *Phys. Rev. Lett.* 75 (1995), pp. 2654–2657. DOI: 10.1103/PhysRevLett.75.2654. arXiv: hep-ex/9504009.

[302] C. A. Argüelles et al. "New opportunities at the next-generation neutrino experiments I: BSM neutrino physics and dark matter". In: *Rept. Prog. Phys.* 83.12 (2020), p. 124201. DOI: 10.1088/1361-6633/ab9d12. arXiv: 1907.08311 [hep-ph].

[303] B. Abi et al. "Prospects for beyond the Standard Model physics searches at the Deep Underground Neutrino Experiment". In: *Eur. Phys. J. C* 81.4 (2021), p. 322. DOI: 10.1140/epjc/s10052-021-09007-w. arXiv: 2008.12769 [hep-ex].

[304] Monojit Ghosh et al. "Can atmospheric neutrino experiments provide the first hint of leptonic CP violation?" In: *Phys. Rev. D* 89.1 (2014), p. 011301. DOI: 10.1103/PhysRevD.89.011301. arXiv: 1306.2500 [hep-ph].

[305] Monojit Ghosh et al. “Evidence for leptonic CP phase from NOνA, T2K and ICAL: A chronological progression”. In: *Nucl. Phys. B* 884 (2014), pp. 274–304. DOI: 10.1016/j.nuclphysb.2014.04.013. arXiv: 1401.7243 [hep-ph].

[306] Anushree Ghosh, Tarak Thakore, and Sandhya Choubey. “Determining the Neutrino Mass Hierarchy with INO, T2K, NOvA and Reactor Experiments”. In: *JHEP* 04 (2013), p. 009. DOI: 10.1007/JHEP04(2013)009. arXiv: 1212.1305 [hep-ph].

[307] Kaustav Chakraborty et al. “Enhancing the hierarchy and octant sensitivity of ESSνSB in conjunction with T2K, NOνA and ICAL@INO”. In: *JHEP* 05 (2019), p. 137. DOI: 10.1007/JHEP05(2019)137. arXiv: 1902.02963 [hep-ph].

[308] Shinya Fukasawa, Monojit Ghosh, and Osamu Yasuda. “Complementarity Between Hyperkamiokande and DUNE in Determining Neutrino Oscillation Parameters”. In: *Nucl. Phys. B* 918 (2017), pp. 337–357. DOI: 10.1016/j.nuclphysb.2017.02.008. arXiv: 1607.03758 [hep-ph].

[309] Monojit Ghosh. “Reason for T2K to run in dominant neutrino mode for detecting CP violation”. In: *Phys. Rev. D* 93.7 (2016), p. 073003. DOI: 10.1103/PhysRevD.93.073003. arXiv: 1512.02226 [hep-ph].

[310] Alessandro Strumia. “Interpreting the LSND anomaly: Sterile neutrinos or CPT violation or...?” In: *Phys. Lett. B* 539 (2002), pp. 91–101. DOI: 10.1016/S0370-2693(02)02042-7. arXiv: hep-ph/0201134.

[311] Tamer Tolba. “The ESS based neutrino Super Beam Experiment (ESSνSB)”. In: *PoS* PANIC2021 (2022), p. 284. DOI: 10.22323/1.380.0284.

[312] A. A. Aguilar-Arevalo et al. “Unexplained Excess of Electron-Like Events From a 1-GeV Neutrino Beam”. In: *Phys. Rev. Lett.* 102 (2009), p. 101802. DOI: 10.1103/PhysRevLett.102.101802. arXiv: 0812.2243 [hep-ex].

[313] C. Giunti et al. “Reactor antineutrino anomaly in light of recent flux model refinements”. In: *Phys. Lett. B* 829 (2022), p. 137054. DOI: 10.1016/j.physletb.2022.137054. arXiv: 2110.06820 [hep-ph].

[314] M. C. Gonzalez-Garcia et al. “Probing long-range leptonic forces with solar and reactor neutrinos”. In: *JCAP* 01 (2007), p. 005. DOI: 10.1088/1475-7516/2007/01/005. arXiv: hep-ph/0609094.

[315] Tommy Ohlsson. “Status of non-standard neutrino interactions”. In: *Rept. Prog. Phys.* 76 (2013), p. 044201. DOI: 10.1088/0034-4885/76/4/044201. arXiv: 1209.2710 [hep-ph].

[316] Z. G. Berezhiani and M. I. Vysotsky. “Neutrino Decay in Matter”. In: *Phys. Lett. B* 199 (1987), p. 281. DOI: 10.1016/0370-2693(87)91375-X.

[317] Dibya S. Chattopadhyay et al. “Analytic treatment of 3-flavor neutrino oscillation and decay in matter”. In: (Apr. 2022). arXiv: 2204.05803 [hep-ph].

[318] Raj Gandhi et al. “Earth matter effects at very long baselines and the neutrino mass hierarchy”. In: *Phys. Rev. D* 73 (5 Mar. 2006), p. 053001. DOI: 10.1103/PhysRevD.73.053001.

[319] T. Alion et al. “Experiment Simulation Configurations Used in DUNE CDR”. In: (2016). arXiv: 1606.09550 [physics.ins-det].

[320] Pilar Coloma, David V. Forero, and Stephen J. Parke. “DUNE Sensitivities to the Mixing between Sterile and Tau Neutrinos”. In: *JHEP* 07 (2018), p. 079. DOI: 10.1007/JHEP07(2018)079. arXiv: 1707.05348 [hep-ph].

[321] Joachim Kopp. “Sterile neutrinos and non-standard neutrino interactions in GLoBES”. In: *https://www.mpi-hd.mpg.de/personalhomes/globes/tools/snu-1.0.pdf* (2010).

[322] Mario A. Acero, Carlo Giunti, and Marco Laveder. “Limits on nu(e) and anti-nu(e) disappearance from Gallium and reactor experiments”. In: *Phys. Rev.* D78 (2008), p. 073009. DOI: 10.1103/PhysRevD.78.073009. arXiv: 0711.4222 [hep-ph].

[323] G. Mention et al. “The Reactor Antineutrino Anomaly”. In: *Phys. Rev.* D83 (2011), p. 073006. DOI: 10.1103/PhysRevD.83.073006. arXiv: 1101.2755 [hep-ex].

[324] P. Adamson et al. “Limits on Active to Sterile Neutrino Oscillations from Disappearance Searches in the MINOS, Daya Bay, and Bugey-3 Experiments”. In: *Phys. Rev. Lett.* 117.15 (2016). [Addendum: Phys. Rev. Lett. **117**, 209901 (2016)], p. 151801. DOI: 10.1103/PhysRevLett.117.151801, 10.1103/PhysRevLett.117.209901.

[325] Ziro Maki, Masami Nakagawa, and Shoichi Sakata. “Remarks on the unified model of elementary particles”. In: *Prog. Theor. Phys.* 28 (1962), pp. 870–880. DOI: 10.1143/PTP.28.870.

[326] B. Pontecorvo. “Neutrino Experiments and the Problem of Conservation of Leptonic Charge”. In: *Sov. Phys. JETP* 26 (1968). [Zh. Eksp. Teor. Fiz. 53, 1717 (1967)], pp. 984–988.

[327] V. N. Gribov and B. Pontecorvo. “Neutrino astronomy and lepton charge”. In: *Phys. Lett.* 28B (1969), p. 493. DOI: 10.1016/0370-2693(69)90525-5.

[328] Y. Fukuda et al. “Evidence for oscillation of atmospheric neutrinos”. In: *Phys. Rev. Lett.* 81 (1998), pp. 1562–1567. DOI: 10.1103/PhysRevLett.81.1562. arXiv: hep-ex/9807003 [hep-ex].

[329] C. Patrignani et al. “Review of Particle Physics”. In: *Chin. Phys.* C40.10 (2016), p. 100001. DOI: 10.1088/1674-1137/40/10/100001.

[330] K. N. Abazajian et al. “Light Sterile Neutrinos: A White Paper”. In: (2012). arXiv: 1204.5379 [hep-ph].

[331] B. Pontecorvo. “Mesonium and anti-mesonium”. In: *Sov. Phys. JETP* 6 (1957). [Zh. Eksp. Teor. Fiz.33,549(1957)], p. 429.

[332] P. Adamson et al. “Search for active-sterile neutrino mixing using neutral-current interactions in NOvA”. In: *Phys. Rev.* D96.7 (2017), p. 072006. DOI: 10.1103/PhysRevD.96.072006. arXiv: 1706.04592 [hep-ex].

[333] P. Adamson et al. “Search for Sterile Neutrinos Mixing with Muon Neutrinos in MINOS”. In: *Phys. Rev. Lett.* 117 (2016), p. 151803.

[334] K. Abe et al. In: *Phys. Rev. D* 91 (2015), p. 052019.

[335] M. G. Aartsen et al. In: *Phys. Rev. Lett.* 117 (2016), p. 071801.

[336] M. G. Aartsen et al. “Search for sterile neutrino mixing using three years of IceCube DeepCore data”. In: *Phys. Rev. D* 95.11 (2017), p. 112002.

[337] Jeffrey M. Berryman et al. “Sterile neutrino at the Deep Underground Neutrino Experiment”. In: *Phys. Rev.* D92.7 (2015), p. 073012. DOI: 10.1103/PhysRevD.92.073012. arXiv: 1507.03986 [hep-ph].

[338] Ivan Esteban et al. "The fate of hints: updated global analysis of three-flavor neutrino oscillations". In: *Journal of High Energy Physics* 2020.9 (Sept. 2020). DOI: 10.1007/jhep09(2020)178.

[339] Monojit Ghosh et al. *Parameter degeneracy and hierarchy sensitivity of NOνA in presence of sterile neutrino*. 2017. DOI: 10.48550/ARXIV.1712.06714.

[340] Monojit Ghosh, Srubabati Goswami, and Sushant K. Raut. "Maximizing the DUNE early physics output with current experiments". In: *Eur. Phys. J. C* 76.3 (2016), p. 114. DOI: 10.1140/epjc/s10052-016-3962-7. arXiv: 1412.1744 [hep-ph].

[341] T. K. Gaisser and M. Honda. "Flux of atmospheric neutrinos". In: *Ann. Rev. Nucl. Part. Sci.* 52 (2002), pp. 153–199. DOI: 10.1146/annurev.nucl.52.050102.090645. arXiv: hep-ph/0203272.

[342] Peter B. Denton. "Sterile Neutrino Search with MicroBooNE's Electron Neutrino Disappearance Data". In: *Phys. Rev. Lett.* 129.6 (2022), p. 061801. DOI: 10.1103/PhysRevLett.129.061801. arXiv: 2111.05793 [hep-ph].

[343] Carlo Bemporad, Giorgio Gratta, and Petr Vogel. "Reactor Based Neutrino Oscillation Experiments". In: *Rev. Mod. Phys.* 74 (2002), p. 297. DOI: 10.1103/RevModPhys.74.297. arXiv: hep-ph/0107277.

[344] M. Estienne et al. "Updated Summation Model: An Improved Agreement with the Daya Bay Antineutrino Fluxes". In: *Phys. Rev. Lett.* 123.2 (2019), p. 022502. DOI: 10.1103/PhysRevLett.123.022502. arXiv: 1904.09358 [nucl-ex].

[345] D. A. Dwyer and T. J. Langford. "Spectral Structure of Electron Antineutrinos from Nuclear Reactors". In: *Phys. Rev. Lett.* 114.1 (2015), p. 012502. DOI: 10.1103/PhysRevLett.114.012502. arXiv: 1407.1281 [nucl-ex].

[346] Marco Drewes. "The Phenomenology of Right Handed Neutrinos". In: *Int. J. Mod. Phys. E* 22 (2013), p. 1330019. DOI: 10.1142/S0218301313300191. arXiv: 1303.6912 [hep-ph].

[347] Alexander Kusenko. "Sterile neutrinos: The Dark side of the light fermions". In: *Phys. Rept.* 481 (2009), pp. 1–28. DOI: 10.1016/j.physrep.2009.07.004. arXiv: 0906.2968 [hep-ph].

[348] A. A. Aguilar-Arevalo et al. "Measurement of muon neutrino quasi-elastic scattering on carbon". In: *Phys. Rev. Lett.* 100 (2008), p. 032301. DOI: 10.1103/PhysRevLett.100.032301. arXiv: 0706.0926 [hep-ex].

[349] A. A. Aguilar-Arevalo et al. "MiniBooNE and MicroBooNE Combined Fit to a 3+1 Sterile Neutrino Scenario". In: *Phys. Rev. Lett.* 129.20 (2022), p. 201801. DOI: 10.1103/PhysRevLett.129.201801. arXiv: 2201.01724 [hep-ex].

[350] Alexis A. Aguilar-Arevalo et al. "A Search for muon neutrino and antineutrino disappearance in MiniBooNE". In: *Phys. Rev. Lett.* 103 (2009), p. 061802. DOI: 10.1103/PhysRevLett.103.061802. arXiv: 0903.2465 [hep-ex].

[351] Ivan Esteban et al. "Updated fit to three neutrino mixing: exploring the accelerator-reactor complementarity". In: *JHEP* 2017 (2017), p. 87.

[352] V. V. Barinov et al. *Results from the Baksan Experiment on Sterile Transitions (BEST)*. 2021. DOI: 10.48550/ARXIV.2109.11482.

[353] S. Kumar Agarwalla, Suprabh Prakash, and S. Uma Sankar. "Hierarchy and Octant Determination Potential of LBNE and LBNO". In: *PoS* EPS-HEP2013 (2013), p. 534. DOI: 10.22323/1.180.0534.

[354] Monojit Ghosh et al. “Parameter degeneracy and hierarchy sensitivity of NOνA in presence of sterile neutrino”. In: *PoS* NuFact2017 (2018), p. 133. DOI: 10.22323/1.295.0133. arXiv: 1712.06714 [hep-ph].

[355] K. Abe et al. “Measurements of neutrino oscillation parameters from the T2K experiment using 3.6×10^{21} protons on target”. In: (Mar. 2023). arXiv: 2303.03222 [hep-ex].

[356] M. A. Acero et al. “Improved measurement of neutrino oscillation parameters by the NOvA experiment”. In: *Phys. Rev. D* 106.3 (2022), p. 032004. DOI: 10.1103/PhysRevD.106.032004. arXiv: 2108.08219 [hep-ex].

[357] V. Alan Kostelecký and R. Potting. “Expectation values, Lorentz invariance, and CPT in the open bosonic string”. In: *Physics Letters B* 381.1-3 (July 1996), pp. 89–96. DOI: 10.1016/0370-2693(96)00589-8.

[358] Takashi Kikuchi, Hisakazu Minakata, and Shoichi Uchinami. “Perturbation theory of neutrino oscillation with nonstandard neutrino interactions”. In: *Journal of High Energy Physics* 2009.03 (Mar. 2009), pp. 114–114. DOI: 10.1088/1126-6708/2009/03/114.

[359] Kaoru Hagiwara et al. “Physics potential of neutrino oscillation experiment with a far detector in Oki Island along the T2K baseline”. In: *JHEP* 06 (2013), p. 036. DOI: 10.1007/JHEP06(2013)036. arXiv: 1209.2763 [hep-ph].